



HAL
open science

Magnétisme dans les Étoiles Froides Évoluées

Stefan Georgiev Mikhov

► **To cite this version:**

Stefan Georgiev Mikhov. Magnétisme dans les Étoiles Froides Évoluées. Astrophysique [astro-ph]. Université Montpellier; Institute of Astronomy and National Astronomical Observatory, Bulgarian Academy of Sciences, Sofia, 2021. Français. NNT : 2021MONT098 . tel-03599880

HAL Id: tel-03599880

<https://theses.hal.science/tel-03599880>

Submitted on 7 Mar 2022

HAL is a multi-disciplinary open access archive for the deposit and dissemination of scientific research documents, whether they are published or not. The documents may come from teaching and research institutions in France or abroad, or from public or private research centers.

L'archive ouverte pluridisciplinaire **HAL**, est destinée au dépôt et à la diffusion de documents scientifiques de niveau recherche, publiés ou non, émanant des établissements d'enseignement et de recherche français ou étrangers, des laboratoires publics ou privés.

THÈSE POUR OBTENIR LE GRADE DE DOCTEUR DE L'UNIVERSITÉ DE MONTPELLIER

En Astrophysique

École doctorale: Information, Structures, Systèmes

Unité de recherche: Laboratoire Univers et Particules de Montpellier

En partenariat international avec Institute of Astronomy and National Astronomical Observatory,
Bulgarian Academy of Science, Sofia

Magnétisme dans les Étoiles Froides Évoluées

Présentée par Stefan Georgiev

Le 10 décembre 2021

Sous la direction de Agnès Lèbre
et Renada Konstantinova-Antova

Devant le jury composé de

Dr. Antoaneta Antonova, Associate Professor, IA and NAO, Bulgarian Academy of Science

Dr. Andrea Chiavassa, CRCN-CNRS, Observatoire de la cote d'Azur

Dr. Fabrice Herpin, Astronome, LAB, Observatoire de Bordeaux

Dr. Renada Konstantinova-Antova, Professor, IA and NAO, Bulgarian Academy of Science

Dr. Agnès Lèbre, Astronome, LUPM, Université de Montpellier

Dr. Dragomir Marchev, Professor, Faculty of Natural Sciences, Shumen University

Dr. Ana Palacios, Astronome, LUPM, Université de Montpellier

Examinatrice

Rapporteur

Rapporteur

Co-directrice de thèse

Co-directrice de thèse

Examineur

Présidente



UNIVERSITÉ
DE MONTPELLIER

*The journey begins with curiosity
and evolves into soul-felt questions
on the stones that we walk
and choose to make our path:
sometimes never knowing,
other times knowing too much.*

Chuck Schuldiner

Contents

Contents	i
Preamble	v
1 Magnetism in red giant and supergiant stars	1
1.1 Classification of stars	2
1.2 Evolution of single stars after the Main Sequence	4
1.2.1 Evolution of low- and intermediate mass stars	4
1.2.2 Evolution of high mass stars	10
1.3 Magnetism in the Sun, solar-type dynamo and Rossby number	12
1.3.1 Solar-type dynamo	12
1.3.2 Rossby number	14
1.3.3 Effects of magnetism in the Sun	15
1.4 Magnetism in single stars at the giant branches	17
1.5 Magnetic fields in Mira and post-AGB stars	21
1.6 Magnetism in RSG stars	21
1.7 Magnetism in cool evolved stars: aims of the study	25
2 Spectropolarimetric observations, methods & tools	27
2.1 Spectropolarimetry: basic concepts	28
2.1.1 Polarization of light	28
2.1.2 Stokes parameters	29
2.1.3 The Zeeman effect	30
2.2 Observations with Narval	33
2.3 Least Square Deconvolution	37
2.3.1 The method	37
2.3.2 Classifying the detection of polarized signatures	41
2.4 Measuring the longitudinal magnetic field	41
2.5 Spectral activity indicators	41
2.6 NeoNarval	43

2.7	Adapting NeoNarval data to the Narval format	45
2.8	Treating the data	46
3	Magnetism in M giant stars	51
3.1	RZ Arietis	53
3.1.1	Observations	54
3.1.2	Magnetic field variability	55
3.1.3	Radial velocity variability and atmospheric dynamics	57
3.1.4	Linear polarization	59
3.1.5	Measuring stellar rotation and macroturbulence via spectrum synthesis and multi-line analysis	61
3.1.6	Determination of stellar parameters in RZ Ari	70
3.1.7	Paper published in <i>Astronomische Nachrichten</i>	72
3.1.8	Period search	80
3.1.9	Mass and evolutionary status	84
3.1.10	Lithium abundance. Planet engulfment scenario and possible dynamo action	86
3.2	β Pegasi	88
3.2.1	Observations	88
3.2.2	Magnetic field variability	89
3.2.3	Radial velocity variability and atmospheric dynamics	92
3.2.4	Linear polarization	92
3.3	EK Boötis	95
3.3.1	Observations	95
3.3.2	Magnetic field variability	97
3.3.3	Radial velocity variability and atmospheric dynamics	98
3.3.4	Linear polarization	98
3.3.5	Paper published in <i>Bulgarian Astronomical Journal</i>	101
4	Surface magnetism in the post-AGB star R Scuti	113
4.1	Introduction	115
4.2	Observations and data treatment	116
4.2.1	Observations	116
4.2.2	LSD line masks	119
4.3	The surface magnetic field	122
4.3.1	The origin of circular polarization	124
4.3.2	Timescales of variation	125
4.4	Atmospheric dynamics	125
4.4.1	Variability of the H α line	126
4.4.2	The Schwarzschild mechanism	128
4.4.3	Variability of metallic lines	128
4.4.4	Atmospheric dynamics: summary	130
4.5	The surface magnetic field: a refined approach	132
4.5.1	Line selection by excitation potential	134

CONTENTS

4.5.2	Magnetism at the photospheric level	138
4.6	Linear polarization	142
4.7	Summary	142
5	Imaging the photosphere of Betelgeuse through spectropolarimetry	145
5.1	Introduction	147
5.2	The method for 2D surface imaging	149
5.2.1	Discovery of linear polarization in the spectrum of Betelgeuse . . .	149
5.2.2	First mapping of bright spots	151
5.2.3	Giant convective cells and imaging through spectropolarimetry . .	152
5.3	The path to 3D-imaging of Betelgeuse	159
5.3.1	Analysing the intensity profiles	159
5.3.2	Characteristic velocities	160
5.3.3	Gray atmosphere	161
5.3.4	The linearly polarized profiles: an in-depth view	164
5.4	Building the 3D-images	167
5.5	Reading the 3D-images	170
5.6	Results and conclusion	171
5.7	Paper accepted for Astronomy & Astrophysics	173
6	Summary, main contributions and future prospects	187
6.1	Summary and main contributions	188
6.1.1	M giant stars	188
6.1.2	R Scuti	189
6.1.3	Betelgeuse	189
6.2	Future prospects	191
6.2.1	M giant stars	192
6.2.2	R Scuti	195
6.2.3	Betelgeuse and other RSG stars	196
	Acknowledgements	197
	Bibliography	199

CONTENTS

Preamble

My PhD is a cotutelle (a joint PhD program) between the *Institute of Astronomy and National Astronomical Observatory* at the Bulgarian Academy of Science (IA & NAO, BAS), situated in Sofia, Bulgaria, and *Laboratoire Univers et Particules de Montpellier* at the University of Montpellier (LUPM, UM), situated in Montpellier, France. As a cotutelle PhD student, I spent roughly half of the three years of my PhD at the LUPM in Montpellier, and the other half - at the IA in Sofia. This allowed me to work directly with both of my PhD supervisors, as well as with other colleagues in both Bulgaria and France. This was a fantastic experience for me, both from a professional and from a personal point of view. It also meant that I had to comply with the requirements of both the BAS and UM for their PhD students, which, along with the frequent changes of location – moving between Bulgaria and France – was often quite time-consuming.

As a PhD student of the BAS, I had to follow certain educational courses, namely: a foreign language course (in English); a course in informatics of my choice (*Statistics with the "R" programming language*); two specialized courses in astrophysics, related closely to the topic of my PhD research. According to the BAS regulations, I also had to take a special exam, called a *doctoral minimum*. This was an exam, both written and oral, during which I was required to demonstrate knowledge in both the theory of stellar atmospheres and the specific topic of my research – magnetism in cool stars. To prepare for the doctoral minimum exam, I spent a little over one month of my PhD. The preparation for this exam was very beneficial for me, especially for the study of the convective motions at the level of the photosphere of Betelgeuse. I was also required by the BAS to have a certain minimum of scientific activity (presentations at international conferences and papers published or submitted to peer-reviewed journals with an impact factor).

As a PhD student of the UM, I had to follow courses (*modules doctoraux de la formation complémentaire*, amounting to 100h) which cover topics outside of my field of research. To fulfill this requirement, I took an introductory course in French. While in Montpellier, I also followed a technical course in observational astronomy – *Forma-*

tion aux Observations de Service au Télescope Bernard Lyot, FOST. I also visited the *Pic du Midi* observatory twice, for periods of one week, to obtain spectropolarimetric observations with the TBL in service mode. Visiting Pic du Midi was a very pleasant experience for me.

I had the misfortune to pursue my PhD during the COVID-19 international crisis. Certain international conferences I wanted to participate in were cancelled, as were also all summer schools in astrophysics. Travelling in general was also either very difficult, or impossible.

In February and March 2021, I was very fortunate to work at the *Institut de Recherche en Astrophysique et Planétologie (IRAP)* in Toulouse, France, under the mentorship of Dr. Arturo López Ariste, with whom we studied the convective motions at the photosphere of the red supergiant Betelgeuse, and created a method for the 3D-imaging of the surface of this star. This two-months stay in Toulouse was possible thanks to the ERASMUS EU program for doctoral mobility.

According to the cotutelle agreement, my PhD defense is to take place at the University of Montpellier, France.

Magnetism in red giant and supergiant stars

In this chapter, I will introduce the class of objects under study in my Thesis: the cool evolved stars. I will first describe the main changes these stars undergo in the course of their evolution. I will then describe key points about magnetism in red giant and supergiant stars, using the case of the Sun as a reference. Finally, I will introduce the particular stars that I study and list the scientific aims of my Thesis.

Summary

1.1	Classification of stars	2
1.2	Evolution of single stars after the Main Sequence	4
1.2.1	Evolution of low- and intermediate mass stars	4
1.2.2	Evolution of high mass stars	10
1.3	Magnetism in the Sun, solar-type dynamo and Rossby number	12
1.3.1	Solar-type dynamo	12
1.3.2	Rossby number	14
1.3.3	Effects of magnetism in the Sun	15
1.4	Magnetism in single stars at the giant branches	17
1.5	Magnetic fields in Mira and post-AGB stars	21
1.6	Magnetism in RSG stars	21
1.7	Magnetism in cool evolved stars: aims of the study	25

1.1 Classification of stars

In stellar astrophysics, it is customary to classify stars according to their luminosity L and effective temperature T_{eff} (the temperature of a blackbody with the same spectral energy distribution). Stars can have a wide range of effective temperatures, reaching as high as about 35000 K for the hottest ones and less than 3000 K for the coolest ones. Typically, classification is done by grouping stars by their spectral type, which has a close relation to temperature: in the temperature range given above, stars can have a spectral type O, B, A, F, G, K or M, where O-stars are the hottest and M-stars are the coolest. Also, within each spectral type, there exist subtypes numbered from 1 to 9, where 1 is the hottest and 9 is the coolest (for example, an M1 star has a higher effective temperature than an M9 one). Stars can also cover an even wider range of luminosities: if L_{\odot} is the luminosity of the Sun, then the brightest stars can have $L \sim 10^6 L_{\odot}$, and the faintest ones – $L \sim 10^{-4} L_{\odot}$. There also exist different luminosity classes, labelled with roman numbers from I (most luminous) to V (least luminous).

Stars can also be quite different in terms of size. Since the geometrical shape of stars is usually very close to a sphere, their size is described by their radius R . If again we use the Sun as a reference with its radius R_{\odot} , then the largest of stars can have radii $R \sim 10^3 R_{\odot}$, while the smallest ones have $R \sim 10^{-2} R_{\odot}$ (de Boer & Seggewiss, 2008). This huge range of radii justifies the fact that stars are often referred to as "supergiants", "giants" or "dwarfs".

To classify stars, it is usual to locate their position on a diagram with temperature (or equivalently, spectral type) on the horizontal axis, increasing from right to left, and luminosity on the vertical axis. This is the so called *Hertzsprung–Russell diagram* (HRD), shown in Figure 1.1. The HRD is important because it gives more information about stars than just their luminosity and effective temperature. It turns out that depending on their evolutionary stage, stars cluster in different parts of the HRD. An important region on the HRD is the Main Sequence (MS): a streak spanning from the top left to the bottom right of the HRD, populated with stars that burn hydrogen in their cores. It is the longest period in the course of stellar evolution.

The cool evolved stars considered in this Thesis have already spent their time on the MS and have parted from it. Such stars are generally located to the right of the MS and above it, towards lower effective temperatures and higher luminosities. In the next section, we will follow the course of their evolution once they leave the MS and go on to become giants or supergiants.

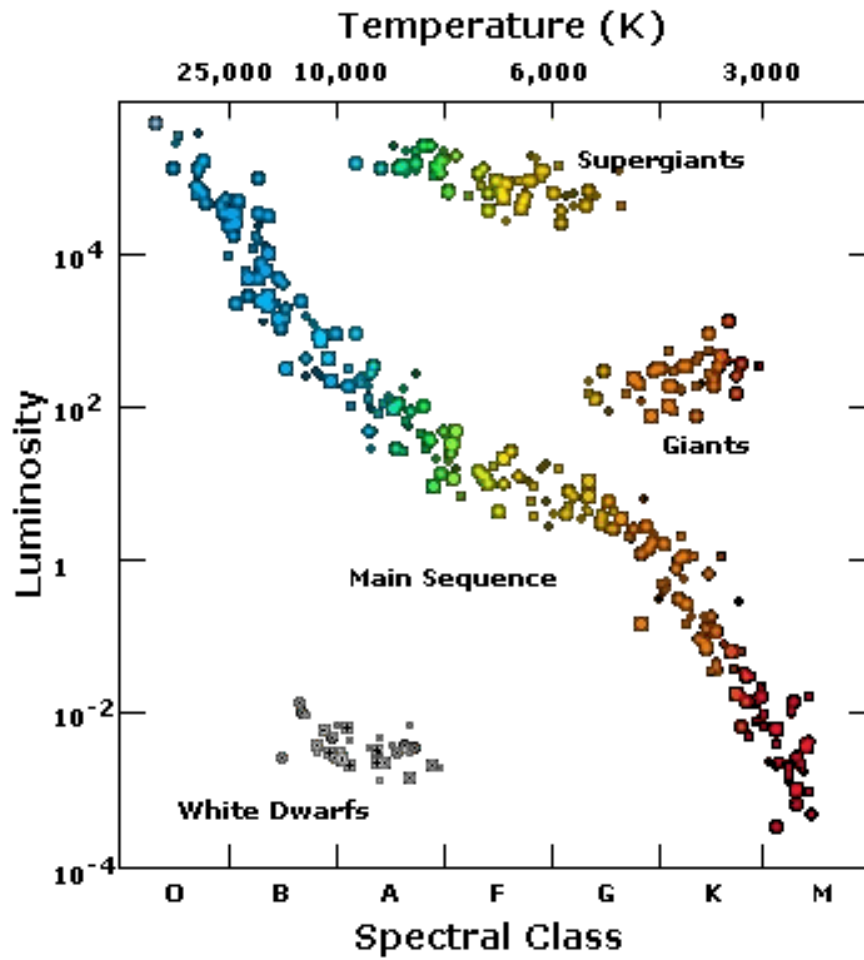


Figure 1.1: HRD. Luminosity is in solar units, L_{\odot} . Image credit: <http://astro.physics.uiowa.edu>.

1.2 Evolution of single stars after the Main Sequence

The position a star has on the MS mostly depends on its mass: more massive stars of early spectral types (O, B, A) are found in the top, more luminous regions of the MS; stars of lower mass and later spectral types (F, G, K, M) are found in its bottom right regions. The course of evolution after the MS also depends on the mass of the star: low- ($M < 1.5M_{\odot}$) and intermediate ($1.5M_{\odot} < M < 8M_{\odot}$) mass stars evolve in a different way from high ($M > 8M_{\odot}$) mass ones (de Boer & Seggewiss, 2008).

1.2.1 Evolution of low- and intermediate mass stars

The subgiant stage

Stars with initial mass $M \leq 1.15M_{\odot}$ burn hydrogen (H) mainly through the proton-proton (PP) chain and have no convection in their cores (de Boer & Seggewiss, 2008). Still, due to the high temperatures present there, particles move at high velocities and mixing occurs. Helium (He) clusters in the center due to its higher molar mass. As the temperature grows, H begins to burn in the outer layers of the core. When the concentration of He in the stellar core becomes high enough, the PP-chain reactions cease. In this way, the star will undergo a smooth transition from core H-burning to shell H-burning, which also leads to a smooth increase in luminosity.

Stars with initial mass $M > 1.15M_{\odot}$ (de Boer & Seggewiss, 2008) have temperatures in their cores high enough to burn H via the carbon-nitrogen-oxygen (CNO) cycle. In this case, the temperature gradient inside the core is very steep, which leads to convection inside the stellar core. Convection transports H-rich material from the shell to the He-rich core and vice versa. When the portion of hydrogen in the core decreases below a certain limit, H-burning ceases somewhat abruptly, leading to a decrease in the temperature of the core, and it begins to contract. Due to the contraction, the temperature and pressure in the shell increase, leading to the onset of shell H-burning.

In both cases (with and without convection in the core), once H-burning begins to occur in a shell in the periphery of the core, the star leaves the MS and becomes a subgiant (luminosity class IV).

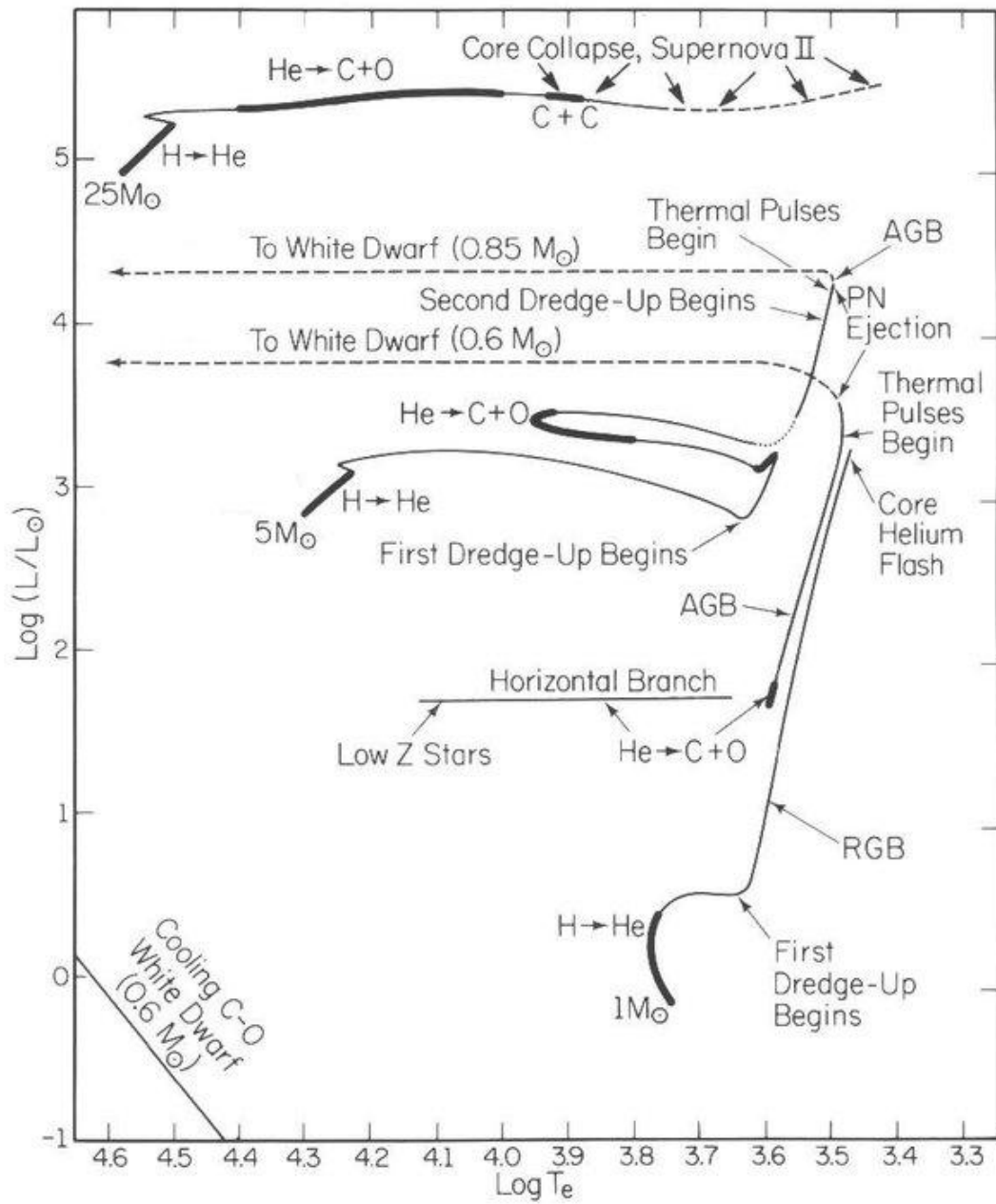


Figure 1.2: Evolutionary tracks on the HRD of stars with $1M_{\odot}$, $5M_{\odot}$ and $25M_{\odot}$. Figure adapted from Iben (1985).

The red giant stage

As the star contracts gravitationally, the temperature at the core and in the H-burning shell increases, and with it increases the rate of shell H-burning. At a certain point in time, the temperature gradient in the envelope becomes steep enough for convection to take place. Once the envelope becomes convective, the star moves on the red giant branch (RGB, luminosity class III) of the HRD, where it spends time $t_{\text{RGB}} \sim 0.1t_{\text{MS}}$ (de Boer & Seggewiss, 2008). A schematic view of the inner structure of an RGB star is shown in Figure 1.3.

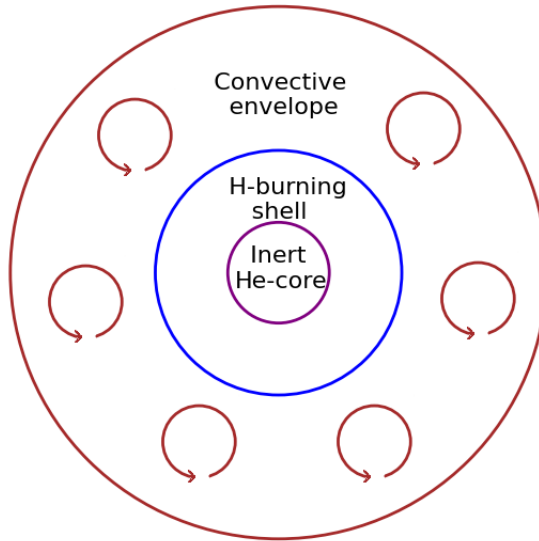


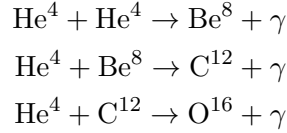
Figure 1.3: Schematic view of the inner structure of a red giant. Not to scale.

When the convective envelope reaches the core regions where there is material processed in the core H-burning reactions, convection lifts this material and takes it to the upper layers. This is called the *first dredge-up* stage. The first dredge-up occurs in the very beginning of the RGB and causes an increase in the surface abundance of He and in the N/C ratio. Lithium (Li) is also destroyed during this stage, causing its observed abundance to decrease. Another indicator for the first dredge-up stage is the $^{12}\text{C}/^{13}\text{C}$ ratio (90 in the Solar case) which decreases to about 20-25 (Dearborn et al., 1976). It is possible that the first dredge-up also transfers angular momentum from the core to the convective envelope, increasing the observed rotational velocity of red giants and decreasing their rotational period (Simon & Drake, 1989; Mosser et al., 2012). The convective zone reaches its maximum span in altitude in the end of the first dredge-up phase, after which its bottom end begins to recede towards the surface.

Helium flash and core He-burning

Shell H-burning increases the He abundance in the core and so, its mass also increases. The core contracts and grows in temperature. For stars with lower mass ($M < 2M_{\odot}$),

the contraction causes degeneracy of the electron gas in the core. Once the pressure of the degenerate electron gas balances the force of gravity, the contraction stops. At this stage, the star has a degenerate He core, a burning H shell, a convective envelope and a large atmosphere. At the tip of the RGB, the temperature and pressure at the core are sufficient for He-burning to occur via the so-called triple-alpha process which fuses He into berilium (Be), carbon (C) and oxygen (O):



The triple-alpha process runs differently for the stars with degenerate cores ($M < 2M_{\odot}$) and for those without such cores ($M > 2M_{\odot}$). He-burning increases the temperature in the core, but in the case of a degenerate gas this does not increase the pressure and the core does not expand. The rate of the triple-alpha process depends very strongly on temperature; for the stars with degenerate He cores, this causes a runaway reaction called a *helium flash*: a sudden release of a large amount of energy which is mostly used to take off the degeneracy of the core. In intermediate mass stars, helium flash does not occur, and instead the triple-alpha process increases the pressure in the core, causing it to expand and cool down. In this way, core He-burning occurs at a steady pace in such stars.

The onset of He-burning in the core leads to an increase in the effective temperature and contraction of the overall radius of the star. On the HRD, the star moves down and left, descending off the RGB and onto what is called the helium Main Sequence (He MS). This evolutionary stage is the second longest one after the MS stage. During it, the main source of energy is the core He-burning. The He MS runs somewhat parallel to the MS. However, since core He-burning stars have a hydrogen envelope with high opacity, they are redder than MS stars and so are shifted towards the right on the HRD. Stars that have thin H-envelopes (stars with small initial masses or which have experienced mass loss during the RGB stage) are less affected by this reddening due to the lower opacity of their envelopes.

Low mass stars ($0.6M_{\odot} < M_{\text{MS}} < 2M_{\odot}$) form the so called *horizontal branch* (HB) which appears on the HRD as a horizontal streak from the He MS on the left to the RGB on the right. Intermediate mass stars ($2M_{\odot} < M_{\text{MS}} < 8M_{\odot}$) after the tip-RGB stage perform what is known as a *blue loop* on the HRD, initially moving left (towards a higher temperature) and then slightly up and right (towards a higher luminosity and a lower temperature; see the evolutionary track of a $5M_{\odot}$ star on Figure 1.2). During this long evolutionary stage ($\sim 20\%t_{\text{MS}}$) these stars may cross a region of the HRD known as the *instability strip* and be observed as Cepheid or WW Virginis variables.

The asymptotic giant branch

Once the star has exhausted He in its core, the degenerate C+O core contracts and the temperature of the shell increases; the shell expands and becomes convective. However, since the conditions in the star are now different from those at the RGB stage, it appears bluer than during the RGB. Its evolutionary path on the HRD approaches the RGB asymptotically, hence this stage is called the *asymptotic giant branch* (AGB). During the AGB stage, He-burning occurs in a shell around the electron degenerate C+O core. AGB stars have very extended envelopes with complex structure (see Figure 1.4 for a schematic view of an AGB star). Above the pulsating photosphere of an AGB star, a very extended ($\sim 10^3 R_\odot$) and cool atmosphere can be found, where the low temperatures allow for the formation of dust and molecules of different elements, and where shock waves may be propagating. Due to the significant mass loss stars experienced during the AGB stage because of the combination of pulsations, a very extended atmosphere and low surface gravity, a circumstellar envelope (CSE) is also present around these stars.

During the first part of this evolutionary stage, called the *early-AGB* phase, the mass and size of the C+O core increases due to the shell He-burning, while the He-burning zone moves radially outwards. In stars with $3M_\odot < M < 5M_\odot$, a *second dredge-up* event occurs. Similarly to the first dredge-up event, this happens when core He-burning ceases and the growing convective envelope reaches the degenerate C+O core. The surface abundance of ^4He and ^{14}N increases, while that of ^{12}O and ^{16}C decreases.

Mira stars are pulsating variables that belong to the AGB. They are known to undergo severe mass loss (between 10^{-7} and $10^{-4} M_\odot \text{yr}^{-1}$), the mechanism behind which is probably radiation pressure on dust (Willson, 2000).

When the expanding He-burning shell reaches the H/He discontinuity, He-burning ceases and the overlying H-shell contracts, causing it to heat up and to ignite H-burning reactions. This marks the beginning of the *thermally pulsating AGB* (TP-AGB) phase. A thermal pulse occurs because as H burns, more and more He is built up on top of the degenerate C+O core. This He layer is compressed and heated by the H-burning shell, and when it reaches a critical mass, the triple-alpha process occurs in a runaway reaction. This event is called a helium shell flash and most of its energy goes into heating up and expanding the overlying layers of the star. As this material expands, the newly ignited He-burning shell also expands and the runaway reaction continues in a quiescent state. Once the He in it is exhausted, H-burning begins again and another thermal pulse can occur.

After the helium shell flash, the convective envelope extends inwards, leading to the *third dredge-up* event, which may bring products of He-burning (mainly C) and heavy s-elements (elements heavier than iron, produced through slow neutron captures) closer to the surface, thus changing the observed chemical composition of the star.

The thermal pulses continue to repeat until the mass of the H-burning shell decreases below a critical value. Once this happens, the star leaves the AGB and moves leftward

on the HRD towards higher effective temperatures. Thermal pulses also contribute to the mass loss of AGB stars.

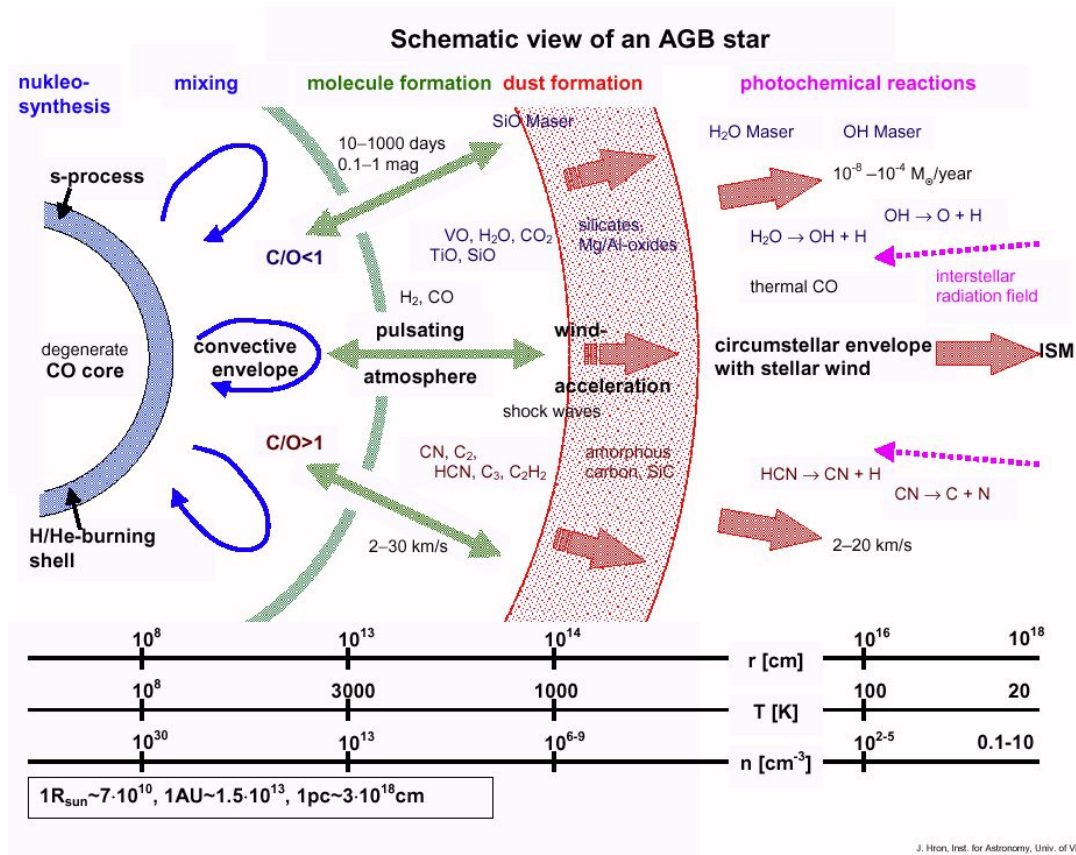


Figure 1.4: Schematic view of an AGB star. The complex structure of the atmosphere is also shown, with pulsations, molecules and dust being present at different altitudes. Image credit: J. Hron, Institute for Astronomy, University of Vienna.

Post-AGB stages

After a star leaves the AGB, it continues to burn hydrogen in a thin layer and evolves rapidly towards higher effective temperatures at nearly constant luminosity, moving towards the left on the HRD. Lower mass ($0.5M_{\odot} < M < 0.75M_{\odot}$) stars may cross the instability strip to become RV Tauri variables (see Chapter 4 for a detailed study of the RV Tauri variable R Sct). Once the leftmost point along this evolutionary track is reached, H-burning ceases and the envelope layers contract towards the core. The star eventually ceases all nuclear burning processes and its hot remnant C+O core which cools off radiatively becomes a *white dwarf* (WD). The outer envelope which had been ejected into the circumstellar and interstellar environment in the course of mass loss during the AGB and post-AGB stages is referred to as a *planetary nebula* (PN).

The last stages of evolution of low- and intermediate mass stars, characterized by severe mass loss, are among the most important sources of heavy nuclei for the enrichment of the interstellar medium.

1.2.2 Evolution of high mass stars

Unlike their lower mass counterparts, stars with masses $M_{\text{MS}} > 8M_{\odot}$ (de Boer & Seggewiss, 2008) begin core He-burning smoothly and not long after hydrogen in their core is exhausted. They leave the MS and move right on the HRD as their surface temperature decreases (see Figure 1.2). In massive stars, the temperature and pressure at the core are high enough to allow C-burning, as well as that of heavier elements. Successive fusion stages take shorter and shorter time, due to the less and less available fuel for them (the material for each stage being created in the previous one). On the HRD, the star moves further to the right and becomes a *red supergiant* (RSG, luminosity class I). A RSG star has an onion-like inner structure (see Figure 1.5), with the heaviest elements being at the core, and elements with lower atomic number residing further and further away from it. RSGs are known to experience severe mass loss that may reach tens of solar masses for the most massive of them. Because of this, supergiants play an important role in the enrichment of the interstellar medium with heavy elements. However, the precise mechanisms behind mass loss in RSG stars are still not known.

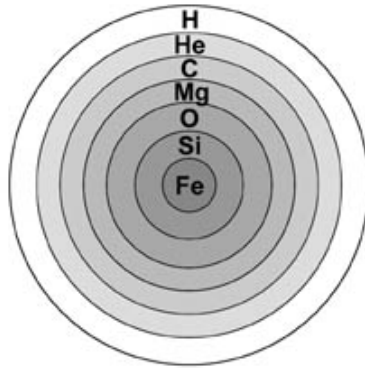


Figure 1.5: Onion-like inner structure of an evolved RSG star. Figure from <https://imagine.gsfc.nasa.gov>.

Possible mass loss mechanisms

A number of processes that could play a role in the mass loss in RSG stars have been proposed. One such is radiation-driven pressure on dust grains, which is the mechanism expected to operate in AGB stars. According to this physical scenario (van Loon, 2006; Höfner, 2008), pulsations lift stellar material to altitudes where the temperature is sufficiently low that dust may form. Once dust grains have formed, radiation pressure

accelerates them outwards, away from the photosphere. The grains then transfer momentum to the nearby gas through collisions. While radiation-driven pressure on dust seems possible in AGB stars, in RSGs the pulsations are much weaker, which suggests that in them this mechanism may not be as effective.

Another scenario which has been proposed to explain the mass loss in RSGs is that the wind is driven by dissipation of Alfvén waves. Hartmann & Avrett (1984) and Airapetian et al. (2000) performed magnetohydrodynamic simulations of Alfvén wave driven wind in Betelgeuse and found that dissipation of Alfvén waves may indeed contribute to the stellar wind. However, both simulations predict very high wind temperatures (~ 9000 K), while the peak temperatures in the chromosphere of Betelgeuse has been measured by O’Gorman et al. (2020) to be 3800 K.

A third hypothesis is that mass loss may be caused by surface convective motions. Josselin & Plez (2007) find variable supersonic velocity fields in the atmospheres of RSG stars, which the authors suspect to be linked to giant convective cells. In this work, the authors point out that such convective motions may create turbulent pressure, which would in turn lead to a strong decrease in effective gravity and could thus contribute to the stellar wind.

Giant convective cells

Schwarzschild (1975) suggested that RSGs host giant convective cells in their atmospheres, and estimated the typical timescale of variability of convective motions to be around 150 d, which is compatible with the velocity variations observed by Josselin & Plez (2007). One of the RSGs with the highest known mass loss rate, VY CMa, hosts an asymmetric nebula in its CSE. Smith et al. (2001) suggest that the arcs found in this nebula are probably formed by multiple ejections which originate from giant convective cells. Circumstellar inhomogeneities have also been observed for α Ori (Plez & Lambert, 2002). Giant convective cells are also predicted in α Ori by simulations (Freytag et al., 2002; Chiavassa et al., 2011b), and evidence for their presence is seen in UV (Gilliland & Dupree, 1996; Dupree et al., 2020) and interferometric observations (Haubois et al., 2009; Montargès et al., 2016). Goldberg et al. (2021) present 3D radiation hydrodynamical simulations of RSGs which also confirm that convection in these stars is dominated by a low number of large convective cells. These authors also confirm the result of Chiavassa et al. (2011a) that in RSGs turbulent pressure is significant and dominates thermal pressure in the outer stellar layers.

López Ariste et al. (2018) present a method for the imaging of the bottom atmospheric layers of the RSG α Ori using high-resolution spectropolarimetric observations in linear polarization by assuming the presence of giant convective cells, and infer images that match well direct imaging via interferometry (see Chapter 2 for details on spectropolarimetric observations and their analysis, and Chapter 5 for a detailed review on the linear polarization imaging method).

Final stages of evolution

RSG stars may perform blue loops on the HRD and may also become Cepheid variables as they cross the instability strip (possibly more than once). The cores of RSGs are so massive that at the end of their life electron degeneracy is not sufficient to prevent their gravitational collapse. The ultimate fate of these objects is a supernova type II explosion in which the stellar envelope is ejected into the interstellar medium, while the core is converted into a neutron star if its mass is below the Chandrasekar limit or, otherwise, into a black hole.

1.3 Magnetism in the Sun, solar-type dynamo and Rossby number

The Sun is the best studied magnetically active star. The first direct observations of the effects of magnetism in the Sun using a telescope were reported by Galileo himself, who in the very beginning of the XVII century observed dark spots on the visible surface of the Sun that would become known as *sunspots*. Since then, the effects of solar magnetism have been extensively studied for centuries. In the following section, I will discuss the mechanisms that lead to the surface magnetic fields found in the Sun, as well as the effects that magnetism has on observations. Later, I will discuss how magnetic fields in other stars have similar or different observational characteristics.

1.3.1 Solar-type dynamo

Magnetism in the Sun is caused by a process generally known as a *magnetic dynamo*, which consists of the cyclic conversion of part of the kinetic energy of the stellar plasma into magnetic energy. Dynamo models are based on the α - and Ω effects (Moffatt 1978, review by Charbonneau 2010).

To understand the physics behind the magnetic dynamo found in the Sun, we need to consider the inner structure of this star. The interior of the Sun (see Figure 1.6) is roughly composed of:

- an active core, where hydrogen is fused into helium and the energy that sustains the hydrostatic equilibrium of the Sun is created;
- a radiative zone, where the energy released in the core is transmitted radiatively outwards from the core;
- a convective shell, where the energy transfer is sustained by convection (hot plasma with high buoyancy rises towards the surface, cools down and then sinks again due to its decreased buoyancy, resulting in net outward transfer of energy);
- the top of the convective shell, called the *photosphere*, where sunspots can be observed.

The photosphere is the top layer of the interior of a star, and also the bottom layer of its atmosphere. It is the layer where the plasma transitions from being opaque to being transparent for radiation and where the continuum is formed. Conversely, the photosphere is the innermost layer of a star that can be observed.

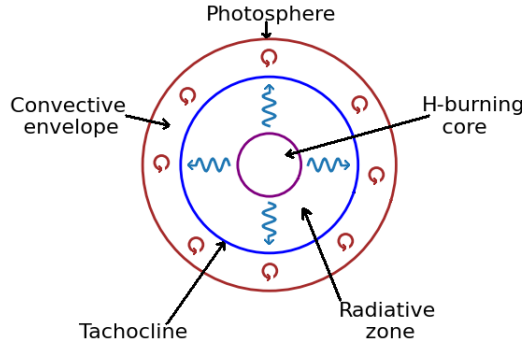


Figure 1.6: Schematic view of the inner structure of the Sun. Certain layers of interest are indicated with arrows.

The rotation of the Sun around its axis as a whole is not that of a rigid body, in which all points of the Sun would rotate with the same angular velocity with respect to its centre. Instead, only the core and radiative shell rotate together as a rigid body, but in the convective envelope above them the rotation is differential: points closer to the equator of the Sun rotate with larger angular velocity around its axis than points closer to its poles do - on the equator, one full revolution takes around 25 d, while close to the poles it takes around 36 d. Below the convective envelope, there is a transitional shear layer, called the *tachocline*, where a smooth transition between rigid body rotation and differential rotation occurs.

Figure 1.7 presents a sketch of the operation of the solar magnetic dynamo. Assume that at some initial moment in time the magnetic field of the Sun has a *poloidal* geometry, meaning that the magnetic field lines are oriented along the solar meridians. As the Sun rotates around its axis, the magnetic field lines that permeate the plasma are twisted due to the differential rotation of the envelope into a *toroidal* geometry, now following the solar parallels (see the upper panel of Figure 1.7). This process of converting the poloidal field into a toroidal one through differential rotation is generally referred to as the Ω effect. On the other hand, the plasma motions in the convective shell twist the magnetic field lines of the toroidal field into loops (see the bottom panel of Figure 1.7), which is referred to as the α effect. The α effect acts on a local scale and in time restores the initial poloidal geometry of the magnetic field, but with opposite polarity.

A magnetic dynamo may consist of the combined action of both the α and Ω effects. Depending on the relative action of either effect, a dynamo may be classified as $\alpha^2\Omega$ -, $\alpha\Omega$ - or $\alpha\Omega^2$ -type. An $\alpha\Omega$ dynamo is also referred to as a *solar-type dynamo*, since it

1.3. MAGNETISM IN THE SUN, SOLAR-TYPE DYNAMO AND ROSSBY NUMBER

is the one that operates in the Sun. For the Sun and other MS stars, the solar-type dynamo is most efficient in the tachocline layer, if the star has one (i.e. for stars hotter than spectral type M3-3.5). An $\alpha^2\Omega$ dynamo is present when differential rotation is weak, in which case both the α effect and differential rotation shear contribute to the production of the toroidal field. Conversely, an $\alpha\Omega^2$ dynamo is present when differential rotation is strong. It is also possible to have an α^2 -type dynamo, in which the α effect is the sole source of both toroidal and poloidal magnetic components; this type of dynamo is believed to be the mechanism behind some planetary magnetic fields.

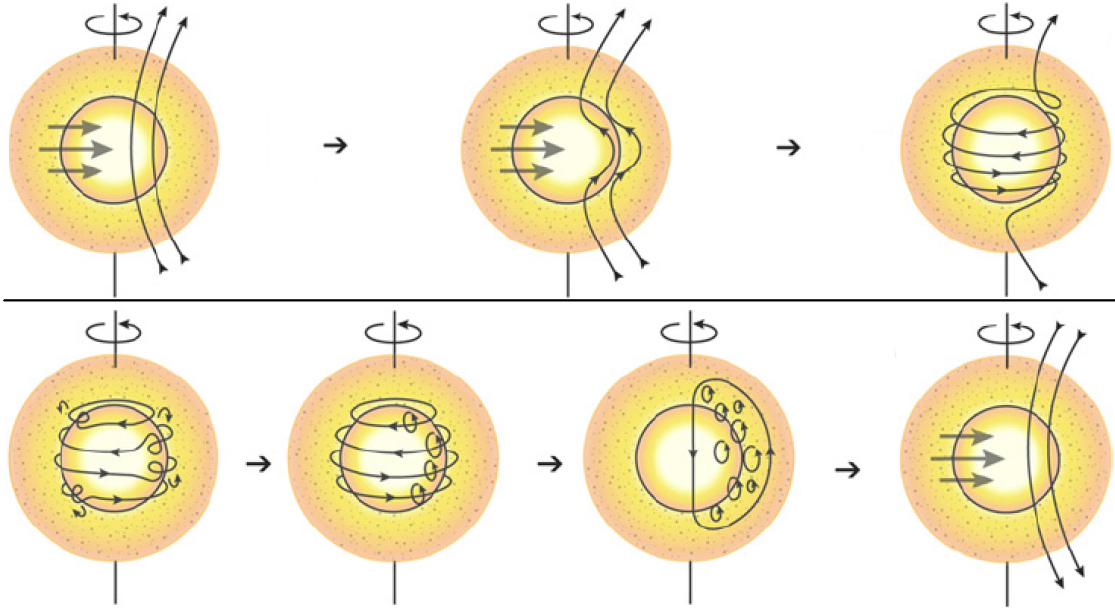


Figure 1.7: Schematic of the solar-type dynamo. The magnetic field lines are shown with thin black lines, and the field orientation is indicated over them with arrows. The direction of axial rotation is also shown. Upper panel: differential rotation turns the poloidal field into toroidal one (Ω effect); lower panel: the interaction of rotation and convective motions creates loops in the toroidal magnetic field, eventually restoring the initial poloidal geometry (α effect). Image credit: Dr. Allan Sacha Brun, Department of Astrophysics, CEA Paris-Saclay.

1.3.2 Rossby number

In order to characterize the efficiency of the solar-type dynamo, it is customary to use the *Rossby number* Ro (Rossby, 1939), which indicates how long the convective timescale is with respect to the rotational period.

The time necessary for the turnover of a convective cell, or the *convective turnover timescale* $\tau_c(r)$ at a given distance r from the base of the convective envelope is defined

by Gilliland (1985) as:

$$\tau_c(r) = \frac{\alpha_{\text{MLT}} H_P(r)}{V_c(r)}, \quad (1.1)$$

where

- $H_P(r)$ is the pressure scale height (the distance Δr at which the pressure $P(r + \Delta r) = P(r)e^{-1}$)
- α_{MLT} is a free parameter called the *mixing length parameter*, which defines how many lengths of the pressure scale height are necessary for the convective cell to travel in order to lose its integrity and become fully mixed with the surrounding matter
- $V_c(r)$ is the convective velocity.

The Rossby number is then defined as the dimensionless ratio of the rotational period of the star P_{rot} to the convective turnover timescale:

$$Ro = \frac{P_{\text{rot}}}{\tau_c(r)}, \quad (1.2)$$

A system which is strongly affected by Coriolis forces will have a low Rossby number. In such cases, the convective motions will no longer happen along a two-dimensional trajectory, but will instead be twisted into a helix by the Coriolis forces. This helicity of the convective flows is a key factor to sustaining an efficient α effect, necessary for a magnetic dynamo. A star with convection is likely to have a solar-type dynamo operating if its Rossby number is on the order of or below unity.

1.3.3 Effects of magnetism in the Sun

The presence of surface magnetic fields in the Sun is evident through a great variety of observational features. Probably the best known such features are sunspots: visually dark spot-like areas on the otherwise bright solar photosphere. A close-up image of the Sun showing sunspots is presented in Figure 1.8. In this Figure, it can also be seen that outside the sunspots the photosphere of the Sun is covered with visually small cells of different shapes and sizes that appear darker at their edges. This phenomenon is known as *granulation*. In fact, these granules are the very top parts of convective cells: the bright central areas are zones where hot plasma rises due to convection towards the photosphere, where it cools down (mainly due to radiative losses into space) and then moves horizontally in a diverging flow towards the edges of the granules. There it cools down, becoming darker than its surroundings, and sinks down due to its increased density.

However, if a magnetic field is present, this scenario changes. In the darkest parts of a sunspot, called the *umbra*, the magnetic field strength can reach up to 3 kG and the field lines are mostly vertical. In the presence of such strong magnetic fields, the ionized material becomes bound to the field lines. Because of this, ionized gas can move freely

1.3. MAGNETISM IN THE SUN, SOLAR-TYPE DYNAMO AND ROSSBY NUMBER

along the field lines, so the upflow of hotter material at the centre and the downflow of cooler material at the edges is not inhibited; however, horizontal motions of the plasma become practically impossible. This prevents normal plasma circulation and effectively inhibits heat transport. As a result, the umbra becomes cooler and visually darker than the rest of the photosphere.

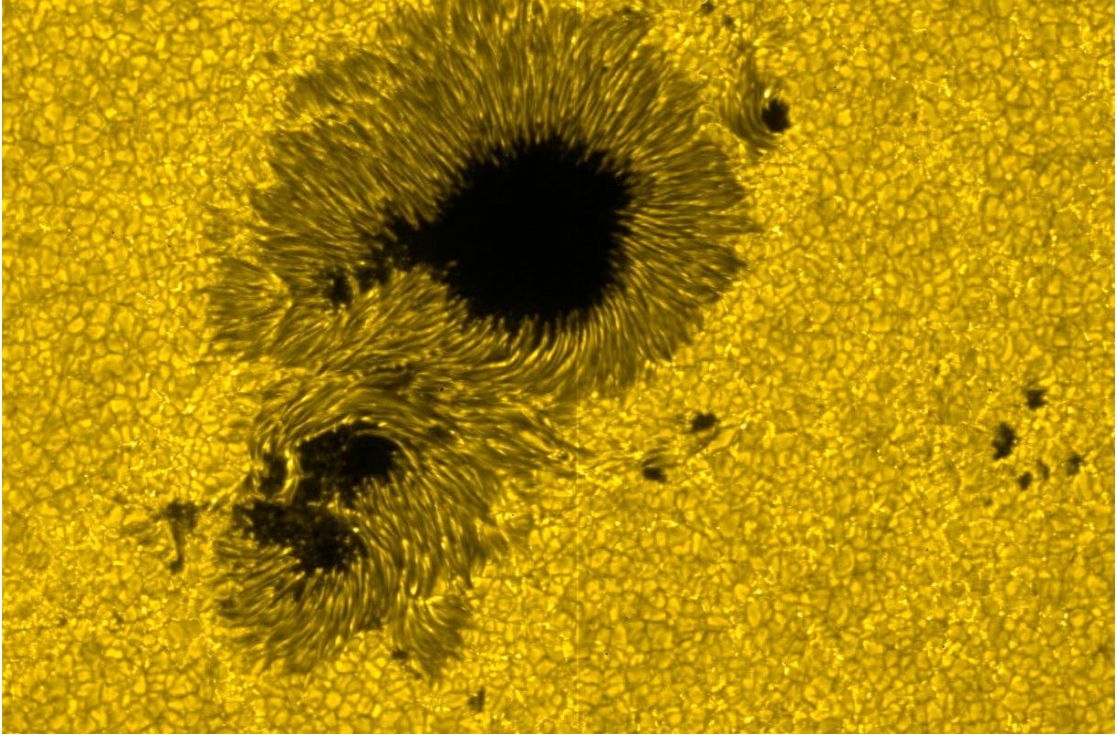


Figure 1.8: Sunspots and granulation on the photosphere of the Sun. Image credit: Hinode's Solar Optical Telescope (SOT), JAXA/NASA/PPARC.

The *chromosphere* is a portion of the solar atmosphere that lies just above the photosphere. In this layer, the temperature increases with altitude, while the density drops by a factor of $\sim 10^4$. In such conditions, certain lines may be formed which cannot be found in the higher densities and lower temperatures of the photosphere: for example, lines of CaII (notably the CaII H&K lines at 396.8 and 393.3 nm, respectively), HII, FeII, SiII and others. The hydrogen Balmer lines may also have chromospheric components; in fact, the name *chromosphere* comes from the greek word $\chi\rho\acute{\omega}\mu\alpha$, meaning "color", and refers to the characteristic red color of the chromosphere which is caused by the emission component of the Balmer line $H\alpha$ present there. The degree of emission in chromospheric lines is proportional to the local magnetic field strength. In contrast with the stellar photosphere where the heating is mostly due to radiative transfer and occurs mainly in the continuum, in the chromosphere the heating is non-radiative and takes place mainly in resonance lines (produced by a transition between the ground

state and the first energy level) of chemically abundant elements. The heating in the chromosphere may be caused by dissipation of acoustic waves or dissipation of magnetohydrodynamic waves. This is why, in stars with surface magnetic fields (including the Sun), the chromospheric emission lines are excellent indicators of the magnetic activity and its variability with time. In the chromosphere of the Sun, chromospheric lines show emission above active regions, where the magnetic field is strongest.

Mass loss

The Sun is known to experience mass loss due to magnetism in the so called coronal mass ejection (CME) events. During a CME, a stream of charged particles (mostly protons and electrons) is ejected from the Sun and released into the interplanetary space of the Solar system. CMEs are typically preceded by a *magnetic reconnection* – an event in which two magnetic fields of opposite directions are brought together and a rapid rearrangement of the magnetic field lines occurs. The rate at which CMEs occur strongly depends on the level of solar magnetic activity: around the maximum of activity, CMEs are observed more frequently, leading to more mass loss.

1.4 Magnetism in single stars at the giant branches

G, K and M giants are expected to have weak surface magnetic fields due to their large radii and slow rotation (see e.g. Landstreet 2004). However, activity signatures in the form of photometric variability, emission in the cores of the absorption components of spectral lines which are indicators of chromospheric activity and X-ray emission is well-known in some such stars (see e.g. Konstantinova-Antova et al. 2013; Korhonen 2014). Magnetic fields have been detected in a large number of single G and K giants using spectropolarimetric observations (Konstantinova-Antova et al., 2013; Aurière et al., 2015; Konstantinova-Antova et al., 2014).

Aurière et al. (2015) present an extensive study of the magnetism in 48 red giant stars of spectral class G and K, and unambiguously detect surface magnetic fields in 29 of them. The largest absolute value of the longitudinal component B_l of the magnetic field that the authors measured from spectropolarimetric observations (see Chapter 2) for these stars is $|B_l|_{\max} = 98.6$ G. An important result found by Aurière et al. (2015) is that the strength of the magnetic field correlates strongly with the rotational period P_{rot} and hence with the Rossby number Ro up to $P_{\text{rot}} \approx 300$ d. The left panel of Figure 1.9 (from Aurière et al. 2015) shows the distribution of $|B_l|_{\max}$ versus P_{rot} for the stars in their study with detected magnetic fields and known rotational periods (for red giant stars, determining P_{rot} is observationally difficult, since it is generally on the order of hundreds or even a thousand days). It can be seen that, generally, the longer the rotational period, the weaker the magnetic field. A similar trend can be seen for the $|B_l|_{\max}(Ro)$ distribution shown in the right panel of Figure 1.9. Based on these facts, Aurière et al. (2015) suspect that an $\alpha\Omega$ -dynamo operates in these stars and is responsible for their

observed surface magnetic fields. However, four stars – EK Eri, OU And, β Cet and 14 Cet – deviate from this general trend. Aurière et al. (2015) consider that these giants are likely evolved stages of Ap-stars that had strong (up to 10 kG) magnetic fields on the MS, and through magnetic flux conservation have kept them as their radii grew during their evolution after the MS. This hypothesis is supported by studies of EK Eri (Aurière et al., 2011) and β Cet (Tsvetkova et al., 2013). The same goes for OU And, although this star, situated before the base of the RGB, appears to also host an active dynamo that interacts with the inherited magnetic field from the Ap-star stage, because of the remnant fast rotation at the Hertzsprung gap (Borisova et al., 2016).

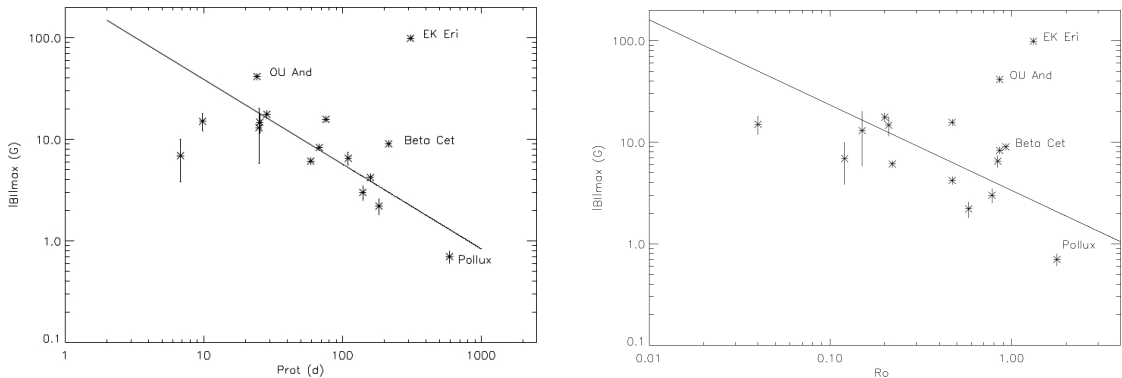


Figure 1.9: Correlations between the maximal longitudinal magnetic field $|B_l|_{\max}$ and the observational rotational period P_{rot} (left panel) and the Rossby number Ro computed for $\tau_{\text{conv max}}$ from models (right panel). Both figures are from Aurière et al. (2015). The positions of Pollux and three outlying giants, likely evolved magnetic Ap-stars, are shown. The straight line fits are computed by least squares regression, excluding EK Eri (known to be overactive with respect to its rotation) and OU And, β Cet and 14 Cet, which the authors consider to be Ap-star descendants.

Konstantinova-Antova et al. (2009) selected a sample of 7 stars – G, K and M giants – on the basis of their fast rotation, and observed them in high resolution spectropolarimetry in Stokes V using the instrument Narval (see Chapter 2 for details on spectropolarimetric observations and the instrument itself). These authors were the first to report a direct detection of a surface magnetic field in an M giant star, namely EK Boo (HD 130144). Later, Konstantinova-Antova et al. (2010) presented an extended study of EK Boo based on Narval observations between April 2008 and March 2009, and found that the magnetic field of this M giant is variable with time (the authors found it to vary between -0.1 and -8 G during the time of their observations). The authors proposed that the possible origin of the magnetic field in EK Boo might be the $\alpha\Omega$ dynamo. In addition, Konstantinova-Antova et al. (2010) also observed 8 other M giant stars in search for magnetic activity, and obtained a definite detection of a surface magnetic field for the stars V669 Her ($B_l \approx 1$ G) and RZ Ari ($B_l \approx 3$ G) and a marginal detection for the star β And ($B_l = -0.95$ G). These detections show that EK Boo is not the only case of a

magnetic M giant.

Konstantinova-Antova et al. (2014) presented the first results of a spectropolarimetric survey on a new sampling, which contained all single G, K and M giants with visual brightness down to $V = 4^{\text{mag}}$ in the Solar vicinity that were observable with Narval. This sample contains a total of 45 stars, of which 29 were already observed by Konstantinova-Antova et al. (2014). The authors measured the longitudinal magnetic field of the stars from their Stokes V observations (see Section 4 of Chapter 2) and also determined their evolutionary status on the basis of evolutionary models with rotation (Lagarde et al., 2012a; Charbonnel et al., 2017) and fundamental parameters, as given by Massarotti et al. (2008a). 13 of the observed stars were found to be ascending towards the tip of the RGB and in the early-AGB phase, and of these stars 8 were found to have a surface magnetic field (61% detection rate). The authors note that, in general, the detected stars show a tendency to "clump" at certain evolutionary stages: the first dredge-up and core He-burning, and the region covering the tip-RGB and early-AGB stages. Konstantinova-Antova et al. (2014) also find indications of a dependence of $|B_l|_{\text{max}}$ on the rotational velocity $v \sin i$, and suspect that the $\alpha\Omega$ dynamo might be operating for these stars, as it has been predicted by Nordhaus et al. (2008).

Magnetic strips

It was established by Konstantinova-Antova et al. (2014) and Aurière et al. (2015) that the giants found to host surface magnetic fields are not chaotically spread over the HRD, but are mostly found in two so called *magnetic strips*: the first one covering the base of the RGB near the first dredge-up stage and the core He-burning stage, and the second one covering the early-AGB stage (see Figure 1.10). The existence of the magnetic strips was theoretically explained by Charbonnel et al. (2017), who demonstrated that an $\alpha\Omega$ -dynamo is possible after the MS for stars with intermediate mass during the stages of stellar evolution where the convective shell is largest and the convective turnover time is long, leading to a decrease of the Rossby number.

The left panel of Figure 1.10 (from Charbonnel et al. 2017) shows the Ro values computed from stellar evolutionary models by Charbonnel et al. (2017) at $r = H_P/2$ (where H_P is the height above the base of the convective envelope at which the pressure $P = e^{-1}P_{\text{BCE}}$, with P_{BCE} being the pressure at the base of the convective envelope) for evolutionary tracks of stars in the mass interval 1 - 6 M_{\odot} with solar metallicity and $v_{\text{rot}} = 30\%v_{\text{crit}}^{\text{ZAMS}}$, the critical rotational velocity (the velocity at which the centrifugal force resulting from rotation would break the hydrostatic equilibrium of the star) at the zero-age main sequence stage. In the left panel of Figure 1.10, the positions of the stars studied by Aurière et al. (2015) are shown and the intensity of their respective magnetic fields is represented by the symbol size (non-detections are marked with an open circle). The dashed lines indicate the beginning and end of the first dredge-up stage: on the left - when the mass of the convective envelope reaches $M_{\text{conv}} = 2.5\%M_{\star}$; on the right - when $M_{\text{conv}} = M_{\star}^{\text{max}}$, i.e. when the convective envelope has reached its full growth and its

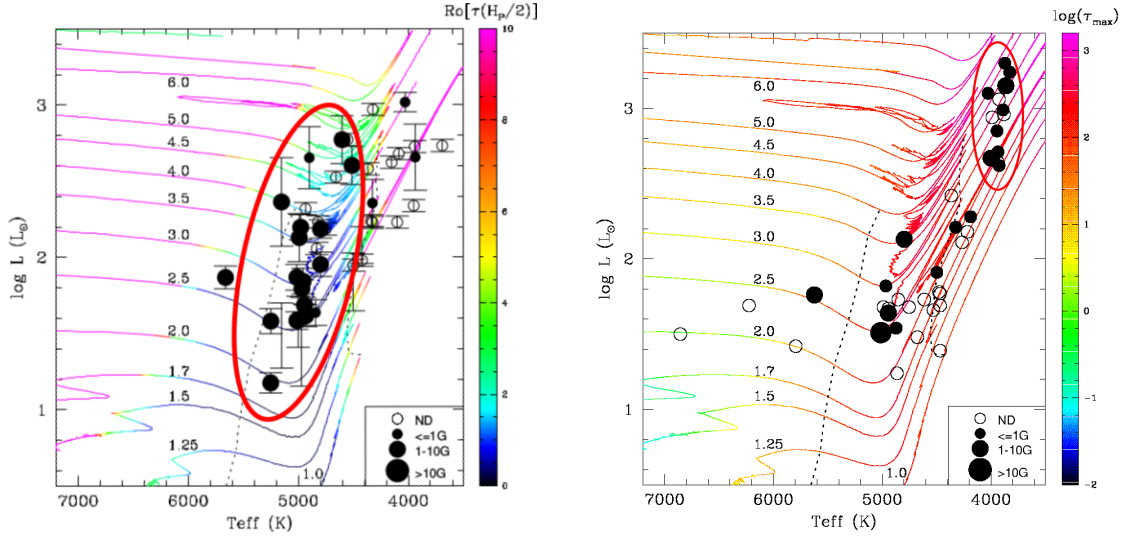


Figure 1.10: Left panel (from Charbonnel et al. 2017): HRD with colorcoded expected values for the Rossby number $Ro(H_P/2)$ for the evolutionary tracks of stars with mass M_{\star} between 1 and $6 M_{\odot}$ with $Z = Z_{\odot}$ and $v_{\text{rot}} = 30\%v_{\text{crit}}^{\text{ZAMS}}$. The points correspond to the stars studied in Aurière et al. (2015), with the size of the filled circles corresponding to the measured magnetic field strength, and the empty circles corresponding to giant stars with no detection of magnetic field. The first magnetic strip is circled in red. Right panel (from Konstantinova-Antova et al. 2014): HRD with colorcoded expected log values for the maximum convective turnover times $\log(\tau_{\text{max}})$ of the same evolutionary tracks. The second magnetic strip is circled in red. The points correspond to the stars studied in Konstantinova-Antova et al. (2014).

base will next start to rise higher towards the photosphere. It can be seen that the G and K giants hosting surface magnetic fields are found mainly in the areas where $Ro(H_P/2)$ is close to its minimal value, thus defining the first magnetic strip (circled in red); on the other hand, most of the G and K giants that show no magnetic field detection lie outside of these areas.

The right panel of Figure 1.10 (from Konstantinova-Antova et al. 2014) shows the expected values (in log scale) for the maximum convective turnover time $\log(\tau_{\text{max}})$ for the same evolutionary tracks. The positions of the stars studied in Konstantinova-Antova et al. (2014) are shown, and again the size of the symbol represents the detected strength of the longitudinal magnetic field (open circles correspond to non-detections). It can be seen that the M giants for which a magnetic field is detected have a tendency to cluster in an area of the HRD which corresponds to the second magnetic strip (circled in red).

1.5 Magnetic fields in Mira and post-AGB stars

Magnetism at the very late stages of evolution of stars with low and intermediate masses – in Mira stars and during the post-AGB stages – is still poorly studied. Lèbre et al. (2014) reported the first direct detection of a surface magnetic field in the Mira star χ Cyg. These authors observed χ Cyg around its phase of maximum light using Narval, and obtained from circular polarization observations a direct measurement of its longitudinal magnetic field B_l of about 2-3 G. The authors suggest that the origin of this magnetic field is a local dynamo powered by convection (as we will see next, this is also the case for RSG stars). However, Mira stars undergo radial pulsations which trigger shockwaves that propagate throughout their atmospheres.

A shockwave is any mechanical wave that propagates through a given medium faster than the local sound velocity. This causes an abrupt change of the pressure, density and temperature of the medium at the shock front. In the case of Mira and post-AGB stars, the shocks are triggered by the pulsation mechanism. Once they emerge from the photosphere, the shockwaves then propagate through the extended atmosphere of the star, imprinting complex ballistic motions which separate the atmospheric layers into different velocity streams and cause atomic spectral lines to have Doppler-shifted or double-peaked profiles (see Section 4.2 of Chapter 4 for more information).

Lèbre et al. (2014) discovered that in χ Cyg, the circularly polarized signatures, which trace the surface magnetic field, are associated only to the blue lobe of atomic spectral lines. This blue lobe is formed by atoms behind the shock front which are being accelerated upwards (away from the star) by the shock. This led the authors to the conclusion that the propagation of a shockwave could introduce a compressive effect on the magnetic field lines, and in this way could locally amplify an already present weak surface magnetic field.

The same connection between atmospheric dynamics and the observed strength of the surface magnetic field is suspected to exist in the post-AGB pulsating variable R Sct by Lèbre et al. (2015). These authors obtain observations of R Sct with Narval and report that, for the observation where a circularly polarized signature is detected, this signature appears centered on the blue lobe of the intensity profile, as it is in the case of the Mira star χ Cyg. A detailed study of the possible connection between atmospheric dynamics and surface magnetism in the post-AGB star R Sct is presented in Chapter 4 of this Thesis.

1.6 Magnetism in RSG stars

Direct measurements of surface magnetic fields using spectropolarimetric observations (see Chapter 2) at the Gauss level have been reported for a few RSG stars, namely Betelgeuse $\equiv \alpha$ Ori (between -2.5 ± 0.1 and 2.5 ± 0.2 G) (Aurière et al., 2010; Mathias et al., 2018), CE Tau (between -2.7 ± 0.5 and -1.2 ± 0.2 G) and μ Cep (1.3 ± 0.3 G) (Tessore et al., 2017). In Figure 1.11 (from Mathias et al. 2018), the

evolution of the longitudinal component of the magnetic field B_l of Betelgeuse in the period March 2010 - April 2017 is shown. Josselin et al. (2015) estimate $Ro \approx 90$ for this star, taking $P_{\text{rot}} \simeq 17$ yr and $v_{\text{conv}} \approx 20$ km s $^{-1}$. A Rossby number so large means that a large-scale dynamo such as the solar type one is not at all expected to operate in this RSG star. However, Dorch & Freytag (2003) and Dorch (2004) show through magnetohydrodynamical simulations that a small-scale dynamo operating between individual convective cells in Betelgeuse may lead to local magnetic fields of strength up to 500 G but with small filling factors. When integrated over the whole visible stellar disk, such small-scale fields may be detected as a global field of a few Gauss, consistent with the direct measurements of Aurière et al. (2010); Mathias et al. (2018).

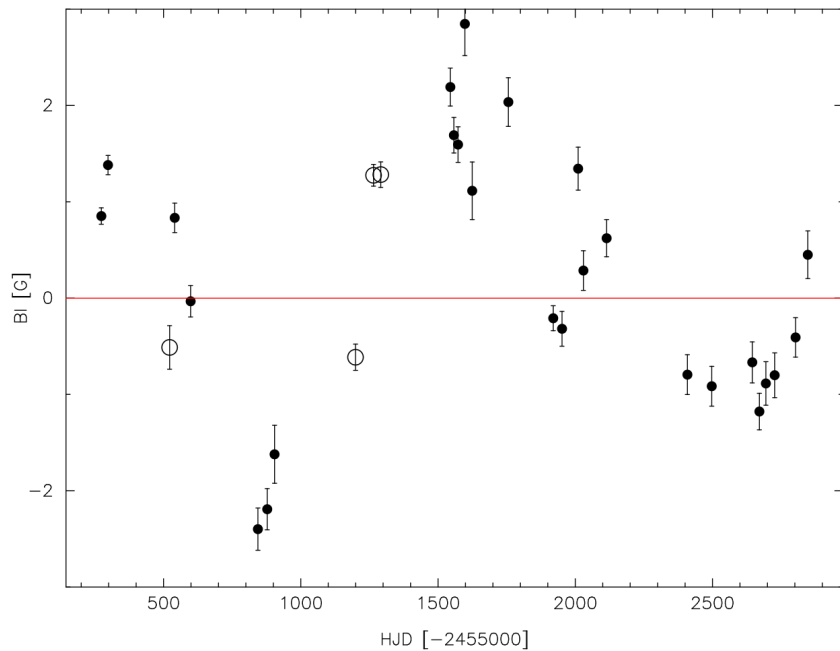


Figure 1.11: Evolution of the longitudinal component of the magnetic field B_l of Betelgeuse in the period March 2010 - April 2017. The open and full symbols represent data obtained with the instruments ESpaDONs and Narval, respectively. Figure from Mathias et al. (2018).

Aurière et al. (2016) present observations of Betelgeuse in linear polarization obtained with the spectropolarimeter Narval (see Chapter 2) in the period 2013-2015 and suggest that the linear polarization signal found in this star is caused by polarization in the continuum due to Rayleigh scattering, followed by depolarization during the formation of atomic spectral lines. According to these authors, observing a net linear polarization signal in this star is only possible if the surface brightness distribution is not uniform across the stellar disk, leading to the conclusion that the surface of Betelgeuse must be covered asymmetrically with bright spots. In a first attempt to map the surface of this supergiant, Aurière et al. (2016) also propose a model which infers the location of such

bright spots over the disk of the star (see Chapter 5 for more details). Direct images obtained through interferometric observations of Betelgeuse (Montargès et al., 2016) also support the idea of bright spots unevenly spread on its surface.

Mathias et al. (2018) present a study of the magnetic field of Betelgeuse using high-resolution spectropolarimetric observations in circular polarization with Narval. The authors find in both the circularly polarized and intensity spectra a periodicity of about 2000 d, close to the so-called long secondary period (LSP) of the star, known from photometry (Kiss et al., 2006). Based on this periodicity and the variability of both linear and circular polarization in amplitude and velocity, Mathias et al. (2018) favour giant convective cells as the main reason for the linearly polarized signatures in this RSG star. These authors also find that the circularly polarized signatures that trace the surface magnetic field are most of the time redshifted with respect to the mean spectral line intensity profile, and suggest that they are formed in the cooler, sinking regions at the borders of giant convective cells. The authors also suggest that the linearly polarized signatures, on the other hand, originate from the uprising central parts of the convective cells, which also explains why they are mostly blueshifted with respect to the intensity profiles. These points were investigated in details during my PhD, and are presented in Chapter 5.

Following the works of Aurière et al. (2016) and Mathias et al. (2018), López Ariste et al. (2018) further explore the possibility to map the surface of Betelgeuse. These authors propose an imaging technique that uses spherical harmonics to fit the observed linear polarization of Betelgeuse under the assumption that it is formed due to surface brightness inhomogeneities caused by the presence of convective cells. The images obtained by López Ariste et al. (2018) using their method are in agreement with direct images obtained from interferometric observations by Kervella et al. (2018) and Montargès et al. (2016). This technique is thoroughly explained in Chapter 5; in the present Chapter, we shall only consider the results that López Ariste et al. (2018) obtain using it.

An example image of Betelgeuse inferred using the technique of López Ariste et al. (2018) is shown in Figure 1.12 (from López Ariste et al. 2018). By obtaining similar surface maps for 43 dates between November 2013 and August 2018, these authors find that the characteristic size of the convective cells is more than 60% of the stellar radius ($R = 1021R_{\odot}$, Ohnaka et al. 2011), and that magnetic fields are concentrated in the relatively dark intergranular lanes where the plasma motions are downflowing, similar to the quiet Sun. The authors also find that changes in the inferred structures occur on timescales of 1 week, but individual structures can be traced over 4 years of observations. This is in good agreement with numerical simulations (e.g. Freytag et al. 2002; Chiavassa et al. 2011b). Furthermore, López Ariste et al. (2018) suggest that such convective structures are likely present not only in Betelgeuse, but may be common in other RSG stars too, giving the M supergiant CE Tau as an example. Inferred images

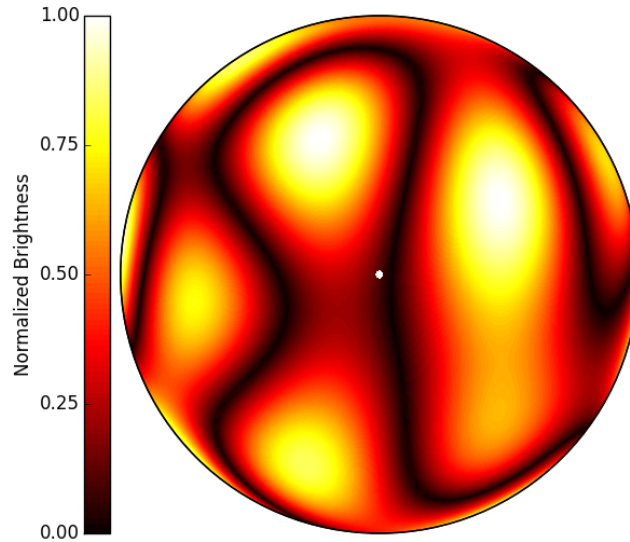


Figure 1.12: Inferred image of Betelgeuse from December 9, 2015. The presence of bright spots at the level of the photosphere can be seen, likely corresponding to the rising regions of giant convective cells. Following Mathias et al. (2018), the magnetic field should be constrained to the dark intergranular lanes. Figure from López Ariste et al. (2018).

of CE Tau using the linear polarization imaging technique are also in good agreement with interferometric observations presented by Montargès et al. (2018).

All the studies described above lead to a consistent physical scenario for the observed magnetic fields in RSG stars, which might appear similar to that of the weakest magnetic fields in the solar photosphere. The local magnetic fields are too weak to affect the convective motions, but are instead completely dominated by them. In the centre of convective granules, hot plasma rises towards the stellar surface. It then moves horizontally across the photosphere, dragging the magnetic field along. When the plasma reaches the dark intergranular lanes and is sufficiently cool, it sinks down towards the center of the star. The magnetic field cannot escape from the intergranular lanes, being constantly pushed towards them. This process leads to the magnetic field being concentrated in the dark intergranular lanes, reaching a large local intensity there but having a small filling factor, being constrained to only a small part of the stellar photosphere.

1.7 Magnetism in cool evolved stars: aims of the study

Magnetism in single giant stars has been well studied in recent years for the hotter G and K stars. However, not so much is known for cool M giants yet. More detailed studies of magnetic M giants is needed in order to understand the mechanisms of stellar magnetism during the tip-RGB and AGB stages.

For post-AGB stars, still too little is known about the impact magnetic fields have on the severe mass loss these objects experience, and the role magnetism has in the formation of planetary nebulae. The possibility for an interplay between magnetic fields and pulsations at this final evolutionary stage is also still poorly studied.

RSGs are also known to experience profound mass loss. However, the exact mechanisms behind it are still unknown. The connections between convective dynamics, magnetism and mass loss need to be further explored in order to reach a more complete understanding of the mechanisms that are at work during the final stages of evolution of massive stars.

In my Thesis, I study five cool evolved stars of different evolutionary stages that have magnetic fields detected at their photospheric levels. These stars are the red giants RZ Arietis, β Pegasi and EK Boötis, the post-AGB star R Scuti (an RV Tauri variable) and the red supergiant Betelgeuse. All five stars are studied in detail using long data sets of high resolution spectropolarimetric observations that cover up to 10 years. The stars were chosen for this study for a number of reasons. First, they are easy to monitor with Narval, each being observable for at least 6 months per year. Also, the stars are sufficiently bright so that high signal-to-noise ratio data can be obtained. A detection of a surface magnetic field has already been reported for each of the M giant stars, making them promising targets to study stellar magnetism in. The post-AGB star R Sct was selected because it is the brightest member of the RV Tauri class, and because it had already been reported to host a variable surface field. Betelgeuse is an interesting target because of the Great Dimming that occurred between the end of 2019 and the beginning of 2020. Lastly, at the start of my PhD study all five stars had already been observed for a long time with Narval and a long-term observational dataset was available for each of them.

In terms of stellar evolution, the three mentioned red giants are all either at the tip of the RGB or at the early-AGB stage. My aim for these stars is to study their surface magnetic field behaviour by using long-term spectropolarimetric datasets, to determine the mechanisms that create it, and finally, to compare the results for the three stars. At these evolutionary stages during which the stellar structure changes, there are three main hypotheses that could explain the origin of the observed surface magnetic field:

1. Operation of a magnetic dynamo, either of the solar type or another, caused by changes in the internal structure of the star that occurred in the course of stellar evolution, or as a result of angular momentum transfer after a planet engulfment event;

2. Local amplification of a weak surface magnetic field by means of compression due to the propagation of shock waves through the photospheric and atmospheric layers of the star as a result of pulsations;
3. Operation of a small-scale magnetic dynamo due to convection, like in the RSG star Betelgeuse.

The study of the three M giant stars is presented in Chapter 3.

Regarding the RV Tauri pulsating variable star R Sct, my aim in this Thesis is to check the hypothesis that radiative shock waves may be locally amplifying the star's surface magnetic field. To do this, the shock waves that occur semi-periodically in the atmosphere of this post-AGB star are thoroughly followed and matched to the star's variable surface magnetic field. This is done using the longest dataset of high-resolution spectropolarimetric observations of R Sct yet, obtained over the course of 5 years. An original improvement of the classical spectropolarimetric approach for the study of stellar surface magnetic fields is used. This improvement is made for the particular case of stars with extended atmospheres and focuses only on the magnetic field at the photosphere, filtering out the contribution of higher atmospheric layers. The study of R Sct is presented in Chapter 4.

The RSG star Betelgeuse experienced its famous Great Dimming episode between October 2019 and February 2020, when its visual brightness decreased by about 1 mag (Guinan et al., 2020). In order to explain this unprecedented decrease in brightness, a number of hypotheses were proposed, including a dust cloud formation due to a mass loss episode (Levesque & Massey, 2020; Dupree et al., 2020; Cotton et al., 2020; Montargès et al., 2021). In my Thesis, I aim to study the convective motions in the photosphere of Betelgeuse, and the forces that act upon them, in order to better understand the processes that may lead to mass loss in this and other RSG stars. In order to do this, I participated in the development of a numerical method to build 3-dimensional (3D) maps of the bottom layers of the atmosphere of RSG stars using high resolution spectropolarimetric observations. The study of convective motions in the photosphere of Betelgeuse is presented in Chapter 5.

Spectropolarimetric observations, methods & tools

In this Chapter, I will first present some basic concepts in spectropolarimetry, such as the Stokes parameters and the Zeeman effect. I will then describe the way that the observations I use in my Thesis were obtained using the spectropolarimeter Narval, and the methods and tools that I used to extract from them information on stellar surface magnetic fields. I will also describe the successor of Narval, the spectropolarimeter NeoNarval.

Summary

2.1	Spectropolarimetry: basic concepts	28
2.1.1	Polarization of light	28
2.1.2	Stokes parameters	29
2.1.3	The Zeeman effect	30
2.2	Observations with Narval	33
2.3	Least Square Deconvolution	37
2.3.1	The method	37
2.3.2	Classifying the detection of polarized signatures	41
2.4	Measuring the longitudinal magnetic field	41
2.5	Spectral activity indicators	41
2.6	NeoNarval	43
2.7	Adapting NeoNarval data to the Narval format	45
2.8	Treating the data	46

2.1 Spectropolarimetry: basic concepts

2.1.1 Polarization of light

Light is a transverse electromagnetic wave: it has an electric component \vec{E} and a magnetic component \vec{B} , which are orthogonal both to each other and to the direction of propagation, given by \vec{S} , the Poynting vector: $\vec{E} \perp \vec{B} \perp \vec{S}$. The electric and magnetic fields may oscillate in any direction, while maintaining orthogonality. By convention, the polarization of light refers to the direction of oscillation of the electric field. When all directions are equally present in a given light beam, this is called fully unpolarized light. Light can also exhibit linear, circular or elliptical polarization.

Linear polarization

If each of the two fields oscillates only in a single direction, this is referred to as *linearly polarized light*: the vector of the electric (or magnetic) field is projected as a line when viewed towards the direction of propagation (see Figure 2.1). The plane which contains the vector of the electric field is referred to as *the plane of polarization*.

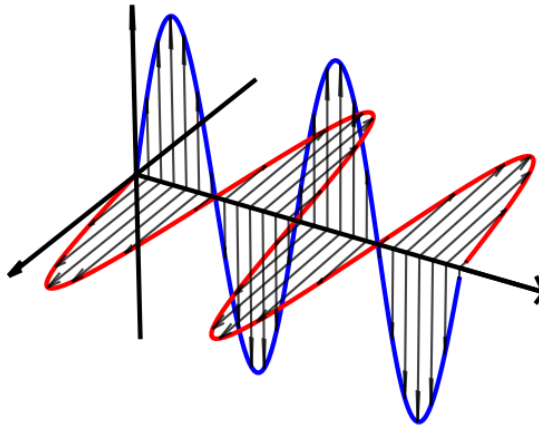


Figure 2.1: An illustration of linearly polarized light beam. The paths of the electric and magnetic field vectors are drawn in red and blue respectively, and the direction of propagation is shown with a black arrow.

Circular polarization

If the vectors of the electric and magnetic fields rotate around an axis containing the Poynting vector \vec{S} in such a way that they draw in space a helix, this is referred to as *circular polarization*, since the helix projects as a circle when viewed towards the direction of propagation (see Figure 2.2). When the direction of rotation of the electric field vector from the observer's point of view is counter-clockwise, by convention the

polarization is considered *right-handed*, and if the rotation is clockwise, it is considered *left-handed*.

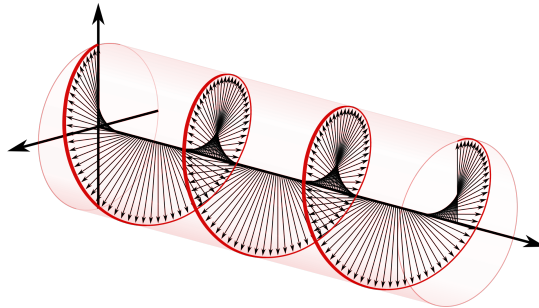


Figure 2.2: An illustration of circular polarization. Only the electric field vector is shown. The rotation of the vector is counter-clockwise (from the point of view of the observer) and by convention the polarization is classified as *right-handed*.

Elliptical polarization

Elliptical polarization is a sum of linear and circular polarization. In this case, the tip of the electric field vector describes an ellipse when viewed towards the direction of propagation. Based on the direction of rotation of the electric field vector, we can again have a *right-handed* or a *left-handed* elliptical polarization.

2.1.2 Stokes parameters

The state and degree of polarization can be fully described by the *four Stokes parameters*: I , Q , U , V .

Suppose that we want to describe the state of polarization of a given light beam and we have a set of six filters (F1 to F6) that transmit polarization as indicated in Figure 2.3: filter F1 only transmits linear horizontal polarization; filter F2 only transmits linear vertical polarization (at 90° with respect to F1); filters F3 and F4 only transmit linear polarization at respectively 45° and 135° with respect to F1; finally, F5 and F6 only transmit left- and right-handed circular polarization.

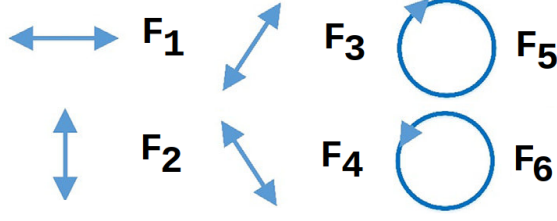


Figure 2.3: Polarization transmitted through each of the six filters that allow measuring the Stokes parameters.

Suppose now that we have a perfect detector that measures the light intensity i transmitted through each of the six filters. The four Stokes parameters I, Q, U, V are then defined as follows:

- Stokes I : the full light intensity, $I = i_{0^\circ} + i_{90^\circ} = i_{45^\circ} + i_{135^\circ} = i_{\text{right}} + i_{\text{left}}$;
- Stokes Q : the difference in intensity between the horizontally and vertically polarized beams, $Q = i_{0^\circ} - i_{90^\circ}$;
- Stokes U : the difference in intensity between the beams polarized at 45° and 135° , $U = i_{45^\circ} - i_{135^\circ}$;
- Stokes V : the difference in intensity between the right- and left-handed circularly polarized beams, $V = i_{\text{right}} - i_{\text{left}}$.

The degree of polarization is defined by the ratio:

$$P = \frac{\sqrt{Q^2 + U^2 + V^2}}{I} \quad (2.1)$$

In particular, the linear polarization ratio $P_L = \sqrt{Q^2 + U^2}/I$, and the circular polarization ratio $P_C = V/I$.

For a fully polarized light beam, $I^2 = Q^2 + U^2 + V^2$ and $P = 1$.

For a fully unpolarized light beam, $I = 1$, $Q = U = V = 0$ and $P = 0$.

2.1.3 The Zeeman effect

The Zeeman effect in atoms is the splitting of a spectral line into more than one component when the absorbing atom is placed in a magnetic field.

In an atom, each electron possesses a spin \vec{s} and an orbital angular momentum \vec{l} . The ensemble of electrons interact together to form a total spin $\vec{S} = \sum \vec{s}_i$ and a total orbital angular momentum $\vec{L} = \sum \vec{l}_i$. The total spin and total orbital angular momentum interact in what is known as the spin-orbit coupling, which results in the full angular momentum $\vec{J} = \vec{L} + \vec{S}$. When placed inside a magnetic field, each energy level with a full angular momentum J splits into $2J + 1$ sublevels which have different magnetic quantum

numbers m . The difference $\Delta\lambda$ between the wavelength of two sublevels is proportional to:

$$\Delta\lambda \propto \lambda_0^2 g B \quad (2.2)$$

where:

- λ_0 is the wavelength of the transition in the absence of magnetic field;
- B is the magnetic field strength;
- g is the Landé factor - a physical quantity representing how efficient the angular momentum of the atom is in generating a magnetic moment.

When the magnetic field strength is below ~ 1 G (in which case we say that the system is in the *weak-field regime*), the Landé factor is given by the formula

$$g = \frac{3}{2} + \frac{S(S+1) - L(L+1)}{2J(J+1)} \quad (2.3)$$

A transition between two energy levels is only possible when the difference Δm between their magnetic quantum numbers is either 0 (in which case the spectral line is called a π -component) or ± 1 (σ_{\pm} -component). The σ -components are shifted in wavelength following Equation 2.2, with the σ_- -component shifted to the blue and the σ_+ -component - to the red. The π -component is not shifted in wavelength. This is shown schematically in Figure 2.4.

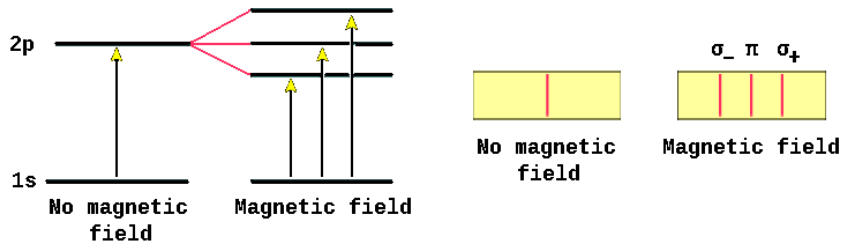


Figure 2.4: An illustration of the Zeeman effect on the energy levels (left) and an example atomic line (right).

The three components also have different polarization depending on the orientation of the external magnetic field. If the field vector \vec{B} forms an angle θ with the line of sight, the π -component is linearly polarized and the two σ -components are elliptically polarized in opposite directions, and the full intensity of the π -component is proportional to $\sin^2 \theta$. In the case when the field vector is transverse (perpendicular to the line of sight, $\theta = \pi/2$), all three components are observable and are linearly polarized, with the π -component being polarized in a perpendicular plane to the plane of polarization of the σ_{\pm} -components. In the case when the field is longitudinal (parallel to the line of sight, $\theta = 0$), the π -component is not observable at all and the σ_{\pm} -components have opposite

circular polarizations. A representation of this case is shown in Figure 2.5, where the intensity profiles of the σ -components are shown in the bottom panel, and their circular polarization profiles are shown in the top panel. The Stokes V signature observed in this case is sometimes referred to as an *S-shape* Stokes V profile. Figure 2.5 shows the case of a positive longitudinal magnetic field, when an *inverted S-shaped profile* is observed; the usual S-shape can be seen in the presence of a negative longitudinal field.

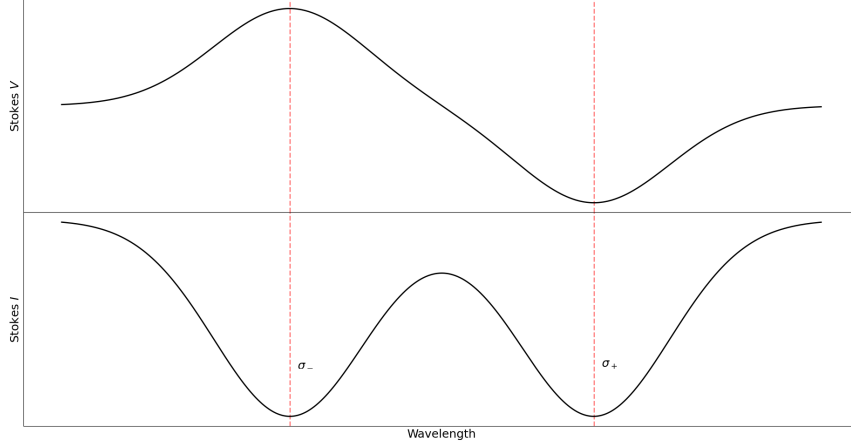


Figure 2.5: An illustration of the Zeeman effect in the case of a positive longitudinal magnetic field in Stokes I (bottom panel) and Stokes V (top panel), where the characteristic (inverted) S-shaped Zeeman profile can be seen.

The Zeeman effect generates both linear and circular polarization, but for magnetic fields in the weak-field regime ($\lesssim 1$ kG) the degree of linear polarization is an order of magnitude lower than that of circular polarization. This is why, in order to study relatively weak (< 20 G) longitudinal stellar magnetic fields, in this Thesis I focus on observations in circular polarization, except for the study of Betelgeuse presented in Chapter 5 where I work with observations in linear polarization. Furthermore, in the weak-field regime ($\lesssim 1$ kG) the degree of circular polarization of the σ_{\pm} -components depends linearly on the longitudinal magnetic field B_l , which makes circular polarization due to the Zeeman effect a promising way to study and measure the magnetic fields of cool evolved stars.

Figure 2.6 shows a schematic of a star with a non-zero disk-averaged surface magnetic field \vec{B} (depicted with a black arrow) and the line-of-sight projection of the surface field vector (depicted with a blue arrow), the longitudinal magnetic field \vec{B}_l – the component of the disk-averaged surface field that can be directly measured from spectropolarimetric observations in circular polarization.

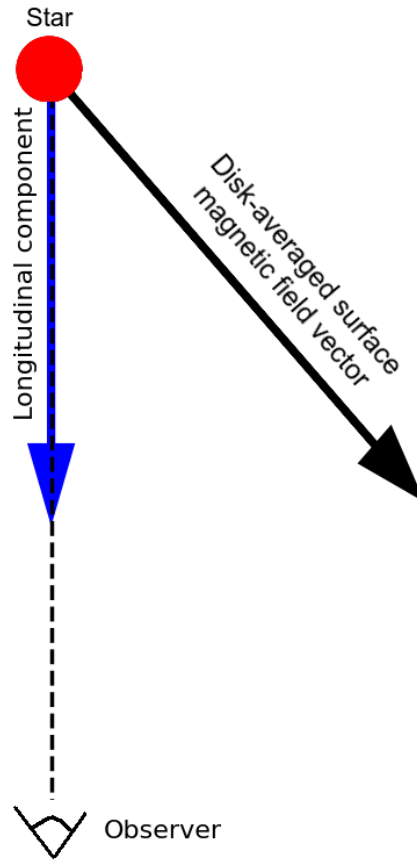


Figure 2.6: A schematic representation of the disk-averaged surface magnetic field vector \vec{B} and its longitudinal component \vec{B}_l , which can be directly measured from spectropolarimetric observations.

2.2 Observations with Narval

Narval (Aurière, 2003) was a fiber-fed *échelle* spectropolarimeter that operated between 2007 and mid-2019 at the 2m *Télescope Bernard Lyot* (TBL) at the *Pic du Midi* observatory in the French *Pyrénées*. In spectropolarimetric mode, this instrument allowed simultaneous measurement of the full intensity as a function of wavelength (Stokes I) and the intensity in linear (Stokes Q or U) or circular (Stokes V) polarization versus wavelength. Narval was capable of detecting polarization within individual lines with an accuracy of about $10^{-4}I_c$ (I_c being the intensity of the unpolarized continuum). The spectral resolution R of Narval in polarimetric mode was $R = 65000$. The instrument could also operate in spectroscopic mode to obtain only the Stokes I intensity spectra, but with a higher spectral resolution $R = 80000$. In both modes, Narval covered the spectral region between 375 and 1050 nm. Narval is a copy of the instrument ESPaDOnS operating at the Canada France Hawaii Telescope (Donati et al., 2006a).

The instrument itself consisted of a polarimeter (Figure 2.7) and a spectrograph (Figure 2.8), which are described below.

The polarimetric analysis with Narval is performed thanks to the polarimeter, which is attached at the Cassegrain focus. It consists of a Wollaston prism, one quarter-wave and two half-wave Fresnel rhombs. Between the Wollaston prism and the second half-wave Fresnel rhomb, a Fabry-Perot element may be inserted to produce interference patterns in the spectra in order to check the stability of the instrument.

The Fresnel rhombs are essentially waveplates made of a birefringent material: in them, the index of refraction is different for light polarized along one or the other of the two perpendicular crystal axes (called the fast axis and the slow axis). This introduces a controlled phase shift in the light beam, thus altering its polarization state at the exit of the waveplate. Each of the half-wave rhombs introduces a 180° phase shift of the electric field component of the light beam, while the quarter-wave rhomb introduces a 90° phase shift. While the quarter-wave Fresnel rhomb remains on the optical path, we can measure the left- and right-handed components of the circular polarization (Stokes V). To measure the state of linear polarization (Stokes U or Q), the quarter-wave rhomb must be removed from the optical path.

At the exit of the polarimetric module, the Wollaston prism splits the incoming light into two orthogonally polarized beams, i_{\parallel} and i_{\perp} , which continue their path through two separate fibers of the optical fiber link. To extract information on the polarization of the stellar spectra, each exposure with Narval is build from four sub-exposures. Each sub-exposure, referred to as its index n (i_n , with $n = 1, 2, 3, 4$), is obtained by rotating the two half-wave Fresnel rhombs to different angles α with respect to a fixed reference and yields two spectra: $i_{n,\parallel}(\alpha)$ and $i_{n,\perp}(\alpha)$.

To construct the intensity spectrum I and the Stokes parameter X (X being either Q , U or V) from the eight collected sub-spectra, the following calculation is performed (Donati et al., 1997; Bagnulo et al., 2009):

$$I = \sum_{n=1}^4 i_{n,\parallel}(\alpha) + i_{n,\perp}(\alpha) \quad (2.4)$$

$$X = \frac{R_X - 1}{R_X + 1}$$

where

$$R_X = \sqrt[4]{\frac{i_{1,\parallel}(\alpha)/i_{1,\perp}(\alpha) \ i_{4,\parallel}(\alpha)/i_{4,\perp}(\alpha)}{i_{2,\parallel}(\alpha)/i_{2,\perp}(\alpha) \ i_{3,\parallel}(\alpha)/i_{3,\perp}(\alpha)}} \quad (2.5)$$

The angles of rotation are different for the three Stokes parameters Q , U and V :

$$\begin{aligned}
 R_Q &= \sqrt[4]{\frac{i_{1,\parallel}(0^\circ)/i_{1,\perp}(0^\circ)}{i_{2,\parallel}(45^\circ)/i_{2,\perp}(45^\circ)} \frac{i_{4,\parallel}(180^\circ)/i_{4,\perp}(180^\circ)}{i_{3,\parallel}(225^\circ)/i_{3,\perp}(225^\circ)}} \\
 R_U &= \sqrt[4]{\frac{i_{1,\parallel}(22.5^\circ)/i_{1,\perp}(22.5^\circ)}{i_{2,\parallel}(67.5^\circ)/i_{2,\perp}(67.5^\circ)} \frac{i_{4,\parallel}(202.5^\circ)/i_{4,\perp}(202.5^\circ)}{i_{3,\parallel}(247.5^\circ)/i_{3,\perp}(247.5^\circ)}} \\
 R_V &= \sqrt[4]{\frac{i_{1,\parallel}(-45^\circ)/i_{1,\perp}(-45^\circ)}{i_{2,\parallel}(45^\circ)/i_{2,\perp}(45^\circ)} \frac{i_{4,\parallel}(135^\circ)/i_{4,\perp}(135^\circ)}{i_{3,\parallel}(225^\circ)/i_{3,\perp}(225^\circ)}}
 \end{aligned} \tag{2.6}$$

Furthermore, a diagnostic *null* spectrum is obtained for each exposure to help diagnose spurious polarization signals. The null spectrum N_V in the case of Stokes V is computed as follows:

$$\begin{aligned}
 N_V &= \frac{R_N - 1}{R_N + 1} \\
 R_N &= \sqrt[4]{\frac{i_{1,\parallel}(-45^\circ)/i_{1,\perp}(-45^\circ)}{i_{2,\parallel}(45^\circ)/i_{2,\perp}(45^\circ)} \frac{i_{3,\parallel}(225^\circ)/i_{3,\perp}(225^\circ)}{i_{4,\parallel}(135^\circ)/i_{4,\perp}(135^\circ)}}
 \end{aligned} \tag{2.7}$$

Similar formulae are used to compute N_Q and N_U .

Attached to the polarimeter is the calibration unit, which contains a removable prism. This prism can be used to direct the light coming from calibration lamps into the polarimeter, and from there, into the spectrograph. The calibration lamps are used for wavelength calibration (ThAr and Ne) and flat-field correction (halogen). In the calibration module, there is also the atmospheric dispersion corrector (ADC), consisting of two prisms that rotate independently from each other and serve to cancel out any atmospheric refraction in real time. Also attached to the polarimeter is the guiding CCD camera that is used to keep the telescope on the observed object.

After exiting the polarimetric module, the light travels through the optical fiber link and into the spectrograph through a slit. After that, the light is reflected from the main collimator to the diffraction grating, which sends it back to the main collimator. From there, the light goes to a flat mirror that reflects it onto a transfer collimator, which directs it to the cross-dispersing double prism. After exiting the cross-disperser, the light is now split into 40 *échelle* orders that finally enter the camera and are picked by the CCD detector.

The path that stellar light follows after reaching the main mirror of the TBL can also be seen in a video found online at <https://www.youtube.com/watch?v=CEvXJjnSVEQ>.

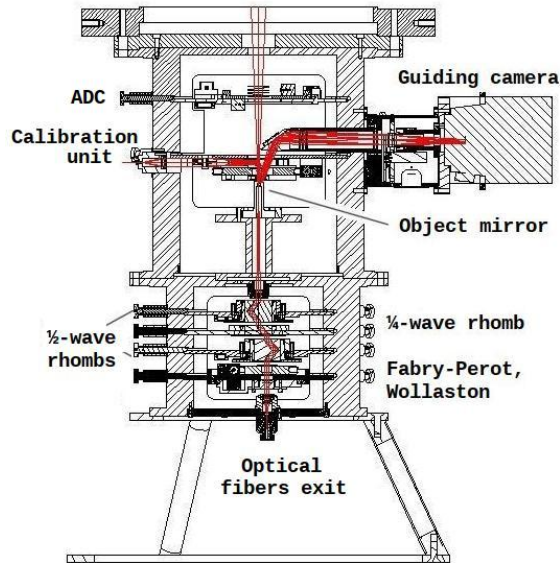


Figure 2.7: The polarimeter of Narval. Image from <https://tbl.omp.eu/>. Copyright: Laurent Parès (IRAP-OMP).

Data format

All Narval observations are treated initially by the fully automatic reduction software *LibreEsprit* (Donati et al., 1997), which performs optimal spectrum extraction, wavelength calibration, heliocentric frame correction and continuum normalization. For each observational sequence, *LibreEsprit* outputs two text files:

- a *.s* extension file containing a two-line header with the object name on the first line and the number of data points in wavelength space on the second, followed by the reduced spectrum in the format of an ASCII table that consists of six columns:
 - wavelength λ , [nm]
 - normalized full intensity $I(\lambda)$
 - normalized polarized intensity $I_{\text{pol}}(\lambda)/I(\lambda)$
 - normalized null #1 profile intensity $N_1(\lambda)/I(\lambda)$
 - normalized null #2 profile intensity $N_2(\lambda)/I(\lambda)$
 - normalized full intensity error $\sigma_I(\lambda)/I(\lambda)$
- a *.out* extension file containing technical information, such as the date and time of observation, CCD exposure time, SNR at the center of each *échelle* order, etc.

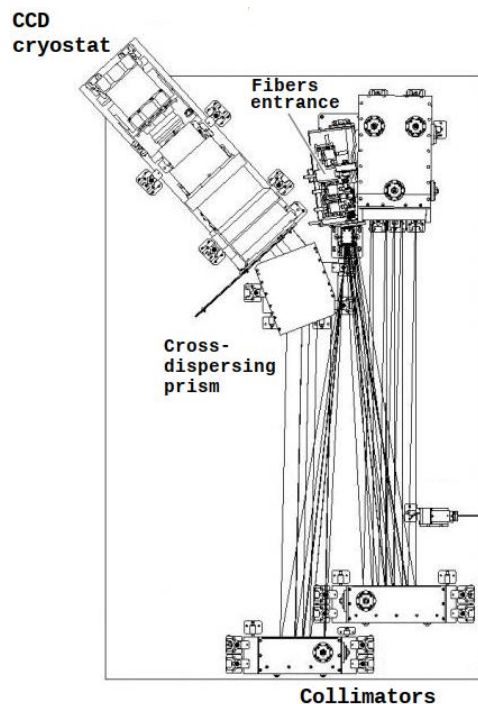


Figure 2.8: The spectrograph of Narval. Image from <https://tbl.omp.eu/>. Copyright: Laurent Parès (IRAP-OMP).

2.3 Least Square Deconvolution

Faint polarization within individual spectral lines can be below the detection limit (typically about 0.5 G for Narval) when dealing with spectropolarimetric data. This is particularly true when observing in circular polarization stars with weak disk-averaged magnetic fields. In this case, the Zeeman signatures, although present, have a very low signal-to-noise ratio (SNR) and accurate measurements on the basis of data from individual lines is impossible. Instead, a multi-line approach must be used.

2.3.1 The method

The *Least Square Deconvolution* (LSD) (Donati et al., 1997) is a method of averaging the shape of thousands (or even tens of thousands) of atomic lines to derive a mean line profile in both Stokes I and polarized light with a greatly increased SNR. It is widely used among the worldwide spectropolarimetric community to detect faint mean polarization profiles, and more specifically, to detect and measure stellar magnetic fields, by confronting the observed spectrum with a numerical line mask which contains information about atomic spectral lines.

LSD works under the assumption that all spectral atomic lines have the same inten-

2.3. LEAST SQUARE DECONVOLUTION

sity profile and only scale in depth. This is a fair approximation for most lines, except for some especially strong ones which are known to trace specific processes (chromospheric activity, atmospheric dynamics) or to have a significant interstellar or circumstellar component. Lines which are excluded from the LSD routine for these reasons are for example the Balmer series, CaH&K and Ca infrared triplet, the sodium D-doublet (D2 at 588.9950 and D1 589.5924 nm), and others. With the exception of these lines, the LSD procedure can be used on the whole 375-1050 nm spectral window to average more than 10 000 atomic lines. This allows the detection of mean polarization signatures with an immensely higher SNR compared to when measuring individual lines.

We suppose that in the case of cool evolved stars with weak surface magnetic fields, the local circularly polarized signal V associated to each spectral line is given by the weak field approximation:

$$V_{\text{loc}} \propto g \lambda \frac{\partial I_{\text{loc}}(v)}{\partial v} \quad (2.8)$$

where v represents the velocity coordinate ($\frac{c\Delta\lambda}{\lambda}$) associated with a wavelength shift $\Delta\lambda$ from the central wavelength λ , and g and $I_{\text{loc}}(v)$ are respectively the Landé factor and local profile of the atomic line. Assuming that the shape of the spectral lines is the same and they only differ in scale by their central depth d , we obtain:

$$V_{\text{loc}} = g \lambda d k_{\text{B}}(v) \quad (2.9)$$

where $k_{\text{B}}(v)$ is a proportionality function which is equal for all lines.

If we integrate the previous equation over the entire stellar disk and assume that limb darkening is not wavelength dependent, we obtain:

$$V(v) = S Z(v) \quad (2.10)$$

Where the function $Z(v)$ is called a mean Zeeman signature, which is constant for all lines and its shape is reproduced by all Stokes V profiles with a scaling factor $S = g \lambda d$.

We define a line pattern function

$$M(v) = \sum_i t_i \delta(v - v_i) \quad (2.11)$$

where v_i and t_i are respectively the position in velocity space and the weight of each spectral line. The line pattern \mathbf{M} , called a *line mask*, contains the parameters of atomic lines that are used in the LSD process: wavelength, relative depth, Landé factor and excitation potential. In order to create an LSD line mask, a model atmosphere is necessary that reflects as closely as possible the physical conditions in the star under study. Also, in order to know the transition wavelengths and parameters of spectral lines, atomic and molecular linelists which contain this information are necessary. In this Thesis, line

masks are computed using MARCS¹ model atmospheres (Gustafsson et al., 2008) and linelists extracted from the Vienna Atomic Line Database (VALD)² (Kupka et al., 1999). The circularly polarized spectrum V can be expressed as a convolution of the line pattern function with the mean Zeeman signature:

$$V = M^* Z \quad (2.12)$$

If we now assume that the intensities of the spectral lines add up linearly, we can rewrite the last expression as a linear system:

$$\mathbf{V} = \mathbf{M} \cdot \mathbf{Z} \quad (2.13)$$

The LSD method computes the least-squares solution for \mathbf{Z} . This solution, equivalent to a deconvolution, is expressed as:

$$\mathbf{Z} = (\mathbf{M}^t \cdot \mathbf{S}^2 \cdot \mathbf{M})^{-1} \mathbf{M}^t \cdot \mathbf{S}^2 \cdot \mathbf{V} \quad (2.14)$$

where \mathbf{S} is a square diagonal matrix whose element S_{jj} contains the inverse error $1/\sigma_j$ of spectral pixel j .

The mean Stokes U and Q signatures can also be computed in the same way.

An example of a Narval observation of the M giant star EK Boo on 2009/03/18 and its LSD output are shown in Figure 2.9. The line mask that was used was computed from a MARCS model atmosphere with the following stellar parameters: $T_{\text{eff}} = 3500$ K, $\log g = 0.5$, microturbulence of 2 km s^{-1} and solar metallicity.

¹<https://marcs.astro.uu.se/>

²<http://vald.astro.uu.se/>

2.3. LEAST SQUARE DECONVOLUTION

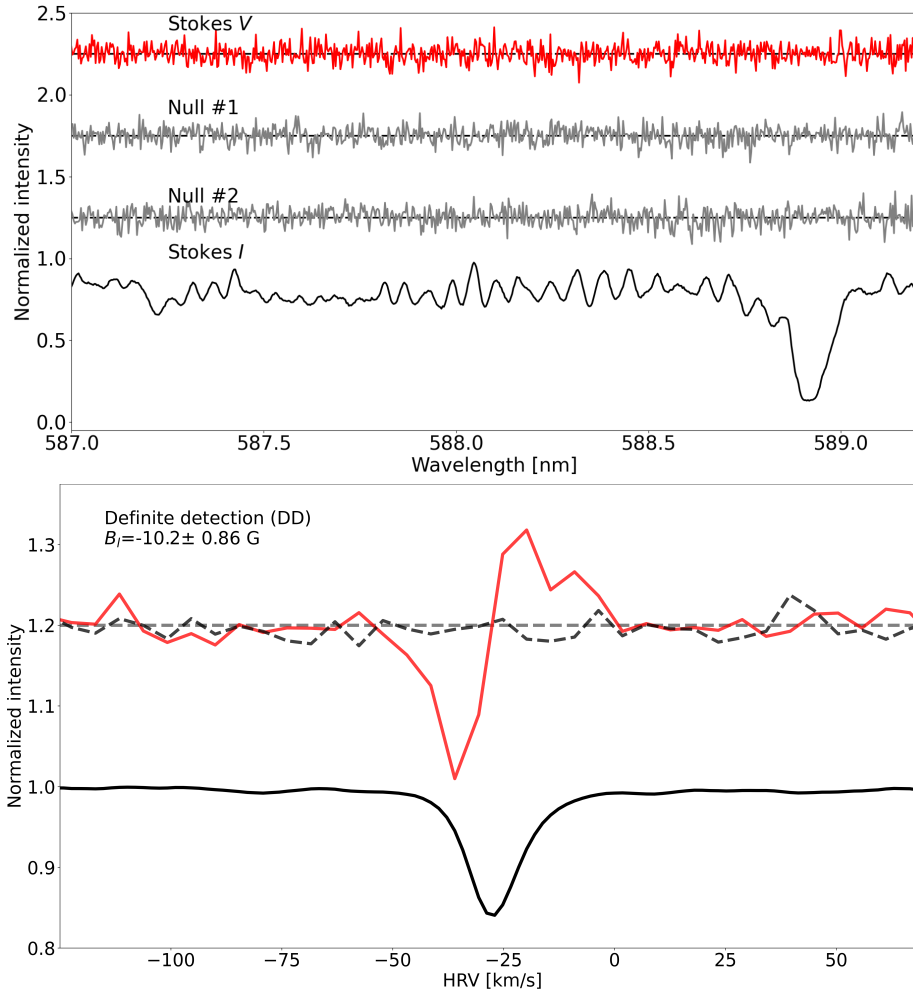


Figure 2.9: Upper panel: an example of a Narval observation of the M giant star EK Boo on 2009/03/18 in a narrow spectral window. The intensity profile is shown in black, the Stokes V profile - in red, and the two null profiles - in gray. The Stokes V and null profiles are shifted vertically and amplified for display purposes, and their zero levels are shown with dashed lines. Lower panel: the LSD profile of the same observation. The intensity profile is shown with the black solid line, the null profile - the black dashed line, and the Stokes V profile - the red solid line. The null and Stokes V profiles are again shifted vertically and amplified, and their zero level is indicated by the horizontal dashed line. The detection type (see Section 2.3.2) and longitudinal magnetic field B_l (see Section 2.4) are written at the top right. Notice the S-shaped Stokes V profile, characteristic for the Zeeman effect (described in Section 2.1.3) in a negative external magnetic field.

2.3.2 Classifying the detection of polarized signatures

To diagnose the presence or absence of signatures in the mean polarized spectrum, a statistical test described in Donati et al. (1997) that measures the detection probability is built into the LSD software. It consists of a reduced χ^2 test, done both inside and outside the mean line profile (whose location in velocity space is derived from the LSD Stokes I profile). The reduced χ^2 test statistics are converted into detection probabilities based on the number of pixels used in the test. According to this procedure, we can have a definite detection (DD) of polarization if the detection probability is higher than 99.999%, a marginal detection (MD) if it is between 99.9% and 99.999% or a non-detection (ND) otherwise. The test is done on both the polarized and the null profiles.

2.4 Measuring the longitudinal magnetic field

Using the output of the LSD procedure, in the Thesis I calculate the disk-averaged longitudinal component of the magnetic field (B_l , [G]) by following the first-order moment method (Rees & Semel, 1979; Donati et al., 1997):

$$B_l = -2.14 \times 10^{11} \frac{\int vV(v)dv}{\lambda_{\text{eff}}g_{\text{eff}}c \int [1 - I(v)]dv} \quad (2.15)$$

where:

- v , [km s⁻¹] is the stellar restframe radial velocity;
- $V(v)$ is the relative intensity of the LSD Stokes V profile;
- λ_{eff} , [nm] is the effective wavelength (see Section 2.8);
- g_{eff} is the effective Landé factor (see Section 2.8);
- c , [km s⁻¹] is the speed of light in vacuum.

The first-order moment method is based on the fact that the Zeeman effect introduces a degree of circular polarization proportional to the longitudinal magnetic field strength, as explained in Section 2.1.3.

2.5 Spectral activity indicators

In this Thesis, to trace the magnetic activity in the studied cool evolved stars, I use three spectral features that have chromospheric components. These are the calcium CaII H&K lines ($\lambda\lambda$ 3968, 3933), the hydrogen H α line (λ 6562) and the calcium CaII infrared triplet ($\lambda\lambda\lambda$ 8498, 8542, 8662; hereafter CaIRT for short). These spectral lines are widely used as indicators of stellar magnetic activity, along with lines like Ly α (λ 1215), MgII h&k ($\lambda\lambda$ 2803, 2796), CII ($\lambda\lambda$ 1334, 1335), CIV ($\lambda\lambda$ 1548, 1550) which however are outside the spectral window covered by Narval. To measure the intensity of the CaII H&K, H α

2.5. SPECTRAL ACTIVITY INDICATORS

and CaIRT, I compute respectively the S -index, the $H\alpha$ -index and the CaIRT-index, which are described in detail below.

The S -index is first described as a spectral indicator of magnetic activity in the Mount Wilson survey (Duncan et al., 1991) and it represents the ratio of the total intensity $F_H + F_K$ in the line cores of the CaII H&K lines to the total intensity $F_R + F_V$ in two adjacent continuum bandpasses R and V on both sides of the two lines. Following Aurière et al. (2015), to compute the S -index in this Thesis I use two rectangular bandpasses (H and K) centered on the cores of the CaII H&K lines with a width $\Delta\lambda_{H\&K} = 0.218$ nm each to measure the flux in the two lines. The sums of the total intensity F_H and F_K are then computed by calculating the weighted sums

$$\begin{aligned} F_H &= \frac{H}{W_H} = \sum_{\lambda} \frac{I(\lambda)}{\frac{1}{4} - \frac{1}{2\Delta\lambda_{H\&K}}|\lambda - \lambda_H|} \\ F_K &= \frac{K}{W_K} = \sum_{\lambda} \frac{I(\lambda)}{\frac{1}{4} - \frac{1}{2\Delta\lambda_{H\&K}}|\lambda - \lambda_K|} \end{aligned} \quad (2.16)$$

where the sums are computed within the limits of the respective bandpass.

Following Duncan et al. (1991), to measure the fluxes at the R and V continuum windows, I use two rectangular bandpasses with a width of 2 nm each, centered on 400.107 (R) and 390.107 nm (V). Finally, the S -index is calculated as follows:

$$S_{\text{index}} = \frac{aF_H + bF_K}{cF_R + dF_V} + e \quad (2.17)$$

where a , b , c , d and e are real coefficients. To measure the values of the S -index for cool giant stars, in this work I use the coefficients computed by Aurière et al. (2015) for Narval:

$$\begin{aligned} a &= 1.55 \\ b &= -1.37 \times 10^1 \\ c &= -3.57 \\ d &= -5.02 \\ e &= 2.21 \times 10^{-2} \end{aligned}$$

Figure 2.10 shows a graphical representation of the bandpasses used for the calculation of the S -index (as well as the two other indexes).

The $H\alpha$ -index is computed in a similar manner to the S -index:

$$H\alpha_{\text{index}} = \frac{F_{H\alpha}}{F_R(H\alpha) + F_V(H\alpha)} \quad (2.18)$$

where $F_{H\alpha}$ is a rectangular bandpass centered on 656.285 nm with a width of 0.36 nm, and $F_R(H\alpha)$ and $F_V(H\alpha)$ are also rectangular bandpasses centered respectively on 656.73 and 655 nm that have a width of 0.22 nm (see Figure 2.10).

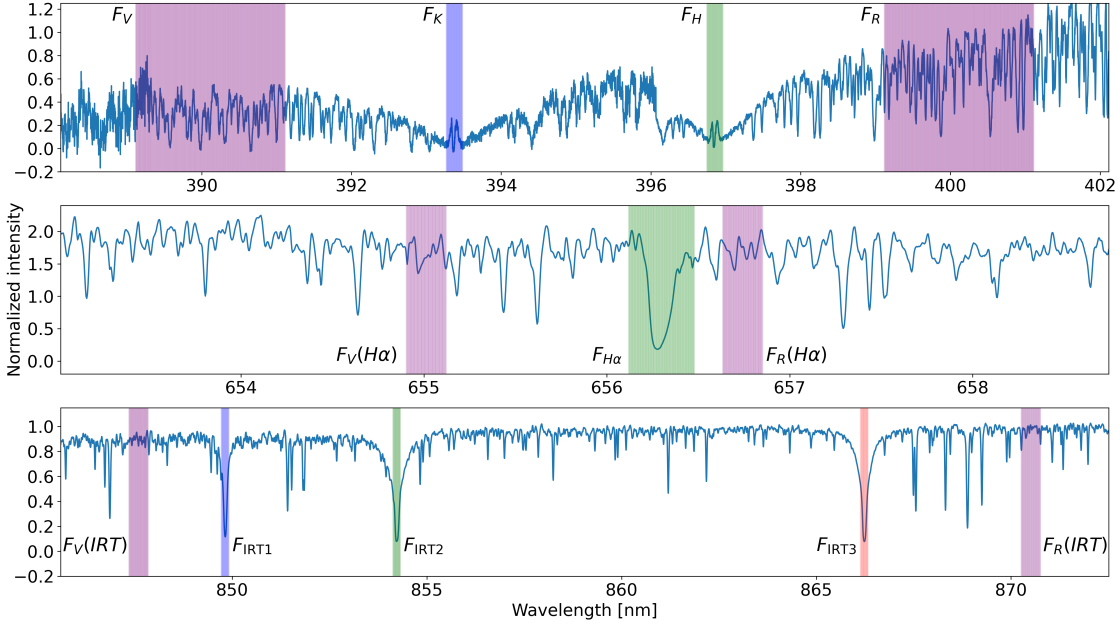


Figure 2.10: An example of the computation of the activity indicators: the S -index (top panel), the $H\alpha$ -index (middle panel) and the CaIRT-index (bottom panel). The bandpasses used are marked in different colors and the variable that corresponds to each of them is noted next to the bandpass. An observation of the M giant star β Peg of 2021/07/21 is used.

A similar formula is used to compute the CaIRT-index:

$$CaIRT_{\text{index}} = \frac{F_{IRT1} + F_{IRT2} + F_{IRT3}}{F_R(IRT) + F_V(IRT)} \quad (2.19)$$

where the $F_{IRT1,2,3}$ fluxes are computed in 0.2 nm-wide rectangular bandpasses centered on the three lines of the CaIRT (849.8023, 854.2091 and 866.2141 nm), and the $F_R(IRT)$ and $F_V(IRT)$ flux bandpasses are centered on 870.49 and 847.58 nm respectively, and have a width of 0.5 nm (see Figure 2.10).

2.6 NeoNarval

In September 2019 Narval was deeply upgraded to NeoNarval. The goal of this upgrade is to allow high-precision velocimetry, in order to study stellar systems that contain exoplanets. In particular, the upgrade to NeoNarval was done to allow the exploration of possible links between stellar magnetism and exoplanets.

NeoNarval keeps the polarimeter of Narval, but uses a new detector - an iXon CCD made by ANDOR. This new CCD has faster readout times of 2-3 seconds and at the

same time shows similar quantum efficiencies to the old detector used for Narval, while the readout noises of the two are also comparable. This allows for a better use of the observational time, with significantly less time being spent for the CCD readout.

The spectrograph has also been stabilized thermally with three concentric enclosures, the middle one of which is actively controlled in temperature. The diffraction grating of NeoNarval is mounted inside an isobaric chamber. The purpose of these changes is to stabilize the spectrograph in order to allow the measurement of velocities with a precision of 3 m s^{-1} . However, to reach this level of precision, a calibration beam is introduced that is fed with a stable Fabry-Perot spectrum. In NeoNarval, each of the 40 spectral orders is split in three. Two beams carry the orthogonal polarizations that allow the polarization modulation, while the third beam carries the Fabry-Perot spectrum.

In order to introduce this third calibration beam, the camera optics and the cross-dispersing prisms of Narval were overhauled, resulting in a raw image of the spectral orders completely different from that of Narval. A new data reduction software (DRS) was necessary in order to handle this change. Instead of upgrading the old *LibreEsprit* code, a new DRS was written from scratch by Arturo López Ariste (IRAP, Toulouse), leading to a new data format of the observations.

Data format

The NeoNarval DRS outputs *.fits* files that are structured in so-called extensions. Each extension is made of a header section and a data section. The header section contains basic information about the number of extensions, the size of the data in the data section, technical details concerning the observation (the object name, time of observation, exposure time, etc.) and specific information about the data contained in the given extension.

The *.fits* files that are distributed to the PIs of programs conducted with NeoNarval contain four extensions. The primary extension contains only the main header (with details about the telescope, instrument and observation) and has no data section. The 2nd extension contains in its data section six columns of floating point numbers, labelled as follows:

- wavelength λ , [\AA]
- normalized full intensity $I(\lambda)$
- normalized polarized intensity $I_{\text{pol}}(\lambda)/I(\lambda)$
- normalized null profile intensity $N(\lambda)/I(\lambda)$
- normalized full intensity error $\sigma_I(\lambda)/I(\lambda)$, computed as the standard deviation of the null profiles in a small range around each wavelength bin
- continuum, containing the continuum factor that has been applied to each wavelength bin of the extracted spectra in order to normalize them

The 3rd extension contains a data column which contains the indices in the six data arrays of the 2nd extension where the spectrograph orders start and end.

Finally, the 4th extension contains the result of an LSD procedure which is performed automatically by the DRS on the extracted spectra. This LSD result however is obtained using a general line mask that is selected by the DRS from a limited collection of masks. Because of this, the LSD result included in the 4th extension of the *.fits* file is only a rough one, as it is not obtained with a mask optimized for the observed star. In my Thesis, I do not use the results of this LSD procedure, since for maximum consistency between results obtained with Narval and NeoNarval, and to ensure that the optimal numerical mask is used, I have computed the LSD profiles of all observations using the same LSD software, described in details in Section 2.3.

2.7 Adapting NeoNarval data to the Narval format

The software tool for performing the LSD method used in this work (Donati et al., 1997) (see Section 2.3) was specifically written to take Narval data as input. However, since the upgrade of Narval to NeoNarval and the introduction of a new DRS and data format, direct usage of the same software on NeoNarval observations became impossible. To solve this problem, and to ensure that data obtained by both Narval and NeoNarval is treated in the same way, I wrote a *python3* program that converts NeoNarval observations to the data format of Narval. The steps followed by the conversion software are:

1. Loading the calibrated, normalized stellar spectrum from the observational *.fits* file into memory along with the *.fits* header;
2. Extracting the 40 individual *échelle* orders ($order_i^{input}, i \in 1, 2, \dots, 40$) from the input spectrum;
3. Building the output spectrum with the *échelle* orders in reverse sequence ($order_i^{input} = order_{40+1-i}^{output}, i \in 1, 2, \dots, 40$), so that the first order in the input becomes the last in the output, the second one in the input becomes second-to-last in the output and so on. This step is necessary because in the NeoNarval *.fits* files the spectral orders are sorted by decreasing wavelength, while in the Narval *.s* files it is the opposite case;
4. Converting the wavelength in the output spectrum from units of \AA to *nm*;
5. Writing the output spectrum in a Narval format ASCII file named `<date> / <object name>_<stokes parameter>_<sequence number>.s`
This is the file naming convention used by Narval. NeoNarval uses a different convention, which my program converts to the Narval one;
6. Extracting the contents of the *.fits* file's header to a *.header* file with the same name as the *.s* one.

The *.s* files outputted in this way are fully compatible with the LSD software described in Donati et al. (1997) that I use in this Thesis to treat the Narval observations. This ensures maximum consistency between the results obtained with the two instruments.

Because of the large worldwide popular demand (from Bulgarian, French and Australian teams) for such a tool that performs the conversion of NeoNarval observations to the Narval format, my program was made publicly available on the official TBL webpage: <https://tbl.omp.eu/instruments/neo-narval/>.

2.8 Treating the data

In this section, I describe how I compute in practice the LSD profiles, the longitudinal magnetic field and spectral activity indicators for each observation used in this Thesis.

An LSD profile is normalized by three coefficients: an equivalent Landé factor g_{eff} , an equivalent depth d_{eff} and an equivalent wavelength λ_{eff} . In general, these coefficients are not equal respectively to the mean values of the Landé factor, depth and wavelength of the lines used in the computation of the LSD profiles. To avoid differences due to this normalization, in the LSD software described in Donati et al. (1997), two parameters are computed that depend on g_{eff} , d_{eff} and λ_{eff} : a mean intensity weight W_{int} and a mean polarization weight W_{pol} . The final LSD profiles are independent of g_{eff} , d_{eff} and λ_{eff} when these two weights W_{int} and W_{pol} are both equal to 1.

In practice, setting the three coefficients to obtain $W_{\text{int}} = W_{\text{pol}} = 1$ is done by first giving λ_{eff} a value that is characteristic for the effective temperature of the star being studied. After that, the effective line depth d_{eff} is set so that $W_{\text{int}} = 1$. Finally, g_{eff} is set so that $W_{\text{pol}} = 1$. It must be noted that changing g_{eff} has no effect on W_{int} , so a solution always exists.

Because W_{int} and W_{pol} need to be iteratively set to 1, computing an LSD profile is essentially a trial-and-error type of operation. The calculation of an LSD profile is somewhat long (a single Narval sequence typically takes about 15 seconds to be processed), and so the whole process of finding the good g_{eff} and d_{eff} parameters for even a single observation usually takes a considerable amount of time. When dealing with large datasets, finding the right values for each observation consumes a considerable amount of time while requiring constant human attention.

To eliminate the need for manual setting of parameters, I wrote a *python3* code which is able to run the LSD software autonomously and to change the values of λ_{eff} , g_{eff} and d_{eff} when needed. The purpose of this program is to find the optimal set of parameters for each observation by iteration without requiring any human activity. While this code does not necessarily speed up the computation process, it greatly reduces the demand on the astronomer who is treating the data. The algorithm that the program follows in

order to treat Stokes V observations is:

1. The program asks which observations will be treated. For each selected observation, the name of the object is extracted from the header of the *.s* files and is ran through a locally stored database of stars containing the right line mask and effective wavelength λ_{eff} . After the mask and λ_{eff} are fixed, the observations are treated one by one;
2. LSD is performed for the first sequence in the first observation, taking the g_{eff} and d_{eff} parameters that were used in the last LSD computation;
3. After the calculations are done, the mean intensity weight W_{int} is extracted from the LSD software's output and compared to unity. In case it is equal to 1, the current value of d_{eff} is stored and the code moves on to step 4. Otherwise, d_{eff} is increased or decreased depending whether the value of W_{int} is respectively above or below 1, and the LSD computation is started again. This is repeated until $W_{\text{int}} = 1$;
4. After d_{eff} has been set, the program varies the effective Landé factor g_{eff} until $W_{\text{pol}} = W_{\text{int}} = 1$;
5. Once both d_{eff} and g_{eff} parameters have been fixed, their values for which the current observational sequence has $W_{\text{pol}} = W_{\text{int}} = 1$ are stored;
6. Steps 3-5 are repeated for each sequence of the current observation. After all the sequences have been treated, the median values $\overline{g_{\text{eff}}}$, $\overline{d_{\text{eff}}}$ of the two parameters are used to run LSD on each of the *.s* files (g_{eff} and d_{eff} are typically constant between sequences of the same observation, i.e. sequences collected on the same night). The result for each sequence is stored in a *.lsd* output file;
7. The LSD outputs of the individual sequences that make up the current observation are averaged in a single LSD output file that has a *.avg* extension. Step 2-6 are then repeated for the next observation.

This algorithm is schematically shown in Figure 2.11.

After the averaged LSD profiles are computed and stored in *.avg* files, the program also takes some other actions for each observation, such as:

- extracting the heliocentric julian date (HJD) from the *.out* files (Narval) or *.header* files (NeoNarval);
- fitting the mean Stokes I profile with a single gaussian and storing its peak position as an estimation of the heliocentric radial velocity of the star v_0 ;
- running the statistical test that determines the type of detection described in Section 2.3.2;

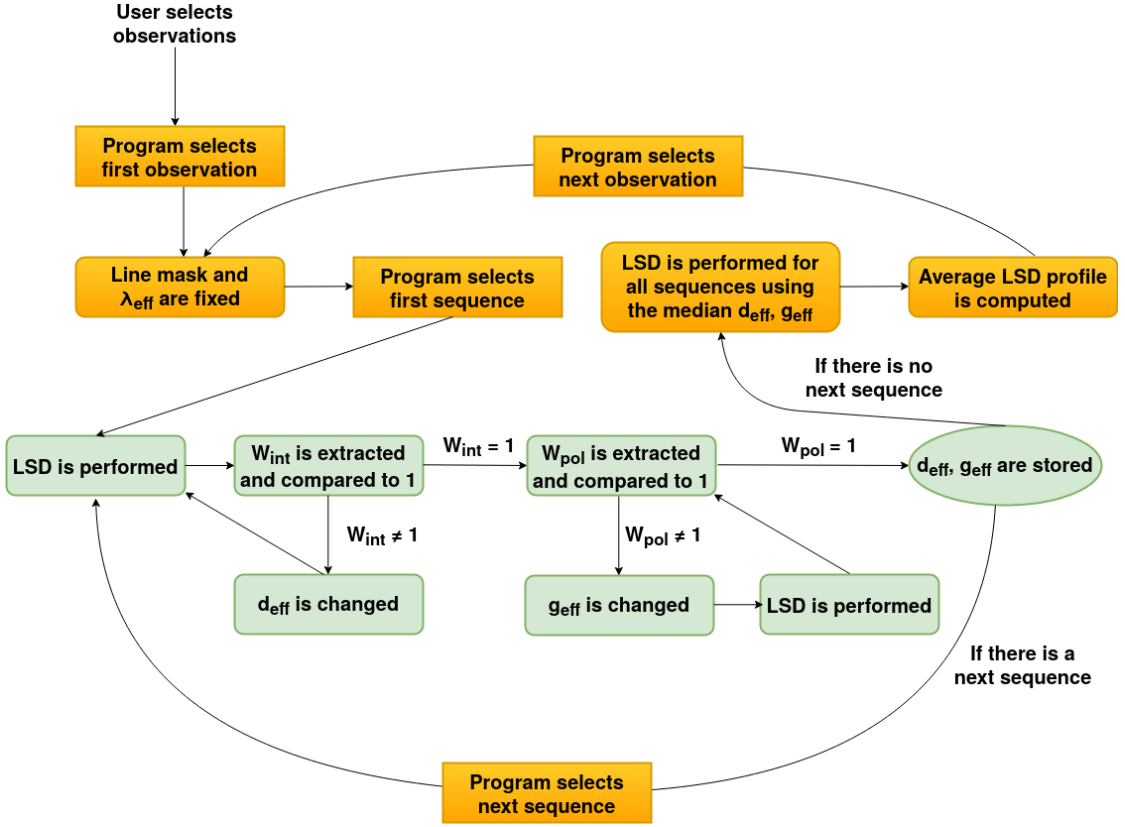


Figure 2.11: Schematic representation of the algorithm followed by the *python3* code in order to compute the LSD profiles of Narval and NeoNarval observations in circular polarization.

- computing the longitudinal component of the magnetic field, B_l , using the first order moment method described in Section 2.4;
- calculating the spectral activity indicators described in Section 2.5, using the velocity v_0 to shift the bandpasses in accordance with the radial velocity of the star;
- storing all the results of the above operations in an ASCII table;
- drawing the LSD profile of the *.avg* file and saving it as a figure.

The same algorithm is followed for the treatment of Stokes Q and U observations, but for them the computation does not depend on $\overline{g_{\text{eff}}}$, in which case $W_{\text{pol}} = \text{const} = 1$; also, no B_l is computed from observations in linear polarization.

In short, the program I wrote performs autonomously most of the tasks that an astronomer would otherwise do manually. This ensures that all data are treated in the exact same way and that the obtained results can be easily reproduced. Also, certain

tasks that are a part of this Thesis require running LSD on *thousands* of spectra - for example, the computation of a grid of synthetic LSD profiles, described in Section 1.5 of Chapter 3. In these cases, performing all operations manually would take so much time and attention that it would likely be impossible in practice.

Magnetism in M giant stars

In this Chapter, I will present my study of the surface magnetism in three M giant stars: RZ Ari, β Peg and EK Boo. The particular case of each star will be presented in a separate Section, where the magnetic field variability will be examined during the course of the available observational dataset. In the Section dedicated to the study of RZ Ari, I will also present a new method for the estimation of rotational and macroturbulent velocities of stars based on high resolution spectral observations, which I will then use to determine the rotational velocity of RZ Ari. For this star, I will also show the results of a period search analysis done on the available measurements, present an estimation of its mass and evolutionary status, and finally discuss a possible planet engulfment scenario based on the high lithium abundance of the star.

Summary

3.1	RZ Arietis	53
3.1.1	Observations	54
3.1.2	Magnetic field variability	55
3.1.3	Radial velocity variability and atmospheric dynamics	57
3.1.4	Linear polarization	59
3.1.5	Measuring stellar rotation and macroturbulence via spectrum synthesis and multi-line analysis	61
3.1.6	Determination of stellar parameters in RZ Ari	70
3.1.7	Paper published in <i>Astronomische Nachrichten</i>	72
3.1.8	Period search	80
3.1.9	Mass and evolutionary status	84
3.1.10	Lithium abundance. Planet engulfment scenario and possible dynamo action	86
3.2	β Pegasi	88
3.2.1	Observations	88
3.2.2	Magnetic field variability	89

3.2.3	Radial velocity variability and atmospheric dynamics	92
3.2.4	Linear polarization	92
3.3	EK Boötis	95
3.3.1	Observations	95
3.3.2	Magnetic field variability	97
3.3.3	Radial velocity variability and atmospheric dynamics	98
3.3.4	Linear polarization	98
3.3.5	Paper published in Bulgarian Astronomical Journal	101

3.1 RZ Arietis

RZ Ari (HD 18191) is a single giant star of spectral class M6III. Different values of its stellar parameters have been reported in previous papers: $T_{\text{eff}} = 3442$ K (van Dyck et al., 1998), $T_{\text{eff}} = 3450$ K (Konstantinova-Antova et al., 2010), $T_{\text{eff}} = 3250$ K, $\log g = 0.30$ and $[\text{Fe}/\text{H}] = -0.24$ (Prugniel et al., 2011).

RZ Ari is also a semi-regular variable star. Semi-regular variables are cool giant or super-giant stars which exhibit periodicity in their lightcurve caused by pulsations, which are triggered by changes in the opacity of the stellar material (the so-called κ -mechanism). The periodicity in semi-regular variables may sometimes be interrupted by irregularities, and the shape of the lightcurve may also vary for the different periods. For RZ Ari, the period of pulsations is of about 50 days and it has a known long secondary period (LSP) of 480 days (Percy et al., 2008; Percy & Deibert, 2016; Tabur et al., 2009). It is typical for semi-regular variables to have a LSP, but its origin is still unclear. Some possible scenarii for its origin are given by Percy & Deibert (2016), which include: rotational modulation caused by spots; presence of oscillatory convective modes; dusty circumstellar clouds; turnover of giant convective cells. Konstantinova-Antova et al. (2018) exclude the first hypothesis (rotational modulation due to spots) on the basis that in many cases of such stars, the rotational period P_{rot} is larger than the LSP and thus rotational modulation seems unlikely; the authors also exclude the dusty cloud hypothesis, since the LSP photometric color variations are similar to those of the pulsation period and have a sine shape.

The only estimations of the projected rotational velocity $v \sin i$ of RZ Ari available in the literature are given by Zamanov et al. (2008), who obtain $v \sin i = 9.6 \pm 2.0$ km s⁻¹ by means of cross-correlation and $v \sin i = 12.0 \pm 2.0$ km s⁻¹ by measuring the full width at half-maximum (FWHM) of spectral lines (both methods of estimation are described in details in Zamanov et al. 2007). However, these values were found to be incompatible with observations when an attempt was made to model the Stokes I and Stokes V LSD profiles of RZ Ari using the Zeeman-Doppler Imaging (ZDI Semel 1989; Donati & Brown 1997; Donati et al. 2006b) method. The reason for this is probably that these estimations of $v \sin i$ were done without properly considering the effect of macroturbulent velocity v_{mac} (see Section 3.1.5) on the spectral lines. As Gray (2013) shows, the use of cross-correlation to estimate $v \sin i$ of cool stars bears uncertainties due to the handling of line broadening caused by the effects of v_{mac} . In order to constrain the origin of the surface magnetic field in RZ Ari, and its connection with rotation, a better estimation of the rotational velocity (one which takes into account the effects of macroturbulence) is needed. In a paper published in 2020 in the journal *Astronomische Nachrichten* (Georgiev et al., 2020b), I estimate the projected rotational velocity of RZ Ari $v \sin i = 6.0 \pm 0.5$ km s⁻¹ and its macroturbulent velocity $v_{\text{mac}} = 2 \pm 1$ km s⁻¹. This estimation is done using an original method presented in details in Section 3.1.5. The paper itself is given at the end of this Section. I also presented the method for the determination of $v \sin i$ and v_{mac} to the international conference *16th Potsdam Thinkshop on Stellar Rotation: The Rotation Periods of Cool stars*, which took place between the 23rd and 26th September 2019 in

Potsdam, Germany.

I participate in a study of the evolutionary stage and magnetism of RZ Ari, the first results of which were presented at the *CoolStars* online conference in 2021. This study will be presented in a paper in preparation for the journal *Astronomy & Astrophysics*. Next in this paragraph, I will list the main results obtained in this paper on the physical parameters and evolutionary stage of the star. Using the interferometer CHARA, the angular diameter d of RZ Ari is measured to be $d = 10.268 \pm 0.0066$ mas. This is in good agreement with the previous estimations made by Richichi et al. (2006), who found $d = 10.22$ mas using lunar occultation and $d = 9.4$ mas using long-base interferometry. Taking into account the Gaia DR3 distance to the star of 97.78 pc, the stellar radius is computed as $R = 107.91 R_{\odot}$, which is fully consistent with the luminosity $L = 1412 L_{\odot}$ found by Villaume et al. (2017) on the basis of infrared measurements. This luminosity, combined with an effective temperature of $T_{\text{eff}} = 3450$ K (Konstantinova-Antova et al., 2010) means that in terms of stellar evolution RZ Ari is however either at the tip of the RGB or at the beginning of the AGB, following the models of Charbonnel et al. (2017). This means that on the HRD, RZ Ari lies outside the magnetic strips (see Section 4 of Chapter 1).

3.1.1 Observations

58 observations of RZ Ari were obtained with Narval in circular polarization (Stokes V) between September 2008 and August 2019, 27 of which show polarization signatures. 7 observations in linear polarization (Stokes $U&Q$) were also obtained between January 2014 and August 2019. A detailed log is shown in Table 3.1 for circular polarization and in Table 3.2 for linear polarization.

During the summers of 2011 and 2012, there was a technical problem with Narval. One of the Fresnel rhombs of the spectropolarimeter was out of position, which resulted in false Stokes V measurements. For the observations that were affected by this issue, only the intensity spectra were used and not the Stokes V profiles, meaning no B_l values are given for these dates in Table 3.1.

To extract the mean polarization signatures of atomic lines from the observations, I applied to them the LSD method (described in Section 3 of Chapter 2) using a dedicated line mask made from atomic line lists from the VALD database (Kupka et al., 1999) with the following parameters: $T_{\text{eff}} = 3400$ K, $\log g = 0.5$, microturbulence of 2 km s^{-1} and $[\text{Fe}/\text{H}] = -0.25$, compatible with the parameters reported for RZ Ari in the literature. The mask includes all spectral lines available from VALD except those that correspond to five chemical elements: H, He, Na, K, and Ca. I excluded these elements from the line mask because some of their lines are known to have strong chromospheric (H, He, Ca) or circumstellar/interstellar components (Na, K). The goal of performing LSD is to trace the magnetic field at the level of the photosphere, and so lines that may potentially have strong contributions from other layers of the stellar atmosphere must not be considered. The total number of excluded lines of the mentioned five elements is 1825. The final number of atomic lines that remain in the LSD mask is 11403, sufficient to produce an

LSD profile with very high SNR (as it can be seen in Table 3.1, the typical SNR of the observations is above 1000).

3.1.2 Magnetic field variability

The LSD profiles of RZ Ari in circular polarization are shown in Figure 3.2. It can be seen from this figure that the Stokes V signatures are variable with time, showing no detection (ND) in some observations and marginal (MD) or definite (DD) detections in others, where clear polarization signatures can be seen. It can also be seen in the Figure that there is a long-term decline in the magnetic activity of RZ Ari after the end of 2015 (after HJD 2457400).

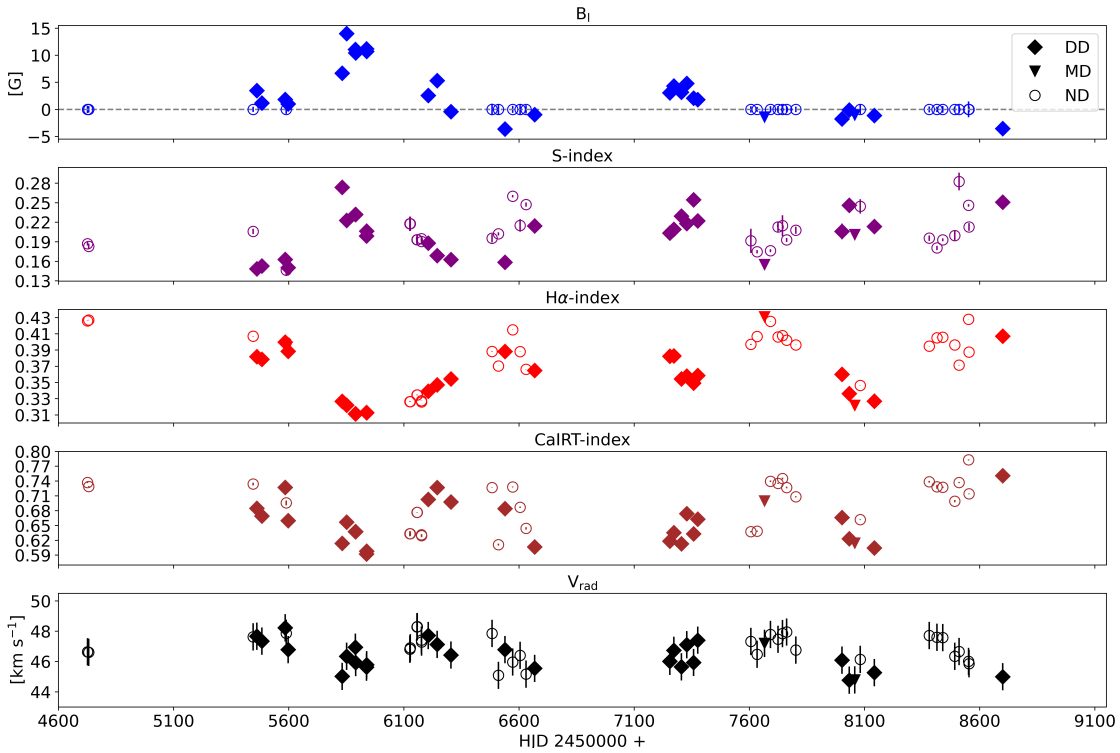


Figure 3.1: Measurements of the longitudinal magnetic field (B_l), the S-, H α - and CaIRT-indexes, and radial velocity (v_{rad}) of RZ Ari. The different symbols represent the different detection types (definite, marginal or no detection) as described in the legend of the top panel. The dashed gray line in the top panel represents the $B_l = 0$ G level. Errorbars are present for all points, but for some are smaller than the symbol used.

The observation on 2011/10/16 shows the strongest longitudinal magnetic field in the dataset for RZ Ari, $B_l = 14.01 \pm 0.34$ G. This is also the highest B_l value for all the M giant stars presented in this Thesis (RZ Ari, EK Boo and β Peg). This fact is of interest because while the two other giant stars belong to the second magnetic strip,

3.1. RZ ARIETIS

Date	HJD	SNR	σ_{LSD} ($10^{-5} I_c$)	Exposure time Stokes V	Detection Stokes V	B_l [G]	σ [G]	S- index	H α - index	CaIRT- index	V_{rad} [km s $^{-1}$]
2008/09/16	4726	1578	1.8	4x800s	ND	—	—	0.187	0.426	0.737	46.6
2008/09/21	4731	1479	1.9	4x600s	ND	—	—	0.183	0.427	0.729	46.6
2010/09/05	5445	1672	1.6	10x600s	ND	—	—	0.206	0.407	0.734	47.6
2010/09/21	5461	1118	1.2	16x400s	DD	3.47	0.36	0.148	0.382	0.685	47.7
2010/10/13	5483	1647	0.8	16x400s	DD	1.17	0.28	0.153	0.379	0.669	47.4
2011/01/22	5584	858	1.5	16x400s	DD	1.82	0.53	0.163	0.400	0.727	48.2
2011/01/27	5589	1078	2.4	4x400s	ND	—	—	0.146	0.399	0.696	47.9
2011/02/04	5597	1314	0.9	16x400s	DD	0.99	0.33	0.150	0.388	0.660	46.8
2011/09/26	5831	1131	1.1	16x400s	DD	6.68	0.43	0.274	0.327	0.614	45.0
2011/10/16	5851	1433	0.9	16x400s	DD	14.01	0.34	0.223	0.322	0.657	46.4
2011/11/23	5889	1311	2.1	4x400s	DD	11.06	0.70	0.232	0.311	0.638	47.0
2011/11/24	5890	1152	1.4	12x400s	DD	10.45	0.50	0.232	0.311	0.638	45.9
2012/01/10	5937	1361	1.3	8x400s	DD	11.17	0.47	0.199	0.313	0.592	45.6
2012/01/11	5938	1201	1.4	8x400s	DD	10.73	0.52	0.206	0.313	0.598	45.8
2012/07/16	6125	1315	2.7	2x400s	N/A	—	—	0.218	0.326	0.633	46.8
2012/07/17	6126	1354	2.0	4x400s	N/A	—	—	0.218	0.326	0.633	46.8
2012/07/18	6127	934	3.9	2x400s	N/A	—	—	0.218	0.326	0.633	46.9
2012/08/16	6156	1041	2.3	5x400s	N/A	—	—	0.193	0.335	0.677	48.3
2012/08/17	6157	1092	2.9	3x400s	N/A	—	—	0.193	0.335	0.677	48.3
2012/09/04	6175	1365	1.7	5x400s	N/A	—	—	0.195	0.328	0.631	47.4
2012/09/05	6176	1456	2.0	3x400s	N/A	—	—	0.191	0.326	0.629	47.3
2012/10/04	6205	1371	1.4	8x400s	DD	2.58	0.49	0.188	0.339	0.703	47.7
2012/11/12	6244	1127	1.7	8x400s	DD	5.30	0.61	0.169	0.347	0.727	47.1
2013/01/11	6304	1301	1.4	8x400s	DD	-0.43	0.53	0.163	0.354	0.698	46.4
2013/07/08	6482	1309	3.0	2x400s	ND	—	—	0.195	0.388	0.727	47.9
2013/08/05	6510	1106	2.6	3x400s	ND	—	—	0.202	0.370	0.611	45.1
2013/09/02	6538	1255	2.1	4x280s	DD	-3.63	0.78	0.159	0.388	0.684	46.8
2013/10/06	6572	1497	1.8	4x400s	ND	—	—	0.260	0.415	0.728	46.0
2013/11/07	6604	1172	2.3	4x400s	ND	—	—	0.215	0.388	0.687	46.4
2013/12/03	6630	1197	2.3	4x400s	ND	—	—	0.247	0.366	0.644	45.2
2014/01/09	6667	1561	1.7	4x400s	DD	-0.97	0.58	0.214	0.365	0.607	45.5
2015/08/19	7254	1242	1.6	8x400s	DD	3.07	0.62	0.203	0.382	0.618	46.0
2015/09/05	7271	1258	1.5	8x400s	DD	4.31	0.61	0.209	0.383	0.635	46.7
2015/10/08	7304	1504	1.3	8x400s	DD	3.17	0.45	0.229	0.354	0.613	45.6
2015/10/31	7327	1384	1.5	8x400s	DD	4.78	0.56	0.218	0.358	0.674	47.1
2015/11/30	7357	1238	1.6	8x400s	DD	2.07	0.55	0.254	0.349	0.633	45.9
2015/12/18	7375	1408	1.4	8x400s	DD	1.79	0.53	0.222	0.359	0.663	47.4
2016/08/05	7606	1119	1.6	8x400s	ND	—	—	0.191	0.397	0.637	47.3
2016/09/01	7633	1399	1.3	8x400s	ND	—	—	0.175	0.407	0.639	46.5
2016/10/03	7665	1374	1.4	8x400s	MD	-1.41	0.50	0.155	0.431	0.700	47.2
2016/10/29	7691	1104	1.8	8x400s	ND	—	—	0.176	0.425	0.740	47.8
2016/12/01	7724	1045	1.9	8x400s	ND	—	—	0.213	0.406	0.735	47.5
2016/12/20	7743	897	2.3	8x400s	ND	—	—	0.215	0.408	0.745	47.9
2017/01/07	7761	1356	1.4	8x400s	ND	—	—	0.193	0.402	0.727	48.0
2017/02/16	7801	1445	1.3	8x400s	ND	—	—	0.208	0.396	0.708	46.8
2017/09/04	8001	869	2.3	8x400s	DD	-1.77	0.86	0.206	0.360	0.666	46.1
2017/10/06	8033	1186	1.6	8x400s	DD	-0.11	0.57	0.246	0.336	0.623	44.8
2017/10/30	8057	1228	1.5	8x400s	MD	-1.03	0.54	0.201	0.322	0.614	44.8
2017/11/23	8081	857	2.3	8x400s	ND	—	—	0.244	0.346	0.662	46.1
2018/01/23	8142	747	2.6	8x400s	DD	-1.15	0.90	0.214	0.327	0.605	45.3
2018/09/18	8380	1278	1.6	8x400s	ND	—	—	0.196	0.395	0.739	47.7
2018/10/22	8414	1300	1.5	7x400s	ND	—	—	0.181	0.405	0.728	47.6
2018/11/16	8439	1219	1.6	8x320s	ND	—	—	0.193	0.406	0.727	47.6
2019/01/07	8491	1362	1.4	8x400s	ND	—	—	0.200	0.396	0.699	46.4
2019/01/26	8510	889	2.3	8x400s	ND	—	—	0.283	0.371	0.737	46.7
2019/03/08	8551	1014	4.5	2x400s	ND	—	—	0.246	0.428	0.783	46.0
2019/03/11	8553	1367	1.5	8x400s	ND	—	—	0.213	0.388	0.714	45.9
2019/08/03	8699	1169	1.8	8x400s	DD	-3.55	0.54	0.251	0.407	0.751	45.0

Table 3.1: Log of observations in circular polarization of RZ Ari. HJD starts from 2450000. The "SNR" column lists the average signal-to-noise ratio of the individual intensity spectra per 1.8 km s $^{-1}$ spectral bin. The " σ_{LSD} " column gives the RMS noise level relative to the unpolarized continuum in the LSD profiles. The "Exposure time" column gives the number of obtained Stokes V sequences times the total exposure time for each one of them (see Section 2 of Chapter 2 for a detailed explanation of the way Narval observations are obtained). No B_l values are computed for the dates affected by the misalignment of the Fresnel rhomb described in Section 3.1.1, and they are marked with "N/A" in the "Detection" column. Following the Nyquist theorem, I estimate the error of the V_{rad} measurements to be 0.9 km s $^{-1}$.

RZ Ari is outside the magnetic strips and solar-type dynamo is not expected to operate in it. This means that some other type of dynamo must be responsible for this magnetic field, which is also relatively strong with respect to other M giants. In Section 3.1.10 I will present the possibility that magnetism in RZ Ari is due to planet engulfment.

3.1.3 Radial velocity variability and atmospheric dynamics

The estimations of the radial velocity of RZ Ari, shown in the bottom panel of Figure 3.1, present some variability in the range of 44-48 km s⁻¹. This variability might be due to pulsations, as the star is known to be a semiregular variable.

To study whether strong atmospheric dynamics (e.g. shock waves) are present in RZ Ari, I examined the intensity profiles of certain spectral lines: the Balmer lines of hydrogen H α , H β and H γ and also the sodium D doublet NaD (D1 at 589.5924 and D2 at 588.9950 nm). These lines are known to display strong variability in the presence of energetic atmospheric dynamics, for example in the case of Mira stars (pulsating AGB stars of spectral type M). In Miras, the periodic emergence of strong radial pulsations leads to radiative and shockwaves which propagate through the atmosphere, causing doubling of metallic lines and emission in the lines of hydrogen lasting up to 80% of the luminosity period (Gillet et al., 1983; Alvarez et al., 2000, 2001). Due to the doubling of metallic lines, the LSD profiles of Mira stars typically show a double-peaked Stokes I profile (see e.g. Lèbre et al. (2014) for the case of χ Cyg). A similar case is that of the post-AGB variable star R Scuti, a detailed study of which is presented in Chapter 4.

However, none of the typical signs of shock waves appear in the Narval observations of RZ Ari. The Balmer lines H α , H β and H γ show no emission, nor any noticeable variability, in any of the data. In Figure 3.3, an example is shown for the H α line. The NaD lines on the other hand show a three-component structure, in which the components display no strong variability, neither in shape nor in position. Finally, the LSD Stokes I profiles (see Figure 3.2) are always single (no splitting is reported) and do not present any large radial velocity shift. All of these facts indicate that atomic lines in the spectrum of RZ Ari are in general not affected by strong variable large-scale velocity fields that could be associated to ballistic motions due to the propagation of shock wave(s), as it is the case for example in the post-AGB star R Sct. A study of the possible connection between the surface magnetism and atmospheric dynamics in R Sct is presented in details in Chapter 4, where it can be seen that the pulsations in this star result in shifts in the LSD Stokes I profiles that have an amplitude of almost 100 km s⁻¹, which is much larger than the 4 km s⁻¹ amplitude observed in the LSD profiles of RZ Ari. While some dynamics may be present in the atmosphere of RZ Ari, they would be relatively weak and may likely have no impact on the magnetic field of the star.

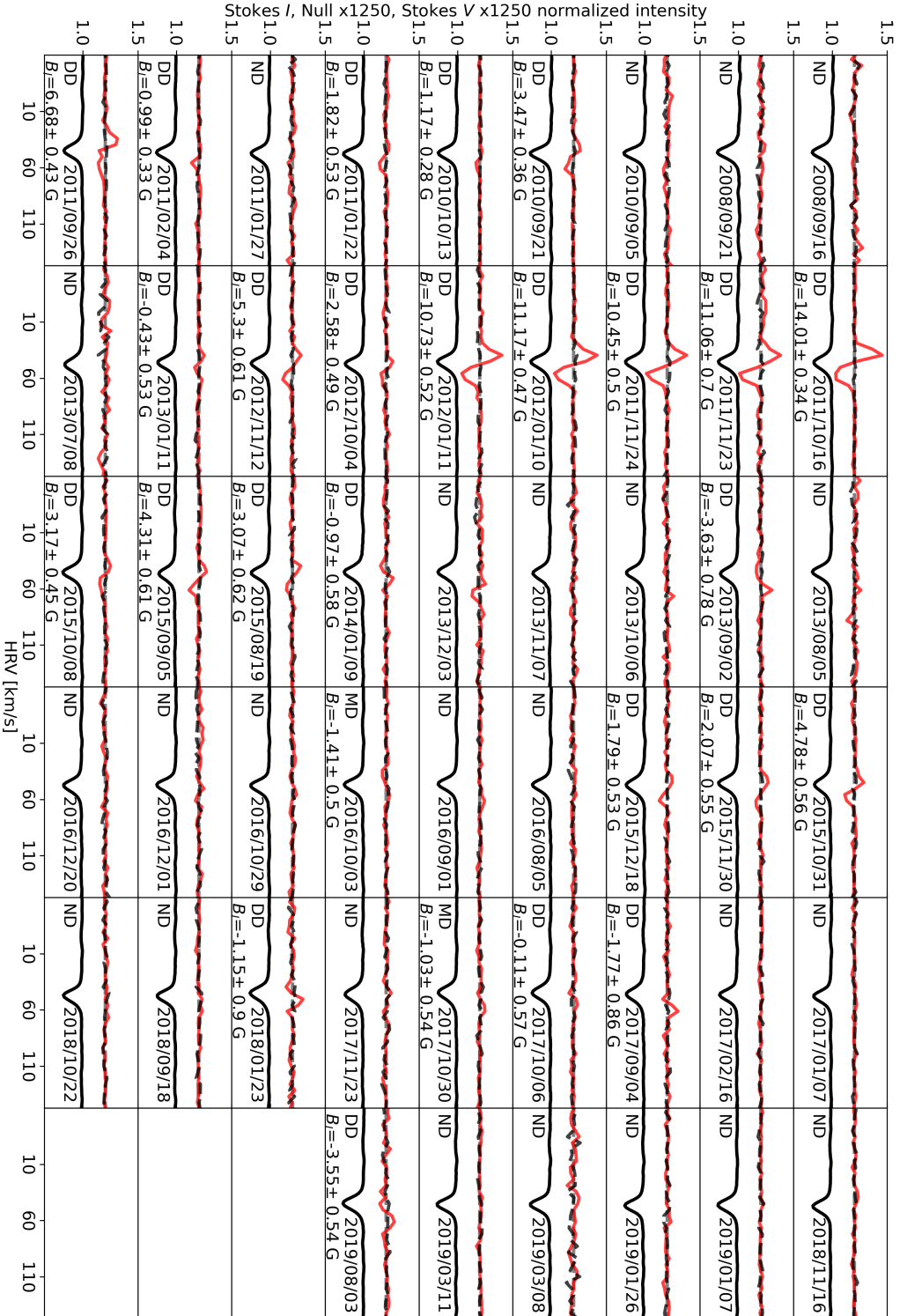


Figure 3.2: LSD profiles of RZ Ari in circular polarization. Each observation is shown in a separate panel with the date and detection type indicated, and for the observations where either a marginal or a definite detection is found, the B_l value and its error are shown. The intensity profiles are shown as solid black lines, the null profiles - as dashed black lines and the Stokes V profiles - as solid red lines. The null and Stokes V profiles are amplified as indicated on the label of the y-axis, shifted vertically and smoothed by averaging every three pixels for display purposes, and their zero level is indicated by dashed gray lines.

3.1.4 Linear polarization

7 observations were obtained in linear polarization for RZ Ari (described in Table 3.2). For these observations, I searched both in individual spectral lines (notably the Balmer lines $H\alpha$, $H\beta$, $H\gamma$ and $H\delta$, the CaIRT lines and the sodium doublet NaD, as well as lines that are close to them in wavelength by 2-3 nm) and the LSD profiles (shown in Figure 3.4) for linearly polarized signatures. Neither the individual lines I examined, nor the LSD profiles of RZ Ari show any linear polarization features. Based on this, I conclude that there is no linear polarization in the atomic lines of RZ Ari above the detection limit during the time of the available Narval observations.

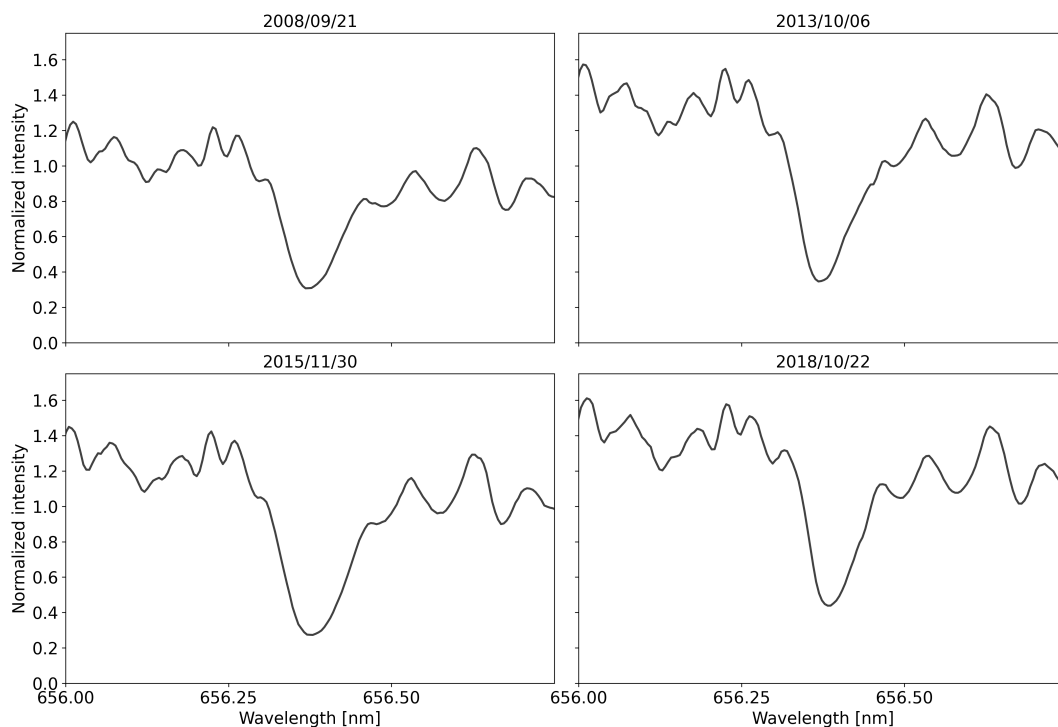


Figure 3.3: The $H\alpha$ line in four different observations of RZ Ari. It can be seen that no emission or significant variability is present in the line profile.

3.1. RZ ARIETIS

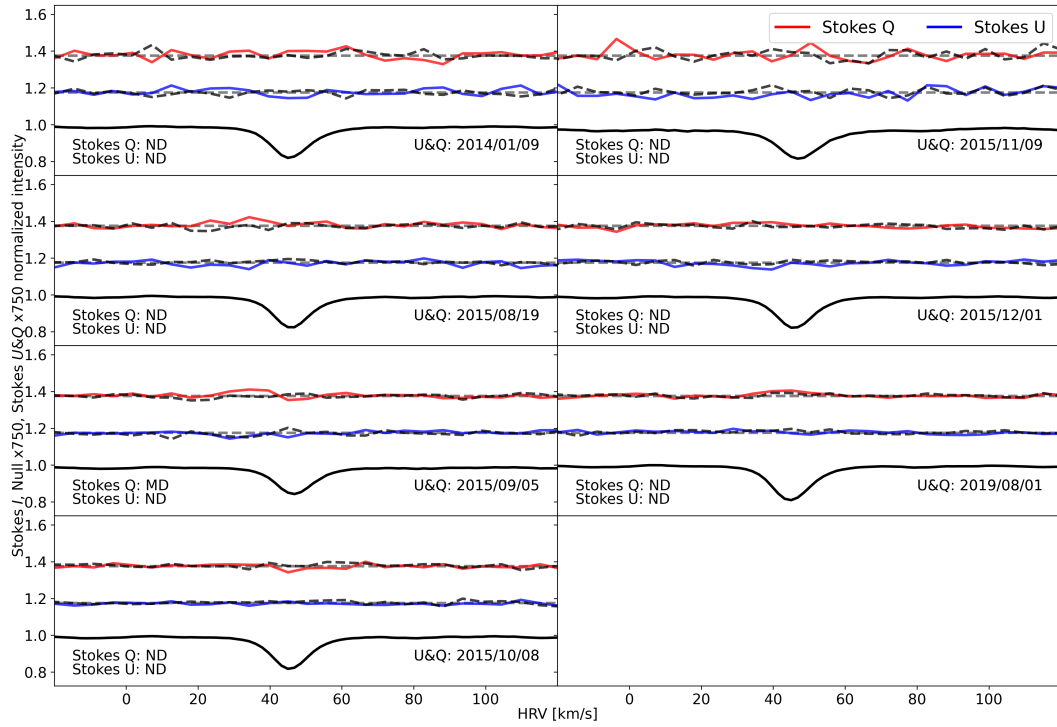


Figure 3.4: LSD profiles of RZ Ari observations in linear polarization. Each panel represents a single date of observation. Stokes U is in blue, Stokes Q is in red, and their respective null profiles are shown as dashed black lines. The types of detection and the date of observation are written at the bottom left and bottom right parts of each panel, respectively. The polarized profiles and their diagnostic nulls are amplified as indicated on the label of the y-axis, shifted vertically and smoothed by averaging every three pixels for display purposes, and their zero levels are indicated by horizontal dashed gray lines. The Stokes I profiles are shown as solid black lines.

Date	HJD	SNR	σ_{LSD} ($10^{-5}I_c$)	Exposure time ($U \& Q$)	Stokes U detection	Stokes Q detection
2014/01/09	6667	1117	4.8	1Ux400s, 1Qx400s	ND	ND
2015/08/19	7254	1162	3.1	2Ux400s, 2Qx400s	ND	ND
2015/09/05	7271	1262	2.6	2Ux400s, 2Qx400s	ND	MD
2015/10/08	7304	1481	2.5	2Ux400s, 2Qx400s	ND	ND
2015/11/09	7336	1052	6.4	2Ux400s, 2Qx400s	ND	ND
2015/12/01	7358	1304	2.6	2Ux400s, 2Qx400s	ND	ND
2019/08/01	8698	1127	2.0	4Ux400s, 6Qx400s	ND	ND

Table 3.2: Log of observations in linear polarization of RZ Ari. HJD starts from 2450000. The " σ_{LSD} " column gives the RMS noise level relative to the unpolarized continuum in the LSD profiles. The "Detection" column uses the notation given in Section 3.2 of Chapter 2.

3.1.5 Measuring stellar rotation and macroturbulence via spectrum synthesis and multi-line analysis

To further explore the magnetism in RZ Ari, an attempt was made to model the surface magnetic field of the star using the ZDI method on the Stokes V observational dataset from Narval. The ZDI method takes as input a large number of free parameters to model the surface field, and one very important such parameter is the projected rotational velocity on the line of sight, $v \sin i$. The only estimation in the literature for the $v \sin i$ of this star was done by Zamanov et al. (2008), who find $v \sin i = 9.6 \pm 2.0 \text{ km s}^{-1}$ by means of cross-correlation and $v \sin i = 12.0 \pm 2.0 \text{ km s}^{-1}$ by measuring the FWHM of spectral lines. However, these values were estimated without taking into account the effects of macroturbulence on the stellar spectrum. It turned out that these values are not compatible with observations when the ZDI method is attempted with them. In order to precise the origin of the detected magnetic field at the surface of RZ Ari, and its connection with rotation, a better estimation of the rotational velocity was needed which takes into consideration the effects of macroturbulence. To make such an estimation, I developed a new method for the determination of $v \sin i$, based on spectrum synthesis and multi-line analysis.

Effects of rotation and macroturbulence on the stellar spectrum

The laboratory wavelength λ_0 of atomic lines is defined by $\Delta E = E_n - E_k = \frac{hc}{\lambda_0}$, where ΔE is the difference in the potential energy of the n and k levels between which the electron transition occurs, and h is the Planck constant. In the absence of any velocity fields (e.g. rotational, macroturbulent) and at zero gas pressure and temperature, the width of lines in the spectrum of a star will be defined by Heisenberg's uncertainty principle. According to this principle, any energy level E above ground state that has a lifetime of Δt has an uncertainty given by $\Delta E \Delta t \geq h/4\pi$. The resulting profile is generally referred

to as the *natural line profile*. The line profile gets broadened by temperature due to the Doppler effect: photons with wavelength λ_0 are absorbed by atoms with mass m that have a radial velocity $\pm v$ described by the Maxwell distribution, and so absorb atoms at wavelength $\mp v\lambda_0/c$. The resulting thermal broadening $\Delta\lambda_T$ of the line will then depend on the temperature T as $\Delta\lambda_T = \frac{\lambda_0}{c} \sqrt{\frac{2k_B T}{m}}$, where k_B is the Boltzmann constant. The gas pressure also broadens the natural line profile.

In the presence of rotation, the observed spectral lines become further broadened depending on the projection of the rotational velocity \vec{v}_{rot} along the line of sight. The projected rotational velocity along the line of sight is commonly denoted as $v \sin i$, where i is the inclination angle between the line of sight and the axis of rotation (see Figure 3.5). The rotational broadening of spectral lines is caused by the Doppler effect: the hemisphere of the star which due to rotation appears to be moving towards the observer contributes to a blue-shifted component of the spectral line, while the hemisphere which appears to be moving away from the observer contributes to a red-shifted one. In the case where all points of the stellar disk have the same temperature, this leads to a spectral profile which appears broader and more shallow than in the case of a non-rotating star (or a star viewed from the pole, where $i = 0$). The effect of rotation on spectral lines is shown schematically in Figure 3.6.

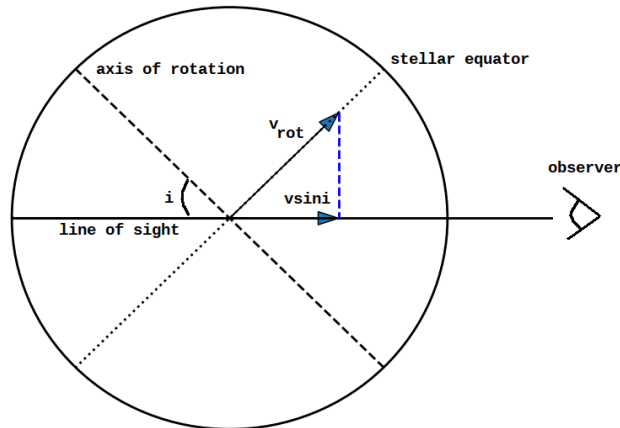


Figure 3.5: Projection of the rotational velocity on the line of sight.

Macroturbulence is a term which describes line broadening caused by the velocity fields of structures larger than the mean free path of the photon, e.g. granulation and supergranulation. This is similar to microturbulence, which in contrast is caused by velocity fields of structures smaller than the mean photon free path. However, both names are somewhat misleading since neither of the two physical quantities is strictly associated to turbulence. While microturbulence changes the equivalent width of spectral lines, macroturbulence does not (Magain, 1984; Mucciarelli, 2011). Were it possible to observe the spectra of individual structures which contribute to macroturbulence, a radially shifted spectrum of the star would be obtained from each such individual element. However,

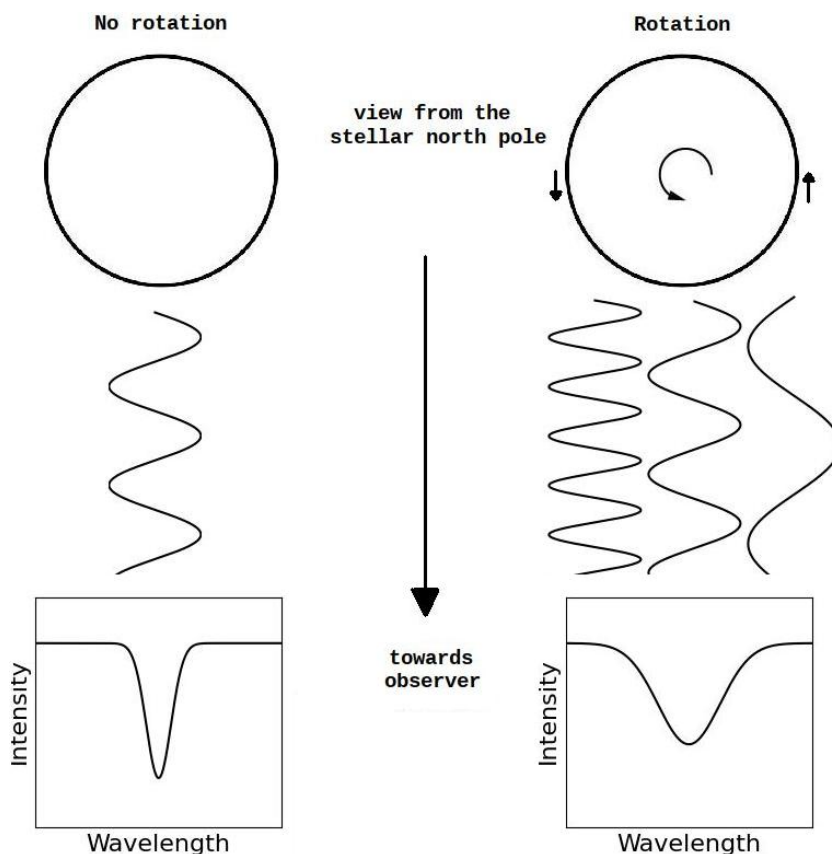


Figure 3.6: Schematic presentation of the effects of stellar rotation on the spectrum.

when observing spatially unresolved stellar disks, the radial shifts of all visible macro-turbulent structures add up, resulting in a net broadening of the spectral features. This broadening is quantitatively described by a parameter called *macroturbulent velocity*, v_{mac} [km s^{-1}].

Spectrum synthesis

The spectrum synthesis method is a classical approach for the determination of stellar parameters, including the rotational velocity projected on the line of sight, $v \sin i$, and the macroturbulent velocity, v_{mac} , with the help of high-resolution spectroscopic observations. In this method, stellar model atmospheres and atomic and molecular linelists are first used to create a synthetic spectrum. The latter is convolved with the instrumental profile of the spectrograph used for the observations and also with profiles of rotational and macroturbulent broadening. The resulting spectrum is then compared, over a large spectral domain, to an observational spectrum to obtain the fundamental parameters of the considered star, including $v \sin i$ and v_{mac} .

Spectrum synthesis using Turbospectrum

Turbospectrum (Plez, 2012) is a 1D LTE spectrum synthesis code which solves the radiative transfer equation using atomic and molecular line lists extracted from VALD. It is capable of working with spherical atmospheric models, which offer a better approximation when building synthetic spectra of giant stars than plane-parallel models do.

Turbospectrum has a built-in procedure for taking both rotational and macroturbulent velocities into account after the synthetic spectrum has been computed. The procedure consists of calculating the convolution of the stellar spectrum (originally computed for $v \sin i = v_{\text{mac}} = 0$) with the broadening profile corresponding to a given value of the selected velocity. In Georgiev et al. (2020b), to take into account the effects of rotation, I use a rotational profile as described by Gray (1992), and for macroturbulence I use a radial-tangential profile, again as given in Gray (1992).

Comparing observational to synthetic data using LSD

In the particular case of cool M giant stars one faces certain difficulties in applying the classical method of spectrum synthesis. One of these difficulties is the great number of spectral features that often blend each other, making it difficult to distinguish between individual lines. Another typical problem in practice is the likely imperfect normalization to the continuum that often affects the observation and prevents a straightforward comparison with a synthetic spectrum. To escape such inconveniences and to obtain a more precise result for $v \sin i$ and v_{mac} , an original multi-line approach based on the use of LSD was developed for the determination of stellar parameters, and it was used to estimate these parameters in the case of RZ Ari.

Instead of comparing individual lines from synthetic spectra computed for different values of $v \sin i$ and v_{mac} to an observed spectrum, in Georgiev et al. (2020b) I perform the comparison on the mean line profiles (computed using the LSD method) of the observed and synthetic spectra. The main advantages of comparing the mean spectral lines over individual lines are:

- significantly higher SNR due to the averaging of thousands of lines;
- line blending is no longer an issue, since both the observed and synthetic spectra are treated using the same line mask in the LSD process;
- since the comparison is performed on only one pair of line profiles and is rather simple, it can be easily automatized, providing the possibility to work with large datasets and thus obtain a more statistically significant result.

To apply this method to Narval observations, I take the following steps:

Processing the observations

1. Spectral window selection

After a careful inspection of the observed spectra obtained with Narval, the computations were limited to the spectral range between 400 and 550 nm. The choice of this window is justified by three facts: first, the normalization to the continuum performed by *LibreEsprit* is done best in the blue part of the spectrum for very cool stars, while in the red part the presence of many molecular bands (mainly of TiO) prevents a good normalization to the continuum; second, the typical SNR of the observations is sufficiently high through this spectral window, allowing for reliable comparison; third, the density of atomic lines in the LSD mask is higher in the blue part of the spectrum, providing enough spectral lines to construct a mean line profile with a high SNR (a histogram of the number of lines in the LSD line mask versus wavelength is shown in Figure 3.7).

2. Removal of polarization features

The spectra obtained with Narval consist of measurements of both intensity I and polarization P (either Stokes V , Q or U) as a function of wavelength λ . When estimating the $v \sin i$ and v_{mac} with the current method however, our focus is set strictly on $I(\lambda)$. Therefore, any polarization data is removed from the cut observed spectra and replaced with a flat, featureless signal for maximum consistency with the synthetic data (which are also treated the same way: see below).

3. Performing LSD

Finally, LSD is performed on the resulting spectra, giving equal weight in the computation process to all lines present in the line mask.

Generating and processing synthetic observations

1. Building the synthetic spectrum with Turbospectrum

The first step in preparing the synthetic observations is the creation of a synthetic spectrum from detailed atomic and molecular linelists and a model atmosphere that corresponds as best as possible to the known parameters of the studied star: effective temperature T_{eff} , surface gravity $\log g$, metallicity $[\text{Fe}/\text{H}]$, mass M and microturbulence. To do this, in Georgiev et al. (2020b) the specialized code for spectrum synthesis Turbospectrum (Plez, 2012) is used, together with atomic and molecular linelists from the VALD database (Kupka et al., 1999) and MARCS model atmospheres (Gustafsson et al., 2008). The MARCS models were selected because they are best suited for cool evolved stars, covering effective temperatures from 2500 to 4000 K in steps of 100 K and logarithmic surface gravities between -1.0 and 3.5 in steps of 0.5 in spherical geometry.

2. Taking into account the instrumental profile

After the synthetic spectrum is created, the next step in the method is to take into

account the instrumental profile of the spectrograph used to obtain the real observations. Turbospectrum has a built-in procedure for doing this, which performs a convolution of the spectrum with the instrumental profile.

3. Setting the $v\sin i$ and v_{mac} parameters

Next, the effects of macroturbulence and rotation have to be considered. This is achieved again using a procedure implemented in Turbospectrum which performs the convolution of the synthetic spectrum with the two corresponding profiles, in successive operations. For M giant stars, a radial-tangential profile was used to model the macroturbulence and a rotational profile, both as described in (Gray, 1992). At this step, a grid of synthetic spectra is produced, covering a range of M macroturbulent velocities between $v_{\text{mac}}^{\text{min}}$ and $v_{\text{mac}}^{\text{max}}$ with a step of Δv_{mac} and R rotational velocities between $v\sin i^{\text{min}}$ and $v\sin i^{\text{max}}$ with a step of $\Delta v\sin i$.

It must be noted that among the three considered profiles – instrumental, macroturbulent and rotational – the instrumental profile is, from a physical point of view, the last one to take into account, since the light passes through the spectrograph after rotation and macroturbulence have left their imprint on the spectrum. However, since all the three mentioned effects are taken into account by performing a convolution of the spectrum with their respective profiles, and convolution is associative – if f , g and h are functions, then $f * (g * h) = (f * g) * h$, – the three profiles can be applied in any order, and the final result would always be the same. I apply the instrumental profile first, because it is computationally more efficient to perform this operation only once instead of $R \times M$ times, if it is performed last.

4. Building a grid of synthetic observations

Each element of the grid of synthetic spectra that is created at the previous step is essentially a table file that contains two columns: wavelength λ and normalized intensity $I(\lambda)$. The next step is to convert these synthetic spectra to the data format expected by the LSD software, which is equivalent to building a grid of synthetic Narval observations (see Section 2 of Chapter 2 for a description of the file format of Narval observations). To do this, I append four more columns to each synthetic spectrum that the LSD software will later interpret as measurements of the normalized polarized intensity $I_{\text{pol}}(\lambda)/I(\lambda)$, the normalized null #1 and null #2 profile intensity $N_{1,2}(\lambda)/I(\lambda)$ and the normalized full intensity uncertainty $\sigma_I(\lambda)$. It must be stressed that this step is performed only in order to make the synthetic spectra compatible with the LSD tool in use and to obtain the mean line profile in Stokes I . Having said that, the first three added columns consist of randomly generated values (noise) within the range $(-10^{-3}, 10^{-3})$. This is the exact same approach as used when removing the polarization signal in the observational data. The last column, $\sigma_I(\lambda)$, is set to the constant value of 1×10^{-2} , which is on the same magnitude as in the observational spectra.

As a last step in the construction of the synthetic observations, a doppler correction is performed to account for the heliocentric radial velocity of the star and the result (for each synthetic spectrum in the grid) is saved in a `.s` file in the exact format

of Narval data. At this stage we have what we will call a grid of synthetic Narval observations.

5. Performing LSD

Finally, LSD is performed on the synthetic observations in the same way as on the real observational data. A grid of synthetic LSD profiles is obtained, where each profile corresponds to a pair of $v \sin i$ and v_{mac} values. The parameters used in order to build the LSD line mask are the same as those used to create the synthetic spectra.

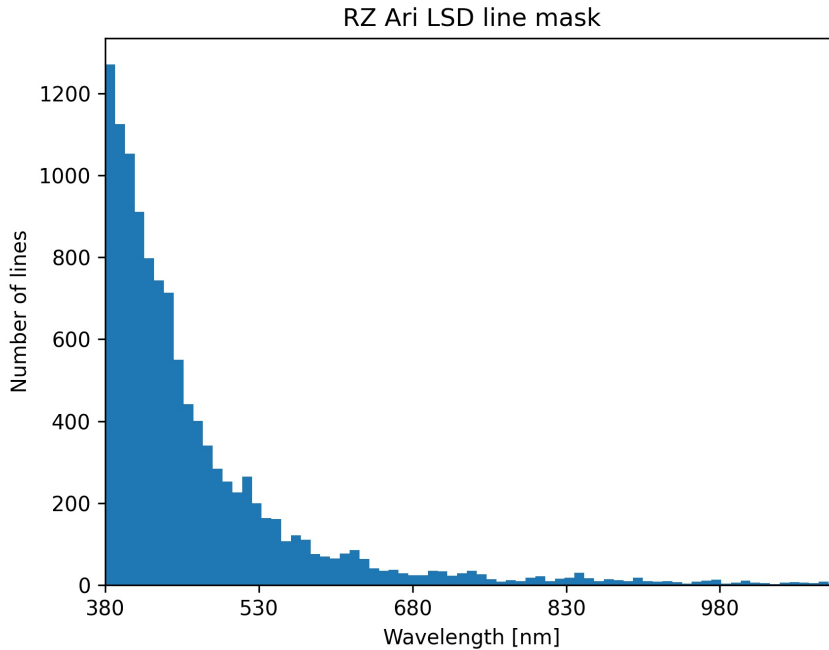


Figure 3.7: A histogram of the number of lines versus wavelength for the full LSD line mask used for RZ Ari. It can be seen that most of the atomic lines are in the blue part of the spectrum.

Comparing the LSD results of observational and synthetic data

The LSD output is an ASCII table file which consists of six columns:

- heliocentric radial velocity v_{rad} ;
- normalized full intensity $I(v_{\text{rad}})$;
- its uncertainty $\sigma_I(v_{\text{rad}})$;
- normalized polarized intensity $P(v_{\text{rad}})$, corresponding to either Stokes V , Q or U ;

- its uncertainty $\sigma_P(v_{\text{rad}})$;
- a diagnostic null spectrum $N(v_{\text{rad}})$;
- its uncertainty $\sigma_N(v_{\text{rad}})$.

The end goal of the described method is to determine the velocities $v_{\text{sin}i}$ and v_{mac} by matching the mean line profile of synthetic data to that of observations. This means that for this task only the first three columns of the LSD output are of importance, which justifies the introduction of an artificial polarization signal in the previous steps, since this signal has no impact on the final result.

In order to determine how well the synthetic mean line profile $I_{\text{syn}}(v_{\text{rad}})$ fits the observational one $I_{\text{obs}}(v_{\text{rad}})$, a quantitative criterium is required. First one must define where in radial velocity space the mean line profile is located in order to do the comparison on this part of the LSD profiles only, otherwise the different normalization to the continuum in the observational and synthetic LSD profiles will introduce noise in the results. In Georgiev et al. (2020b), I constrain the comparison interval by fitting the observational intensity profile $I_{\text{obs}}(v_{\text{rad}})$ with a gaussian to isolate the mean line profile. To make the fit, I use the function `optimize.curve_fit()` from the library `scipy` in `python3`. To ensure that the line profile is properly fit, I enforce the starting value of the gaussian peak $v_{0\text{ fit}}$ in the fitting process to correspond to the minimum intensity $I_{\text{obs}}^{\text{min}}(v_{\text{rad}})$ in the LSD output, which makes the fitting faster and more reliable.

The fitting process yields three values that describe the gaussian fit: the peak position $v_{0\text{ fit}}$, the full width at the half-maximum (FWHM) σ_{fit} and the peak depth $I_{0\text{ fit}}$. I use the peak position and the FWHM of the fit in order to find the limits of the mean line profile in radial velocity space. For the purposes of comparison with the synthetic profiles, I consider that the mean line profile is located in the range $[v_{0\text{ fit}} - 1.5\sigma_{\text{fit}}, v_{0\text{ fit}} + 1.5\sigma_{\text{fit}}]$. In Figure 3.8, we see an example of this for 2011/09/26, where the LSD profile of the observation is shown (in black) along with the gaussian fit (in red) and the limits as described above (as green vertical lines).

In the example given in Figure 3.8, it can be seen that for RZ Ari the red wing of the mean line profile deviates from the shape of a gaussian, showing a depression in intensity which is not so developed in the blue wing. This asymmetric shape can be found in all the LSD profiles of the 400-550 nm cut spectra of this star, but never in those of the full 375-1050 nm spectra (shown in Figure 3.2). The reason for this asymmetric shape may be due to the lines contained in the spectral window of 400-550 nm being used. On average, these lines that are in the blue part of the visible spectrum have higher excitation potentials χ and should be formed deeper in the stellar atmosphere. If these lines are more sensitive to downward motions, this could distort their profiles, especially in the red. This might to some extent explain the asymmetry between the blue and red wings of the observational profiles. It might also be that the asymmetry

disappears when using the full spectra because the effect is cancelled out when lines with lower excitation potential are introduced.

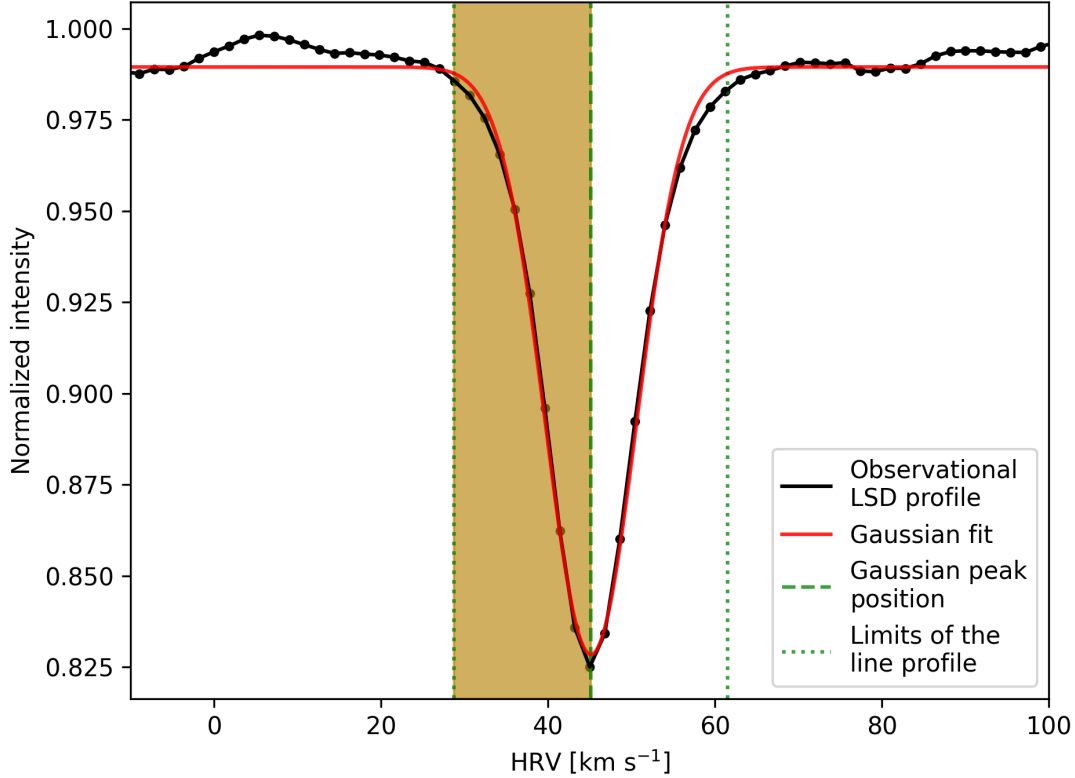


Figure 3.8: The gaussian fit of the LSD profile of RZ Ari on 2011/09/26. The LSD profile is shown in black, the gaussian fit - in red, its peak position is indicated by the dashed green line, and the green dotted lines show the part of the LSD profile that is considered to contain the mean line profile according to the criterium described in Section 3.1.5. The orange covered area is the part of the line profile used for the final estimation of $v \sin i$ and v_{mac} .

The asymmetry mentioned above is also never reproduced by the synthetic spectra. However, the blue wing of the mean observational line is well fit by them. The blue wing of the mean line also appears consistent between the LSD profiles of the cut and full spectra. This is why I decided to further constrain the window of comparison only to the blue part of the mean line profile, meaning only the interval $[v_{0 \text{ fit}} - 1.5\sigma_{\text{fit}}, v_{0 \text{ fit}}]$ is used, or in the example given in Figure 3.8 - the portion between the left green dotted line and the green dashed line, which is colored in orange.

Now that we have constrained the part of the LSD profiles which will be used for the comparison, let us define the criterium by which the observational and synthetic LSD

profiles will be compared, so that the best fitting pair of $v \sin i$ and v_{mac} is chosen. Since the LSD procedure is performed in the exact same way for all the data (observational and synthetic ones), the distribution of points in the velocity space is uniform for the profiles, beginning at -243 km s^{-1} and ending at 243 km s^{-1} with a step of 1.8 km s^{-1} . This means that comparison between different mean line profiles can be done simply by comparing the differences between their individual intensities $I(v_{\text{rad}})$ that share the same radial velocity. To estimate the correspondance between observational and synthetic LSD profiles, I calculate the sum

$$S = \sum_{v_{\text{rad}}=v_{\text{rad min}}}^{v_{\text{rad max}}} (I_{\text{syn}}(v_{\text{rad}}) - I_{\text{obs}}(v_{\text{rad}}))^2 \quad (3.1)$$

The criterium to select the best fit of the LSD profile for each observation is the minimal sum for all synthetic observations in the grid, $S = S_{\text{min}}$.

3.1.6 Determination of stellar parameters in RZ Ari

The method described in Section 3.1.5 was designed specifically to precise $v \sin i$ and v_{mac} of RZ Ari. To do this, 57 observations obtained with Narval in the period September 2008 - March 2019 (see Table 3.1) were used. I processed the data following the steps described in Section 3.1.5. The typical SNR value of the spectra in the wavelength range used for the computation of the mean line profile is about 190, which allows the data to be reliably used.

To build the synthetic data, first a model atmosphere was necessary. To determine $v \sin i$ and v_{mac} in RZ Ari, I used a MARCS model atmosphere (Gustafsson et al., 2008) with $T_{\text{eff}} = 3400 \text{ K}$, $\log g = 0.5$, $[\text{Fe}/\text{H}] = -0.25$, microturbulent velocity of 2 km s^{-1} , $M = 1M_{\odot}$. These values are consistent with the line mask used in the LSD procedure for RZ Ari (see Section 3.1.1).

Once the model atmosphere was selected, I used it to build with Turbospectrum a synthetic spectrum in the wavelength window 400 - 550 nm. After that, I accounted for the instrumental profile of the spectrograph using the built-in procedure in Turbospectrum. In Georgiev et al. (2020b), the instrumental profile of Narval is considered to be a gaussian with a FWHM of 77 mÅ. I then constructed the grid of synthetic observations for rotational velocities between $v \sin i^{\text{min}} = 4.5 \text{ km s}^{-1}$ and $v \sin i^{\text{max}} = 10 \text{ km s}^{-1}$ with a step of $\Delta v \sin i = 0.5 \text{ km s}^{-1}$ and macroturbulent velocities between $v_{\text{mac}}^{\text{min}} = 1 \text{ km s}^{-1}$ and $v_{\text{mac}}^{\text{max}} = 6 \text{ km s}^{-1}$ with a step of $\Delta v_{\text{mac}} = 1 \text{ km s}^{-1}$.

Because the radial velocity of RZ Ari is variable (as shown in the bottom panel of Figure 3.1), I compared each observational spectrum to a synthetic one that matches its own radial velocity (estimated by gaussian fitting).

For each of the 57 observational spectra, I computed the sum S from Equation 3.1

for each synthetic observation in the grid and selected the best fit based on the rule $S = S_{\min}$. After obtaining the best results according to this criterium, I examined each of the fits individually. 16 out of the 57 dates showed LSD profiles significantly different from the other mean line profiles and could not be correctly fit by the synthetic data. This is maybe due to the physical variability of RZ Ari. The 16 outlying dates were not considered in the final estimation of $v\sin i$ and v_{mac} .

For each of the 41 observations that were well fit by the synthetic data, I noted the best fitting $(v\sin i, v_{\text{mac}})$ pair on a two-dimensional colorplot with $v\sin i$ and v_{mac} on the horizontal and vertical axis, respectively. This plot is shown in Figure 3.9, where the colorcode represents the number of best fits obtained for each pair of parameters.

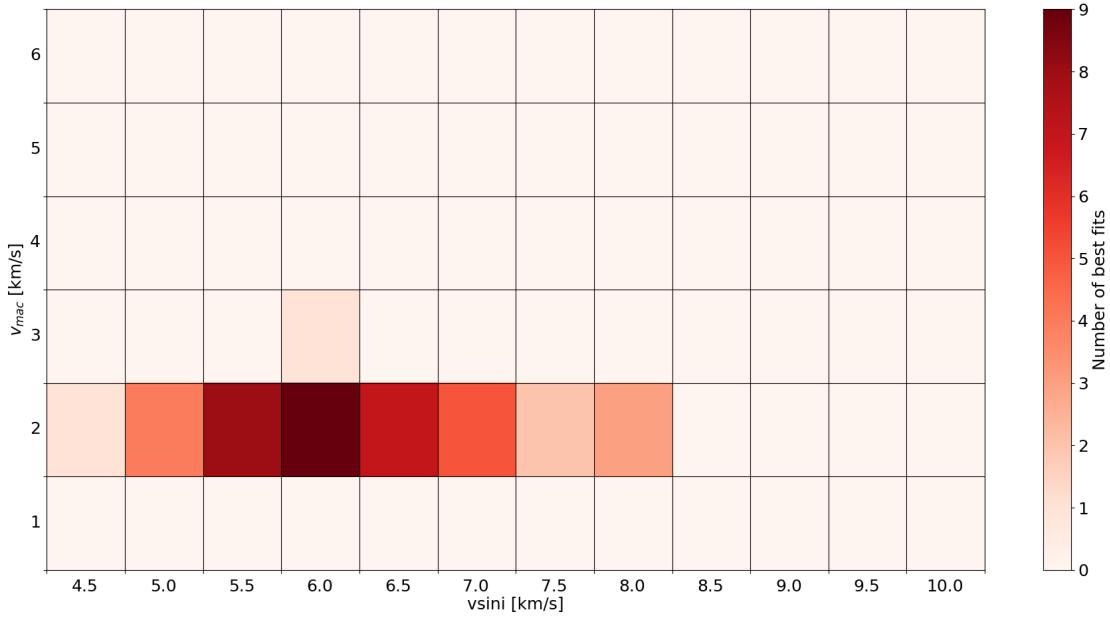


Figure 3.9: Distribution of the results for the 41 well fit observations of RZ Ari with respect to $v\sin i$ and v_{mac} .

It can be seen from Figure 3.9 that the best fits are most often obtained with the set of parameters $v_{\text{mac}} = 2 \text{ km s}^{-1}$ and $v\sin i = 6.0 \text{ km s}^{-1}$ (9 best fits), 5.5 km s^{-1} (8) and 6.5 km s^{-1} (7). Other, less populated peaks in the distribution are seen at $v\sin i = 7.0 \text{ km s}^{-1}$ (5) and 5.0 km s^{-1} (4) for the same macroturbulent velocity. Individual fits that match the minimization criterium appear for other combinations of the two parameters. Except for a single observation that is best fit with $v_{\text{mac}} = 3 \text{ km s}^{-1}$ and $v\sin i = 6.0 \text{ km s}^{-1}$, no result is obtained with $v_{\text{mac}} \neq 2 \text{ km s}^{-1}$.

Based on the statistical distribution presented in Figure 3.9, I estimate for RZ Ari the values of $v_{\text{mac}} = 2 \pm 1 \text{ km s}^{-1}$ and $v\sin i = 6.0 \pm 0.5 \text{ km s}^{-1}$, where the errorbars correspond to the steps in the grid of synthetic observations. Such an estimation of

the error is obviously very rough. The uncertainties in the selected values of T_{eff} , $\log g$, $[\text{Fe}/\text{H}]$ and macroturbulence when computing the synthetic spectrum and line mask all impact the errorbars of $v \sin i$ and v_{mac} . It must also be mentioned that the precision of the estimated parameters depends on the step of the grid of the model atmospheres. For cool stars ($T_{\text{eff}} < 4000$ K) the steps in the MARCS models for, e.g. T_{eff} and $\log g$ are respectively 100 K and 0.5. In a subsequent study, a more quantitative error estimation will be necessary.

3.1.7 Paper published in *Astronomische Nachrichten*

ORIGINAL ARTICLE

Determining rotational and macroturbulent velocities of cool magnetic giant stars

Stefan Georgiev^{1,2} | Agnès Lèbre² | Eric Josselin² |
Renada Konstantinova-Antova¹ | Julien Morin²

¹Institute of Astronomy and NAO,
Bulgarian Academy of Science, Sofia,
Bulgaria

²LUPM, UMR 5299, Université de
Montpellier, CNRS, Montpellier, France

Correspondence

S. Georgiev, Institute of Astronomy and
NAO, Bulgarian Academy of Science, 72,
Tsarigradsko Chaussee Boulevard, 1784
Sofia, Bulgaria.

Email: sgeorgiev@astro.bas.bg

Abstract

An original method of estimating the projected rotational velocity, $v \sin i$, and the macroturbulent velocity, v_{mac} , of evolved M giant stars is presented. It is based on the use of spectrum synthesis and multiline analysis tools. The goal is to fit the mean line profile of observations with that of synthetic spectra. The method is applied to the red giant star RZ Ari, and the results $v \sin i = 6.0 \pm 0.5 \text{ km s}^{-1}$ and $v_{\text{mac}} = 2.0 \pm 1.0 \text{ km s}^{-1}$ are obtained.

KEYWORD

stars: fundamental parameters – stars: individual (RZ Arietis) – stars: late-type – stars: rotation

1 | INTRODUCTION

RZ Ari (HD 18191) is a magnetically active M6 III semiregular variable star (see Konstantinova-Antova et al. 2018 and references therein). The physical scenario behind the magnetic variability of this star is still unclear and so is the role of rotation in it. The rotational period of RZ Ari is not precisely known, as is the case for most M giants. Based on results of Zeeman-Doppler Imaging (ZDI, Semel 1989; Donati & Brown 1997; Donati et al. 2006) and period analysis of spectral activity indicators, Konstantinova-Antova et al. (2020, in prep.) suggest that, for this star, the rotational period should be between 700 and 1,100 days. On the other hand, the only estimations of the projected rotational velocity of RZ Ari available in the literature are given by Zamanov et al. (2008), who obtain $v \sin i = 9.6 \pm 2.0 \text{ km s}^{-1}$ by means of cross-correlation and $v \sin i = 12.0 \pm 2.0 \text{ km s}^{-1}$ by measuring the full width at half-maximum (FWHM) of spectral lines (both methods of estimation are described in Zamanov et al. 2007). However, we find that these values

are not compatible with observations when we attempt to model the unpolarized and circularly polarized profiles of spectral lines of RZ Ari using the ZDI method. We suspect that these estimations of $v \sin i$ are in fact upper limits of the real value because they were carried out without properly considering the effect of macroturbulence: as Gray (2013) shows, the use of cross-correlation techniques to estimate $v \sin i$ of cool stars bears uncertainties due to the handling of line broadening caused by macroturbulence. In order to constrain the origin of the detected magnetic field at the surface of RZ Ari, and its connection with rotation, a better estimation of the rotational velocity that properly takes into account the effects of macroturbulence is needed. Such an estimation is the goal of the present work.

A classical approach for the determination of stellar parameters, including $v \sin i$ and the macroturbulent velocity v_{mac} , is the spectrum synthesis method, which relies on high-resolution spectroscopic observations. Stellar model atmospheres and atomic and molecular linelists are required to create a synthetic spectrum. The latter is convoluted with the instrumental profile of the spectrograph used for the observations and also with profiles of rotational and macroturbulent broadening. It is then

Based on data obtained using the T telescope Bernard Lyot at
Observatoire du Pic du Midi, CNRS and Universit  de Toulouse, France.

compared, over a large spectral domain, to an observed spectrum to obtain the fundamental parameters (including v_{ini} and v_{mac}) of the considered star. However, in the case of cool M giant stars, one faces certain difficulties in applying this method, such as the great number of spectral features that often blend with each other and the likely imperfect normalization to the continuum, often affecting the observation and preventing a straightforward comparison with a synthetic spectrum.

Another method for estimating stellar parameters, including v_{ini} , is using the cross-correlation technique. For example, the instrument SOPHIE (Bouchy et al. 2006; Perruchot et al. 2008) can obtain high-resolution stellar spectra and calculate the cross-correlation function (CCF) of the observed spectrum and a numerical mask. The CCF is then fit with a Gaussian profile, and stellar parameters are derived from its parameters. A detailed explanation of the cross-correlation technique can be found in Melo et al. (2001).

To estimate the rotational and macroturbulent velocities in the case of the cool M giant RZ Ari, we propose using an original multiline approach, using the Least Square Deconvolution method (LSD, Donati et al. 1997). LSD works under the assumption that all spectral lines, excluding very strong ones (like the Balmer or CaII H&K lines), are similar in shape and simply scale up in depth. Using LSD, a mean spectral line profile is produced for both observational and synthetic data. By doing this, we can base our comparison on an observational line and a synthetic mean spectral line that encode the fundamental stellar parameters for several different pairs of v_{ini} and v_{mac} . Because thousands of spectral lines are considered in the calculation of the mean profile, the comparison is performed with observational data with significantly increased signal/noise ratio (SNR) with respect to that of the spectra. Working with the mean line profiles instead of the full spectra also has the advantage of simplicity and allows some degree of automation. The latter provides a possibility for working with large datasets to obtain a more statistically significant result. This method is original in the sense that LSD has not been used together with spectrum synthesis to obtain stellar parameters before. In contrast to cross-correlation, the parameters are not derived from a simple Gaussian fit to the mean line profile.

2 | OBSERVATIONS AND LSD SOFTWARE

Observations of RZ Ari were carried out using the spectropolarimeter Narval on the 2 m Telescope Bernard-Lyot (TBL) at the Pic du Midi observatory, France. The Narval instrument (Aurière 2003) has a resolving power of

65,000 and operates in the spectral range of 375–1,050 nm. It allows simultaneous measurement of the full intensity (Stokes I) and the intensity in linear (Stokes U or Q) or circular (Stokes V) polarization as a function of wavelength.

RZ Ari has been observed (in circular polarization) during the period September 2008–March 2019. The 57 collected spectra were initially treated by the automatic software LibreEsprit (Donati et al. 1997) that performs spectrum extraction, wavelength calibration, heliocentric frame correction, and continuum normalization. A log of observations is presented in Table 1.

The LSD software uses a line mask to average the profiles of a large number of atomic lines, assuming that they have the same shape scaled by a certain factor. The line mask is a reference line pattern that indicates the laboratory wavelengths of spectral lines along with the atomic number of the chemical element they are associated with, their local depth (as a percentage of local continuum level), excitation potential, and Landé factor. The mask is computed by solving the radiative transfer equation for a model atmosphere using atomic and molecular linelists. LSD then performs a cross-correlation of the observed spectrum with the line mask to compute the mean line profile (the reader can refer to section 4 of Donati et al. 1997, for an in-depth description of the LSD method). The result is a mean line profile (called an LSD profile) in heliocentric velocity space in both Stokes I and polarized light (Stokes V for our observations). This tool is widely used in high-resolution spectropolarimetry to detect mean polarization signatures with very high SNR. For example, in the case of RZ Ari, it was by detecting a strong signal in the LSD Stokes V profiles that the presence of a surface magnetic field was found (Konstantinova-Antova et al. 2013). In the present study, however, only the LSD Stokes I profile is used. To perform LSD on RZ Ari data, we used a mask computed using a MARCS model atmosphere (Gustafsson et al. 2008) and atomic and molecular linelists extracted from the Vienna Atomic Line Database (VALD) (Kupka et al. 1999) for the following stellar parameters: $T_{\text{eff}} = 3,400$ K, $\log g = 0.5$, and microturbulent velocity of 2 km s^{-1} . The mask covers $\approx 19,000$ lines in the full spectral domain of Narval.

3 | DETERMINATION OF V_{SINI} AND V_{MAC}

Our goal is to determine the v_{ini} and v_{mac} parameters by comparing the Stokes I LSD profiles of observations to those of synthetic spectra. To create the synthetic spectra, first, a model of the stellar atmosphere is necessary.

Different values for the stellar parameters have been reported for RZ Ari: $T_{\text{eff}} = 3,442$ K (van Dyck et al. 1998),

TABLE 1 Log of observations of RZ Ari

Date	HJD 2450000+	Mean SNR 400–550 nm	Date	HJD 2450000+	Mean SNR 400–550 nm
16sep08	4727	249	03dec13	6630	168
21sep08	4732	215	09jan14	6667	241
05Sep10	5446	243	19aug15	7255	179
21sep10	5462	167	05sep15	7272	178
13oct10	5484	280	08oct15	7305	197
22jan11	5584	127	31oct15	7328	179
27jan11	5589	174	30nov15	7358	165
04feb11	5597	224	18dec15	7375	201
26sep11	5832	177	05aug16	7607	179
16oct11	5851	236	01sep16	7634	208
23nov11	5889	187	03oct16	7666	205
24nov11	5890	177	29oct16	7691	153
10jan12	5937	236	01dec16	7724	144
11jan12	5938	218	20dec16	7743	109
16jul12	6126	224	07jan17	7761	200
17jul12	6127	214	16feb17	7801	208
18jul12	6128	146	04sep17	8002	114
16aug12	6157	164	06oct17	8034	184
17aug12	6158	169	30oct17	8057	204
04sep12	6176	225	23nov17	8081	116
05sep12	6177	251	23jan18	8142	103
04oct12	6206	206	18sep18	8381	154
12nov12	6244	170	22oct18	8415	186
11Jan13	6304	202	16nov18	8439	167
08jul13	6483	176	07jan19	8491	194
05aug13	6511	183	26jan19	8510	108
02sep13	6539	207	08mar19	8551	119
06oct13	6573	230	11mar19	8554	166
07nov13	6604	165			

Note: The calendar date, HJD, and SNR in the spectral window used in the estimation of $v_{\text{sin}i}$ and v_{mac} are shown in their respective columns. Abbreviations: HJD, heliocentric Julian date; SNR, mean signal/noise ratio.

$T_{\text{eff}} = 3,450$ K (Konstantinova-Antova et al. 2010a, 2010b), $T_{\text{eff}} = 3,250$ K, $\log g = 0.30$, and $[\text{Fe}/\text{H}] = -0.24$ (Prugniel et al. 2011). We used a MARCS model atmosphere with standard composition in spherical model geometry with the following stellar parameters: $T_{\text{eff}} = 3,400$ K, $\log g = 0.5$, $[\text{Fe}/\text{H}] = -0.25$, $v_{\text{mic}} = 2 \text{ km s}^{-1}$, and $M = 1M_{\odot}$. We chose to work with an effective temperature of 3,400 K because the difference in the normalization to the continuum between our observations and the synthetic spectra is the smallest for this T_{eff} .

Using this model atmosphere, a synthetic spectrum was constructed with the software Turbospectrum (Plez 2012) that solves the radiative transfer equation using atomic and molecular linelists extracted from VALD. The computations were limited in wavelength between 400 and 550 nm, with a step of 10^{-3} nm. The choice of this spectral window is justified by three facts: first, the normalization to the continuum of the observational data performed by LibreEsprit is performed best in the blue part of the spectrum for very cool stars, while in the red part, the presence

of many molecular bands (mainly of TiO) prevents good normalization to the continuum; second, the typical SNR of the observations is sufficiently high (≈ 190) through this spectral window, allowing reliable comparison; and third, the density of atomic lines in the LSD mask is higher in the blue part of the spectrum. The observations were also cut to match this spectral region.

Having created the synthetic spectrum, it is necessary to take into account the instrumental profile of Narval, which we consider to be a Gaussian with an FWHM of 77 mÅ. Turbospectrum has a built-in procedure for performing this step, which consists of carrying out a convolution of the spectrum with the instrumental profile.

Next, the effects of macroturbulence and rotation have to be considered. This is again achieved using the procedure implemented in Turbospectrum, which performs the convolution of the synthetic spectrum with the two corresponding profiles in successive operations. We used a radial–tangential profile to model the macroturbulence and a rotational profile, both as described in Gray (1992). Then, a grid of synthetic spectra was produced, covering the range of v_{mac} between 1 and 6 km s⁻¹ with a step of 1 km s⁻¹ and $v\sin i$ between 4.5 and 10 km s⁻¹ with a step of 0.5 km s⁻¹. Finally, a Doppler velocity correction was applied to take into account the radial velocity of RZ Ari (46.5 ± 0.9 km s⁻¹ as measured from the observational data). In this way, we obtained what we call a grid of synthetic Narval observations.

The LSD software was then applied to this grid of synthetic data using the same line mask as that of the Narval observations. The typical number of lines used by LSD when working with the 400–550 nm spectra was $\approx 7,000$.

The mean spectral line profile computed for each synthetic datum in the grid was then compared to that of each individual observation. The LSD output gives the light intensity, I , as a function of heliocentric velocity, V .

As the LSD procedure was performed in the exact same way for all the data (synthetic and observational ones), the distribution of points in the velocity space is uniform for the profiles, beginning at -243 km s⁻¹ and ending at 243 km s⁻¹ with a step of 1.8 km s⁻¹. This means that comparison between the different mean line profiles can be performed simply by comparing the differences between their individual intensities $I(V)$ that share the same velocity coordinates. To estimate the correspondence between each pair of observational and synthetic LSD profiles, we calculate the sum

$$S = \sum_{V=V_{\min}}^{V_{\max}} (I_{\text{syn}}(V) - I_{\text{obs}}(V))^2 \quad (1)$$

The criterion to select the best fit of the LSD profile for each observation is the minimal sum for all synthetic observations in the grid, $S = S_{\min}$.

The values V_{\min} and V_{\max} are calculated by fitting the observed mean line profile with a Gaussian function with a peak at V_0 and $\text{FWHM} = \sigma$. We then set $V_{\min} = V_0 - 1.5\sigma$ and $V_{\max} = V_0$, that is, we only consider the blue part of the mean line profile (Figure 1). Initially, the whole line profile was used; however, this approach did not lead to convergence of the results for the $v\sin i$ and v_{mac} parameters. As one can see in Figure 1, the red wing of the observational mean line profile in the 400–550 nm region displays a dip in intensity, which is never matched by the synthetic mean line profile and is not seen in the blue wing. This asymmetric shape is not found when examining the observational mean line profiles of the full 375–1,050 nm spectra. The blue wing, however, appears consistent between the mean profiles of the cut and full spectra, and it is also well reproduced by the synthetic observations, which is why it was the only one used. The lines used in our analysis are in the blue part of the visible domain. On average, they have

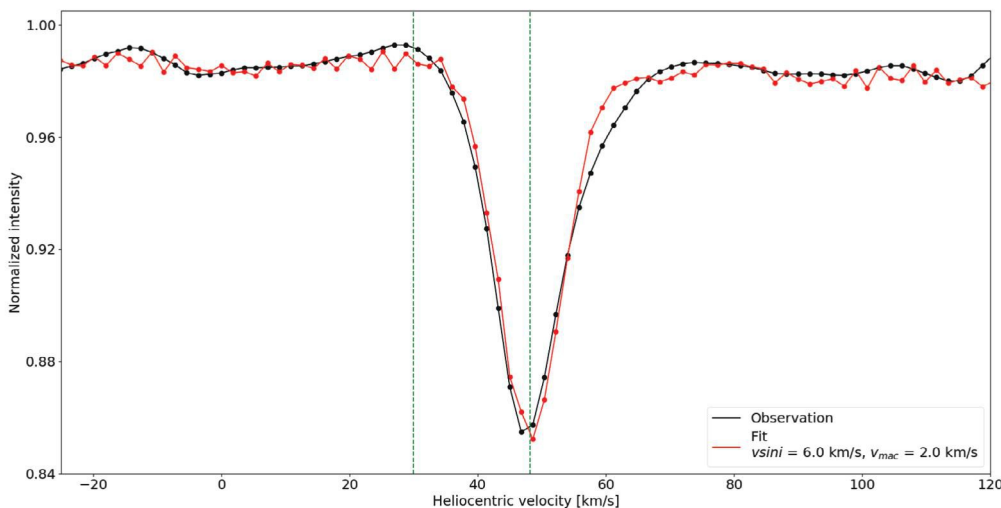


FIGURE 1 Example of the comparison between Least Square Deconvolution Stokes I profiles of observed (black line) and synthetic spectra (red line). The observation is collected on December 20, 2016. The vertical green dashed lines show the range in which the evaluation sum has been calculated. Note the asymmetry between the blue and red wings of the observational mean line profile (see the text)

higher excitation potentials; we think that if these lines (formed deeper in the atmosphere) are sensitive to downward motions, this could distort their profiles, especially in the red part. We suspect that this effect might, to some extent, explain the asymmetry between the blue and red wings of the mean line profiles. The asymmetry could then disappear when using the full visible domain as the effect would be canceled out when lower excitation lines in the red are introduced.

After obtaining the best results according to the minimization rule, the fits were examined individually. Sixteen (of the 57) dates showed LSD profiles significantly different from the other mean line profiles and could not be correctly fit by the synthetic data. We think that this is due to the physical variability of RZ Ari. These outlying dates were not considered in the final estimation of v_{mac} and v_{mac} .

For each of the 41 observations that were well fit by the synthetic data, the best-fitting (v_{mac} , v_{mac}) pair was noted on a two-dimensional color plot, with the v_{mac} and v_{mac} on the horizontal and vertical axis, respectively. The plot is shown in Figure 2, where the color code represents the number of best fits obtained for each (v_{mac} , v_{mac}) pair.

From the distribution presented in Figure 2, it is clear that the best fits are most often obtained with the set of parameters $v_{\text{mac}} = 2.0 \text{ km s}^{-1}$ and $v_{\text{mac}} = 6.0 \text{ km s}^{-1}$ (nine best fits), 5.5 km s^{-1} (eight), and 6.5 km s^{-1} (seven). Other, less populated peaks in the distribution are seen at $v_{\text{mac}} = 7.0 \text{ km s}^{-1}$ (five) and 5.0 km s^{-1} (four) for the same macroturbulent velocity. Individual fits that match the minimization criterion appear for other combinations of the two parameters. Except for a single observation that is best fit with $v_{\text{mac}} = 3.0 \text{ km s}^{-1}$ and $v_{\text{mac}} = 6.0 \text{ km s}^{-1}$, no result is obtained with $v_{\text{mac}} \neq 2.0 \text{ km s}^{-1}$.

Based on the statistical distribution presented in Figure 2, we estimate for RZ Ari the values of $v_{\text{mac}} = 2.0 \pm 1.0 \text{ km s}^{-1}$ and $v_{\text{mac}} = 6.0 \pm 0.5 \text{ km s}^{-1}$, where the error bars correspond to the steps in the grid we used. Such an estimation of the error is obviously very rough. The uncertainties in the selected values of T_{eff} , $\log g$, $[\text{Fe}/\text{H}]$, and microturbulence used when computing the synthetic spectrum and line mask all impact the error bars of v_{mac} and v_{mac} . It must also be mentioned that the precision of the estimated parameters depends on the step of the grid of the model atmospheres. For cool stars ($T_{\text{eff}} \leq 4,000 \text{ K}$), the steps in the MARCS models for, for example, T_{eff} and $\log g$ are respectively 100 K and 0.5 . In a subsequent study, a more quantitative error estimation will be required.

To test the method, we also used it to estimate the v_{mac} and v_{mac} parameters of another star, EK Boo (HD 130144), which is of spectral type M5 III, very similar to that of RZ Ari. Konstantinova-Antova et al. (2010a, 2010b) report for EK Boo the values $v_{\text{mac}} = 8.5 \pm 0.5 \text{ km s}^{-1}$ and $v_{\text{mac}} = 2.0 \text{ km s}^{-1}$ obtained using classical spectrum synthesis. For our calculations, we used a mask computed using linelists extracted from VALD for the following parameters: $T_{\text{eff}} = 3,500 \text{ K}$, $\log g = 0.5$, and microturbulent velocity of 2 km s^{-1} . The MARCS model atmosphere used to create the synthetic spectrum was computed using standard composition in spherical model geometry with $T_{\text{eff}} = 3,500 \text{ K}$, $\log g = 0.5$, $[\text{Fe}/\text{H}] = 0$, microturbulent velocity of 2 km s^{-1} , and $M = 1M_{\odot}$. We used 54 Narval observations of EK Boo restricted to the same spectral window (400–550 nm). Following the same minimization criterion as in the case of RZ Ari, we obtain the results shown in Figure 3 and find final values of $v_{\text{mac}} = 8.0 \pm 0.5 \text{ km s}^{-1}$ and $v_{\text{mac}} = 1.0 \pm 1.0 \text{ km s}^{-1}$, in good agreement with Konstantinova-Antova et al. (2010a, 2010b).

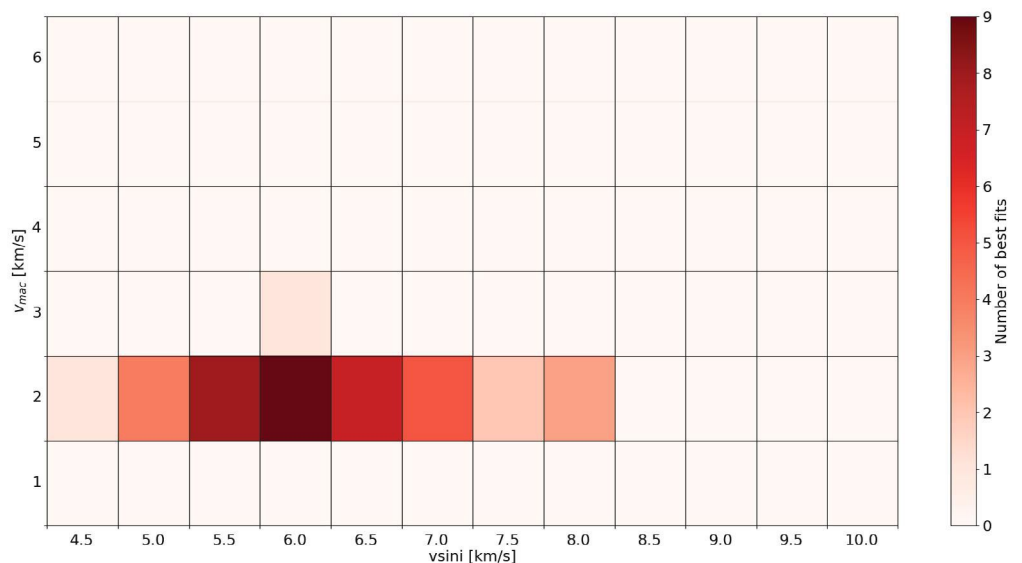


FIGURE 2 Distribution of the results for the 41 well-fit observations with respect to v_{mac} and v_{mac}

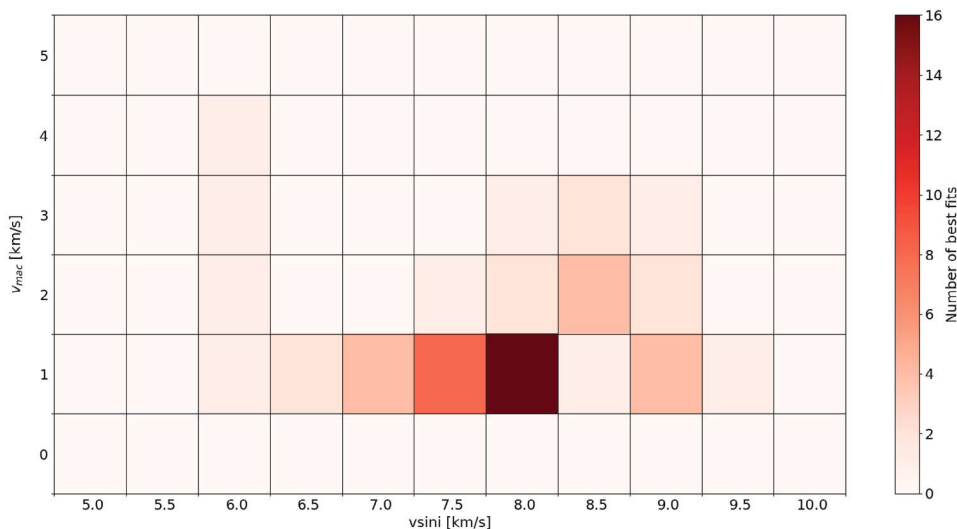


FIGURE 3 Distribution of the results for EK Boo with respect to v_{sini} and v_{mac}

4 | SUMMARY

An original method is presented for better estimation of the rotational and macroturbulent velocities of cool stars based on a multiline approach and using spectrum synthesis. A grid of synthetic spectra using MARCS models of atmosphere that take into account a range of v_{sini} and v_{mac} is produced. Using the LSD method, a mean spectral line profile is obtained for each synthetic datum in the grid and then compared to the mean line profiles obtained from Narval data. Using a minimization rule, the best-fitting pair of parameters (v_{sini} , v_{mac}) is selected for each observation. After inspection, counting of the individual resulting best fits is carried out to obtain a statistical final result. Applying the method to the M giant RZ Ari, values of $v_{\text{sini}} = 6.0 \pm 0.5 \text{ km s}^{-1}$ and $v_{\text{mac}} = 2.0 \pm 1.0 \text{ km s}^{-1}$ are derived. These values are reasonable for the spectral type of RZ Ari (M6 III), considering the estimations of Zamanov et al. (2008) as upper limits for M giants, as explained in the Introduction.

The goal of future work will be the application of the ZDI method to the same Narval observations using this refined value of v_{sini} in order to map the surface magnetic field of RZ Ari and its temporal evolution. Doing this could help better understand the origin and evolution of magnetism in this cool evolved star.

ACKNOWLEDGMENTS

We thank the TBL team for providing service observations using Narval. We thank A. Palacios and S. Tsvetkova for their ideas, careful reading of the manuscript, and constructive comments. S. G., A. L., and R. K. -A. acknowledge partial support by the Bulgarian NSF project DN 18/2, including also observations in semester 2019A. A. L., R. K. -A., and J. M. acknowledge partial support under

DRILA 01/3. R.K.-A. acknowledges support for the observational time in 2010 by the Bulgarian NSF project DSAB 01/2. The observations in 2008 and 2011 were obtained under an OPTICON program. The observations in 2013 were obtained under financial support by the OP “Human Resources Development,” ESF and the Republic of Bulgaria, project BG051PO001-3.3.06-0047. Since 2015, the Narval observations are obtained under the French “Programme National de Physique Stellaire” (PNPS) of CNRS/INSU cofunded by CEA and CNES. This work has made use of the VALD database, operated at Uppsala University, the Institute of Astronomy RAS in Moscow, and the University of Vienna. We are grateful to the anonymous referee for giving valuable comments and remarks on this paper.

REFERENCES

- Aurière, M. 2003, in: Magnetism and Activity of the Sun and Stars, eds. J. Arnaud, & N. Meunier, EAS Publ. Ser., 9, 105.
- Bouchy, F., & The Sophie Team. 2006, in Tenth Anniversary of 51 Peg-b: Status of and Prospects for Hot Jupiter Studies, eds. L. Arnold, F. Bouchy, & C. Moutou, 319.
- Donati, J.-F., & Brown, S. F. 1997, *A&A*, 326, 1135.
- Donati, J.-F., Semel, M., Carter, B., et al. 1997, *MNRAS*, 291, 658.
- Donati, J.-F., Howarth, I., Jardine, M., et al. 2006, *MNRAS*, 370, 629.
- van Dyck, H., van Belle, G., & Thompson, R. 1998, *AJ*, 116, 981.
- Gray, D. 1992, *The Observation and Analysis of Stellar Photospheres*, Cambridge University Press.
- Gray, D. 2013, *A&A*, 146, 29.
- Gustafsson, B., Edvardsson, B., Eriksson, K., et al. 2008, *A&A*, 486, 951.
- Konstantinova-Antova, R., Aurière, M., Charbonnel, C., et al. 2010a, *A&A*, 524, A57.
- Konstantinova-Antova, R., Aurière, M., Schröder, K.-P., et al. 2010b, *Publ. Astron. Obs. Belgrade*, 90, 151.
- Konstantinova-Antova, R., Aurière, M., Charbonnel, C., et al. 2013, *BlgAJ*, 19, 14.

- Konstantinova-Antova, R., Lèbre, A., Aurière, M., et al. 2018, PAS "Rudjer Bošković" No 18, 93.
- Kupka, F., Piskunov, N., Ryabchikova, T., et al. 1999, *A&AS*, 138, 119.
- Melo, C., Pasquini, L., & De Medeiros, J. 2001, *A&A*, 375, 851.
- Perruchot, S., Kohler, D., Bouchy, F., et al. 2008, in: *Ground-Based and Airborn Instrumentation for Astronomy II*, eds. I. McLean, & M. Casali, Proc. SPIE, 7014, 70140J.
- Plez, B. 2012, *Astrophysics Source Code Library*, record ascl:1205.004.
- Prugniel, P., Vauglin, I., & Koleva, M. 2011, *A&A*, 531, A165.
- Semel, M. 1989, *A&A*, 225, 456.
- Zamanov, R., Bode, M., Melo, C., et al. 2007, *MNRAS*, 380, 1053.
- Zamanov, R., Bode, M., Melo, C., et al. 2008, *MNRAS*, 390, 377.

AUTHOR BIOGRAPHY

Stefan Georgiev is a PhD student in a joint program between the Institute of Astronomy and NAO,

BAS (Sofia, Bulgaria) and the University of Montpellier (Montpellier, France). The title of his PhD thesis is "Magnetism in Cool Evolved Stars". His scientific interests include stellar magnetism and stellar evolution.

How to cite this article: Georgiev S, Lèbre A, Josselin E, Konstantinova-Antova R, Morin J. Determining rotational and macroturbulent velocities of cool magnetic giant stars. *Astron. Nachr.* 2020;341:486–492. <https://doi.org/10.1002/asna.202013725>

3.1.8 Period search

To precise the origin of magnetism in RZ Ari, a period search was performed on both the values of the B_l and activity indicators measured from the Narval observations (see Table 3.1) and the lightcurve in V filter (shown in Figure 3.10) obtained from the American Association of Variable Star Observers (AAVSO¹) database. In order to perform the period search, the Lomb-Scargle method was used (Lomb, 1976; Scargle, 1982). This method was selected because it is designed to work with datasets that are unevenly populated in time, which is the case for the available observations of RZ Ari.

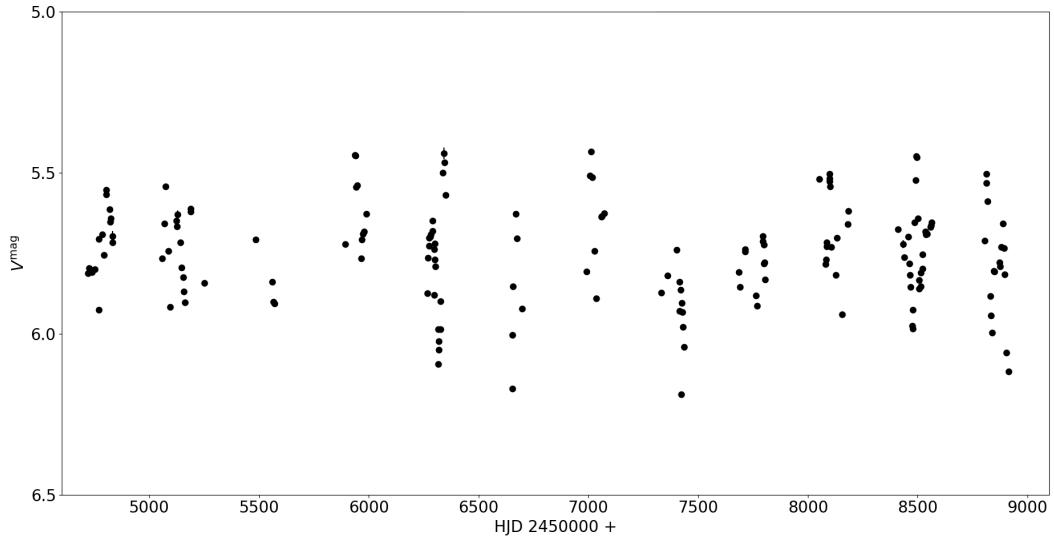


Figure 3.10: The lightcurve of RZ Ari in V filter during the time of Narval observations. Source: AAVSO.

The periodograms for the longitudinal magnetic field B_l and the spectral activity indicators and v_{rad} are shown respectively in the upper and bottom panels of Figure 3.11. In the B_l dataset, a period of 1280d (between 1243 and 1319d) is found with a false alarm probability (FAP) of 6.1%; also, a period of 493 d is found. For the activity indicators, periods are found of 688d (between 668 and 707d, FAP 2%, S-index), 707d (between 696 and 738d, FAP 0.8%, H α -index) and 717d (between 696 and 738d, FAP 0%, CaIRT-index). For the v_{rad} , a period of 707d (between 687 and 728d, FAP 0.6%) is found.

The 493d period found in the B_l variation is very close to the LSP of 480d of RZ Ari, obtained using photometry. Taking into account the radius estimation $R = 107.91R_{\odot}$ (computed from the Gaia DR3 distance and the angular diameter of the star) and the

¹<https://www.aavso.org/>

$v \sin i = 6 \text{ km s}^{-1}$ (estimated in Georgiev et al. 2020b), the upper limit for the rotational period is found to be 910d. This means that the 1280d period found in the B_l is longer than the upper limit of P_{rot} and thus cannot be due to rotational modulation. In the variability of the spectral activity indicators and radial velocity, a mean period of $\sim 704\text{d}$ appears. We suspect that this could in fact be the rotation period of the star, P_{rot}

From the AAVSO lightcurve, several short periods ($< 100\text{d}$) were obtained that are probably linked to pulsations. The results with $\text{FAP} \leq 1\%$ are 55.1d (FAP 0%), 58.5d (1%), 64.8d (0%), 66.8d (0.06%) and 78.6d (0.08%). Concerning longer periods ($\geq 100\text{d}$), the results found are 544.6d (540.5 - 548.7d, FAP 1%) and 1105.6d (1089.1 - 1122.7d, FAP 0.7%). However, the 544.6d period is about twice as short as the 1105.6d one, meaning that it might be an artefact and hence, might not be real.

A period search on the shape of the LSD Stokes V profiles was also attempted using ZDI. A period of 1100d was found. The periodogram is shown in Figure 3.13. This period is in agreement with the 1105.6d period found in the photometric variability. It is longer than the upper estimation of the rotational period (910d), which means that the variability of the magnetic field does not follow the rotational modulation, as it is observed in magnetic G and K giants (Aurière et al., 2015). This result also prevents the mapping of the surface magnetic field of RZ Ari using ZDI.

3.1. RZ ARIETIS

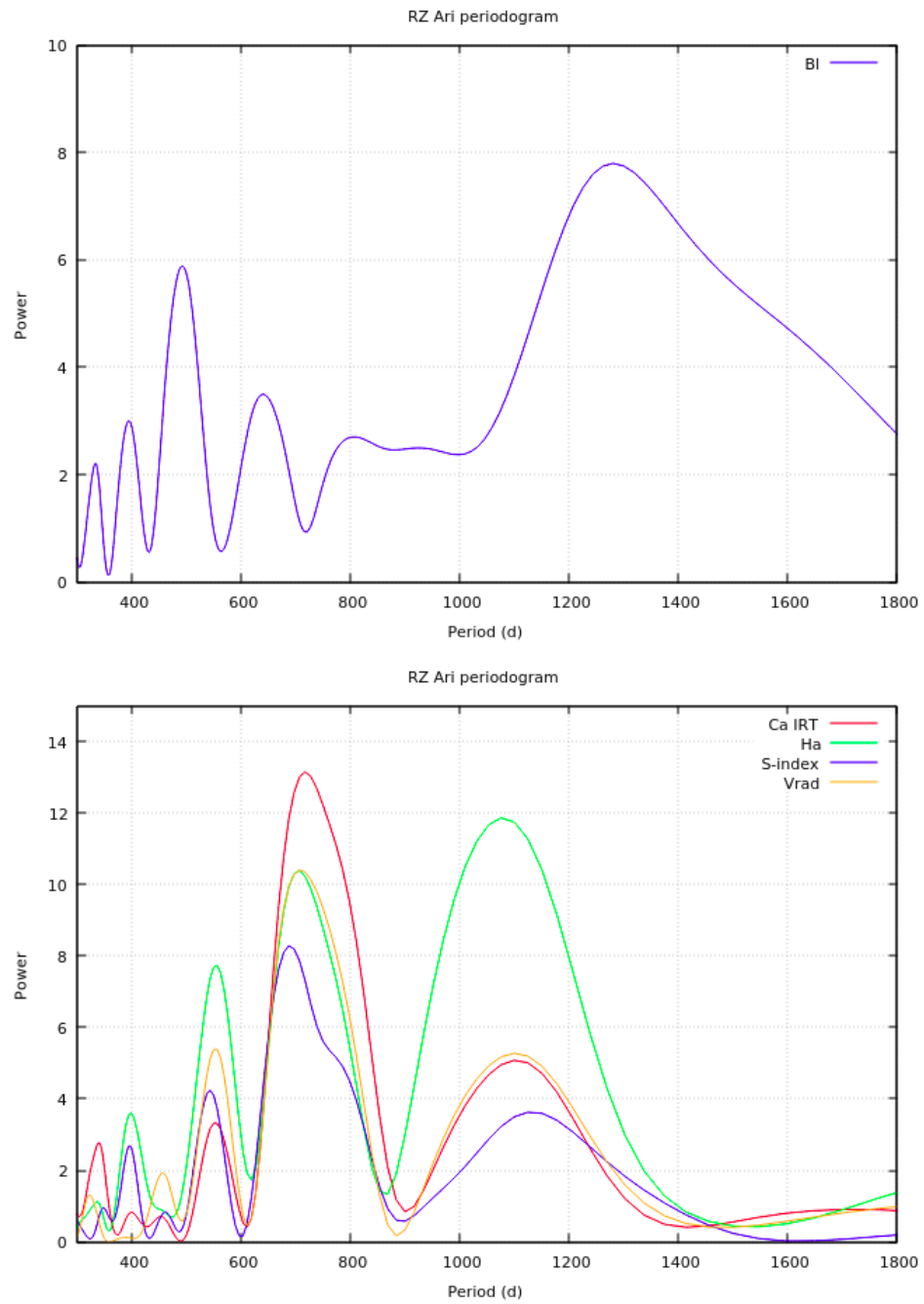


Figure 3.11: Lomb-Scargle periodograms of the measurements reported in Table 3.1 for RZ Ari. Upper panel: B_I ; lower panel: spectral activity indicators and v_{rad} .

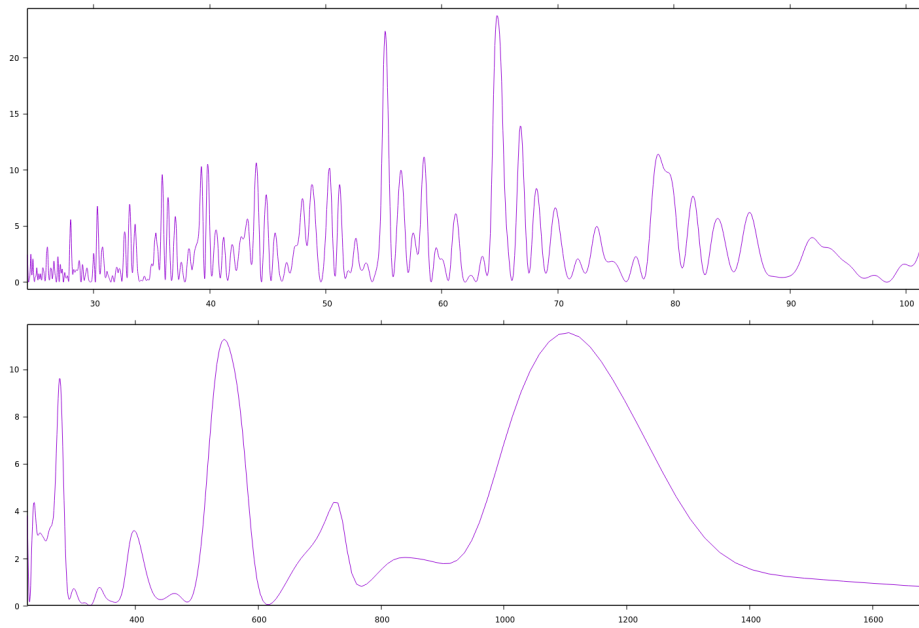


Figure 3.12: Lomb-Scargle periodograms of photometric observations from AAVSO of RZ Ari in V filter. Upper panel: $< 100\text{d}$; lower panel: $\geq 100\text{d}$.

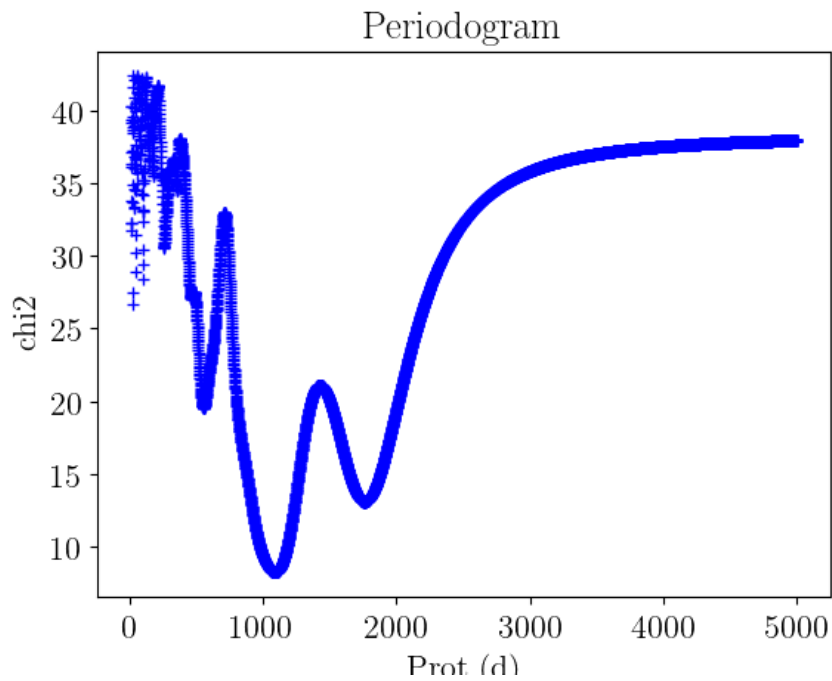


Figure 3.13: ZDI periodogram for the Stokes V profiles of RZ Ari.

3.1. RZ ARIETIS

$\log(L/L_{\odot})$	R (R_{\odot})	T_{eff} (K)	$A(^7\text{Li})$	$^{12}\text{C}/^{13}\text{C}$	$^{16}\text{O}/^{17}\text{O}$	$^{16}\text{O}/^{18}\text{O}$
3.178 [*]	123.728 [*]	3236 [*]	$\gtrsim 1^*$	$6 \pm 1^*$	$958^{+912}_{-467}^*$	$2422^{+1185}_{-796}^*$
3.15[†]	107.91[*]	3341 [‡]	$\gtrsim 1^*$	$7.9 \pm 0.8^{\ddagger}$	$607 \pm 48^{\ddagger}$	–

Table 3.3: Parameters and chemical composition of RZ Ari as determined by various observations and model predictions compatible with the radius (as derived in this work by interferometry) and luminosity (as derived by IR measurements by Villaume et al. 2017; both values highlighted in bold face in the table).

References: ^{*} - Lebzelter et al. (2019). The radius, not given in that paper, is computed using the luminosity and the temperature. [‡] - Tsuji (2008). ^{*} - this work. [†] - Villaume et al. (2017).

3.1.9 Mass and evolutionary status

In order to estimate the mass and evolutionary status of RZ Ari, determinations of the surface abundances of Li and the $^{12}\text{C}/^{13}\text{C}$, $^{16}\text{O}/^{17}\text{O}$ and $^{16}\text{O}/^{18}\text{O}$ isotopic ratios were taken from the literature. These values are summarized in Table 3.3.

As it is observed in most evolved low-mass giants (Charbonnel & Do Nascimento, 1998), the carbon isotopic ratio is close to the nuclear equilibrium value in RZ Ari. This indicates that it has undergone extra-mixing during the RGB ascent, which connected the convective envelope to the H-burning shell, where the CNO cycle occurs. Such transport processes are expected to efficiently destroy Li (Charbonnel & Zahn, 2007; Lagarde et al., 2012b). However, this may represent a challenge for RZ Ari given its large Li abundance $A_{\text{Li}} > 1.5$ dex (see Section 3.1.10), which is not typical for the classical post first dredge-up (without extra-mixing) stages of low-mass stars. Finally, the isotopic ratio $^{16}\text{O}/^{17}\text{O}$, estimated from molecular bands in the spectrum of RZ Ari, is lower than 1000. According to predictions of classical evolution for first dredge-up abundances of cool giants, such values are reached by models with initial masses between $1.3M_{\odot} \leq M \leq 2M_{\odot}$ (Dearborn, 1992; Karakas & Lattanzio, 2014). The $^{16}\text{O}/^{18}\text{O}$ isotopic ratio is more than 2000 (Lebzelter et al., 2019), which is expected for massive AGB stars with $M \geq 6M_{\odot}$ experiencing hot bottom burning. However, the $^{16}\text{O}/^{17}\text{O}$ isotopic ratio and the luminosity of RZ Ari are incompatible with such an evolutionary status and Lebzelter et al. (2019) argues that it cannot be more massive than $3M_{\odot}$.

Given its surface chemical composition, RZ Ari should be the descendant of a 1.3 to $2M_{\odot}$ star. This is compatible with previous mass estimates for this star from comparisons to stellar evolutionary models (Tsuji, 2008; Halabi & El Eid, 2016; Lebzelter et al., 2019).

Taking into account the known parameters of RZ Ari – T_{eff} , $\log g$, R_{\star} , L_{\star} and surface chemical abundances – a dedicated $1.5M_{\odot}$ stellar evolution model was computed using an updated version of the STAREVOL code (Dumont et al., 2021a,b) and also using the models from Charbonnel et al. (2017). An analytical formula was used for the atmosphere (Krishna Swamy, 1966), with a photosphere defined as the layer for which the optical depth τ is between 5×10^{-3} and 10, and T_{eff} and R_{\star} are classically defined at $\tau = 2/3$. This leads to more realistic tracks on the RGB compared to what can be

obtained using a gray atmosphere (Salaris et al., 2002). Convective mixing is modelled according to the mixing length theory with $\alpha_{\text{MLT}} = 1.6$ as in Lagarde et al. (2012b); Charbonnel et al. (2017). A subsolar metallicity $[\text{Fe}/\text{H}] = -0.25 \text{ dex}^2$ and solar isotopic ratios are adopted, both as recommended by Asplund et al. (2009). Finally, nominal nuclear reaction rates are adopted from the Nacre II compilation (Xu et al., 2013).

Based on the radius obtained from interferometry, stellar evolution models which comply with the fundamental parameters L_* , T_{eff} and metallicity of RZ Ari are found. RZ Ari is well fitted by the $1.5M_{\odot}$, $[\text{Fe}/\text{H}] = -0.25$ evolution model. However, its location on the HRD does not permit to pinpoint its evolutionary status: it is compatible with both the tip-RGB and the early-AGB stages. However, considering the predicted surface chemical composition, the early-AGB status is preferred. The location of the giant branches for the model used is the same as the model of $1.5M_{\odot}$ and solar metallicity of Charbonnel et al. (2017), and also with similar convective turnover timescales at the tip-RGB and early-AGB stages. This allows for an estimation of the Rossby number. For RZ Ari, $Ro \gg 10$. RZ Ari lies well outside the magnetic strips, meaning that an $\alpha\Omega$ dynamo cannot be efficient for this star. The estimated position of RZ Ari on the HRD is shown in Figure 3.14.

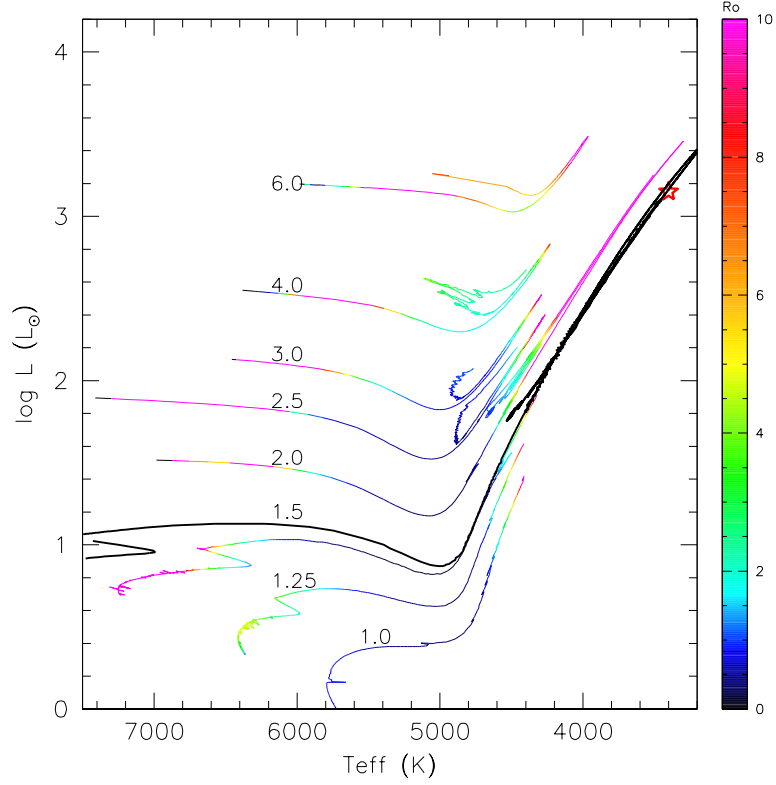


Figure 3.14: HRD with evolutionary tracks for stars with different masses from Charbonnel et al. (2017) with colorcoded expected Ro values, computed at $H_p/2$ above the base of the convective envelope. The track of the model used to determine the position of RZ Ari is shown with a black line.

3.1.10 Lithium abundance. Planet engulfment scenario and possible dynamo action

In order to determine the lithium abundance in RZ Ari, the LiI resonance doublet at 6708 \AA was used. A grid of synthetic spectra with different lithium abundances were built with Turbospectrum using VALD linelists and the same model atmosphere as for the $v \sin i$ and v_{mac} determination presented in Section 3.1.6: $T_{\text{eff}} = 3400 \text{ K}$, $\log g = 0.5$, $[\text{Fe}/\text{H}] = -0.25$, $v_{\text{mic}} = 2 \text{ km s}^{-1}$ and $M = 1M_{\odot}$ in spherical geometry. The synthetic spectra were limited in wavelength in a narrow range around the LiI line and compared to spectra obtained with Narval. However, only a lower limit for the lithium content could be derived: $A_{\text{Li}} > 1.5 \text{ dex}$.

This is a very interesting result. Any Li content above 1 dex is abnormally high for RZ Ari, considering the theory of stellar evolution. This means that in RZ Ari lithium would either be created internally, e.g. by the Cameron-Fowler mechanism (Cameron, 1955; Cameron & Fowler, 1971), which however is expected only at the end of the AGB,

and thus is also excluded, or it was obtained externally, for example in a planet engulfment event. As it has been shown by Siess & Livio (1999), a planet engulfment may increase the surface abundance of lithium in AGB stars by a factor of 2 – 8.

A planet engulfment could also have implications for the origin of the observed magnetism in RZ Ari. Since the star is well outside the magnetic strips, an $\alpha\Omega$ dynamo is not expected to operate in its interior. However, if a planet engulfment event indeed has occurred, this could have increased the angular momentum of RZ Ari, possibly allowing the operation of a magnetic dynamo. This suspected increase in angular momentum might perhaps be sufficient to allow an $\alpha^2\Omega$ type dynamo to operate in RZ Ari. Thus, it might be that the origin of the magnetic field in this M giant is related to a planet engulfment event.

Another possible dynamo which could be operating in RZ Ari is the turbulent dynamo (Soker & Zoabi, 2002); however, it is not expected to produce surface fields stronger than 1 G in giant stars and thus is improbable. A third possibility is a local dynamo, like the one operating in the RSG star Betelgeuse (Aurière et al., 2010) due to the presence of large convective cells. Indeed, such cells have already been found in the giant star π^1 Gru (Paladini et al., 2018) using interferometric observations. Currently, there are ongoing interferometric observations of RZ Ari using the CHARA instrument which might bring more information on this matter.

3.2 β Pegasi

β Peg is an M2.5II-III semi-regular variable star with $P = 43.3$ d (Tabur et al., 2009). It is known to be an early-AGB magnetic star that falls within the second magnetic strip (Konstantinova-Antova et al., 2014). The latest estimations of the stellar parameters of β Peg are $T_{\text{eff}} = 3864$ K, $\log g = 1.0$, $[\text{Fe}/\text{H}] = -0.11$ (Massarotti et al., 2008b) and $T_{\text{eff}} = 3689$ K, $\log g = 1.2$, $[\text{Fe}/\text{H}] = -0.11$ (Soubiran et al., 2008).

In the Thesis I present a continuation of the study of Konstantinova-Antova et al. (2014) of the magnetic field in β Peg, along with the first observations of this star in linear polarization. This work is presented at the international Joint SREAC (Sub-Regional European Astronomical Committee) & BgAS (Bulgarian Astronomical Society) conference which took place between the 4th and 8th of June 2019 in Sofia, Bulgaria. The work is also published in a paper in *Bulgarian Astronomical Journal* (Georgiev et al., 2020a). Using the method presented in Georgiev et al. (2020b), I determined the projected rotational velocity of β Peg to be $v \sin i = 7$ km s⁻¹; this value is reported in Georgiev et al. (2020a) and is in agreement with the estimation of Konstantinova-Antova et al. (2014).

3.2.1 Observations

We obtained 20 observations in circular polarization of β Peg between November 2011 and August 2019, 13 of which show polarization signatures. Also, 4 observations in linear polarization were obtained between July 2015 and August 2019. A detailed log is given in Table 3.4 for the observations in circular polarization and in Table 3.5 for those in linear polarization.

In order to extract the mean polarization signatures from the spectropolarimetric observations, I applied to them the LSD method using a dedicated line mask constructed with atomic line lists from the VALD database (Kupka et al., 1999) with the following parameters: $T_{\text{eff}} = 3700$ K, $\log g = 1.0$, microturbulence of 2 km s⁻¹ and solar metallicity, consistent with the known parameters of the star. As in RZ Ari, I removed the lines of the elements H, He, Na, K, and Ca from the mask in order to avoid eventual contamination from the chromosphere and circumstellar and interstellar environment. The total number of lines in the LSD mask is 12633.

Date	HJD	SNR	σ_{LSD} ($10^{-3} I_c$)	Exposure time Stokes V	Detection Stokes V	B_l [G]	σ [G]	S- index	H α - index	CaIRT- index	V_{rad} [km s $^{-1}$]
2011/11/29	5895	1408	0.7	9x90s	DD	2.49	0.25	0.279	0.279	0.426	7.4
2012/01/10	5937	1295	0.6	16x60s	DD	1.23	0.18	0.290	0.278	0.406	6.9
2015/07/08	7213	1683	0.7	8x80s	DD	-1.17	0.22	0.291	0.333	0.744	8.4
2015/09/06	7273	1138	1.0	8x70s	MD	-0.69	0.29	0.274	0.351	0.716	9.2
2015/12/02	7359	798	1.3	8x70s	ND	—	—	0.299	0.331	0.733	8.2
2016/07/03	7574	1604	0.7	8x70s	DD	1.62	0.22	0.292	0.281	0.752	7.3
2016/09/01	7633	1271	0.9	8x70s	DD	0.64	0.31	0.331	0.303	0.729	9.2
2016/10/03	7665	1317	0.9	8x70s	ND	—	—	0.326	0.300	0.710	9.7
2016/10/30	7692	1294	0.9	8x70s	MD	-0.28	0.27	0.309	0.306	0.687	9.0
2016/12/01	7724	1155	1.0	8x70s	MD	-0.08	0.31	0.304	0.333	0.706	9.8
2016/12/17	7740	1049	0.9	8x70s	MD	0.48	0.30	0.344	0.319	0.720	8.5
2018/06/30	8301	1361	0.9	8x80s	MD	-0.16	0.24	0.280	0.328	0.674	9.4
2018/07/23	8324	1062	1.2	8x80s	DD	-0.92	0.39	0.317	0.329	0.717	10.3
2018/08/14	8346	1477	0.7	8x80s	DD	-0.32	0.26	0.283	0.339	0.701	9.7
2018/10/23	8416	1388	0.9	8x80s	ND	—	—	0.243	0.384	0.688	9.9
2018/12/04	8457	1188	1.1	7x80s	ND	—	—	0.306	0.368	0.727	9.5
2019/01/06	8490	1597	0.8	8x80s	ND	—	—	0.293	0.342	0.774	9.1
2019/06/22	8658	1240	1.0	8x80s	ND	—	—	0.384	0.343	0.524	6.7
2019/07/21	8687	1258	0.9	8x80s	ND	—	—	0.362	0.346	0.503	6.5
2019/08/28	8725	1497	0.8	8x80s	DD	1.22	0.23	0.380	0.335	0.506	7.3

Table 3.4: Log of observations in circular polarization of β Peg. See the caption of Table 3.1.

3.2.2 Magnetic field variability

The LSD profiles of β Peg in circular polarization are shown in Figure 3.15. The Stokes V signatures show clear detections in some observations, while in others they remain featureless, showing that the circularly polarized signal in β Peg varies with time. Looking at Figure 3.15, it can be seen that when a Stokes V signature in β Peg is present, it can usually be traced for about 2-3 months. The best example is the signature found on 2016/07/03 that persists for at least 2 months, but on the third month it vanishes; the same timescale holds true for the detections on 2015/07/08 and 2018/07/23. Keeping in mind the observational bias (the star is observable for only 6-7 months every year, between end-June and January), it can also be seen that the detections of clear S-shaped signatures occur about once per year. Moreover, in November 2011 the field is of negative polarity, as it is four years later, in July 2015. In July and September 2016, the polarity is positive. It is negative again in July 2018, then positive in August 2019. It appears that the field polarity changes about once per year, and that there is an unexpected change of polarity that occurred at some point in time between December 2016 and June 2018. This suggests that the magnetic field might have a period of about two years. As it will be shown in Chapter 6, this is in agreement with subsequent observations made with NeoNarval, which show that the field is negative in July and August 2020, while in June 2021 it is positive. However, the Lomb-Scargle method was applied to the values of both the B_l and the activity indicators and no statistically significant periods were derived. This is also the case when the dataset is split in two – before and after the suspected change in polarity between December 2016 and June 2018. Further observations of β Peg are necessary in order to confirm or reject the hypothesis of a periodicity in the polarity changes of its magnetic field.

To gain more insight on the magnetic field and its variability, the spectral activity indicators were also measured: the S-, H α - and CaIRT-index (see Section 5 of Chapter 2

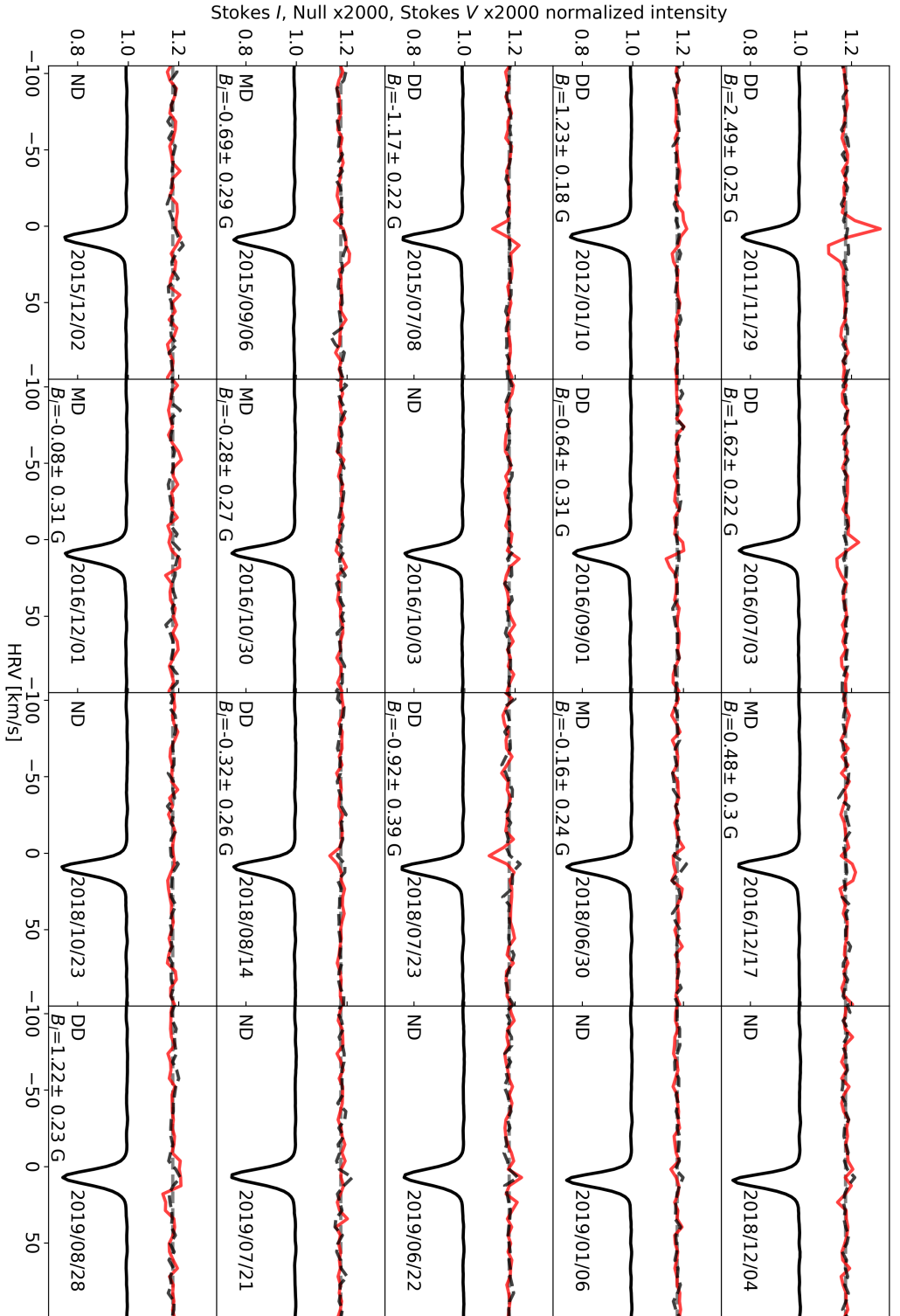


Figure 3.15: LSD profiles of β Peg in circular polarization. See the caption of Figure 3.1.

for a description of these indexes and the method of their computation). For each observation I also estimated the radial velocity v_{rad} of the star by fitting the LSD Stokes I profile with a gaussian and taking the peak of the function as the v_{rad} value; since the velocity bin I used for the LSD procedure is 1.8 km s^{-1} , following the Nyquist theorem I evaluate the precision of these estimations to be a half of the bin, or 0.9 km s^{-1} . These measurements, together with the B_l values for β Peg, are shown in Figure 3.16. In this figure, a clear variability can be seen in both the B_l and the spectral activity indicators. The variability is most prominent in the beginning of the dataset (between July 2015 and December 2016, HJD 2457200 and 2457750) where the most magnetic field detections are found. The behavior of the activity indicators seems to closely follow that of the longitudinal magnetic field: the S- and CaIRT-index are mostly in correlation with the B_l , while the $H\alpha$ is mostly in anticorrelation with it.

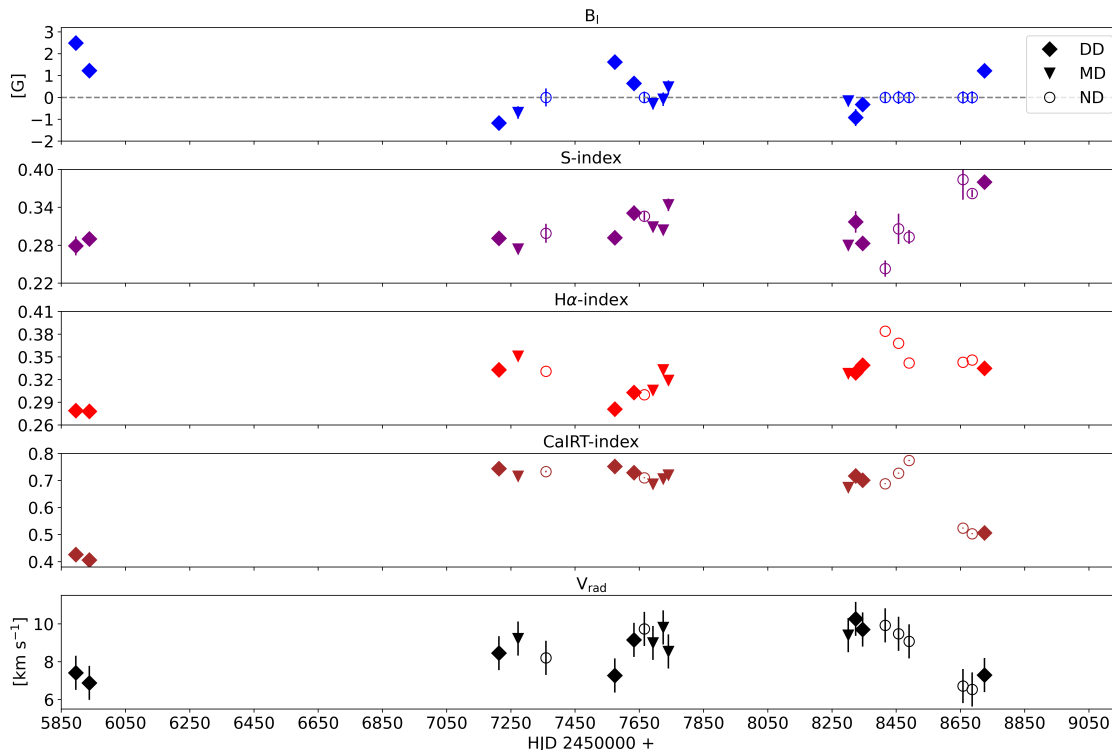


Figure 3.16: Measurements of the longitudinal magnetic field (B_l), the S-, $H\alpha$ - and CaIRT-indexes, and radial velocity (v_{rad}) of β Peg. See the caption of Figure 3.1.

The magnetic field itself is a vector, \vec{B} , but from spectropolarimetric observations one can only measure its line-of-sight component integrated over the visible stellar hemisphere, the scalar B_l . Due to the vector nature of the magnetic field, two fields of opposite polarities would cancel each other out in the B_l measurement if their longitudinal components are equal in absolute values.

Regarding the spectral activity indicators, the exact opposite is true. Since the CaH&K,

H α and CaIRT lines trace the heating in the stellar atmosphere due to the magnetic field, their indexes that are measured in the Thesis are independent of the polarity of the fields that cause the heating. Two fields with the same intensity but of opposite polarities would both contribute to the values of the activity indicators in the same way. This means that if at a certain moment on the visible hemisphere of the star there are fields of opposite polarities that have Stokes V signatures which cancel each other out, we would not be able to detect the fields by looking at the circularly polarized signatures only. However, by measuring the variability of the spectral activity indicators, we could still see the effect of magnetic fields due to the magnetic heating of the chromosphere. Keeping in mind the arguments above, in Georgiev et al. (2020a) the synchronous variability of the longitudinal magnetic field and the spectral activity indicators is interpreted as a result of a magnetic field composed of a simple structure: at those times when a detection of Stokes V signatures is obtained, the visible hemisphere of the star is dominated by magnetic field lines that have the same polarity. Such a field is expected to have a simple, close to poloidal geometry. In the future, this could be confirmed by using the ZDI method to image the stellar magnetic field when more data are collected.

3.2.3 Radial velocity variability and atmospheric dynamics

The estimations of the radial velocity of the star presented in the bottom panel of Figure 3.16 show some variability in the 6-10 km s⁻¹ interval, which might be due to pulsations. This is not unexpected, since β Peg is known to be a semiregular variable star.

To explore whether shock waves are present in the atmosphere of β Peg, I examined the same spectral lines as for RZ Ari (see Section 3.1.3) and obtained similar results. The Balmer lines show no emission, as shown for the H α line in Figure 3.17. The lines of the sodium doublet display a poorly defined two-component structure that shows no strong variability in time, the two components hardly being separated from each other. The LSD mean line profiles are always single and never display large deviations in their radial velocity, similar to the case of RZ Ari. Based on this analysis, it appears that there are no strong shock waves propagating in the atmosphere of β Peg.

3.2.4 Linear polarization

Let us now examine the star in linear polarization. Observations of β Peg with Narval in Stokes U & Q are available for a total of 4 nights, as reported in Table 3.5. For these observations, as in RZ Ari I analyzed both individual lines in the high-resolution spectra (the Balmer lines H α , H β , H γ and H δ , the CaIRT lines and the sodium doublet NaD, as well as nearby spectral lines) and the LSD profiles in search for polarized signatures. Regarding the individual lines I examined, none of them show any clear associated polarized signature. The same holds true for the LSD profiles, which are presented in Figure 3.16.

Based on this analysis, it appears that the atomic lines in β Peg show no linear polarization above the detection threshold of Narval during the interval of observations.

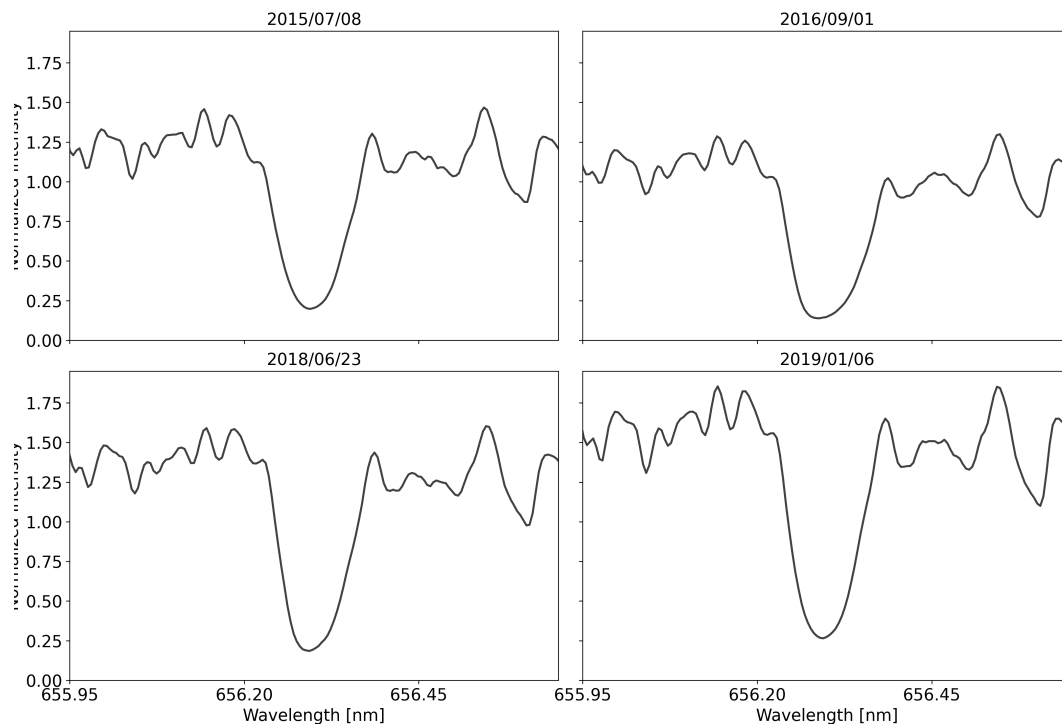


Figure 3.17: The $H\alpha$ line in four different observations of β Peg. No significant variability in time is present.

Date	HJD	SNR	σ_{LSD} ($10^{-5} I_c$)	Exposure time ($U \& Q$)	Stokes U detection	Stokes Q detection
2015/07/08	7212	1694	1.5	2Ux80s, 2Qx80s	ND	ND
2015/09/06	7272	1158	2.2	2Ux68s, 2Qx68s	ND	ND
2019/07/21	8686	1315	1.5	4Qx80s	N/A	ND
2019/07/22	8687	1215	1.6	4Ux80s	ND	N/A
2019/08/29	8725	1592	1.2	4Ux80s, 4Qx80s	ND	ND

Table 3.5: Log of observations in linear polarization of β Peg. See the caption of Table 3.2.

3.2. β PEGASI

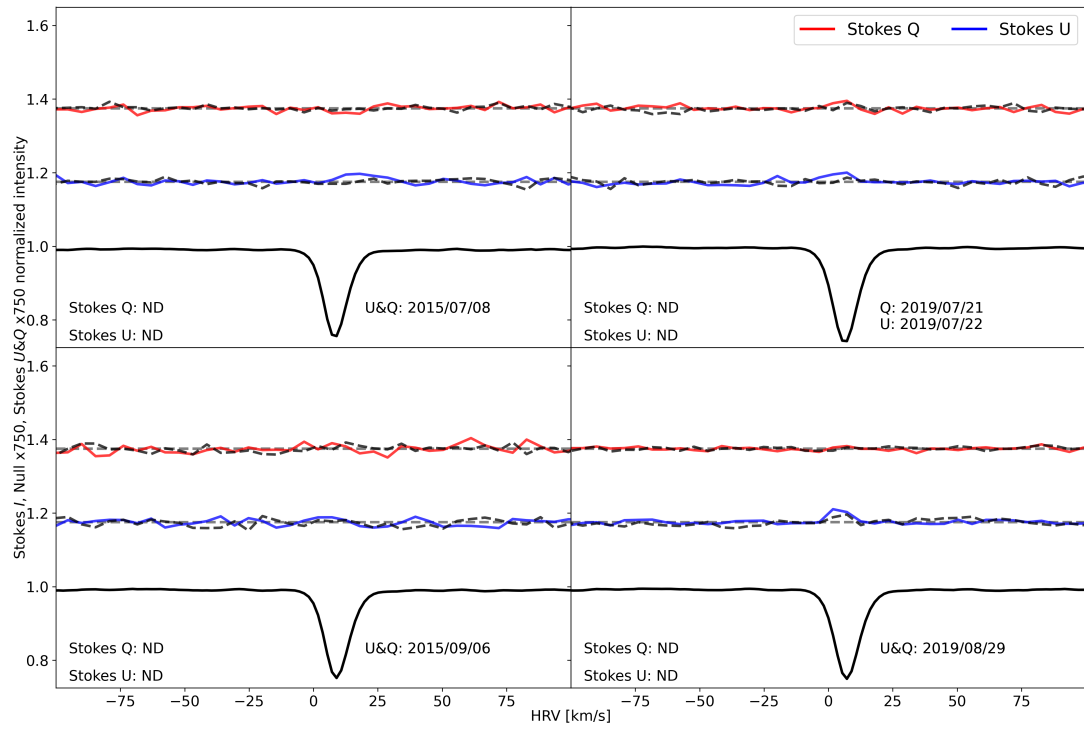


Figure 3.18: LSD profiles of β Peg observations in linear polarization. See the caption of Figure 3.4.

3.3 EK Boötis

EK Boo (HD 130144) is an M5III semi-regular variable giant star (Samus et al., 2017). van Dyck et al. (1998) estimate $T_{\text{eff}} = 3577$ K. On the HRD, EK Boo is inside the second magnetic strip. A direct detection of the surface magnetic field of EK Boo was first reported by Konstantinova-Antova et al. (2009), which these authors consider to be the first ever magnetic detection in a single M giant. Konstantinova-Antova et al. (2010) find that EK Boo is either a $2M_{\odot}$ star located at the tip of the RGB, or a $3.6M_{\odot}$ early-AGB star. Konstantinova-Antova et al. (2010) also determine the projected rotational velocity of the star, $v \sin i = 8.5 \pm 0.5$ km s⁻¹, using classical spectrum synthesis. EK Boo has an X-ray luminosity $L_X > 10^{30}$ erg s⁻¹ (Hünsch et al., 1998) which is unusually high for its spectral type. Hünsch et al. (2004) find that in this star L_X and the spectral activity indicators H α and CaII H&K are variable in time. EK Boo is considered by Famaey (2005) to be single.

In the Thesis I present an extension of previous studies of the magnetic field of EK Boo (Konstantinova-Antova et al., 2009, 2010), and I present the first detections of linear polarization in its spectral lines. This work is published in a paper in *Bulgarian Astronomical Journal* (Georgiev et al., 2020a), where it is also shown that EK Boo is likely a wide binary system (also explained in Section 3.3.3). I also confirm in Georgiev et al. (2020b) the value of $v \sin i$ reported by Konstantinova-Antova et al. (2010) using the method presented in Section 3.1.5.

3.3.1 Observations

In the period April 2008 - July 2019 a total of 54 observations in circular polarization were obtained for EK Boo, 18 of which show detections of polarization signatures. A detailed log of these observations is given in Table 3.6. Unfortunately, some of the data were affected by the misalignment of the Fresnel rhomb described in Section 3.1.1 and no B_l values were computed for them. The star was also observed in linear polarization on 9 nights between March 2019 and July 2019. The log of the observations in linear polarization is given in Table 3.7.

To apply the LSD method to the observations of EK Boo, I used a line mask built from atomic line lists from VALD (Kupka et al., 1999) with parameters $T_{\text{eff}} = 3500$ K, $\log g = 0.5$, microturbulence of 2 km s⁻¹ and solar metallicity, following Konstantinova-Antova et al. (2010). As in the other two M giants, I removed the lines of H, He, Na, K, and Ca from the mask (see Section 3.1.1). The total number of lines in the LSD mask is 13458.

3.3. EK BOÖTIS

Date	HJD	SNR	σ_{LSD} ($10^{-3} I_c$)	Exposure time Stokes V	Detection Stokes V	B_l [G]	σ [G]	S- index	H α - index	CaIRT- index	V_{rad} [km s $^{-1}$]
2008/04/04	4562	1472	1.3	4x400s	DD	-3.38	0.74	0.242	0.356	0.648	-26.5
2008/04/05	4563	1358	1.4	4x400s	DD	-6.41	0.76	0.254	0.361	0.653	-26.5
2008/04/06	4564	1064	1.9	4x400s	DD	-6.97	1.01	0.272	0.360	0.655	-26.6
2008/12/20	4822	1181	1.4	6x400s	ND	—	—	0.469	0.408	0.575	-28.1
2009/02/25	4889	1280	1.1	8x400s	DD	-0.74	0.61	0.431	0.401	0.578	-27.5
2009/03/09	4900	1191	1.5	8x400s	DD	-3.84	0.53	0.420	0.392	0.575	-27.1
2009/03/13	4904	1396	1.3	8x400s	DD	-4.93	0.46	0.422	0.405	0.577	-27.2
2009/03/18	4910	904	1.3	8x400s	DD	-10.20	0.86	0.478	0.401	0.578	-27.3
2010/01/18	5216	601	3.3	4x400s	ND	—	—	0.413	0.372	0.579	-25.7
2010/02/12	5241	918	2.0	8x400s	ND	—	—	0.296	0.393	0.641	-24.8
2010/03/13	5270	1097	1.4	8x400s	MD	1.48	0.70	0.322	0.393	0.630	-24.5
2010/04/15	5303	1281	1.2	8x400s	MD	-0.80	0.61	0.302	0.376	0.632	-25.2
2010/04/23	5311	1269	1.3	8x400s	ND	—	—	0.281	0.382	0.657	-24.3
2010/06/22	5370	1223	1.3	8x600s	ND	—	—	0.297	0.379	0.657	-23.2
2010/07/07	5385	1177	1.1	8x400s	MD	1.76	0.63	0.270	0.384	0.617	-25.4
2010/07/23	5401	1133	1.3	8x400s	ND	—	—	0.296	0.393	0.656	-24.6
2010/08/17	5426	1095	1.5	8x400s	ND	—	—	0.278	0.407	0.684	-23.3
2011/01/13	5576	721	2.0	8x400s	ND	—	—	0.316	0.416	0.672	-24.0
2011/01/15	5578	1187	1.1	8x400s	ND	—	—	0.287	0.415	0.667	-23.8
2011/02/04	5598	1412	1.0	8x400s	ND	—	—	0.259	0.402	0.657	-24.0
2011/03/18	5640	1015	1.4	8x400s	ND	—	—	0.303	0.388	0.641	-25.4
2011/03/31	5653	763	1.9	8x400s	ND	—	—	0.325	0.399	0.678	-24.6
2011/04/07	5660	1171	1.2	8x400s	DD	3.25	0.69	0.313	0.395	0.672	-24.4
2011/04/30	5683	963	1.5	8x400s	ND	—	—	0.319	0.369	0.611	-25.7
2011/05/12	5695	1386	1.0	9x400s	ND	—	—	0.303	0.361	0.597	-25.9
2011/06/13	5726	1196	1.2	8x400s	ND	—	—	0.307	0.363	0.619	-25.8
2011/07/01	5744	1223	1.2	8x400s	ND	—	—	0.309	0.357	0.597	-25.9
2011/07/11	5754	1243	1.1	8x400s	N/A	—	—	0.316	0.351	0.604	-25.6
2011/08/20	5794	1167	1.2	8x400s	N/A	—	—	0.296	0.337	0.583	-26.5
2012/01/07	5935	1332	1.2	8x400s	DD	4.93	0.71	0.320	0.326	0.604	-24.8
2012/01/24	5952	1290	1.1	8x400s	MD	2.89	0.66	0.320	0.341	0.612	-24.5
2012/03/13	6001	1286	1.2	8x400s	ND	—	—	0.344	0.361	0.642	-23.5
2012/05/09	6058	799	2.0	8x400s	ND	—	—	0.333	0.376	0.658	-23.1
2012/06/14	6094	754	2.2	8x400s	ND	—	—	0.301	0.349	0.607	-23.9
2012/07/16	6125	1243	1.2	8x400s	N/A	—	—	0.259	0.368	0.652	-23.1
2012/08/17	6157	1031	1.4	8x400s	N/A	—	—	0.253	0.355	0.585	-24.2
2013/03/21	6374	839	2.6	4x400s	DD	-8.12	1.51	0.281	0.354	0.645	-25.1
2013/04/21	6405	1011	1.9	4x400s	DD	-4.96	1.14	0.276	0.350	0.593	-24.0
2013/06/10	6454	891	2.4	4x400s	ND	—	—	0.262	0.371	0.653	-22.4
2013/08/11	6516	1288	1.6	4x400s	MD	-3.34	0.91	0.224	0.366	0.624	-23.9
2016/01/24	7413	968	2.3	4x400s	ND	—	—	0.284	0.389	0.628	-21.9
2016/02/16	7436	1185	1.3	8x400s	ND	—	—	0.263	0.399	0.615	-21.8
2016/03/16	7465	1025	1.5	8x400s	ND	—	—	0.259	0.395	0.614	-21.8
2018/04/13	8223	564	3.3	7x400s	ND	—	—	0.287	0.360	0.590	-23.7
2018/05/05	8244	1001	1.6	8x400s	ND	—	—	0.228	0.374	0.612	-21.7
2018/06/14	8284	1153	1.3	8x400s	ND	—	—	0.209	0.381	0.559	-21.8
2018/07/17	8317	1233	1.3	8x400s	MD	-0.86	0.63	0.202	0.388	0.578	-21.7
2018/08/07	8338	906	1.8	8x400s	ND	—	—	0.224	0.390	0.612	-20.7
2018/08/27	8358	980	1.7	8x400s	ND	—	—	0.246	0.382	0.588	-21.2
2019/01/14	8499	1088	1.5	8x400s	ND	—	—	0.232	0.392	0.683	-21.1
2019/04/19	8594	882	1.8	8x400s	MD	1.22	1.02	0.214	0.374	0.660	-22.8
2019/06/07	8642	1093	1.7	8x400s	ND	—	—	0.319	0.404	0.788	-22.8
2019/06/28	8663	1231	1.5	8x400s	ND	—	—	0.288	0.392	0.786	-22.3
2019/07/28	8693	1046	1.8	8x400s	ND	—	—	0.295	0.398	0.755	-24.0

Table 3.6: Log of observations in circular polarization of EK Boo. See the caption of Table 3.1. No B_l values are computed for the dates affected by the misalignment of the Fresnel rhomb described in Section 3.1.1, and they are marked with "N/A" in the "Detection" column.

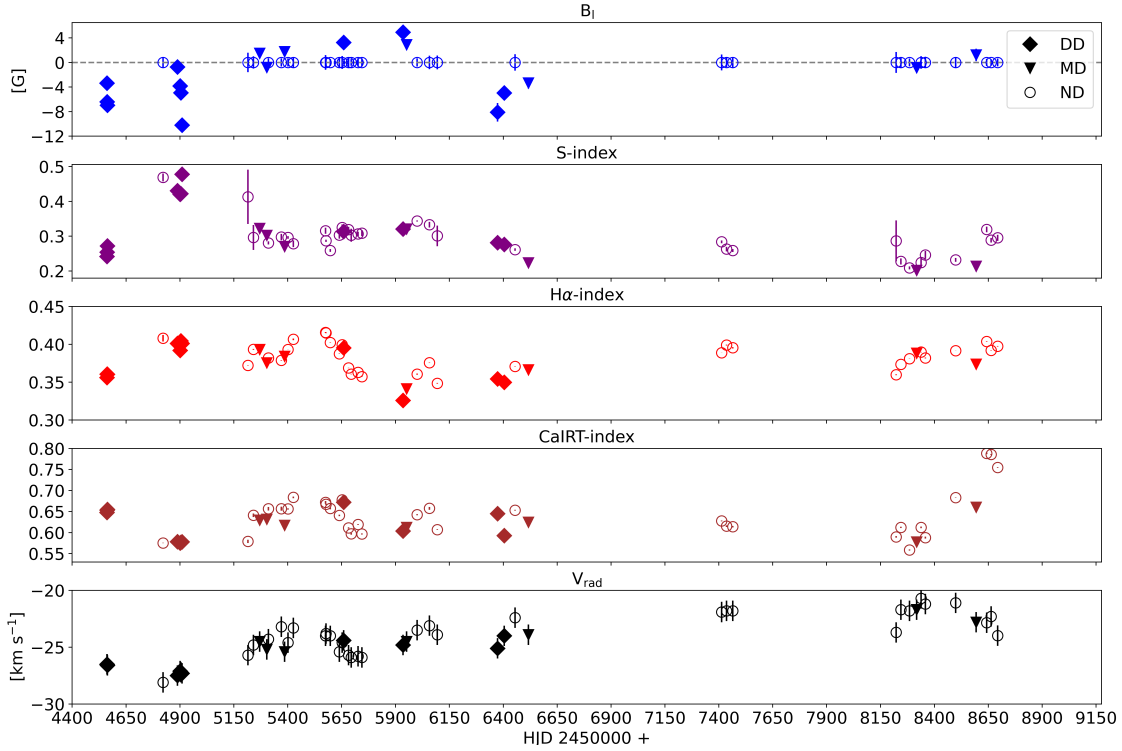


Figure 3.19: Measurements of the longitudinal magnetic field (B_l), the S-, $H\alpha$ - and CaIRT-indexes, and radial velocity (v_{rad}) of EK Boo. See the caption of Figure 3.1.

3.3.2 Magnetic field variability

The LSD profiles I obtain for EK Boo are shown in Figure 3.20. The magnetic field observed in this star is significantly stronger than the one found in β Peg, even reaching the 10 G level on 2009/03/18. The Stokes V signatures in EK Boo show significant variability in the course of a single month in the period March-April 2011: no signature is found on 2011/03/31, then on 2011/04/07 a clear S-shaped profile can be seen that yields $B_l = 3.25 \pm 0.69$ G, followed shortly by a featureless signal on 2011/04/30. From these cases of rapid change in the Stokes V , it seems that the longitudinal magnetic field in EK Boo may vary by up to 5 G on the monthly timescale.

Figure 3.19 shows the temporal evolution of the B_l , activity indicators and v_{rad} in EK Boo. In this figure we find that the behavior of the spectral activity indicators is different than in the case of β Peg. Here, there is no apparent correlation between the activity indicators and the B_l . In Georgiev et al. (2020a), this is interpreted as a sign of a magnetic field with a complex geometry, composed of a number of small-scale magnetic structures that all contribute to the magnetic heating of the stellar atmosphere (that is traced by the spectral activity indicators), but cancel each other out, either partially or fully, in the averaged Stokes V profile and the B_l . Moreover, from Figure 3.19 it can

also be seen that the magnetic field of EK Boo shows a long-term variability with time as well: in the beginning of the dataset (April 2008 – August 2013, or HJD between 2454500 and 2456600) there are more detections than in the second part of the dataset.

3.3.3 Radial velocity variability and atmospheric dynamics

The radial velocity curve of EK Boo (Figure 3.19, bottom panel) is particularly interesting. For the observations in the beginning of the dataset in 2008 I estimate $v_{\text{rad}} \approx -27.5 \text{ km s}^{-1}$ by applying a gaussian fit to the LSD Stokes I profile; however, after the first few observations the radial velocity steadily grows with time and reaches $\approx -21 \text{ km s}^{-1}$ in 2018. Such a long-term trend in the radial velocity suggests that EK Boo is in fact a binary system. In a binary system, the two components orbit around the center of mass of the system. For each component, the radial velocity measured from observations will vary with time due to this orbital movement, except in the case where the component orbits the center of mass in a plane which is perpendicular to the line of sight.

In the case of EK Boo, no indications of binarity are found in the high-resolution spectra, which means that the secondary component is much fainter than the primary one. This excludes the possibility that the circularly polarized signatures found in EK Boo are related to the secondary component, since only a sufficiently bright source could be detected in polarized light. Taking into account the unusually high X-ray luminosity of EK Boo and the low luminosity of the suspected companion in the visible domain, in Georgiev et al. (2020a) it is suggested that the companion star may be a magnetically active red dwarf which is responsible for the high X-ray luminosity.

Over the course of the available dataset the radial velocity does not show periodicity. This suggests that the orbital period of the system is long and we are facing a wide binary system, where the distance between the components is much larger than their size. This in turn excludes the possibility that tidal interactions play a role in the faster rotation of the giant and its magnetic field.

To determine whether shock waves propagate through the atmosphere of EK Boo, I examined the same spectral lines as I did in Section 3.1.3 for RZ Ari. The Balmer lines show no emission, as shown in the example in Figure 3.21. The lines of the sodium doublet present a four-component structure. After fitting each of the sodium doublet lines in each observation with a sum of four gaussians, I found that each component shows variability mainly in their equivalent width, but not in their radial velocity. The LSD mean line profiles are always single, and in Georgiev et al. (2020a) we consider that their large radial velocity shifts are due to binarity. Based on this analysis, it appears that there are no strong shock waves propagating in the atmosphere of EK Boo.

3.3.4 Linear polarization

9 observations of EK Boo were obtained in linear polarization between March and July 2019. The log of observations is given in Table 3.7. As in the other M giants, I examined

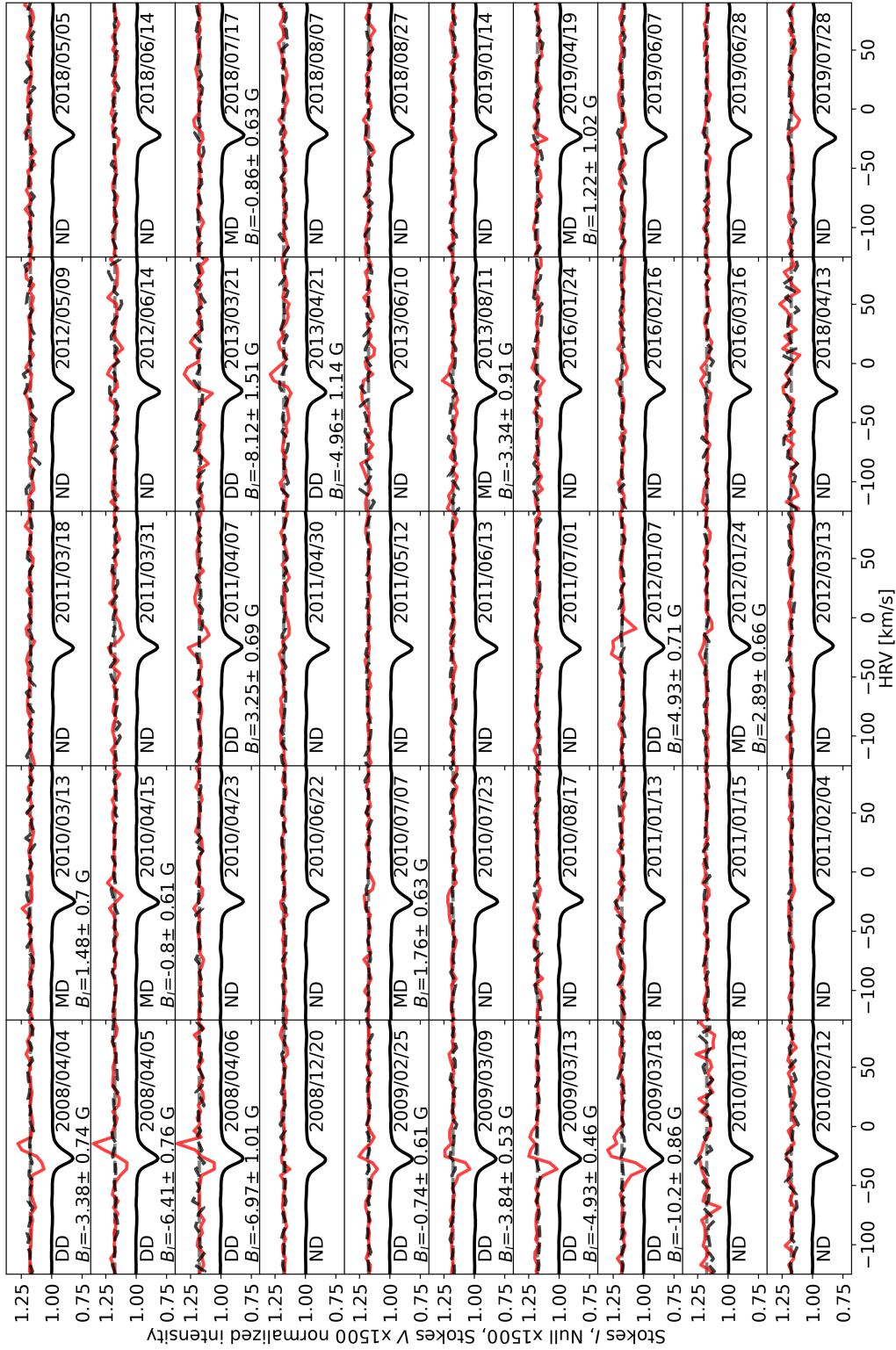


Figure 3.20: LSD profiles of EK Boo in circular polarization. See the caption of Figure 3.15.

3.3. EK BOÖTIS

several lines ($H\alpha$, $H\beta$, $H\gamma$, $H\delta$, the CaIRT and the NaD, as well as lines adjacent to them) and found no clear polarization signatures associated to any of them. I also investigated the LSD profiles, which are shown in Figure 3.22. The LSD profiles of EK Boo present linearly polarized signatures in both Stokes U and Stokes Q that also show variability with time. The strongest signal I find is on 2019/07/28, where the polarization level in Stokes U peaks at 2.3×10^{-4} the intensity of the unpolarized continuum.

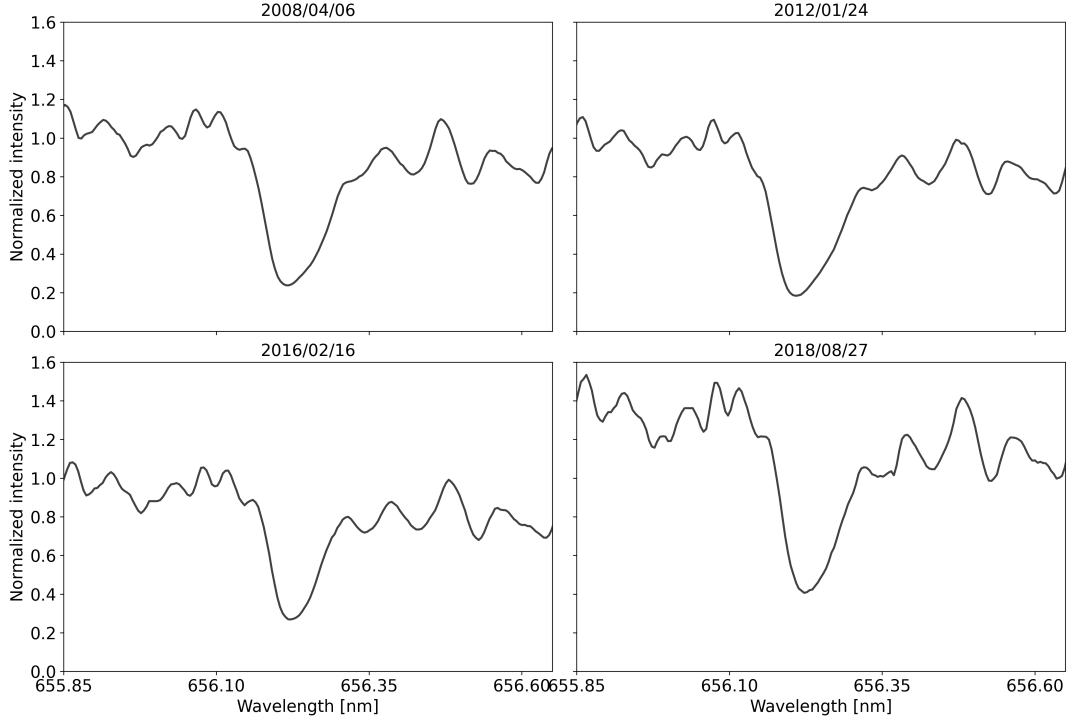


Figure 3.21: The $H\alpha$ line in four different observations of EK Boo. No emission or significant variability is observed.

From the available dataset it appears that the polarized signatures do not vary on the daily timescale - the profiles observed on 2019/05/30 are very similar to those from 2019/05/31; the same is also true for 2019/06/28 and 2019/06/29.

Some differences can be seen in the Stokes Q profiles that are about one month apart, e.g. 2019/04/30, 2019/05/30, 2019/06/28-29 and 2019/07/25. Interestingly, the S-shaped signature in Stokes U observed first on 2019/04/30 seems to persist for three months up to 2019/07/28 without changing its shape significantly, but only its amplitude in the blue lobe in July 2019. During the same period of time, the Stokes Q profiles appear and disappear, but also retain the same S-shape when present; it may be that this S-shape signature was always present in Stokes Q between April and July 2019, but

its amplitude occasionally dropped below the detection limit of Narval. However, more observations are needed to study whether the variability of EK Boo in linear polarization is periodic, and if it is, to estimate its timescale of variation.

Date	HJD	SNR	σ_{LSD} ($10^{-5} I_c$)	Exposure time ($U\&Q$)	Stokes U detection	Stokes Q detection
2019/03/15	8558	955	3.7	2Ux400s, 2Qx400s	MD	MD
2019/04/30	8604	1049	2.0	4Ux400s, 4Qx400s	DD	ND
2019/05/30	8634	1120	2.0	4Ux400s, 4Qx400s	DD	DD
2019/05/31	8635	1137	1.9	4Ux400s, 3Qx400s	DD	DD
2019/06/02	8637	916	3.1	4Qx400s	N/A	DD
2019/06/28	8663	1026	3.0	4Ux400s	DD	ND
2019/06/29	8664	1047	2.5	4Ux400s, 4Qx400s	DD	MD
2019/07/25	8690	1225	3.3	2Ux400s, 4Qx400s	DD	DD
2019/07/28	8693	935	2.6	4Ux400s	DD	N/A

Table 3.7: Log of observations in linear polarization of EK Boo. See the caption of Table 3.2.

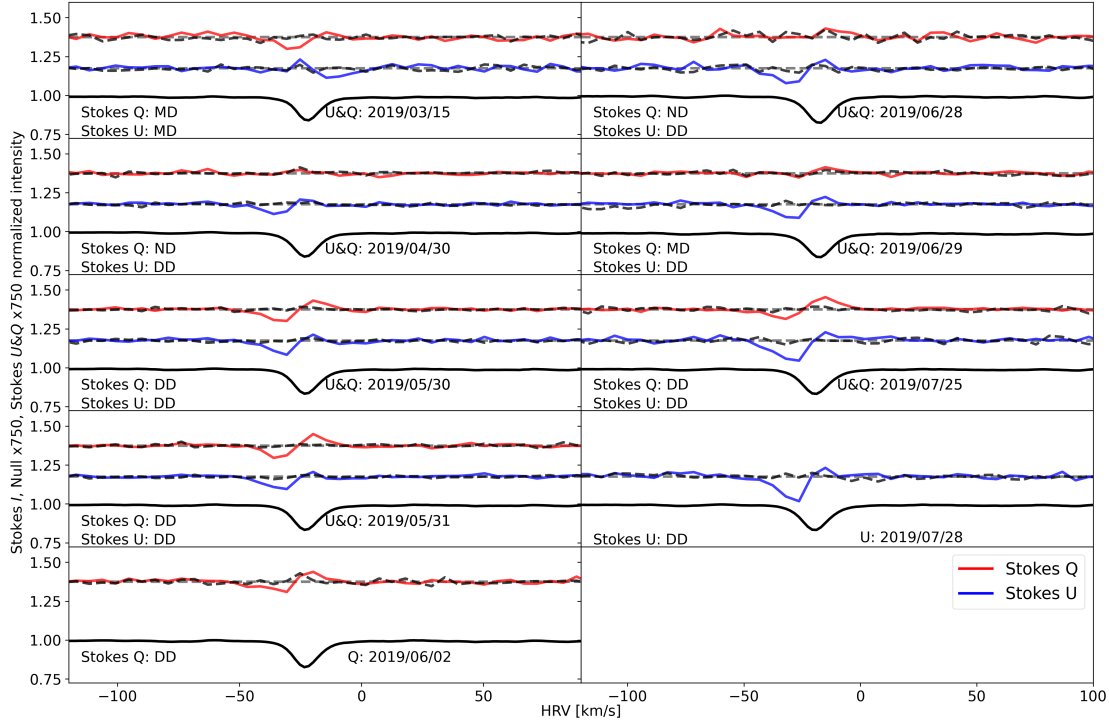


Figure 3.22: LSD profiles of EK Boo observations in linear polarization. See the caption of Figure 3.18.

3.3.5 Paper published in Bulgarian Astronomical Journal

Magnetism in Cool Evolved Stars: the M giants EK Bootis and β Pegasi

S. Georgiev^{1,2}, R. Konstantinova-Antova¹, A. Lèbre², M. Aurière³, C. Charbonnel^{3,4}, A. Palacios², N. Drake^{5,6,7}, R. Bogdanovski¹

¹ Institute of Astronomy and NAO, Bulgarian Academy of Science, 1784 Sofia, Bulgaria

² LUPM, UMR 5299, Université de Montpellier, CNRS, place Eugène Bataillon, 34095 Montpellier, France

³ Université de Toulouse, Institut de Recherche en Astrophysique et Planétologie, 14 avenue Édouard Belin, 31400 Toulouse, France

⁴ Department of Astronomy, University of Geneva, Chemin des Maillettes 51, 1290 Versoix, Switzerland

⁵ Laboratory of Observational Astrophysics, Saint Petersburg State University, Universitetski pr. 28, Petrodvoretz 198504, Saint Petersburg, Russia

⁶ Observatório Nacional/MCTIC, Rua Gen. José Cristino, 77, 20921-400, Rio de Janeiro, Brazil

⁷ Laboratório Nacional de Astrofísica/MCTIC, Rua dos Estados Unidos 154, 37504-364, Itajubá, Brazil

sgeorgiev@astro.bas.bg

(Submitted on xx.xx.xxxx; Accepted on xx.xx.xxxx)

Abstract. We present a long-term spectropolarimetric study of the active M giants EK Bootis (M5III) and β Pegasi (M2.5II-III). For each star, the variability of the surface-averaged longitudinal component of the magnetic field (B_l) is shown, along with the behavior of different spectral activity indicators. The possible existence of a companion is discussed for EK Boo, a thought to be single star. We compare the observed variations in the activity proxies of each of the two giants and discuss possible physical explanations for the structure of their respective magnetic fields. For both objects, observations in linear polarisation are also presented and briefly discussed.

1. Introduction

Magnetism in cool evolved stars has been extensively studied in the case of G- and K giants (see Konstantinova-Antova et al. 2013; Aurière et al. 2015). Aurière et al. (2015) studied 48 such giants and magnetism was detected in 29 of them. A correlation between the magnetic field strength and the Rossby number in the magnetically detected stars was determined, favoring the operation of an $\alpha - \omega$ dynamo. The positions of these magnetic giants in the Hertzsprung-Russell diagram (HRD) define two so-called "magnetic strips" that correspond to specific evolutionary stages: 1) around the first dredge-up at the base of the Red Giant Branch (RGB) and during the core-helium burning and 2) at the tip of the RGB and early Asymptotic Giant Branch (AGB) stage. Based on observational results, a theoretical framework was built by Charbonnel et al. (2017) to explain the existence of surface magnetic fields in these stars. In the samples of M giants studied by Konstantinova-Antova et al. (2010; 2013; 2014) more than 60% of the stars are magnetically active. However, recent results (Konstantinova-Antova et al. 2018; 2019, in prep.) do not favor the $\alpha - \omega$ dynamo to explain the magnetic field in these stars. Here we present a further study of magnetism in two M giants, EK Boo and β Peg.

2. Data and methods

2.1. Observations and data reduction

The M giants EK Boo and β Peg were observed using the instrument Narval mounted on the 2m Telescope Bernard-Lyot (TBL) at the Pic du Midi observatory, France. Narval is a high-resolution fiber-fed echelle spectropolarimeter (Aurière 2003). This instrument works in the spectral range of 375 – 1050 nm and has a resolving power of 65000. It allows simultaneous measurement of the full intensity as a function of wavelength (Stokes I) and the intensity in linear (Stokes U or Q) or circular (Stokes V) polarisation versus wavelength. Narval is capable of detecting polarisation within individual lines with an accuracy of about $10^{-4}I_c$ (I_c being the intensity of the unpolarised continuum).

We used Narval for observations in circular polarisation to search for Zeeman signatures in the Stokes V profiles, indicative of the presence of a magnetic field. Some observations in linear polarisation were also obtained. All data were treated initially by the automatic reduction software LibreEsprit (Donati et al. 1997), which performs optimal spectrum extraction, wavelength calibration, heliocentric frame correction and continuum normalization.

2.2. Data analysis

Having obtained the reduced data by LibreEsprit, we used the Least Square Deconvolution (LSD) method (Donati et al. 1997), which averages the profiles of more than ten thousand spectral lines (≈ 15000 in the cases of EK Boo and β Peg) to generate a mean line profile both in Stokes I and in polarised light. In this way the detection of weak polarised structures associated to spectral lines, and resulting from magnetic fields of low intensity, becomes possible. The method also gives a diagnostic null spectrum which should not present any feature. Its purpose is to diagnose the presence of spurious contributions to the Stokes V/U/Q spectrum. To perform the LSD method we used line masks constructed from the VALD database (Kupka et al. 1999) with the following parameters: $T_{eff}=3500$ K, $\log g=0.5$, microturbulence of 2.0 km/s for EK Boo and $T_{eff}=3700$ K, $\log g=1.0$, microturbulence of 2.0 km/s for β Peg. Both masks are calculated for solar abundances.

The method has a built-in procedure for statistical evaluation of the signal detection probability. According to this procedure we can have a definite detection of polarisation, a marginal detection or a non-detection (DD, MD and ND respectively). The procedure is based on a reduced χ^2 test and yields a DD if the false alarm probability is smaller than 10^{-5} , MD if it is larger than 10^{-5} but smaller than 10^{-3} and ND otherwise.

2.3. Measurements of magnetic field strength and activity indicators

Using the Stokes V data, we calculated the line-of-sight component of the magnetic field (B_l) using the first-order moment method (Rees & Semel 1979; Donati et al. 1997); the typical error in the B_l calculations is 0.7 G for EK Boo and 0.3 G for β Peg. Using the Stokes I data we measured the intensity of the spectral activity indicators CaII H&K, H α and CaIRT by calculating the S-index, defined in the Mount Wilson survey (Duncan et al. 1991) and the related H α and CaIRT indices. By fitting the mean Stokes I profiles with a gaussian we also calculated the stellar radial velocity V_{rad} . The radial velocity bin in the LSD output is 1.8 km/s and following the Nyquist theorem we estimate an error of 0.9 km/s for our V_{rad} measurements.

Due to a technical problem with Narval in the summers of 2011 and 2012 (one of the spectropolarimeter's Fresnel rhombs was out of position, hence giving false Stokes V data) we could not obtain reliable B_l measurements for these periods. However, the unpolarised spectra were not affected, allowing the measurement of the spectral activity indicators and the V_{rad} .

The results for both stars are described in the following two sections.

3. EK Boo

3.1. General characteristics

EK Boo (HD 130144) is an M5III semiregular variable giant star (Samus et al. 2017) of visual magnitude $V = 5.63^m$ (Ducati 2002). EK Boo is considered to be single (Famaey et al. 2009). This star has an X-ray luminosity $L_X > 10^{30}$ erg s $^{-1}$ (Hünsch et al. 1998), which is unusually high for this spectral type. EK Boo has a projected rotational velocity $v \sin i = 8.5 \pm 0.5$ km/s and it is the first apparently single M giant for which a direct detection of a surface magnetic field was reported (Konstantinova-Antova et al. 2010).

3.2. Magnetic field strength, spectral activity indicators and radial velocity

We obtained 49 Stokes V observations of EK Boo between April 2008 and April 2019, of which only 16 show detections. The log of observations is shown in Table 1 in the Appendix. Typical signal-to-noise ratios (SNR) of the spectra peak at about 1200. The mean Stokes V profiles of EK Boo constructed with the LSD method show strong variability both at long- and short-term timescales. A sample of the LSD results is presented in Figure 1, showing the LSD profiles for the dates March 31st 2011 (ND), April 7th 2011 (DD) and April 30th 2011 (ND). In this plot we see the mean Stokes V profile changing considerably in the course of a single month, while the accuracy of the measurements for these observations does not vary considerably. Measured values

of the B_l , spectral activity indicators and radial velocities are presented in Figure 2. The longitudinal component of the magnetic field varies on both long and short time scales: observations for which we have a definite detection of mean Stokes V signatures are followed shortly by observations with no detection. The B_l varies in the range of -10.20 ± 0.86 G to 4.93 ± 0.71 G.

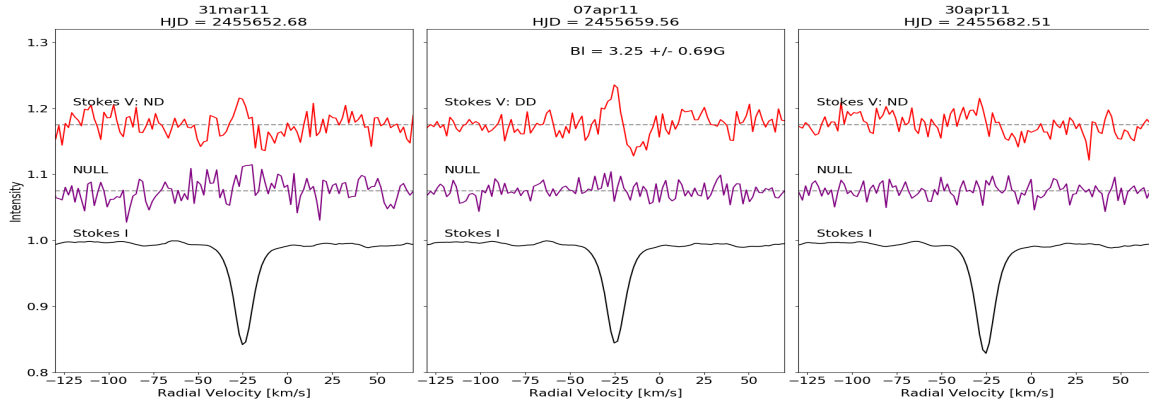


Fig. 1. Example of LSD results from EK Boo observations. The result of the statistical test is indicated for each observation and the B_l value is given for the detections.

The magnetic field is a vector, and we can only measure its line-of-sight component integrated over the whole visible stellar hemisphere, B_l . The individual magnetic structures contribute to the B_l with different signs depending on their polarity: structures of opposing polarities would cancel each other out in their contribution to the line-of-sight component. On the other hand, the spectral proxies trace the magnetic heating in the stellar atmosphere. Their variability depends on the integrated heating by the magnetic structures, regardless of their polarity. In EK Boo, the spectral activity indicators show a complex behavior with respect to the B_l . No clear correlation is observed. This suggests that the field is not of simple geometry: instead, it seems that small-scale magnetic structures contribute to the magnetic heating of the stellar atmosphere. Because of the relatively low $v \sin i$ however, we cannot resolve fine details on the stellar disc.

In Figure 2, a long-term variability of the B_l and the activity indicators is obvious. In the first half of our dataset, between April 2008 and August 2013 (HJD 2454562 to 2456516) the B_l as well as the spectral activity indicators vary more than in the second half of the dataset where they display a more steady behavior. Also, before August 2013 we report more detections of magnetic field, while between January 2016 and April 2019 (HJD 2457413 to 2458594) we have only two marginal detections. This behavior of the magnetic field strength and spectral indicators means that the magnetic activity of EK Boo declines after January 2016 and is mostly absent or is below the detection limit.

Within the timescale of one month (April 2011) we observe fast variability of the magnetic field, which indicates dynamics in the magnetic structures.

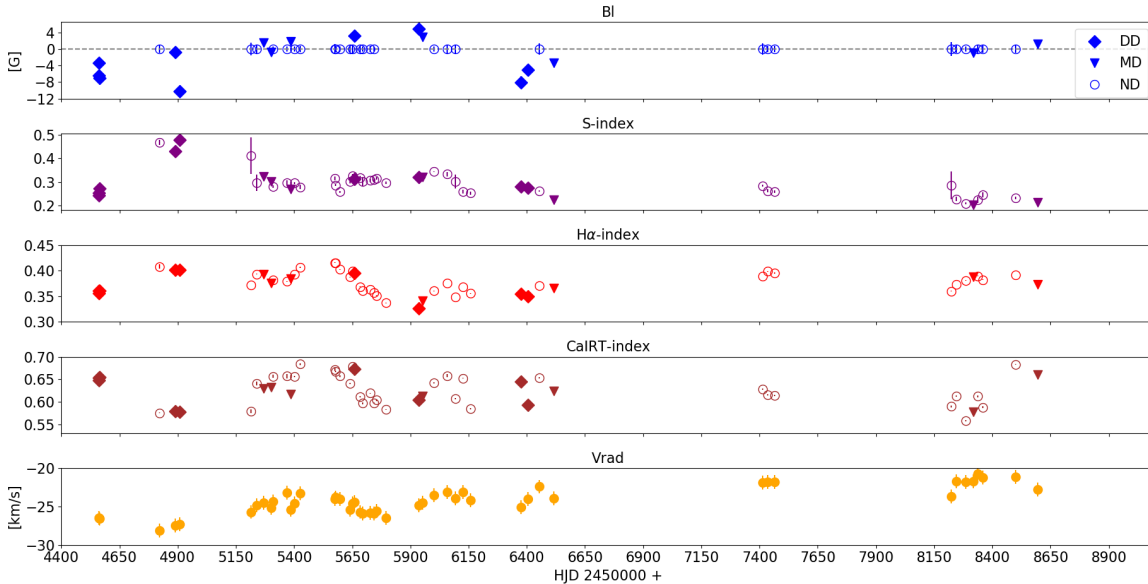


Fig. 2. Magnetic field, spectral activity indicators and radial velocity measurements of EK Boo. The different symbols denote the type of detection of circular polarisation.

Looking at the activity indicators however, we do not find evidence of flares. This means that the magnetic variability in EK Boo is rather different than that in the G and K giants studied in detail, e.g. V390 Aur (Konstantinova-Antova et al. 2012), OU And (Borisova et al. 2016), β Cet (Tsvetkova et al. 2019), OP And (Georgiev et al. 2018). Such vigorous dynamics might be associated to changes in the convective structure as a tracer of the magnetic field. Whether an $\alpha - \omega$ or another kind of dynamo is operating in such conditions is a subject of a further study.

The behavior of the radial velocity of EK Boo is interesting, as can be seen in Figure 2. At the very beginning of our dataset we have $V_{rad} \approx -27.5$ km/s, after which the value steadily grows over time and our last observations yield $V_{rad} \approx -21.5$ km/s. While this star is known from the literature to be a single one, a long-term trend in the radial velocity is apparent, suggesting the possible existence of a companion. Such a component must be much fainter than the primary star, since we observe no spectral indications of binarity. This excludes the possibility that the observed polarised signatures are related to the secondary component, as only a sufficiently bright object could cause a detection of polarised signal. Taking into account the unusually high X-ray luminosity of EK Boo and the low luminosity of the suspected companion in the visible domain, we suggest that the secondary component could be an active red dwarf, responsible for the large L_X .

Our dataset spans over 11 years and during this time the V_{rad} variation does not exhibit periodicity. This suggests that the orbital period of the system is long, meaning that the distance between the components is very large with respect to their size, i.e. we have a wide binary system. This excludes the possibility that the activity of EK Boo is caused by tidal interactions like in RS CVn variables.

3.3. Linear polarisation

We observed EK Boo in linear polarisation during three nights in 2019: March 15 (HJD = 2458558), 30 April (HJD = 2458604) and May 30 (HJD = 2458634). For all of them we have both Stokes U and Q measurements. We analyzed the data and found no polarisation signatures linked to individual spectral lines. We then applied the LSD method to the observations in search for a mean polarisation signal. The output is shown in Figure 3 and the results of the statistical test are indicated for each observation. The LSD method reveals a clear mean linear polarisation signal in all of our observations. A clear signature seems to always be present in Stokes U, which is not the case in Stokes Q. The appearance of signal in the LSD profiles and not in the observational spectropolarimetric data means that a mean polarisation exists in the spectra of EK Boo, but the signal within individual lines is below our detection limit. Recent studies (Aurière et al. 2016, Mathias et al. 2018, López Ariste et al. 2018) have explained the linear polarisation observed in the cool evolved supergiant Betelgeuse with the presence of giant convective cells at the photospheric layer. Further observations of EK Boo are necessary in order to explain if the observed linear polarisation signal in EK Boo is due to surface brightness inhomogeneities (similarly to the case of Betelgeuse) or if it has some other origin.

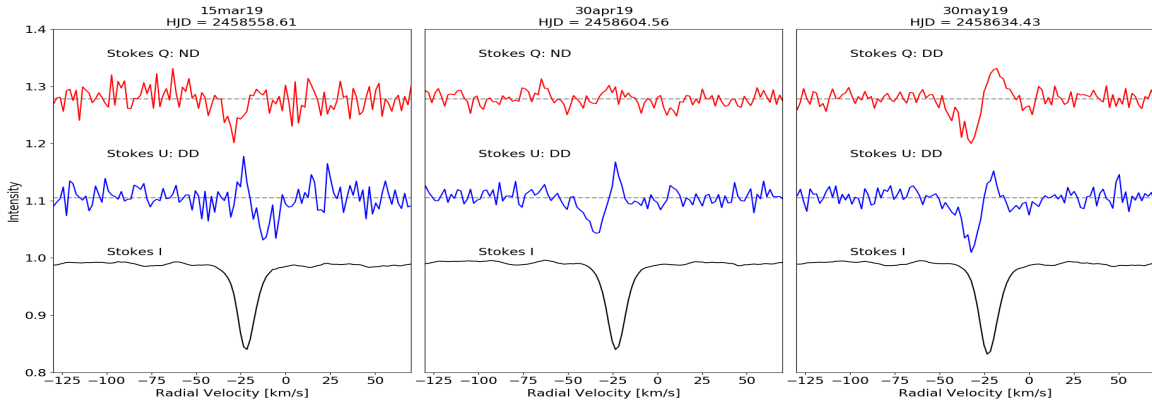


Fig. 3. LSD profiles of observations in linear polarisation of EK Boo. The diagnostic null spectra are all flat and are not shown. The result of the statistical test is indicated for each observation.

4. β Peg

4.1. General characteristics

β Peg (HD 217906) is a $V = 2.4^m$ (Ducati 2002) M2.5II-III semiregular variable star with $P = 43.3d$ (Tabur et al. 2009). We estimate a value of

$v \sin i = 7$ km/s for this giant. β Peg is known to be a magnetic early-AGB star (Konstantinova-Antova et al. 2014).

4.2. Magnetic field strength, spectral activity indicators and radial velocity

In the period July 2015 – January 2019 we obtained 15 observations of β Peg in circular polarisation, out of which 10 yield magnetic field detections. The typical SNR of the spectra is ≈ 1400 . The log of observations is presented in Table 2 in the Appendix. Applying the LSD method to the observations of β Peg, we find significant variability in the mean Stokes V profiles, as well as in the value of the B_l . An example of the LSD results is given in Figure 4 and the measurements of the B_l , spectral activity indicators and radial velocities are shown in Figure 5.

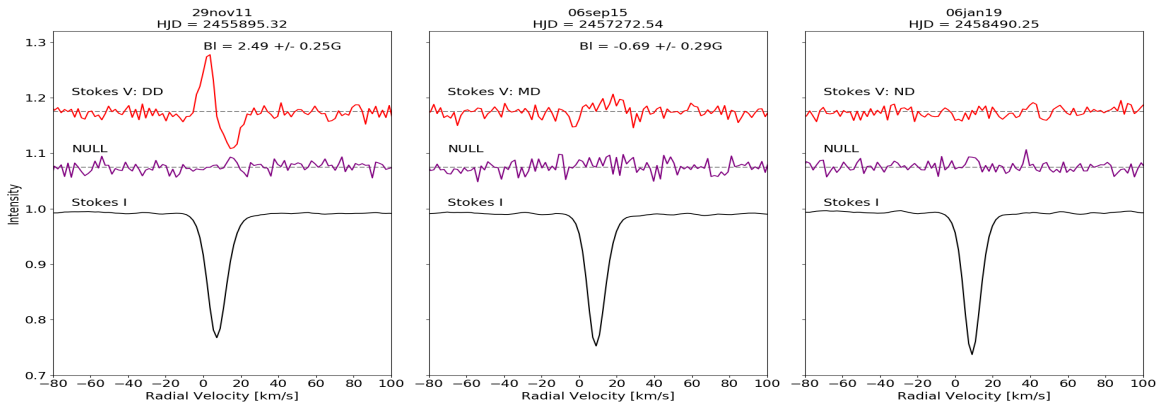


Fig. 4. Example of LSD results from β Peg observations. The result of the statistical test is indicated for each observation and the B_l value is given for the detections.

Figure 5 clearly shows variability in the longitudinal component of the magnetic field, both in strength and polarity. Also, variability in the activity indicators is apparent. The S-, H α - and CaIRT-indices seem to vary together with the magnetic field. This is especially obvious in the first half of our dataset (HJD 2457150 to 2457750) where we have the most detections. We interpret the observed correlation between the B_l and the spectral activity indicators of β Peg as an indication of a magnetic field dominated by large-scale structures. We thus expect the field to have a more simple poloidal geometry.

The V_{rad} shows some variability which could be caused by pulsations, as expected since β Peg is a semiregular variable star.

4.3. Linear polarisation

We observed β Peg in linear polarisation during two nights in 2015: 8 July (HJD = 2457212) and 6 September (HJD = 2457272). For these dates we

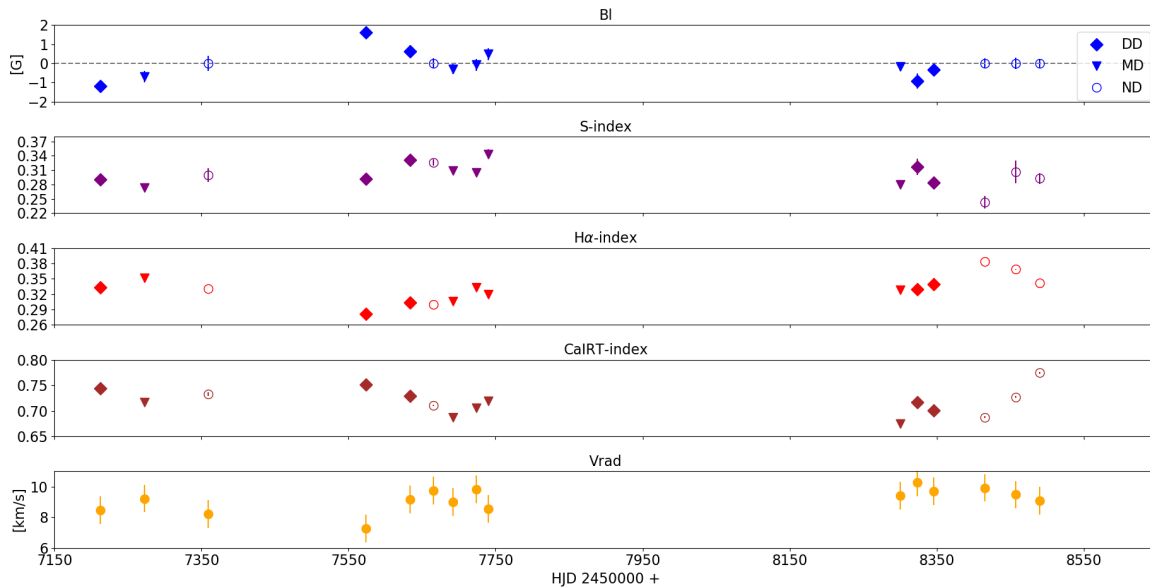


Fig. 5. Magnetic field, spectral activity indicators and radial velocity measurements of β Peg. The different symbols denote the type of detection of circular polarisation.

have both Stokes U and Q measurements. No polarisation signatures were found associated to individual lines, nor to the LSD profiles.

5. Summary

The long-term variability of the active M giants EK Boo and β Peg is studied and presence of magnetic field of variable intensity is observed in both objects. It is stronger in EK Boo, which also has the higher $v \sin i$ (8.5 km/s). Analysis of the behavior of the magnetic field line-of-sight component B_l together with the spectral activity indicators, the CaII H&K, H α and CaIRT lines shows that in the two stars the magnetic field topologies differ: in EK Boo we observe evidences for small-scale magnetic structures, while in β Peg the magnetic field seems to have a more simple dipole structure. Also, in EK Boo we observe a decline of the magnetic activity after January 2016.

We measure a long-term trend in the radial velocity curve of EK Boo, suggesting the existence of a companion. We think that EK Boo is in fact a wide binary system consisting of an M giant main component and a red dwarf companion, the latter being responsible for the high X-ray luminosity of the system. The magnetic variability, on the other hand, should be an intrinsic property of the main component, the giant star.

In terms of stellar evolution, β Peg and EK Boo appear at different evolutionary stages. While β Peg seems to be an early-AGB star of 3.5 solar masses (Konstantinova-Antova et al. 2014), EK Boo is of 2 or 3.6 solar masses and is respectively either at the tip RGB or the beginning of the TP-AGB stage (Konstantinova-Antova et al. 2010). EK Boo has a larger $v \sin i$ and more magnetic field dynamics than β Peg, where the magnetic field and activity indicators behavior presume a more simple, poloidal structure. Whether an $\alpha - \omega$ dynamo or some other kind of dynamo could operate in the conditions

of EK Boo remains an open question and needs a further study. An $\alpha - \omega$ dynamo seems possible in β Peg, taking into account its evolutionary stage and magnetic field behavior.

We detect a definite presence of linear polarisation in EK Boo, while in β Peg no such polarisation is found. The Stokes U & Q signal of EK Boo could in principle be caused by surface brightness inhomogeneities such as giant convective cells (similarly to the case of red supergiant stars). The existence of such giant convective cells would be in agreement with the predictions of stellar evolution theory if we consider EK Boo to be in the beginning of the TP-AGB stage. Determining the origin of net linear polarisation in this star is the aim of future works.

Acknowledgements

We thank the TBL team for proving service observing with Narval. S.G., R.K.-A., R.B., A.L. and A.P. acknowledge partial support by the Bulgarian NSF project DN 18/2, including also observations in semester 2019A. R. K.-A. and A.L. acknowledge partial support under DRILA 01/3. R.K.-A. acknowledges support for the observational time in 2010 by the Bulgarian NSF project DSAB 01/2. The observations in 2008 and 2011 are under an OPTICON program. The observations in 2013 are under financial support by the OP "Human Resources Development", ESF and the Republic of Bulgaria, project BG051PO001-3.3.06-0047. Since 2015 the Narval observations are under the French "Programme National de Physique Stellaire" (PNPS) of CNRS/INSU co-funded by CEA and CNES. N.A.D. acknowledges financial support by Russian Foundation for Basic Research (RFBR) according to the research projects 18-02-00554 and 18-52-06004. This work has made use of the VALD database, operated at Uppsala University, the Institute of Astronomy RAS in Moscow, and the University of Vienna.

References

- Aurière, M. 2003, in *Magnetism and Activity of the Sun and Stars*, eds. J. Arnaud, & N. Meunier, *EAS Publ. Ser.*, 9, 105
- Aurière, M., López Ariste, A., Mathias, P., et al. 2016, *A&A*, 591, A119
- Aurière, M., Konstantinova-Antova, R., Charbonnel, C., et al. 2015, *A&A*, 574, A90
- Borisova, A., Aurière, M., Petit, P., et al. 2016, *A&A*, 591, A57
- Charbonnel, C., Decressin, T., Lagarde, N., et al. 2017 *A&A*, 605, 102
- Donati, J.-F., Semel, M., Carter, B. D., et al. 1997 *MNRAS*, 291, 658
- Duncan, D. K., Vaughan, A. H., Wilson, O. C., et al. 1991, *ApJS*, 76, 383
- Famaey, B. 2005, Radial velocities for 6691 K and M giants, *Catalogue (Famaey)*
- Georgiev, S., Konstantinova-Antova, R., Borisova, A., et al. 2018, *AIP Conf. Proc.*, Vol. 2075, Iss. 1
- Hünsch, M., Schmitt, J. H. M. M., Schröder, K. P., et al. 1998, *A&A*, 330, 225
- Konstantinova-Antova, R., Aurière, M., Charbonnel, C., et al. 2010, *A&A*, 524, A57
- Konstantinova-Antova, R.; Aurière, M.; Petit, P.; Charbonnel, C. et al. 2012, *A&A* 541, A44
- Konstantinova-Antova, R., Aurière, M., Charbonnel, C., et al. 2013, *Bulg. Astron. J.*, 19, 14
- Konstantinova-Antova, R., Aurière, M., Charbonnel, C., et al. 2014, in *Magnetic Fields throughout Stellar Evolution*, eds. P. Petit, M. Jardine, & H. Spruit, *IAUS.*, 302, 373
- Konstantinova-Antova, R., Lèbre, A., Aurière, M., et al. 2018, *PAS "Rudjer Bošković" No 18*, 93-98
- Kupka, F.; Piskunov, N.; Ryabchikova, T. A., et al. 1999, *A&AS*, 138, 119-133
- López Ariste, A., Mathias, P., Tessore, B., et al. 2018, *A&A*, 620, A199
- Mathias, P., Aurière, M., López Ariste, A., et al. 2018, *A&A*, 615, A116
- Rees, D. E., & Semel, M. D. 1979, *A&A*, 74, 1
- Samus N.N., Kazarovets E.V., Durlevich O.V., et al. 2017, *GCVS 5.1, Astronomy Reports*, 2017, vol. 61, No. 1, pp. 80-88
- Tabur, V., et al. 2009, *MNRAS*, 400, 1945T
- Tsvetkova, S., Petit, P., Konstantinova-Antova, R., et al. 2017, *A&A*, 599, A72

Appendix: Log of observations

Date	HJD - 2450000	SNR	σ_{LSD} ($10^{-5} I_c$)	Exposure time	Detection	B_l [G]	σ [G]	S-index	H α -index	CaIRT-index	RV [km/s]
04apr08	4562	1472	1.3	4x400 s	DD	-3.38	0.74	0.242	0.356	0.648	-26.5
05apr08	4563	1358	1.4	4x400 s	DD	-6.41	0.76	0.254	0.361	0.653	-26.5
06apr08	4564	1064	1.9	4x400 s	DD	-6.97	1.01	0.272	0.360	0.655	-26.6
20dec08	4822	1181	1.4	6x400 s	ND	N/A	N/A	0.469	0.408	0.575	-28.1
25feb09	4889	1280	1.1	8x400 s	DD	-0.74	0.61	0.431	0.401	0.578	-27.5
18mar09	4910	904	1.3	8x400 s	DD	-10.20	0.86	0.478	0.401	0.578	-27.3
18jan10	5216	601	3.3	4x400 s	ND	N/A	N/A	0.413	0.372	0.579	-25.7
12feb10	5241	918	2.0	8x400 s	ND	N/A	N/A	0.296	0.393	0.641	-24.8
13mar10	5270	1097	1.4	8x400 s	MD	1.48	0.70	0.322	0.393	0.630	-24.5
15apr10	5303	1281	1.2	8x400 s	MD	-0.80	0.61	0.302	0.376	0.632	-25.2
23apr10	5311	1269	1.3	8x400 s	ND	N/A	N/A	0.281	0.382	0.657	-24.3
22jun10	5370	1223	1.3	8x600 s	ND	N/A	N/A	0.297	0.379	0.657	-23.2
07jul10	5385	1177	1.1	8x400 s	MD	1.76	0.63	0.270	0.384	0.617	-25.4
23jul10	5401	1133	1.3	8x400 s	ND	N/A	N/A	0.296	0.393	0.656	-24.6
17aug10	5426	1095	1.5	8x400 s	ND	N/A	N/A	0.278	0.407	0.684	-23.3
13jan11	5576	721	2.0	8x400 s	ND	N/A	N/A	0.316	0.416	0.672	-24.0
15jan11	5578	1187	1.1	8x400 s	ND	N/A	N/A	0.287	0.415	0.667	-23.8
04feb11	5598	1412	1.0	8x400 s	ND	N/A	N/A	0.259	0.402	0.657	-24.0
18mar11	5640	1015	1.4	8x400 s	ND	N/A	N/A	0.303	0.388	0.641	-25.4
31mar11	5653	763	1.9	8x400 s	ND	N/A	N/A	0.325	0.399	0.678	-24.6
07apr11	5660	1171	1.2	8x400 s	DD	3.25	0.69	0.313	0.395	0.672	-24.4
30apr11	5683	963	1.5	8x400 s	ND	N/A	N/A	0.319	0.369	0.611	-25.7
12may11	5695	1386	1.0	9x400 s	ND	N/A	N/A	0.303	0.361	0.597	-25.9
13jun11	5726	1196	1.2	8x400 s	ND	N/A	N/A	0.307	0.363	0.619	-25.8
01jul11	5744	1223	1.2	8x400 s	ND	N/A	N/A	0.309	0.357	0.597	-25.9
11jul11	5754	1243	1.1	8x400 s	N/A	N/A	N/A	0.316	0.351	0.604	-25.6
20aug11	5794	1167	1.2	8x400 s	N/A	N/A	N/A	0.296	0.337	0.583	-26.5
07jan12	5935	1332	1.2	8x400 s	DD	4.93	0.71	0.320	0.326	0.604	-24.8
24jan12	5952	1290	1.1	8x400 s	MD	2.89	0.66	0.320	0.341	0.612	-24.5
13mar12	6001	1286	1.2	8x400 s	ND	N/A	N/A	0.344	0.361	0.642	-23.5
09may12	6058	799	2.0	8x400 s	ND	N/A	N/A	0.333	0.376	0.658	-23.1
14jun12	6094	754	2.2	8x400 s	ND	N/A	N/A	0.301	0.349	0.607	-23.9
16jul12	6125	1243	1.2	8x400 s	N/A	N/A	N/A	0.259	0.368	0.652	-23.1
17aug12	6157	1031	1.4	8x400 s	N/A	N/A	N/A	0.253	0.355	0.585	-24.2
21mar13	6374	839	2.6	4x400 s	DD	-8.12	1.51	0.281	0.354	0.645	-25.1
21apr13	6405	1011	1.9	4x400 s	DD	-4.96	1.14	0.276	0.350	0.593	-24.0
10jun13	6454	891	2.4	4x400 s	ND	N/A	N/A	0.262	0.371	0.653	-22.4
11aug13	6516	1288	1.6	4x400 s	MD	-3.34	0.91	0.224	0.366	0.624	-23.9
24jan16	7413	968	2.3	4x400 s	ND	N/A	N/A	0.284	0.389	0.628	-21.9
16feb16	7436	1185	1.3	8x400 s	ND	N/A	N/A	0.263	0.399	0.615	-21.8
16mar16	7465	1025	1.5	8x400 s	ND	N/A	N/A	0.259	0.395	0.614	-21.8
13apr18	8223	564	3.3	7x400 s	ND	N/A	N/A	0.287	0.360	0.590	-23.7
05may18	8244	1001	1.6	8x400 s	ND	N/A	N/A	0.228	0.374	0.612	-21.7
14jun18	8284	1153	1.3	8x400 s	ND	N/A	N/A	0.209	0.381	0.559	-21.8
17jul18	8317	1233	1.3	8x400 s	MD	-0.86	0.63	0.202	0.388	0.578	-21.7
07aug18	8338	906	1.8	8x400 s	ND	N/A	N/A	0.224	0.390	0.612	-20.7
27aug18	8358	980	1.7	8x400 s	ND	N/A	N/A	0.246	0.382	0.588	-21.2
14jan19	8499	1088	1.5	8x400 s	ND	N/A	N/A	0.232	0.392	0.683	-21.1
19apr19	8594	882	1.8	8x400 s	MD	1.22	1.02	0.214	0.374	0.660	-22.8

Table 1. Log of observations in circular polarisation of EK Boo. The " σ_{LSD} " column gives the RMS noise level relative to the unpolarised continuum in the LSD profiles. The "Detection" column uses the notation given in Section 2.2. The typical standard deviations of the S-, H α - and CaIRT-index measurements are 0.007, 0.001 and 0.002 respectively. We estimate the error of our RV measurements to be 0.9 km/s. The dates 11jul11, 20aug11, 16jul12 and 17aug12 are affected by the Fresnel rhomb misalignment described in Section 2.3.

Date	HJD - 2450000	SNR	σ_{LSD} ($10^{-5} I_c$)	Exposure time	Detection	B_l [G]	σ [G]	S- index	H α - index	CaIRT- index	RV [km/s]
08jul15	7213	1683	0.7	8x80 s	DD	-1.17	0.22	0.291	0.333	0.744	8.5
06sep15	7273	1138	1.0	8x70 s	MD	-0.69	0.29	0.274	0.351	0.716	9.2
02dec15	7359	798	1.3	8x70 s	ND	N/A	N/A	0.299	0.331	0.733	8.2
03jul16	7574	1604	0.7	8x70 s	DD	1.62	0.22	0.292	0.281	0.752	7.3
01sep16	7633	1271	0.9	8x70 s	DD	0.64	0.31	0.331	0.303	0.729	9.2
03oct16	7665	1317	0.9	8x70 s	ND	N/A	N/A	0.326	0.300	0.710	9.7
30oct16	7692	1294	0.9	8x70 s	MD	-0.28	0.27	0.309	0.306	0.687	9.1
01dec16	7724	1155	1.0	8x70 s	MD	-0.08	0.31	0.304	0.333	0.706	9.8
17dec16	7740	1049	0.9	8x70 s	MD	0.48	0.30	0.344	0.319	0.720	8.5
30jun18	8301	1361	0.9	8x80 s	MD	-0.16	0.24	0.280	0.328	0.674	9.4
23jul18	8324	1062	1.2	8x80 s	DD	-0.92	0.39	0.317	0.329	0.717	10.3
14aug18	8346	1477	0.7	8x80 s	DD	-0.32	0.26	0.283	0.339	0.701	9.7
23oct18	8416	1388	0.9	8x80 s	ND	N/A	N/A	0.243	0.384	0.688	9.9
04dec18	8457	1188	1.1	7x80 s	ND	N/A	N/A	0.306	0.368	0.727	9.5
06jan19	8490	1597	0.8	8x80 s	ND	N/A	N/A	0.293	0.342	0.774	9.1

Table 2. Log of observations in circular polarisation of β Peg. The " σ_{LSD} " column gives the RMS noise level relative to the unpolarised continuum in the LSD profiles. The "Detection" column uses the notation given in Section 2.2. The typical standard deviations of the S-, H α - and CaIRT-index measurements are 0.009, 0.001 and 0.002 respectively. We estimate the error of our RV measurements to be 0.9 km/s.

Surface magnetism in the post-AGB star R Scti

In this Chapter, I will present my study of the surface magnetic field in the post-AGB star R Sct, and its possible connection with the dynamics present in the atmosphere of the star. I will begin with a short introduction of the target star, followed by a description of the observations used. I will then address the need to use different line masks for the computation of the LSD profiles of different observations. Following this, I will explore the Stokes V signatures obtained from the basic LSD procedure to make certain of their Zeeman origin and to determine their typical timescale of variation. Next, I will follow the atmospheric dynamics of R Sct by analyzing the variability of individual spectral atomic lines. After that, I will present a refined approach for the application of LSD to study surface magnetic fields in the case of stars with extended atmospheres such as R Sct. I will then briefly present the LSD profiles of R Sct in linear polarization, and give a summary of the study.

Summary

4.1	Introduction	115
4.2	Observations and data treatment	116
4.2.1	Observations	116
4.2.2	LSD line masks	119
4.3	The surface magnetic field	122
4.3.1	The origin of circular polarization	124
4.3.2	Timescales of variation	125
4.4	Atmospheric dynamics	125
4.4.1	Variability of the $H\alpha$ line	126
4.4.2	The Schwarzschild mechanism	128
4.4.3	Variability of metallic lines	128
4.4.4	Atmospheric dynamics: summary	130

4.5	The surface magnetic field: a refined approach	132
4.5.1	Line selection by excitation potential	134
4.5.2	Magnetism at the photospheric level	138
4.6	Linear polarization	142
4.7	Summary	142

4.1 Introduction

RV Tauri stars are high luminosity pulsating variables. Their lightcurves show alternating deep and shallow minima in a quasi-periodic manner, the periodicity being sometimes interrupted by irregular intervals which is of physical origin and not due to the seasons the star is not observable. During regular parts of the lightcurve, the photometric variability period P is defined as the time interval between two consecutive deep minima. The values of P are usually between 30 and 150 d (Wallerstein & Cox, 1984). Jura (1986) studied the mass loss rates of RV Tauri stars and concluded that these objects have recently left an evolutionary phase of rapid mass loss, and considering their luminosities ($\sim 10^3 L_\odot$) and formation rate (roughly $6 \times 10^{-4} \text{ kpc}^{-3} \text{ yr}^{-1}$, about 0.1 of the rate of formation of PNe), proposed that they are post-AGB objects in transition from the Asymptotic Giant Branch to the White Dwarf stage.

R Sct (HD 173819) is the brightest member of the RV Tauri type stars. According to the General Catalogue of Variable Stars (GCVS¹), at maximum luminosity its visual magnitude is ≈ 4.2 , while during a deep photometric minimum it is ≈ 8.6 , and its photometric variability period is between 138.5 and 146.5 d. Because of the strong photometric variability R Sct exhibits, its spectral class also varies significantly: from G0 Iae during maximum to K2p(M3) Ibe during deep minimum. Kipper & Klochkova (2013) measure for R Sct the following values of the stellar parameters: $T_{\text{eff}} = 4500 \text{ K}$, $\log g = 0.0$, $[\text{Fe}/\text{H}] = -0.5$. These values are estimated from observations taken during the phases of shallow minimum and just after a maximum in the lightcurve.

During each photometric period, two accelerations of the atmospheric layers occur that are caused by radiative shockwaves (Gillet et al., 1989). Lèbre & Gillet (1991a,b) find that the expansion of the atmosphere due to the passing of shockwaves may reach up to a few photospheric radii by studying the variability of spectral lines. The propagation of these shocks produces significant ballistic motions in the atmosphere, which can be traced through dedicated spectral features, such as splitting of metallic lines and emission in the lines of hydrogen. These studies also show that the two shockwaves – main and secondary one – appear respectively just before the deep and shallow minimum, and that they may both be present at the same time in the extended atmosphere of R Sct. The authors also point out that these complex atmospheric dynamics may be at the origin of the mass loss the star experiences at this late evolutionary stage.

The first discovery of a surface magnetic field in R Sct is reported by Lèbre et al. (2015), who estimate the longitudinal magnetic field $B_l = 0.9 \pm 0.6 \text{ G}$. Sabin et al. (2015) find that the magnetic field of R Sct is variable with time, sometimes being not present or below their detection limit. They also observe a connection between the spectral line profiles which trace the propagation of radiative shockwaves (see Section 4.4) and the Zeeman signatures in circular polarization, and on this basis suggest there could be a

¹<http://www.sai.msu.su/gcvs/gcvs/>

link between the dynamical state of the extended stellar atmosphere and the magnetic field. Such a link has already been proposed for the pulsating variable Mira star χ Cyg (Lèbre et al., 2014), where the propagation of shock wave through the atmosphere seems to amplify through compression the present weak surface magnetic field.

My objective in this Thesis is to continue the study of surface magnetism in R Sct in order to check if there is indeed an interplay between the surface magnetic field and the atmospheric dynamics present in this cool evolved star.

In the present Chapter, Section 4.2 presents the Narval observations used for the study of R Sct. In Section 4.3, the classical analysis of the Stokes V profiles obtained using LSD is done. The atmospheric dynamics of R Sct is briefly illustrated from our Narval observations in Section 4.4. In Section 4.5, I present a refined approach for the study of surface magnetism in such pulsating stars with extended atmospheres, and apply it to the case of R Sct. Section 4.6 presents briefly the observations of R Sct in linear polarization. Finally, in Section 4.7, a summary of the obtained results is given.

4.2 Observations and data treatment

4.2.1 Observations

Observations of R Sct were obtained between July 2014 and August 2019 using Narval. This is the longest monitoring of R Sct using high resolution spectropolarimetry so far. It corresponds to 6 seasons of observability of R Sct, which will hereafter be referred to as 6 datasets, from set 1 to set 6. Each observation consists of measurements of both linear (Stokes Q and U) and circular (Stokes V) polarization, taken either in a single night or during consecutive nights, depending on the observational conditions. The total dataset spans over 67 different dates of observation, 31 of which contain Stokes V measurements, giving access to information about the surface magnetism. The observations which contain measurements on linear polarization are presented in Section 4.6, but the Stokes Q and U data are not exploited in this study; instead, only the high resolution unpolarized spectra (Stokes I) are used to trace the atmospheric conditions. The full log of observations is given in Table 4.1. Unfortunately, the dataset is limited to end-August 2019 due to the shutting down of Narval and its transition to NeoNarval.

In order to correlate the information on the atmospheric dynamics and the magnetic field obtained from Narval observations to the photometric variability of R Sct, the visual lightcurve of the star was retrieved from the AAVSO² database. The AAVSO visual lightcurve of R Sct is shown in Figure 4.1. The dates for which observations with Narval are obtained are marked on the lightcurve with blue and green vertical lines for circular and linear polarization, respectively.

²<https://www.aavso.org/>

Date	HJD	Phase	Sequences	Date	HJD	Phase	Sequences
2014/07/15	6854.5	0.576	1Q,1U,2V	2016/10/27	7689.3	6.476	1U
2014/07/22	6861.4	0.625	10V	2016/10/28	7690.3	6.483	2Q
2014/09/01 [‡]	6902.3	0.914	1Q,1U	2017/04/18	7862.6	7.700	9V
2014/09/02 [‡]	6903.3	0.921	6V	2017/04/20	7864.6	7.714	2U
2014/09/11 [‡]	6912.3	0.984	1Q,6V,1U	2017/04/21	7865.6	7.722	2Q
2015/04/13	7126.6	2.499	3V	2017/08/21 [‡]	7987.4	–	6V
2015/04/14	7127.6	2.506	1Q,1U	2017/08/22 [‡]	7988.4	–	2Q
2015/04/23	7136.6	2.570	2V	2017/09/02	7999.4	–	4Q
2015/05/27	7170.5	2.809	3V,1Q,1U	2017/09/06	8003.3	–	2Q
2015/06/02	7176.6	2.852	9V	2017/09/07	8004.3	–	2U
2015/06/26 [‡]	7200.5	3.021	2U,2Q,9V	2017/09/08	8005.3	–	3V
2015/08/05	7240.4	3.303	2Q,2U	2017/10/02 [‡]	8029.3	–	2U
2015/08/06	7241.9	3.314	16V	2017/10/04 [‡]	8031.3	–	2Q
2015/08/10	7245.4	3.339	6V	2017/10/05 [‡]	8032.3	–	3V
2015/08/26 [‡]	7261.4	3.452	2Q	2017/10/30 [‡]	8057.3	–	2U
2015/08/28 [‡]	7263.4	3.466	2U,6V	2017/10/31 [‡]	8058.2	–	2Q
2015/10/08	7304.3	3.755	1Q,1U	2017/11/01 [‡]	8059.8	–	9V
2015/10/09	7305.3	3.762	6V	2018/06/18	8288.5	0.058	2U,2Q
2015/10/29	7325.3	3.903	1Q,1U	2018/06/19	8289.5	0.064	3V
2015/10/30	7326.3	3.910	5V	2018/07/27	8327.5	0.322	2U,2Q
2016/03/17 [‡]	7465.6	4.895	1U,1Q	2018/07/28	8328.5	0.329	3V
2016/05/04	7513.6	5.234	1U,1Q	2018/08/15	8346.5	0.451	2Q,2U
2016/05/15	7524.6	5.312	3V	2018/08/31	8362.4	0.559	2Q,2U
2016/05/20	7529.6	5.347	3V	2018/09/08	8370.4	0.614	3V
2016/06/02	7542.6	5.439	1U,1Q	2018/10/24 [‡]	8416.3	0.925	2Q
2016/06/22	7562.5	5.580	1U,1Q	2018/10/25 [‡]	8417.3	0.932	2U
2016/07/12	7582.5	5.721	1U,1Q	2019/06/15	8650.5	2.515	3V,2Q
2016/07/24	7594.4	5.805	3V	2019/06/27	8662.5	2.596	3V
2016/08/03	7604.4	5.876	1U,1Q	2019/07/15	8680.4	2.718	2Q,2U
2016/09/01	7633.3	6.080	1Q,1U	2019/07/18	8683.5	2.739	3V
2016/09/24	7656.4	6.243	1Q	2019/08/05	8701.5	2.861	2U
2016/09/28	7660.3	6.271	3V,1U	2019/08/13	8709.4	2.915	2Q
2016/10/03	7665.3	6.306	3V	2019/08/31 [‡]	8727.4	3.037	6V
2016/10/21	7683.3	6.433	1Q,1U				

Table 4.1: Log of spectropolarimetric observations. Calendar and heliocentric Julian dates (HJD) are given in the first two columns. HJD starts from 2 450 000. The horizontal lines show the limits of the 6 observational sets described in Section 4.2.1. The phase (calculated according to Equations 1 or 2) is given in the third column. The fourth column indicates the number of Stokes $Q/U/V$ sequences collected for each date. The dates for which the "cool" mask is used are marked with [‡], and for the rest, the standard mask is used (see Section 4.2.2).

During the first part of the observational dataset, between April 2014 (HJD = 2 456 773) and June 2016 (HJD = 2 457 905), the lightcurve of R Sct appears regular (showing the usual alteration of deep and shallow minima). However, after this, the next expected deep minimum appears shallow instead, and after that the periodicity is lost. It is restored again in June 2019 (HJD 2 458 905). The limits of the irregular portion of the lightcurve between June 2016 and June 2019 are marked on Figure 4.1 with dashed red vertical lines.

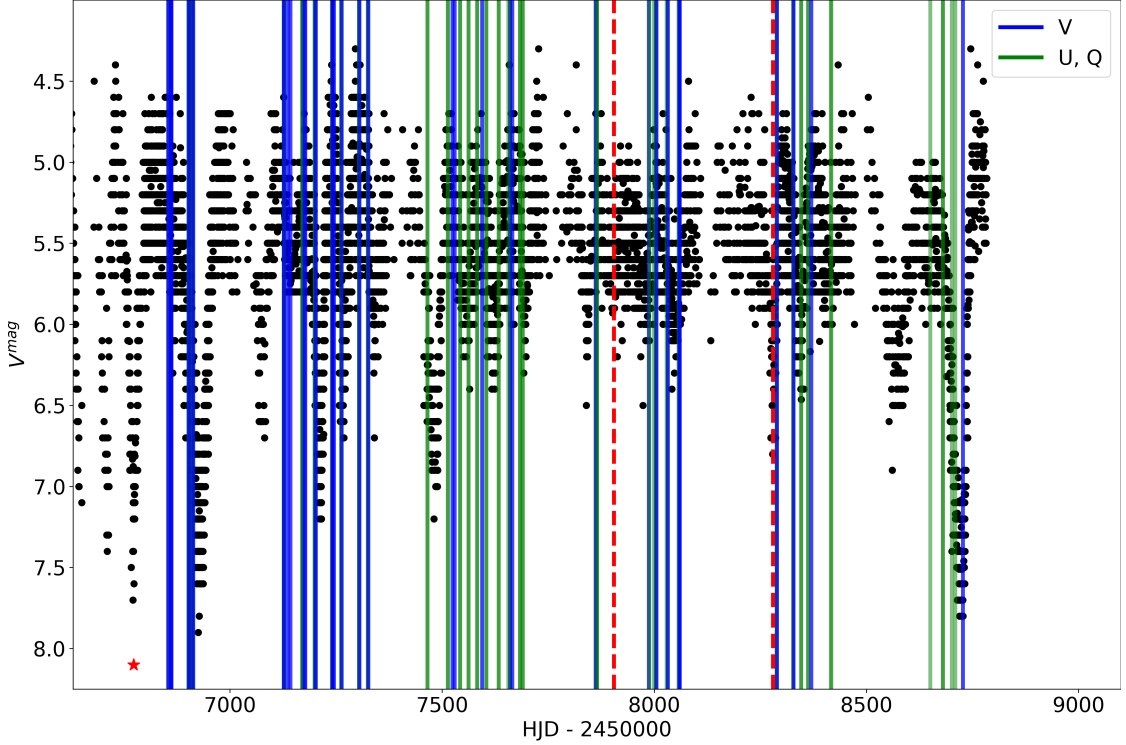


Figure 4.1: Visual lightcurve of R Sct from AAVSO. The dates of spectropolarimetric observations (see Table 4.1) are indicated by vertical lines (blue and green lines for the circular and linear polarization observations, respectively). The limits of the irregular interval of photometric variability (see Section 4.2.1) are denoted by the dashed red lines. The red star shows the date which I choose to be the beginning of period 0 in the first phase computation (see Equation 4.1); the beginning of period 0 in the second phase computation (see Equation 4.2) is the right vertical dashed line, i.e. the date the regularity of the lightcurve is restored.

The photometric period of R Sct, when it is apparent (i.e. outside the irregular portion of the lightcurve) is variable from one cycle to the next. I find that the average period length in the first regular part of the observational dataset is 141.50 d, and in the second (after the irregular portion) it is 147.33 d. Using these periods, I compute the

photometric phase according to the following ephemerids:

$$\text{HJD (minimum light I)} = 2456773 + 141.50E \quad (4.1)$$

$$\text{HJD (minimum light I)} = 2458280 + 147.33E \quad (4.2)$$

I use Equation 4.1 for the first regular portion of the lightcurve (in Figure 4.1: between the red star and the first vertical dashed red line) and Equation 4.2 for the second one (in Figure 4.1: after the second vertical dashed red line).

4.2.2 LSD line masks

In order to extract the mean circular polarization signatures from the data, I used the LSD method. In the course of its photometric variability, R Sct changes significantly not only its visual magnitude, but also its spectral type, hence its effective temperature T_{eff} . From the literature it is known that during a shallow luminosity minimum and around a maximum, the effective temperature of the star is 4500 K. However, this cannot always be the case, since the spectral type changes to a much later one near a deep minimum, suggesting a lower effective temperature. The available Narval observations also show that close to a deep minimum, TiO molecular bands appear in the spectrum of R Sct, indicating a significant decrease in T_{eff} . This means that using a single LSD mask computed with a unique effective temperature to treat the whole dataset may not be the best approach. A more reliable result would be obtained if, instead, the observations obtained around a deep minimum (and showing these TiO band features) are treated using an LSD mask computed for another (lower) effective temperature, one which is closer to that of the star at this photometric stage.

To estimate the effective temperature of R Sct during a deep luminosity minimum, I used *Turbospectrum* (see Section 1.5 of Chapter 3) to construct a series of synthetic spectra around two molecular bands of TiO (TiO 7054 Å and TiO 7589 Å) which are present in the spectrum of R Sct during times of photometric deep minimum. To construct the synthetic spectra, I used linelists extracted from the VALD database and MARCS model atmospheres computed for $1M_{\odot}$, $\log g = 0.0$, microturbulence of 2 km s^{-1} and $T_{\text{eff}} = 4500, 3800, 3600, 3400$ and 3200 K . I used the built-in procedure in *Turbospectrum* to take into account the instrumental profile of Narval. After that, I had to introduce the effects of rotational and macroturbulent velocities. Neither value is known for R Sct, and due to the spectroscopic variability of the star (see Section 4.4), estimating $v \sin i$ and v_{mac} using the method presented in Section 1.5 of Chapter 3 would be very inaccurate. I assigned to $v \sin i$ and v_{mac} the *ad hoc* values of 5 and 2 km s^{-1} which are reasonable for AGB and post-AGB stars. It must be noted that there is no particular reason to pick these exact values, and that they have no impact on the task at hand. My goal was not to determine velocities, but instead only to give a rough estimation of T_{eff} ; for this purpose, any reasonable pair of the two velocities would suffice.

Having computed the synthetic spectra, I compared them to four observational spectra of R Sct, obtained on 2015/04/23 (corresponding to a shallow minimum), 2014/09/11, 2017/11/01 (both taken close to a deep minimum) and 2019/08/31 (taken at the exact time of a deep minimum). This comparison is shown in Figure 4.2. It can be seen from the synthetic spectra that the 7054 Å TiO band (upper panel) begins to develop only at temperatures below 3800 K. On the other hand, this band is present in the observations during times of deep minimum, but not during a shallow minimum. This is consistent with the 4500 K estimation Kipper & Klochkova (2013) obtain for the shallow minimum and maximum phases. The synthetic spectra also show that the band continues to develop in both depth and width as temperature decreases until $T_{\text{eff}} = 3400$ K. Further decreasing the temperature makes the band more shallow instead. The 7589 Å TiO band (lower panel) is again only present in observations obtained around a deep minimum, being most developed on 2019/08/31 (obtained at the exact time of a deep minimum). In the synthetic spectra, this band is not present at 4500 K and even at 3800 K. It begins to develop only at 3600 K and grows in depth and width as temperature decreases, reaching maximum depth in the 3200 K spectrum. We can draw two certain conclusions from this: 1) during a shallow luminosity minimum, the effective temperature of R Sct is above 3800 K, in good agreement with the measurements of Kipper & Klochkova (2013); 2) during a deep minimum, the effective temperature is below 3800 K, since both TiO bands are present in the spectrum.

Before drawing any further conclusions however, it must be kept in mind that there are two factors which prevent a precise determination of T_{eff} : the first and most important one is the imperfect normalization to the continuum in the observations; the second and less important one are the *ad hoc* values assigned to $v \sin i$ and v_{mac} in the making of the synthetic spectra. Because of these factors, any further constraint on the effective temperature will only be a rough one. With that being said, in the three observations taken around a deep minimum, the two TiO bands appear to be best described by the synthetic spectra computed for 3400 and 3600 K. For this reason, I decided to perform LSD in the following manner:

- For all observations in which TiO bands are not present, i.e. except those obtained close to a deep minimum - using a mask computed for $T_{\text{eff}} = 4500$ K (henceforth, the *standard* mask);
- For the observations in which TiO bands are present, i.e. those obtained close to a deep minimum - using a mask computed for $T_{\text{eff}} = 3500$ K (henceforth, the *cool* mask).

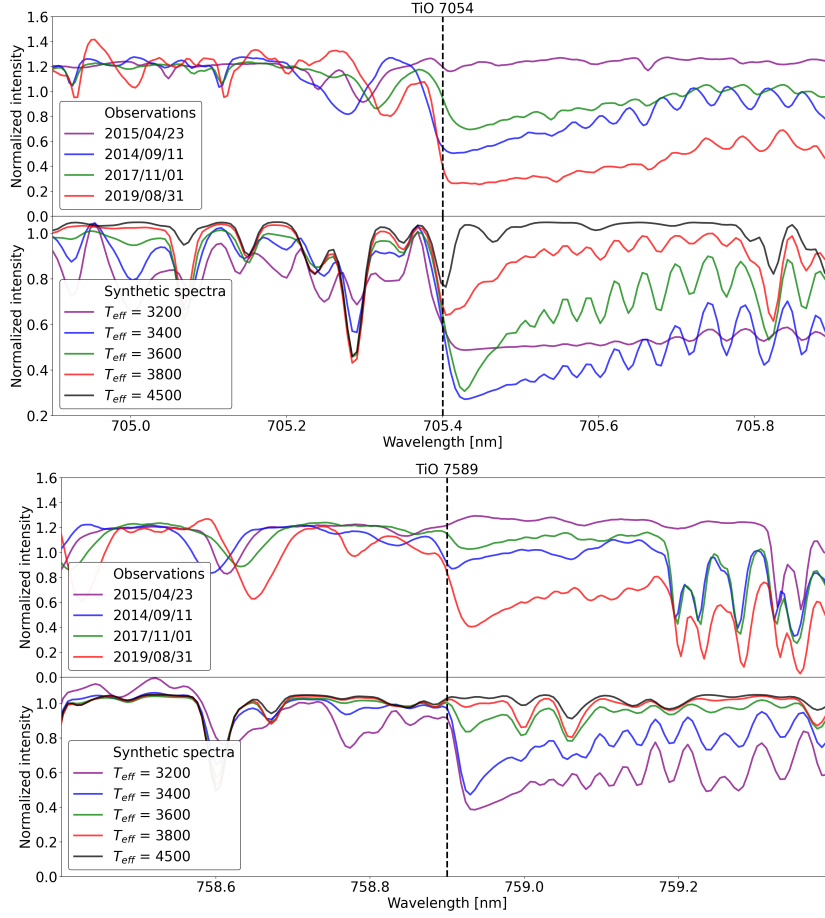


Figure 4.2: TiO 7054 Å (upper panel) and TiO 7589 Å (lower panel) bands in the spectrum of R Set. For each band, the top subpanel shows four observed spectra, obtained on 2015/04/23 (corresponding to a shallow minimum), 2014/09/11, 2017/11/01 (both taken around a deep minimum) and 2019/08/31 (corresponding to the exact time of a deep minimum). The bottom subpanels show synthetic spectra computed for different values of T_{eff} .

A last justification for the use of the "cool" line mask is that even if it does not perfectly reflect the effective temperature of R Set during a deep minimum, it certainly gives a better approximation than the "standard" mask does. The other stellar parameters the two masks were computed for (from MARCS model atmospheres) are $\log g = 0.0$, microturbulence of 2 km s^{-1} and $[\text{Fe}/\text{H}] = -0.5$, in agreement with Kipper & Klochkova (2013). As in the study of M giants presented in Chapter 3, linelists extracted from the VALD database were used, and the lines of the elements H, He, Ca, Na and K were removed from the two line masks to avoid contamination from the very high atmosphere, the circumstellar envelope and the interstellar medium. The total number of lines in each of the two masks is approximately 17 000.

As we shall see in Section 4.5, the selection of lines in the LSD mask can be further constrained in order to trace only the contribution of the photosphere.

4.3 The surface magnetic field

I applied the LSD method to the Narval observations of R Sct in circular polarization in order to extract the mean polarized signatures and trace the surface magnetic field. The resulting LSD profiles are shown in Figure 4.3. It can be seen in this figure that Stokes V signatures are often found in the spectrum of R Sct, and that they present variations in both shape and position relative to the rest frame velocity of the star $v_{\text{rad}} = 42.47 \text{ km s}^{-1}$ (Kunder et al., 2017), indicated with a dashed vertical black line. When present, the mean Stokes V signatures are typically weak, on the order of 5×10^{-5} the intensity of the unpolarized continuum. Signatures can be seen for example in July and September 2014, in April and August 2015, in May 2016 and in June 2018. In some observations however, there is no trace of a Stokes V signature, for example in June and October 2015 and in April and August 2017.

Figure 4.3 shows that the LSD Stokes I profiles of R Sct also present significant variability with time, both in shape and position. In some observations, the Stokes I profile appears single and redshifted with respect to the stellar restframe velocity (e.g. 2015/08/28), while in others it is again single but blueshifted (e.g. 2015/10/09), and other times it clearly displays a double-peak structure (e.g. 2017/04/18). We will see in Section 4.4 that this variability is caused by the atmospheric dynamics and traces shockwaves propagating through the atmosphere of R Sct.

In Figure 4.3 it can also be seen that always when the mean intensity profile has a double-peak structure, the Stokes V signatures (if present) are centered on its blueshifted lobe, e.g. on 2014/07/22, 2016/05/20, 2018/06/19. This effect was already reported for R Sct by Sabin et al. (2015), who interpret it as the magnetic field being associated to the radially outward moving material which is being lifted and compressed by a passing shock wave. The same trend was reported for the Mira star χ Cyg by Lèbre et al. (2014), who suggest that the shock in χ Cyg amplifies a very weak surface magnetic field, through a compression effect. It is also because of this behaviour of the Stokes V profile that the statistical test which is commonly used to determine the type of detection of polarized signatures (see Section 3.2 of Chapter 2) was not used for the observations of R Sct, since it takes into account the whole span of the Stokes I profile (i.e. both lobes). For the observations where the Stokes V signature is clearly only associated to the blueshifted lobe, the noise associated to the redshifted one would deteriorate the determination of the type of detection.

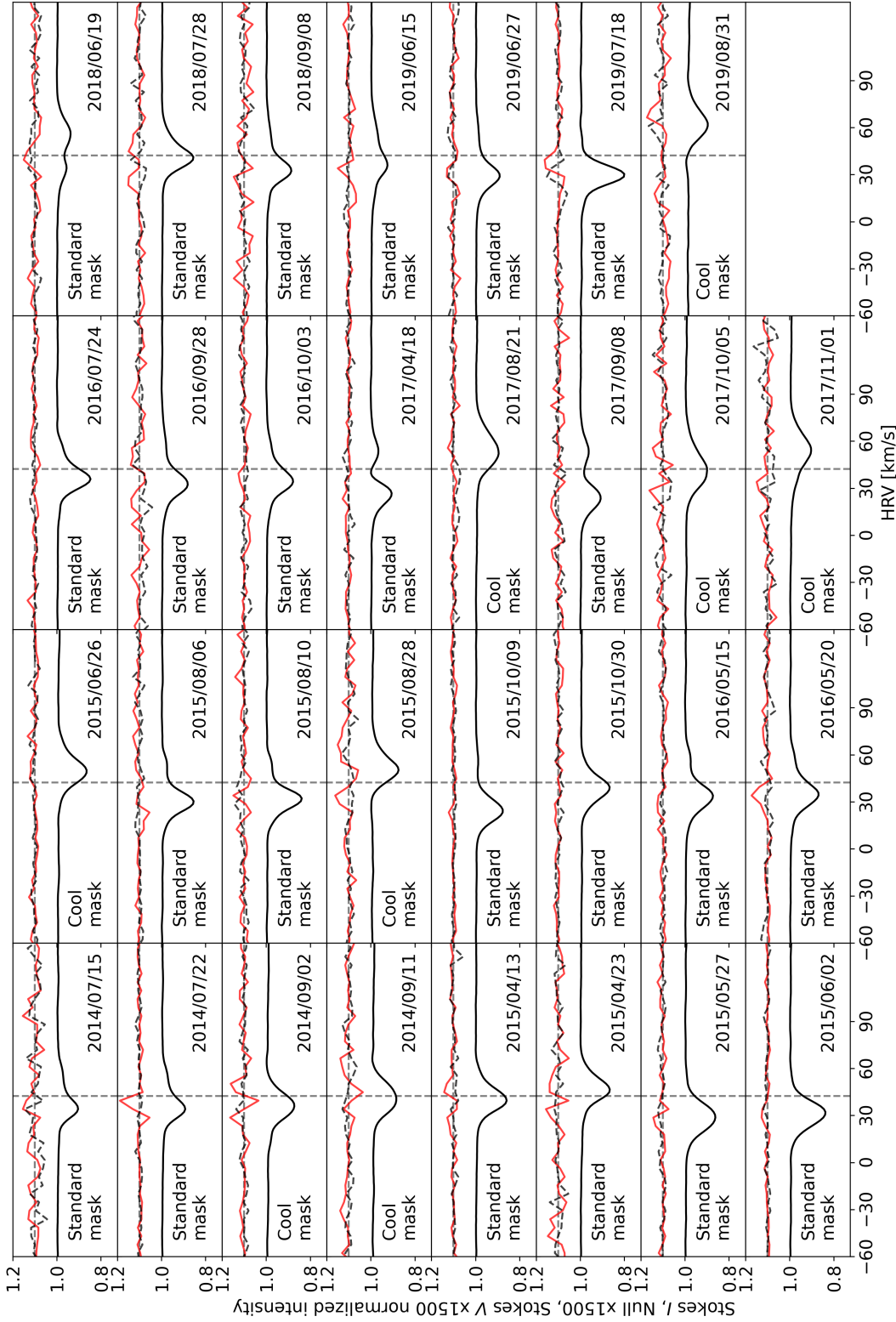


Figure 4.3: LSD profiles of R Sct in circular polarization. Each observation is shown in a separate panel with the date and the mask used indicated respectively at the bottom right and bottom left. The intensity profiles are shown as solid black lines, the null profiles - as dashed black lines and the Stokes V profiles - as solid red lines. The null and Stokes V profiles are amplified as indicated on the label of the y-axis, shifted vertically and smoothed by averaging every three pixels for display purposes, and their zero level is indicated by a dashed horizontal gray line. For each observation, the radial velocity of the star $v_{\text{rad}} = 42.47 \text{ km s}^{-1}$ (Kunder et al., 2017) is indicated with a dashed vertical gray line.

4.3.1 The origin of circular polarization

To investigate if the detected Stokes V profiles are of stellar origin and not due to a cross-talk between linear and circular polarization, I compared the linearly polarized LSD profiles to the circularly polarized ones for those dates of observation when both are available. Indeed, the Narval observations of R Sct show linear polarization with amplitudes on the order of 3×10^{-4} the level of the unpolarized continuum (see Section 4.6). However, I found no similarities between the LSD profiles (their peak positions, width and shape) in Stokes Q and U and those in Stokes V taken in the same night or in consecutive nights, which shows that there is no cross-talk involved in the formation of the circularly polarized signatures. I thus conclude that the detected Stokes V signatures are of stellar origin.

Next, to test if the Stokes V signal found in the LSD profiles of R Sct is due to the Zeeman effect, I performed three tests using LSD with different line masks, as it has been proposed by Mathias et al. (2018). The tests aimed to check if:

1. Spectral lines with high effective Landé factors g_{eff} show stronger Stokes V signatures than those with low g_{eff} ;
2. Deep spectral lines show stronger Stokes V signatures than shallow ones do;
3. Spectral lines formed at longer wavelengths show stronger Stokes V signatures than those formed at shorter wavelengths.

To perform the first test, I split each of the two line masks ("standard" and "cool" one) into two sub-masks of high and low g_{eff} using the median value $g_{\text{eff}} = 1.2$ as the division limit. For the observations where a Stokes V signature was already found using the full mask ("standard" or "cool" one), I applied the LSD process using the respective "standard" or "cool" sub-masks for high and low g_{eff} and then compared the results. I found that the degree of circular polarization is indeed stronger for lines with high g_{eff} . I performed the other two tests in a similar manner, using the median values of line depth and wavelength as division limits – 0.66 and 446 nm, respectively. The line depth test also showed that deeper lines are more strongly polarized in Stokes V than shallow ones, which according to Mathias et al. (2018) favours the Zeeman origin of the circularly polarized signal. However, the wavelength test was inconclusive as it did not yield any well-defined circularly polarized signatures. Examples of the results of the tests are shown in Figure 4.4.

Based on these results and considering that the circularly polarized signals are of stellar origin, I conclude that the observed Stokes V profiles are of Zeeman origin and they show the presence of a surface magnetic field in R Sct.

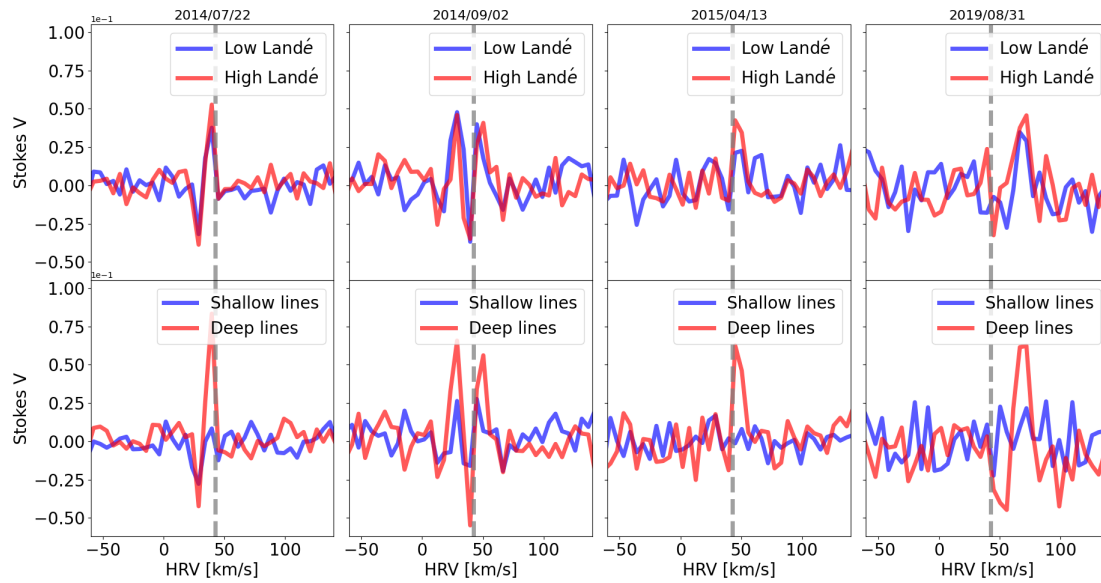


Figure 4.4: Comparison of a sample of LSD profiles of R Sct computed with two different sub-masks to test the Zeeman origin of the Stokes V signal (see Section 4.3.1). Each column represents a single date of observation: 2014/07/22 is obtained just after a maximum visual brightness, 2014/09/02 corresponds to a deep minimum, 2015/04/13 is obtained between a maximum and a shallow minimum and 2019/08/31 corresponds to a deep minimum.

4.3.2 Timescales of variation

From Figure 4.3, a rough estimation can be made of the typical timescale of Stokes V variability. Let us consider the data from 2015. There, a signal appears to be present in the beginning of April, which is not visible in May and June. It then reappears in August and vanishes again in October. From this variation, a rough timescale of 2-3 months can be deduced. This timescale does not contradict the rest of the dataset: for example the two observations of September 2014 show that the Stokes V signal may persist for at least one week, while on the other hand, it obviously changes quicker than on timescales ≥ 1 yr.

4.4 Atmospheric dynamics

The first qualitative model of the pulsation of the photosphere of R Sct was introduced by Gillet et al. (1989). From spectroscopic observations, these authors reported that two shockwaves propagate throughout the stellar atmosphere per pulsation period (defined as the time between two consecutive deep photometric minima). The first (main) shockwave is found to emerge from the photosphere just before the phase of deep photometric minimum (around $\phi = 0$). This main shock is supposed to produce a large elevation of

the atmosphere, followed by a subsequent infalling motion due to the force of gravity (ballistic motion). A secondary (and weaker) shockwave emerges from the photosphere just before the occurrence of a shallow photometric minimum (around $\phi = 0.5$), while the main shock is vanishing in the upper atmosphere.

This work was extended by Lèbre & Gillet (1991a,b) who investigated the profile variations of selected spectral lines which turned out to be good indicators of the motions at the photospheric level and of ballistic motions in the upper atmosphere. These lines include $H\alpha$, several FeI lines and TiI 5866 Å. In the spectrum of R Sct, the $H\alpha$ line shows an emission component which varies in strength along the photometric phase.

4.4.1 Variability of the $H\alpha$ line

Figure 4.5 shows the profile variation of the $H\alpha$ line along the complete observational dataset. It can be seen in this figure that $H\alpha$ shows a variable profile which consists of an absorption component, usually redshifted with respect to the restframe velocity of the star, and an emission component with variable amplitude, which is blueshifted with respect to the restframe velocity of R Sct. It can be seen that the apparition of the main shockwave from the photosphere around phase $\phi = 0$ (around a deep photometric minimum) usually results in a strong $H\alpha$ emission component (e.g. on 2015/10/29 and 2015/10/30, before the minimum on 2015/11/13; on 2016/03/17, before the minimum on 2016/04/02). This is in agreement with the work of Gillet et al. (1989), who present the complex $H\alpha$ profile as a full emission originating from the front region of a radiative shock wave, where the temperature and pressure conditions are favorable to produce an emission line; then the cool hydrogen (either static or relaxing) located above the shock front introduces an absorption component to the central and/or redshifted part of the line. The secondary shock is also detectable through the $H\alpha$ emission around phase $\phi = 0.5$ (around a shallow photometric minimum). This emission feature then decreases until a new strong emission occurs due to the emergence of a new main shock. A few dates (2014/07/22, 2015/06/26, 2016/10/27-28, 2017/11/01) show a very faint $H\alpha$ emission, illustrating the few moments when the atmosphere is relaxing in a global infalling motion.

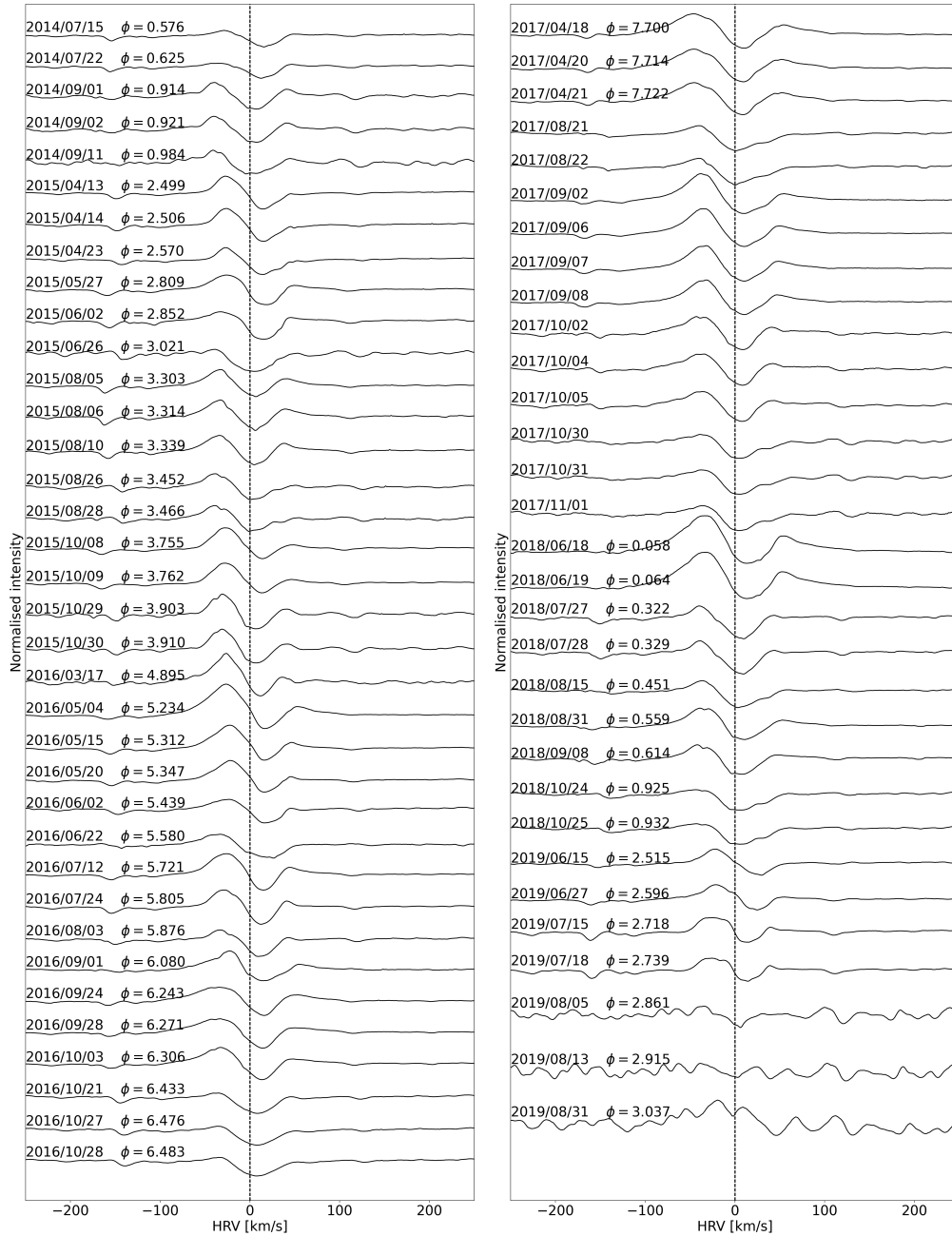


Figure 4.5: Time variation of the $H\alpha$ line profile in the spectrum of R Sct. Each observation is shifted vertically for display purposes, and its date is indicated on the left. The restframe velocity of R Sct is indicated with a vertical dashed line. For the observations which have a phase assigned to them following Equations 4.1 and 4.2, the phase is also noted. It can be seen that during the two regular portions of the lightcurve, the emission component of $H\alpha$ is usually strongest close to and before phases $\phi = 0$ and $\phi = 0.5$, corresponding respectively to times of deep and shallow photometric minimum.

4.4.2 The Schwarzschild mechanism

Atomic lines of elements such as Fe and Ti also display profiles that vary with the photometric phase, being either fully blueshifted, double-peaked or fully redshifted. To explain this behaviour, in this Thesis I will refer to the Schwarzschild mechanism.

Schwarzschild (1975) proposed a mechanism to explain the observed doubling of atomic spectral lines in pulsating stars. According to this explanation, the passing of a shock wave through the stellar atmosphere first makes the layers closest to the photosphere move upwards (towards the observer), thus causing the spectral lines formed in these layers to be blueshifted; after the shock has passed, the same layers fall ballistically downwards (away from the observer), thus causing the spectral lines to be redshifted.

This is illustrated in Figure 4.6. When integrated over the entire atmosphere, this effect yields:

- a fully redshifted spectral profile (t_1), if the entire layer of line formation is moving downwards after the passage of a previous shock and before the arrival of a next one;
- a fully blueshifted spectral profile (t_4 in Figure 4.6), if the entire layer of line formation is moving upwards;
- a double-peak split profile (t_3 and t_2), if some parts of the layer of line formation are moving upwards and some are moving downwards.

This basic scenario may be more complicated in the case of a very extended atmosphere, where the imprints of two consecutive shockwaves may be present at the same time in atomic lines, as it has been shown to be the case for R Sct by Lèbre & Gillet (1991b) (from the lines of the sodium doublet).

4.4.3 Variability of metallic lines

To study the motions in the atmosphere of R Sct during the longest high resolution spectropolarimetric monitoring ever realized, I will use two atomic lines: FeI 6569 Å and TiI 5866 Å. Lèbre & Gillet (1991a) showed that the FeI 6569 Å line is formed in the lower part of the atmosphere of R Sct, very close to the photosphere, while on the other hand the TiI 5866 Å line is formed in the upper atmosphere.

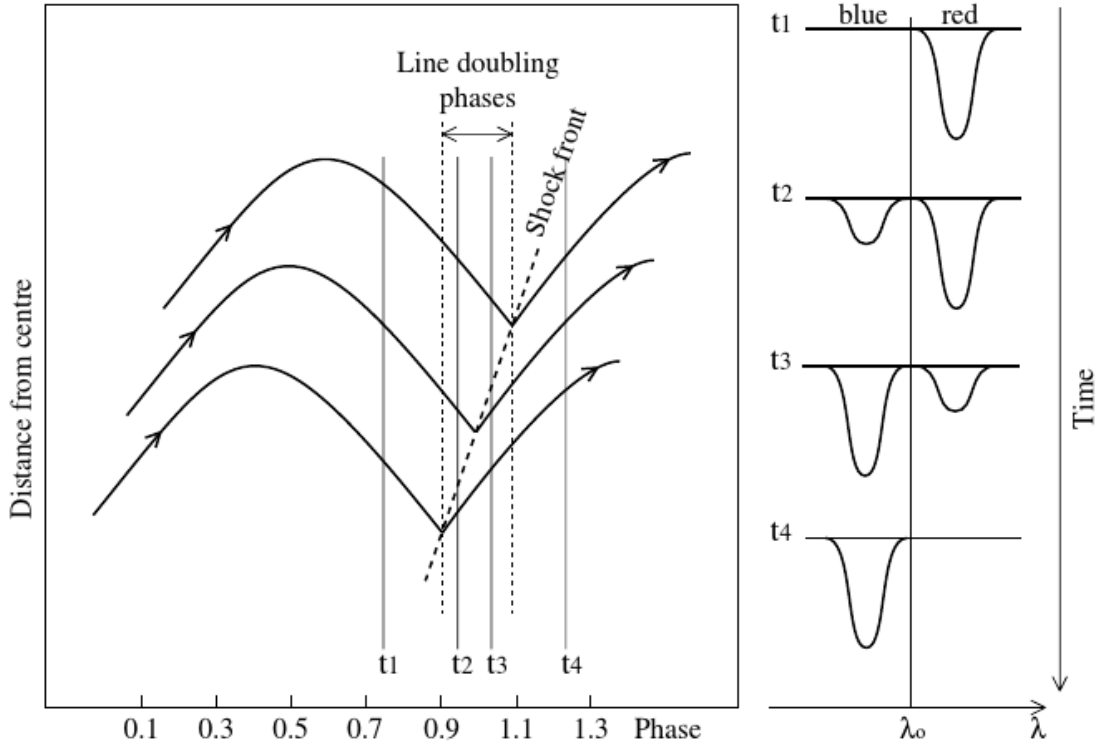


Figure 4.6: Schematic of the Schwarzschild mechanism. In the left panel, the variation of the distance from the centre of the star with time is shown for three different layers of the atmosphere. In the right panel, the observed spectra at 4 particular moments t_1 to t_4 are shown. At t_1 , the whole atmosphere is relaxing and the spectrum is fully redshifted. At t_2 , the bottom part of the atmosphere is rising due to an emerging shock, and the spectrum shows a weak blueshifted lobe and a strong redshifted one. At t_3 , most of the atmosphere is rising, resulting in a strong blueshifted component and a weak redshifted one. Finally, at t_4 , the entire atmosphere is rising and the spectrum is fully blueshifted. Figure from Alvarez et al. (2000).

4.4.3.1 The lower atmosphere: the FeI 6569 Å line

The profile variation of the FeI 6569 Å line is shown in Figure 4.7. It can be seen in this figure that this line always shows a single gaussian profile, either blueshifted or redshifted with respect to the restframe velocity of R Sct. Following the Schwarzschild mechanism, this corresponds respectively to phases t_4 and t_1 in Figure 4.6, i.e. times during which the layer of formation of this atomic line is rising (for the blueshifted profiles) or falling (for the redshifted ones). The absence of a double-peak profile (corresponding to phase t_2 or t_3 in Figure 4.6) of the FeI 6569 Å line in any of the observations shows that the layer in which this line forms is very narrow and thus is affected only by a single global motion (upward or downward) at any given time. Considering that Lèbre & Gillet (1991a) showed that the FeI 6569 Å line is formed close to the photosphere, this line can

be used to trace the motion of the photosphere.

In order to trace the emergence of shockwaves through the photosphere of R Sct, I constructed the radial velocity curve of the FeI 6569 Å line by fitting its profile with a gaussian function in the spectra of R Sct obtained during observational sets 2 and 3 (between April 2015 and October 2016). I selected these two sets because they offer the best phase coverage and also contain the most observations ($\sim 50\%$ of the total dataset). The result is shown in Figure 4.8. In this figure it can be seen that indeed there are two upward accelerations per photometric period, found around phases $\phi = 0$ and $\phi = 0.5$, which correspond respectively to the times of deep and shallow photometric minima, confirming the results of Gillet et al. (1989). In Figure 4.8, global motion (up and down) is clearly seen. The observed dispersion in the radial velocity curve most likely corresponds to cycle-to-cycle variations, as the intensity of the shocks is probably different for the different periods.

4.4.3.2 The upper atmosphere: the TiI 5866 Å line

Next, the behaviour of the TiI 5866 Å line will be examined. The time variability of the profile of this spectral line is shown in Figure 4.9. It was shown by Lèbre & Gillet (1991a) that this line is formed in the upper atmosphere. In Figure 4.9 we see that the profile of this line is very different from that of the FeI 6569 Å one: complex and strongly variable profiles, both single and double-peaked, are observed on different dates. Following the Schwarzschild mechanism, this suggests that the TiI 5866 Å line is formed in a thick layer of the atmosphere, since we observe double-peaked profiles similar to those expected at t_2 and t_3 in Figure 4.6 (e.g. on 2015/08/26, 2016/05/15, 2017/10/05), which on the contrary are not present in the FeI 6569 Å line profiles.

4.4.4 Atmospheric dynamics: summary

The analysis of the variability of the H α and FeI 6569 Å line profiles confirms the results of Gillet et al. (1989), who found that two shockwaves per photometric period emerge from the photosphere of R Sct around the deep and shallow photometric light minima (or, equivalently, just before phases $\phi = 0$ and $\phi = 0.5$). Considering also the TiI 5866 Å line variability, it is evident that spectral lines which form at layers of different altitudes and different thickness are also affected by the propagating shockwave in different ways: "photospheric" lines (i.e. lines which form in a very narrow region near the photosphere, such as the FeI 6569 Å line) always show a single global motion – upward or downward – when affected by the passing of a shockwave, and also indicate the moment at which the shock emerges from the photosphere; lines which form in wider regions of the atmosphere (such as the TiI 5866 Å line), on the other hand, may trace more than one global motion, depending on the location of the shockwave through them (as shown in Figure 4.6).

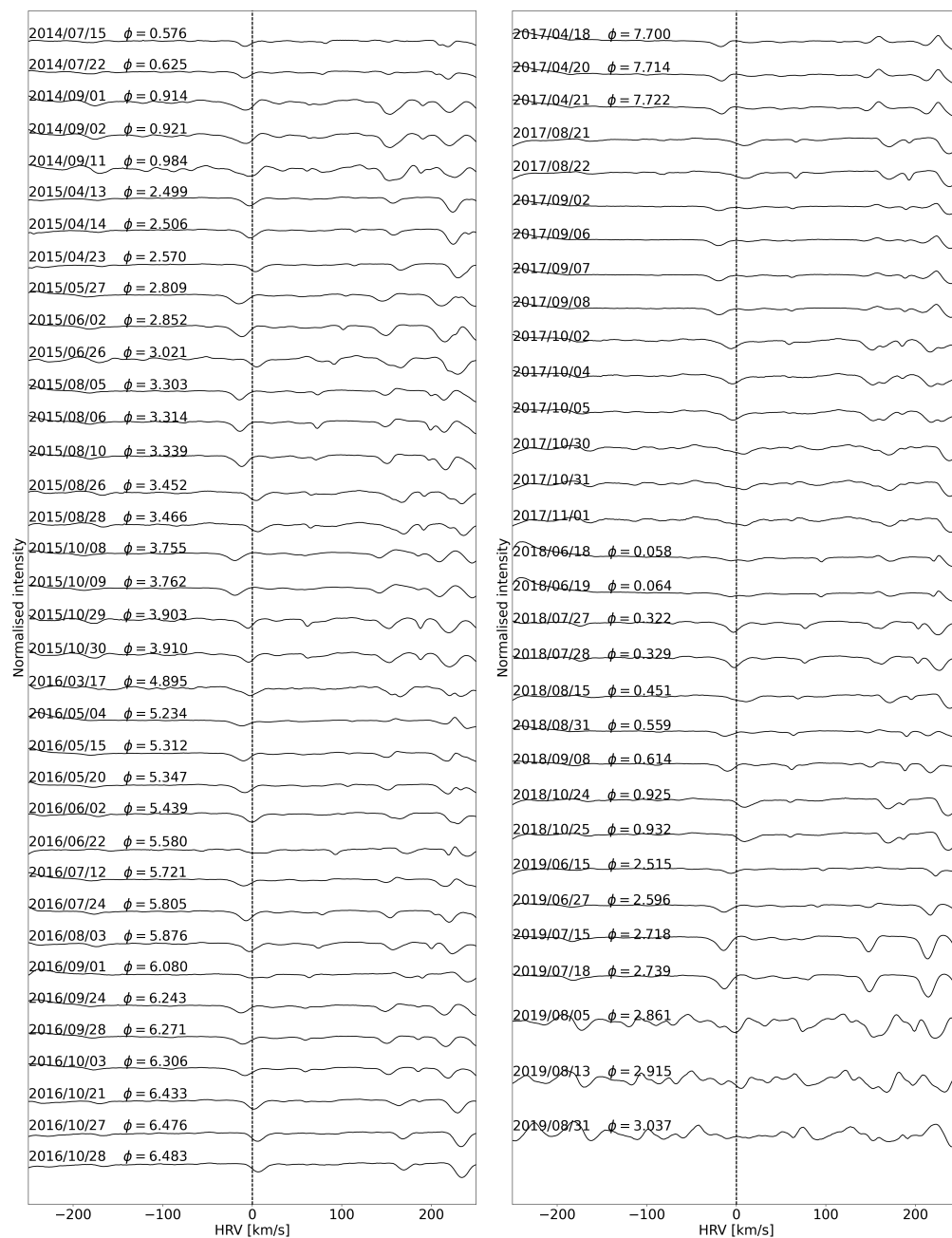


Figure 4.7: Time variation of the FeI 6569 Å line profile in the spectrum of R Sct. Each observation is shifted vertically for display purposes, and its date is indicated on the left. The restframe velocity of R Sct is indicated with a vertical dashed line. For the observations which have a phase assigned to them following Equations 4.1 and 4.2, the phase is also noted.

4.5 The surface magnetic field: a refined approach

The LSD Stokes V profiles presented in Figure 4.3 are obtained in the "classical" way undertaken when studying surface magnetic fields using high resolution spectropolarimetry (see Chapter 2). However, before going any further in the analysis of these LSD profiles, we must consider that this usual approach may not be the best one to use in the case of stars hosting strong pulsations in their atmospheres, such as R Sct. This is so because these stars have very extended atmospheres, which means that at a given moment in time different layers of the extended atmosphere might be affected by very different dynamics. Thus, an LSD line mask computed without considering the conditions under which spectral lines form (like the "standard" and "cool" masks used in Section 4.3) will surely mix together information from very different altitudes with various physical conditions. In particular, the different layers of the extended atmosphere are surely affected, at any given moment in time, by very different dynamics, as it was shown in Section 4.4. This means that the line masks used in Section 4.3 yield LSD profiles that combine the full complexity of the atmospheric motions, which may be different for different layers. In the particular case where the objective is to study the **surface** magnetic field (i.e. its condition at the level of the photosphere), introducing information from the higher atmosphere is certainly not the best approach.

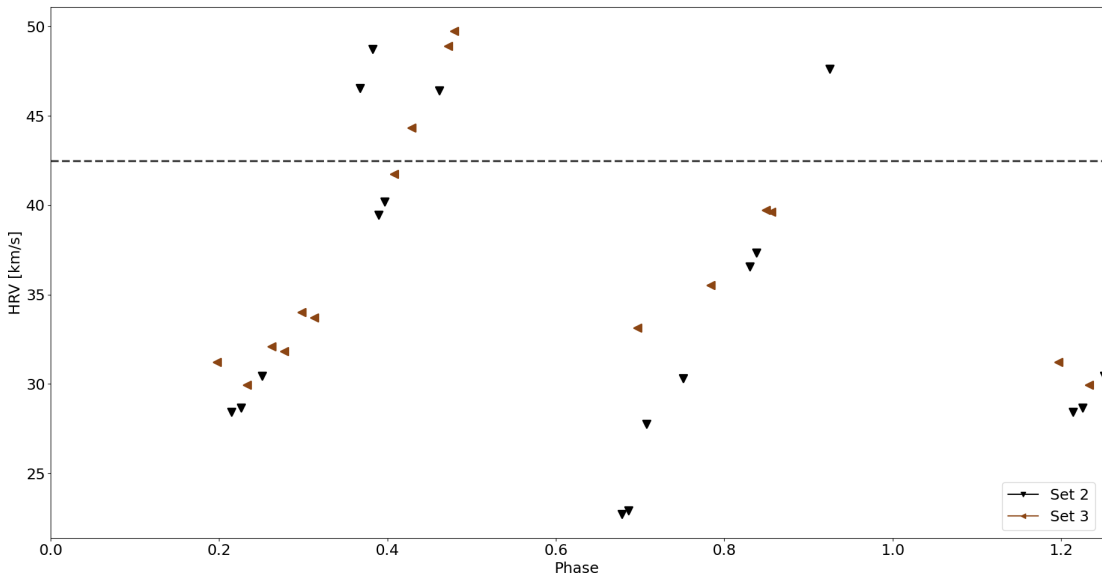


Figure 4.8: Radial velocity curve of the near-photospheric layers of the atmosphere of R Sct obtained from gaussian fits on the FeI 6569 Å line. Points obtained from sets 2 and 3 are displayed with different symbols. The restframe velocity of R Sct is indicated by a dashed horizontal gray line.

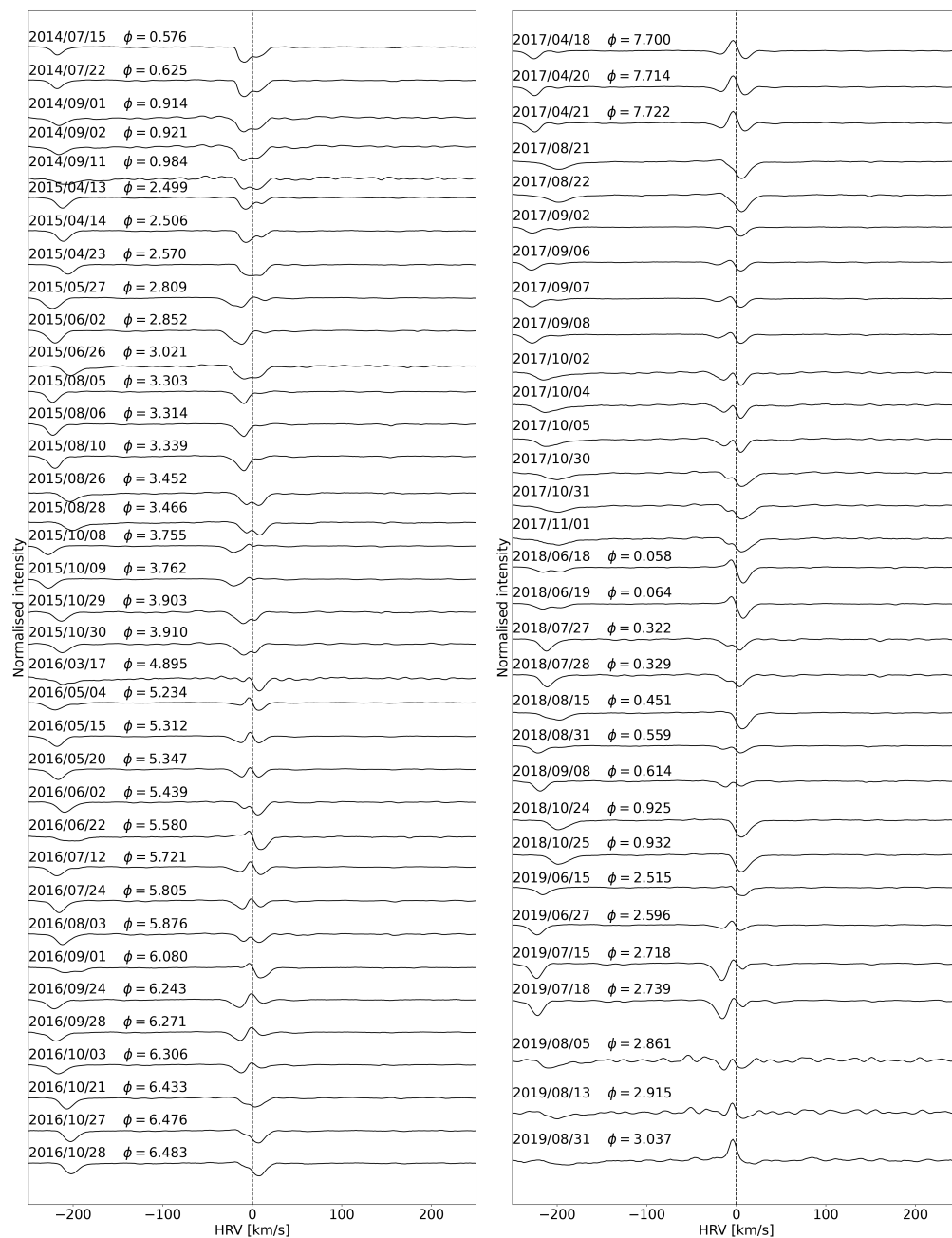


Figure 4.9: Time variation of the TiII 5866 Å line profile in the spectrum of R Sct. See the caption of Figure 4.7.

4.5.1 Line selection by excitation potential

The higher the excitation potential χ of atomic lines is, the less extended their zone of formation in the stellar atmosphere is. In particular, lines with large χ can only be formed in a thin layer near the photosphere. This narrow region is expected to be affected, at any given moment in time, by only one dynamical effect: an upward global motion due to the presence of a single shock wave passing through it, or a downward global motion due to the relaxation of the layer after the passage of a shock wave. For example, the FeI 6569 Å line, which was shown in Section 4.4.3.1 to be formed only in a narrow region near the photosphere of R Sct, has an excitation potential of 4.7 eV (according to the VALD linelists). On the other hand, lines which have a low excitation potential can be formed under a wider variety of conditions, met both at the photospheric layers and at higher altitudes. These lines are thus expected to combine the complexity of a large portion of the stellar atmosphere, which may contain layers affected by different global motions – upwards and downwards. For example, the TiI 5866 Å, shown in Section 4.4.3.2 to be formed in an extended region of the atmosphere of R Sct, has an excitation potential of 1.06 eV (according to the VALD linelists).

This physical scenario is presented schematically in Figure 4.10. In the upper panel of this figure, a schematic representation of the atmosphere of R Sct is shown (not up to scale). Periodically, a shockwave emerges from the photosphere. The narrow region just above the photosphere is affected by the shock and moves in a global upward motion. The higher atmosphere however is not yet affected by this shock; instead, it is moving down, falling ballistically after having been lifted in the past by a previous shockwave. An LSD mask χ_{high} which contains only lines with excitation potential high enough to probe only the atmospheric layers lying close to the photosphere would yield an LSD profile showing a fully blueshifted intensity profile, since these layers are globally moving away from the star. If there is a surface magnetic field above the detection threshold, the LSD profile would also show a Stokes V signature associated to the blueshifted intensity profile.

On the other hand, an LSD mask χ_{low} containing lines with lower excitation potential which may be formed at any altitude in the atmosphere of the star would probe both the photosphere and the higher atmosphere: it would yield an LSD profile containing a mixture of information from both the layers adjacent to the photosphere (which are moving globally upwards) and the higher layers of the atmosphere (which are moving globally downwards as they are relaxing after the passage of a previous shock). This means that the intensity profile will have a double peak according to the Schwarzschild mechanism (see Section 4.4.2), and the Stokes V signature associated to its blueshifted lobe will have a lower amplitude than the one obtained using the χ_{high} mask. Finally, an LSD line mask which contains all atomic lines regardless of their excitation potential (i.e. containing all the lines in both the χ_{high} and χ_{low} masks) would produce an LSD profile similar to the one shown in black in the bottom panel: containing information predominantly from the near-photospheric layer, since both the high- and low excitation

potential lines trace the conditions in it, but also information from the higher atmosphere, which is not relevant when studying magnetism and dynamics at the level of the photosphere.

To examine the effect lines with different excitation potential have on the LSD profiles, I made a test by splitting the "standard" LSD mask into two sub-masks: one with $\chi < 2$ (7903 lines) and one with $\chi \geq 2$ eV (9031 lines). These masks will hereafter be referred to respectively as $\chi_{\text{low}}^{\text{standard}}$ and $\chi_{\text{high}}^{\text{standard}}$. I picked 2 eV to be the limit because this value had to be high enough to successfully restrict the LSD process to the near-photospheric layers of the atmosphere and at the same time low enough to allow for a sufficient number of lines in the mask, in order to get Stokes V signatures with high SNR. I then applied the LSD method using both sub-masks to the observations obtained outside a deep minimum and compared the results. I did the same for observations treated with the "cool" mask. An example of this comparison for some observations is shown in Figure 4.11. In this figure, it can be seen that the Stokes I profiles obtained with the $\chi_{\text{low}}^{\text{standard}}$ and $\chi_{\text{high}}^{\text{standard}}$ sub-masks have completely different shapes, showing that indeed the lines used for their construction probe layers of the atmosphere with different extent, and which are also affected by different dynamics, and thus should be mixed together only with great caution. It can also be seen in Figure 4.11 that the lines with higher excitation potential, which are expected to trace only one atmospheric dynamics at a given moment in time, show a stronger degree of circular polarization. While for some observations the $\chi_{\text{high}}^{\text{standard}}$ sub-mask yields LSD profiles with clear Stokes V signatures, the $\chi_{\text{low}}^{\text{standard}}$ sub-mask never produces any LSD profiles with a signature in Stokes V . From this figure, one can appreciate the level of contamination low excitation potential lines introduce to the signal originating from the photosphere.

The Stokes I and Stokes V profiles obtained using the $\chi_{\text{high}}^{\text{standard}}$ sub-mask are similar in shape to the ones obtained using the full "standard" mask. This is in agreement with the scenario presented in Figure 4.10, since it shows that while both lines with low and high excitation potentials (which together constitute the full "standard" LSD mask) trace the photospheric layer, only the higher excitation potential ones are limited strictly to it, while lines with lower χ also contain information from higher atmospheric layers (and hence unrelated to the surface magnetic field).

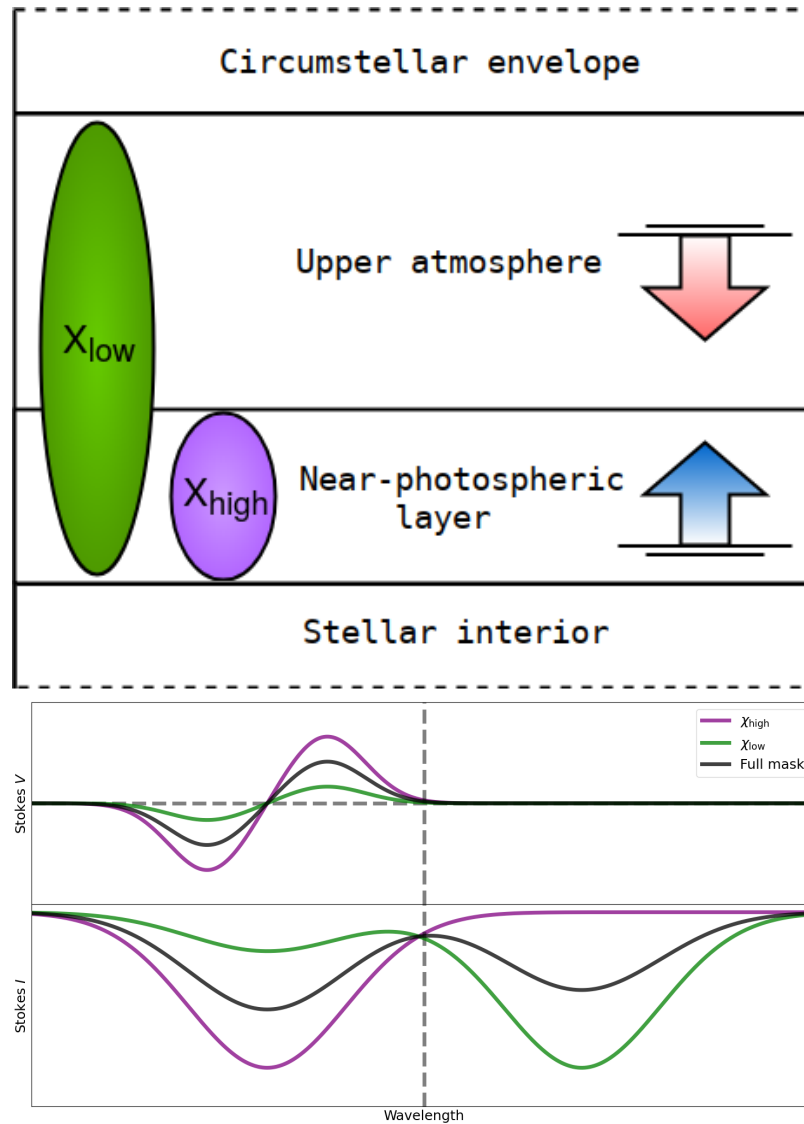


Figure 4.10: Upper panel: a schematic representation (not up to scale) of two global motions in the atmosphere of R Sct – an upward one in the near-photospheric layers, caused by the passing of a radiative shockwave, and a downward one in the higher atmosphere, caused by the gravitational infall occurring after the propagation of the previous shockwave. Bottom panel: the LSD profiles that would be obtained by using a mask containing only lines with high χ which probe only the near-photospheric layers of the atmosphere (purple), low χ which probe the same layers plus the higher atmosphere (green), and a mask which contains a mixture of both (black).

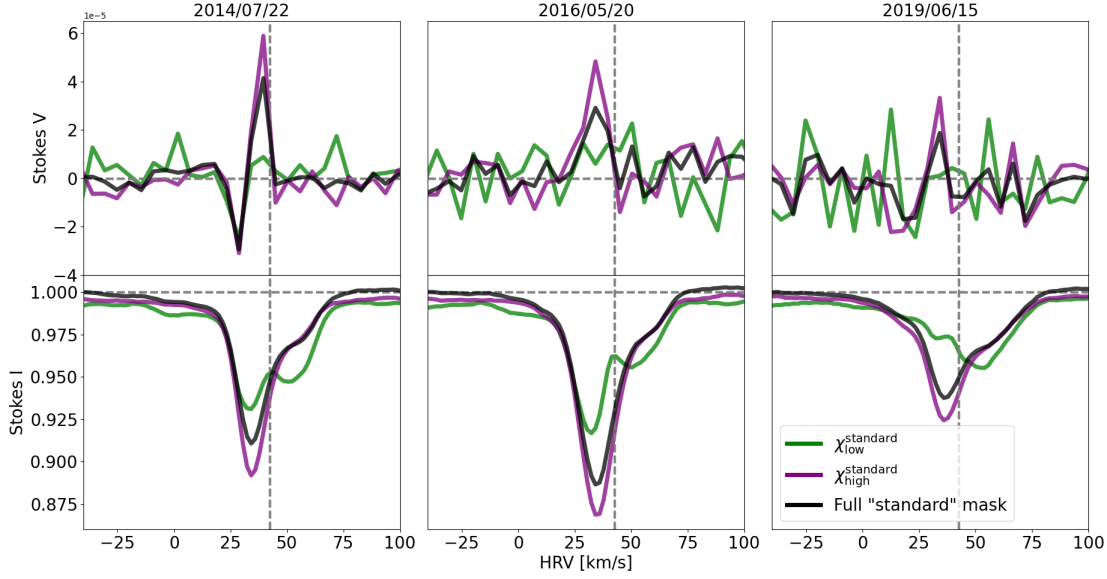


Figure 4.11: Comparison between the LSD profiles obtained with the $\chi_{\text{low}}^{\text{standard}}$ (containing 7903 lines, in green), $\chi_{\text{high}}^{\text{standard}}$ (containing 9031 lines, in purple) and full "standard" (containing 16934 lines, in black) line masks for 2014/07/22 (left column), 2016/05/20 (middle column) and 2019/06/15 (right column). The Stokes V and intensity profiles are shown in the top and bottom rows respectively. The zero-level of the Stokes V and the continuum level of the intensity are indicated by the dashed horizontal lines in their corresponding panels, and the radial velocity of R Sct is indicated by the dashed vertical line.

From what is seen in Figure 4.11, it can also be concluded that while the photospheric layers of R Sct show traces of a variable magnetic field, the atmosphere of the star as a whole (represented by the $\chi_{\text{low}}^{\text{standard}}$ sub-mask) does not. Furthermore, the absence of Stokes V signatures in the LSD profiles obtained with the $\chi_{\text{low}}^{\text{standard}}$ sub-mask for the observations where the $\chi_{\text{high}}^{\text{standard}}$ one shows a clear feature suggests that the higher atmospheric layers introduce signals that may compensate the contribution of the lines formed at the photospheric level. This is another proof that mixing together atomic lines formed in different atmospheric layers can have a serious impact when investigating surface magnetism in pulsating stars hosting extended atmospheres. The valuable result from this new approach for the analysis of the surface magnetic field is then a better definition of the Stokes V profiles which originate at the level of the photosphere.

Considering what has been said so far, the $\chi_{\text{high}}^{\text{standard}}$ sub-mask appears to be a better choice when analysing the magnetic field at the surface level. The exact same logic applies to the observations obtained near a deep luminosity minimum, for which I constructed a $\chi_{\text{high}}^{\text{cool}}$ mask by extracting from the "cool" mask the lines with $\chi \geq 2$ eV.

4.5.2 Magnetism at the photospheric level

To better constrain the analysis of the LSD profiles, and more specifically, the Stokes V signatures, to the level of the photosphere, I computed a new set of LSD profiles for the Narval observations in circular polarization, this time using the $\chi_{\text{high}}^{\text{standard}}$ and $\chi_{\text{high}}^{\text{cool}}$ masks, which I built as described in the previous section. The dates for which in Section 4.3 the "standard" mask was used were treated with the $\chi_{\text{high}}^{\text{standard}}$ mask, and the rest were treated with the $\chi_{\text{high}}^{\text{cool}}$ one (see Table 4.2). The resulting LSD profiles are shown in Figure 4.12. It can be seen in this figure that generally, the LSD profiles resemble those obtained using the full "standard" and "cool" masks (presented in Figure 4.3). The Stokes V profiles obtained by using only high excitation potential lines however are more well-defined. This result is in agreement with the assumption of the zones of formation described in Section 4.5.1. It also shows that the magnetic field at the surface level differs from that in the higher atmosphere, otherwise the Stokes V profiles presented in Figures 4.12 and 4.3 would be identical. For some particular dates (2015/08/28, 2016/05/20) it is also possible to notice a signature when using the χ_{high} masks, while it is not apparent with the full one. However, the timescale of variation given in Section 4.3.2 still applies. In Figure 4.12 it can be seen again that for some observations (e.g. 2014/07/22, 2016/05/20) where the LSD intensity profile shows a double-peak structure, the Stokes V signature is clearly only associated to the blueshifted lobe. I propose that this magnetic field detection may be indeed associated to an ascending global motion of the photosphere caused by a radiative shock wave propagating outwards. As previous studies of cool pulsating stars by Lèbre et al. (2015) and Sabin et al. (2015) have suggested, the propagation of a shock wave may locally amplify a weak surface magnetic field due to a compression of the magnetic field lines.

The fact that in Figure 4.12 a few observations still show a double-peak Stokes I profile (e.g., 2017/04/18 and 2017/09/08) indicates that the χ_{high} mask does not fully constrain the LSD process to the near-photospheric layers (otherwise all LSD intensity profiles would have the shape of a single gaussian). This most likely means that the 2 eV limit may be too low, and a higher threshold is necessary in order to fully isolate the contribution of the near-photospheric layers in the computation of the LSD profiles. However, setting the excitation potential limit higher would further limit the number of lines in the mask, which would in turn decrease the SNR of the LSD profiles.

Using the LSD profiles shown in Figure 4.12, I computed the longitudinal component B_l of the magnetic field vector for those observations where a clear Stokes V signature can be seen, using the first order moment method described in Chapter 2. For the observations where the signal appears clearly associated to the blueshifted lobe of the intensity profile, I fitted the LSD Stokes I profile with a sum of two gaussians representing the two components; I then limited the B_l computation to the blueshifted lobe only, using the HRV window $[v_{0 \text{ fit}} - 1.5\sigma_{\text{fit}}, v_{0 \text{ fit}} + 1.5\sigma_{\text{fit}}]$, where $v_{0 \text{ fit}}$ and σ_{fit} are respectively the gaussian's peak position and its FWHM (in km s^{-1}). The resulting B_l values are shown in Figure 4.13 together with the visual lightcurve. It can be seen in this figure that the

Date	HJD	Signature (full mask)	Signature ($\chi \geq 2$ eV)	B_l [G] ($\chi \geq 2$ eV)	σ [G] ($\chi \geq 2$ eV)
2014/07/15	6854.5	no	no	–	–
2014/07/22	6861.4	yes	yes	-0.51	0.29
2014/09/02 [‡]	6903.3	yes	yes	-0.45	0.51
2014/09/11 [‡]	6912.3	no	no	–	–
2015/04/13	7126.6	yes	yes	-0.06	0.46
2015/04/23	7136.6	ambiguous	ambiguous	1.38	0.67
2015/05/27	7170.5	no	ambiguous	-0.27	0.52
2015/06/02	7176.6	no	ambiguous	-0.10	0.20
2015/06/26 [‡]	7200.5	no	no	–	–
2015/08/06	7241.9	ambiguous	ambiguous	-0.37	0.36
2015/08/10	7245.4	no	no	–	–
2015/08/28 [‡]	7263.4	ambiguous	yes	-1.27	0.79
2015/10/09	7305.3	no	ambiguous	0.14	0.30
2015/10/30	7326.3	no	no	–	–
2016/05/15	7524.6	no	no	–	–
2016/05/20	7529.6	ambiguous	yes	0.63	0.49
2016/07/24	7594.4	no	no	–	–
2016/09/28	7660.3	no	no	–	–
2016/10/03	7665.3	no	no	–	–
2017/04/18	7862.6	no	no	–	–
2017/08/21 [‡]	7987.4	no	no	–	–
2017/09/08	8005.3	no	no	–	–
2017/10/05 [‡]	8032.3	no	no	–	–
2017/11/01 [‡]	8059.8	no	no	–	–
2018/06/19	8289.5	ambiguous	yes	-2.67	1.32
2018/07/28	8328.5	no	ambiguous	0.92	0.52
2018/09/08	8370.4	no	no	–	–
2019/06/15	8650.5	no	no	–	–
2019/06/27	8662.5	no	no	–	–
2019/07/18	8683.5	no	no	–	–
2019/08/31 [‡]	8727.4	no	no	–	–

Table 4.2: Log of Stokes V observations. Calendar and heliocentric Julian dates (HJD) are given in the first two columns. HJD starts from 2 450 000. The third and fourth columns show if a signature is present in the Stokes V profile obtained respectively with the full mask and the χ_{high} mask: yes, no or ambiguous. The last two columns show the B_l and its errorbar, computed from the χ_{high} LSD profiles. The dates for which the $\chi_{\text{high}}^{\text{cool}}$ mask is used are marked with [‡], and for the rest, the $\chi_{\text{high}}^{\text{standard}}$ mask is used (see Section 4.2.2).

4.5. THE SURFACE MAGNETIC FIELD: A REFINED APPROACH

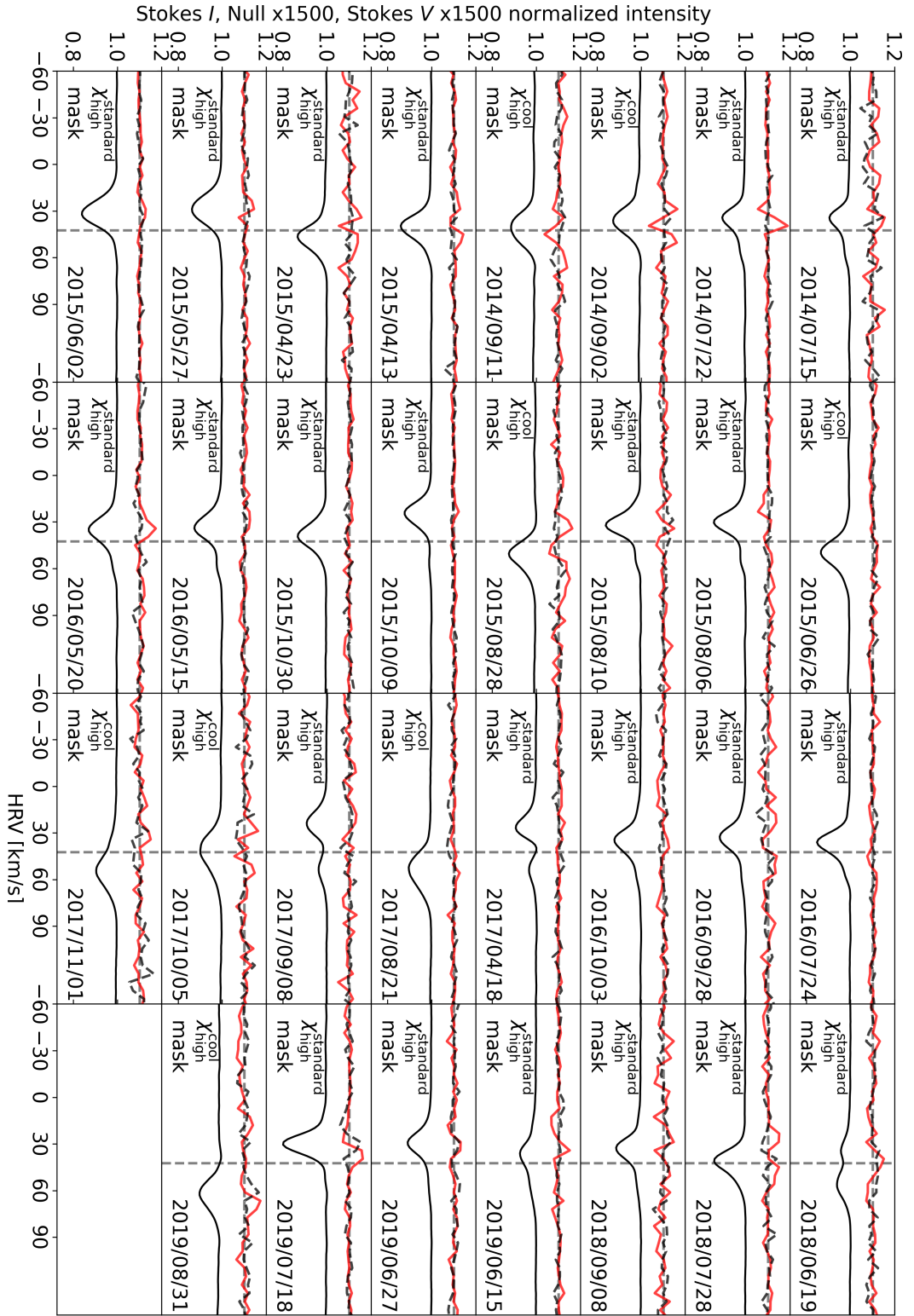


Figure 4.12: LSD profiles of R Set in circular polarization using only lines with $\chi \geq 2$ eV. See the caption of Figure 4.3.

longitudinal magnetic field varies significantly in time, both in strength and in position relative to the intensity profile.

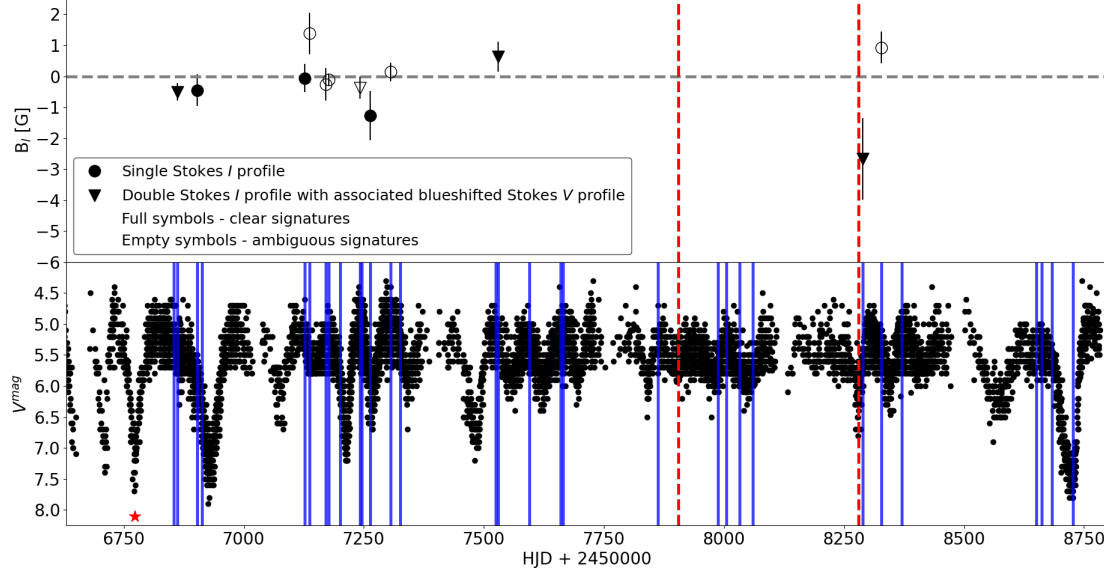


Figure 4.13: Temporal evolution of the longitudinal component of the magnetic field $B_l(t)$ of R Sct (upper panel) and lightcurve (bottom panel). The blue vertical lines in the bottom panel indicate the time of Narval observations that contain Stokes V measurements, and the red star indicates the date considered as the start of period 0 (see Section 4.2.1). The dashed vertical red lines indicate the approximate beginning and end of the irregular part of the lightcurve, during which no Stokes V signatures are observed.

The first half of the dataset, before the irregular portion of the lightcurve (delimited by the dashed red vertical lines), contains 20 observations, of which 10 show a signature in Stokes V (5 of which are unambiguous). For 3 dates – 2014/07/22, 2015/08/06, 2016/05/20 – the Stokes V signature appears to be associated only to the blueshifted lobe of the intensity profile. The B_l varies roughly between -1.3 and 1.4 G in this first part of the observational dataset.

During the irregular part of the lightcurve, none of the 4 available observations show a clear polarized signature in Stokes V .

In the last part of the dataset, after the irregular portion of the lightcurve, only 2 out of 7 observations show signatures in Stokes V : 2018/06/19 and 2018/07/28. For the date 2018/06/19, the B_l value measured is impressive: -2.67 ± 1.32 . Even though the errorbar is large for this measurement due to the noise in the polarized spectrum, the B_l value is higher than those measured from the rest of the observations. For this observation, the signature seems to be associated to the blueshifted lobe of the intensity profile, in agreement with the hypothesis that the magnetic field is associated to the matter being

affected by an emerging shockwave.

4.6 Linear polarization

Linearly polarized signatures in the spectrum of R Sct were reported previously by Lèbre et al. (2015). I computed the LSD profiles of the Narval observations in linear polarization listed in Table 4.1 using the full "standard" and "cool" masks as described in Section 4.3. I took into account all atomic lines, without discriminating them by their excitation potential. The resulting LSD profiles are presented in Figures 4.14 and 4.15. In this figure, the presence of variable signatures in both Stokes Q and U in the spectrum of R Sct can be seen. In my Thesis however, I only use the linearly polarized LSD profiles to check for cross-talk between linear and circular polarization in Narval (see Section 4.3.1) in order to confirm the stellar origin of the Stokes V signal. The analysis of the Stokes Q and U profiles of R Sct, and their origin, is to be done in a future study not in the scope of the present Thesis.

4.7 Summary

In this chapter, the longest monitoring of the RV Tauri variable star R Sct using high resolution spectropolarimetry is presented. Circular polarization signatures are detected in several observations and their stellar and Zeeman origin is confirmed. The timescale of variation of these signatures appears to be of a few months, similar to the timescale of pulsation of the star. The differences between the dynamics of the lower (near-photospheric) and upper layers of the extended atmosphere of R Sct are presented. These differences introduce the need for a refined approach for the application of the LSD method when investigating the surface magnetic field. Such an approach is suggested and applied to the observational dataset. LSD profiles constructed from lines formed mostly in the near-photospheric layers of the atmosphere are produced, and from their Stokes V signatures, the longitudinal magnetic field is measured. Always when the Stokes I LSD profile shows a double-peak profile, the Stokes V signature, when present, appears to be associated to its blueshifted lobe, suggesting a connection between the shockwave propagating outwards from the photosphere and the detection of a surface magnetic field, perhaps due to compression of magnetic field lines at the shock front. However, further investigation is needed in order to prove or disprove such a connection between atmospheric dynamics and surface magnetism in R Sct.

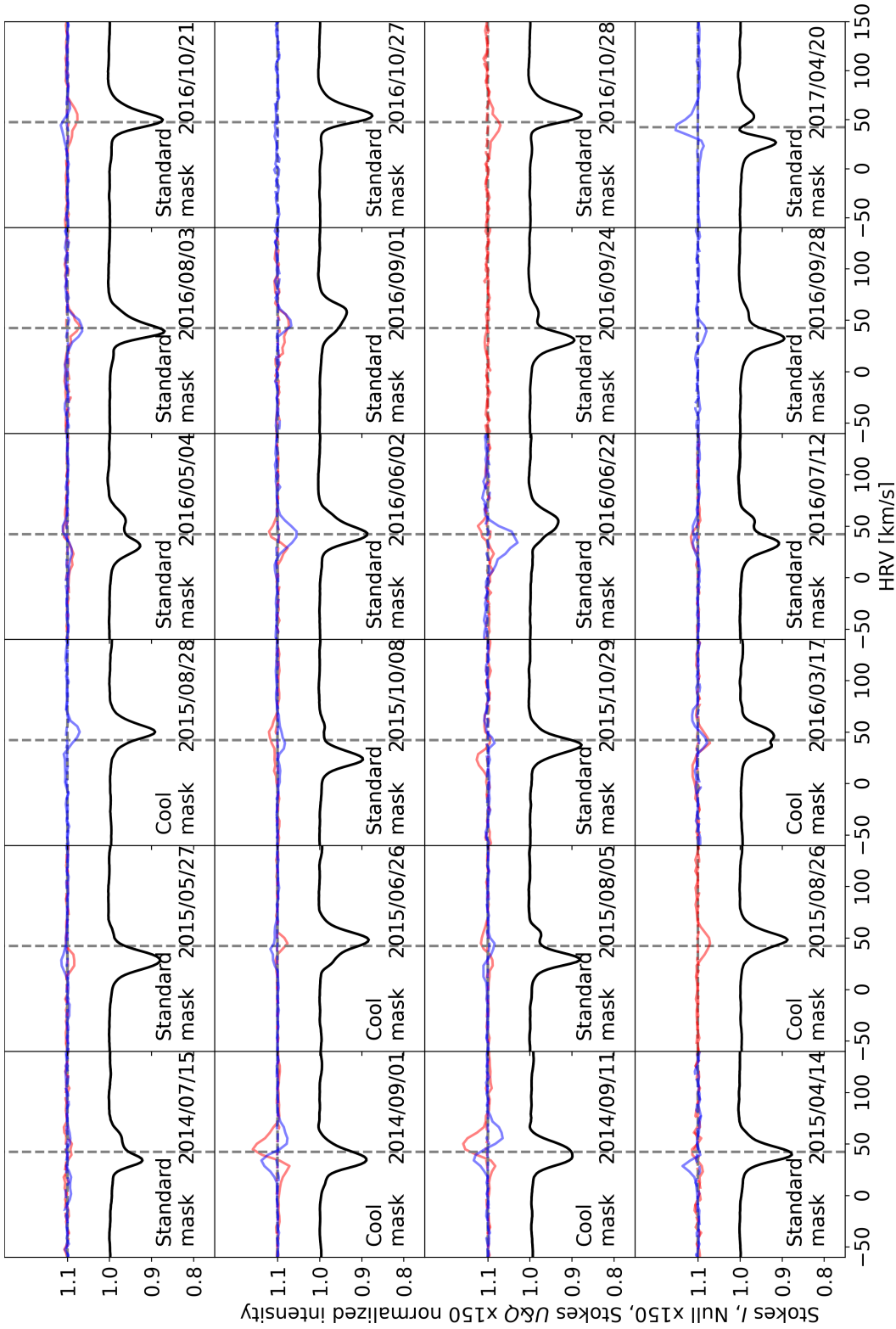


Figure 4.14: LSD profiles of R Sct for observations in linear polarization (part 1). The date of observation and the mask used are noted respectively in the bottom right and bottom left part of each panel. The Stokes QU (shown in red and blue solid lines, respectively) and their respective diagnostic null profiles (shown respectively in red and blue dashed lines) are smoothed by averaging every three pixels, shifted vertically and amplified 150 times for display purposes and their zero levels are indicated with dashed gray lines. The Stokes I profiles are shown in black. For each observation, the radial velocity of the star $v_{\text{rad}} = 42.47 \text{ km s}^{-1}$ (Kunder et al., 2017) is indicated with a dashed vertical line.

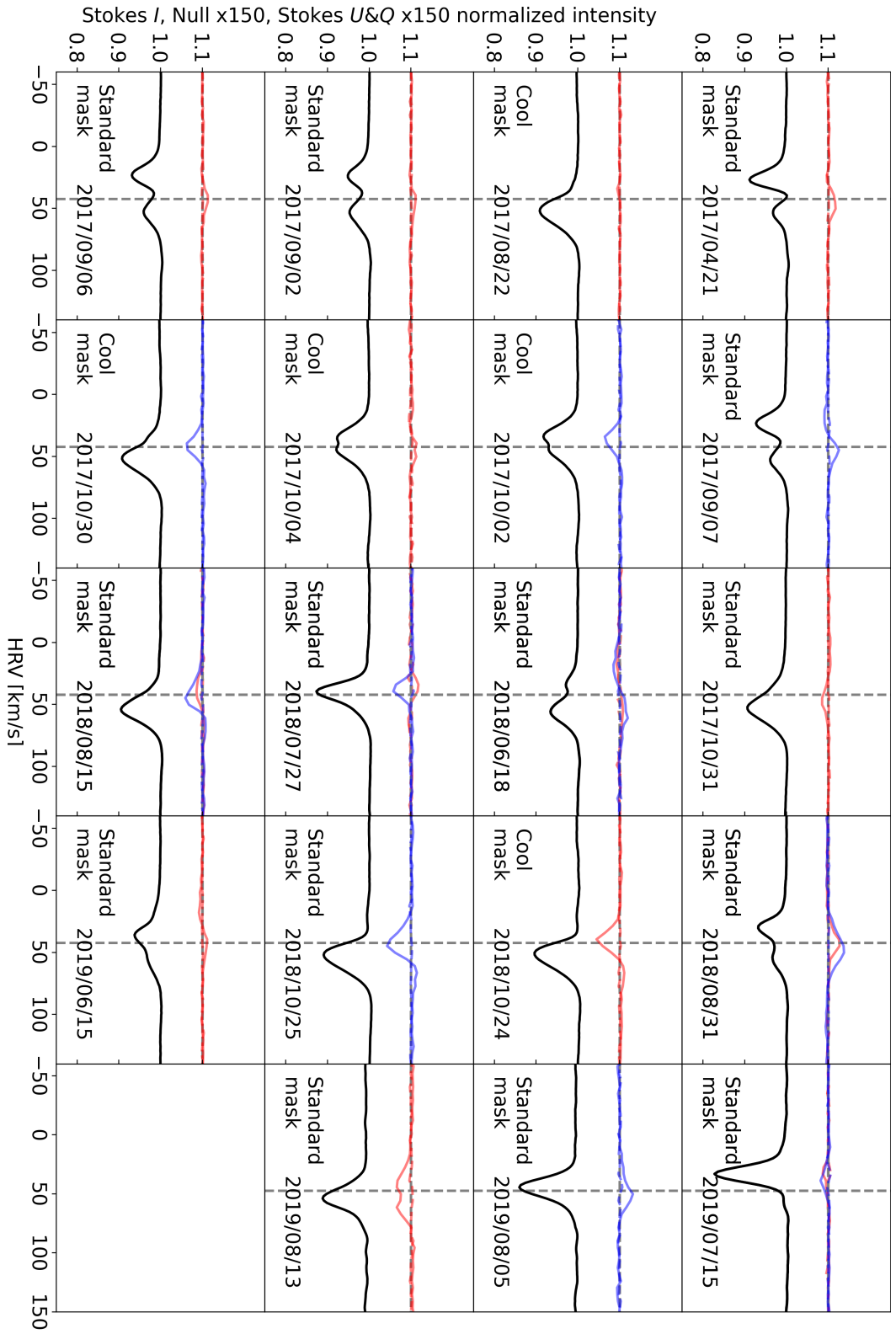


Figure 4.15: LSD profiles of R Sct for observations in linear polarization (part 2). See the caption of Figure 4.14

Imaging the photosphere of Betelgeuse through spectropolarimetry

In this Chapter, I will present my study of the convective motions in the lower atmosphere of the red supergiant Betelgeuse using a new method for 3-dimensional (3D) imaging based on spectropolarimetric observations in linear polarization. First, I will give a brief introduction of the target star. After that, I will summarize the results of previous spectropolarimetric studies of Betelgeuse that lay the foundations for the 3D-imaging of its atmosphere. I will then explain in details how the 3D brightness maps are built from spectropolarimetric observations and how they should be interpreted. Finally, I will give a summary of the results and a conclusion. This study is also presented in a paper accepted for publishing in the journal *Astronomy & Astrophysics*, and this paper can be found at the very end of this Chapter.

Summary

5.1	Introduction	147
5.2	The method for 2D surface imaging	149
5.2.1	Discovery of linear polarization in the spectrum of Betelgeuse	149
5.2.2	First mapping of bright spots	151
5.2.3	Giant convective cells and imaging through spectropolarimetry	152
5.3	The path to 3D-imaging of Betelgeuse	159
5.3.1	Analysing the intensity profiles	159
5.3.2	Characteristic velocities	160
5.3.3	Gray atmosphere	161
5.3.4	The linearly polarized profiles: an in-depth view	164
5.4	Building the 3D-images	167
5.5	Reading the 3D-images	170
5.6	Results and conclusion	171
5.7	Paper accepted for Astronomy & Astrophysics	173



5.1 Introduction

Betelgeuse (α Ori, HD 39801) is a nearby ($d = 200$ pc, Joyce et al. 2020) M2Iab red supergiant (RSG) star. Betelgeuse recently experienced an unusual decrease in visual brightness by about 1 mag (Guinan et al., 2020), which is commonly referred to as the Great Dimming of Betelgeuse. It lasted between October 2019 and February 2020, which unfortunately coincided with the shutdown of Narval due to its upgrade to NeoNarval. Because of the transition to NeoNarval, there are practically no observations of Betelgeuse in high-resolution spectropolarimetry during its Great Dimming.

The surface parameters of Betelgeuse as determined by Lambert et al. (1984) and Joselin & Plez (2007) are $T_{\text{eff}} = 3750$ K, $\log g = 0.0$, solar metallicity and microturbulence of 4.0 km s^{-1} . Being a visually bright object and the star with the largest angular diameter (42.11 mas, Montargès et al. 2021) after the Sun, Betelgeuse has been a target of many observations, including spectropolarimetric and interferometric ones. Aurière et al. (2010) obtained high resolution spectropolarimetric observations of Betelgeuse in circular polarization (Stokes V) in the period March - April 2010 using Narval. These authors were the first to report a direct measurement of the surface magnetic field of Betelgeuse, which they measured to be of the order of 1 G. The authors also suggest that, since RSG stars rotate very slowly (for Betelgeuse $P_{\text{rot}} \approx 12$ to 25 years, Uitenbroek et al. 1998; Kervella et al. 2018) and have very extended atmospheres, neither a solar-type dynamo nor a fossil magnetic field from a magnetic main sequence star progenitor are possible explanations of the observed magnetic field of Betelgeuse. Aurière et al. (2010) instead point to a local-type dynamo due to the presence of giant convective cells as a possible origin of the magnetic field. Such cells were predicted to exist on the surface of Betelgeuse by Schwarzschild (1975) and also appear in numerical simulations by Freytag et al. (2002) and Dorch (2004) and the interferometric observations available at the time (Haubois et al., 2009; Chiavassa et al., 2010).

A few years later, the first detection of a linearly polarized signal in the spectrum of Betelgeuse was reported by Aurière et al. (2016), who measured from Narval observations rather strong signatures in Stokes Q and U , of the order of 10^{-4} the intensity of the unpolarized continuum. By analyzing the linearly polarized signatures in individual spectral lines, namely the sodium doublet NaD, these authors conclude that the net signal observed with Narval is due to depolarization of the continuum of Betelgeuse (which is polarized due to Rayleigh scattering) in the absorption lines. Since this effect should yield zero net linear polarization if the visible disk of the star were uniformly bright, Aurière et al. (2016) conclude that surface brightness inhomogeneities must be present in Betelgeuse, and propose a geometrical model to infer their positions on the disk of the star.

Mathias et al. (2018) studied the long-term variability of the magnetic field of Betelgeuse using Narval observations in Stokes V . The authors show that the circularly polarized

signatures in this star vary on timescales similar to those of linear polarization (around 300 d and 2000 d), suggesting that the two types of signatures originate from the same structures. The authors point out that the timescale of 2000 d coincides with the typical long secondary period (LSD) for RSG stars, and that it could be associated with giant convective cells, since such cells are expected to have lifetimes of the order of years (Chiavassa et al., 2009, 2010, 2011b).

López Ariste et al. (2018) developed a numerical method to map the surface brightness of the RSG star Betelgeuse using high-resolution spectropolarimetric observations. The method is based on the works of Aurière et al. (2016) and Mathias et al. (2018) who respectively study the linearly and circularly polarized signal in Betelgeuse. It is structured around the idea that the continuum radiation in Betelgeuse is linearly polarized due to Rayleigh scattering, and gets then depolarized by atomic lines forming above the continuum. As Aurière et al. (2016) propose, this effect yields a non-zero polarization signal in Stokes Q and U due to the presence of surface brightness inhomogeneities at the surface of Betelgeuse. López Ariste et al. (2018) suggest that these inhomogeneities are in fact giant convective cells that appear at the level of the photosphere, in agreement with numerical simulations (Freytag et al., 2002; Dorch, 2004; Chiavassa et al., 2011a). Using an original method, the authors were able to reconstruct 2D images of the surface brightness of Betelgeuse for several dates of spectropolarimetric observations and monitor the evolution of convective patterns in its photosphere. The obtained results are in good accordance with images of Betelgeuse inferred from interferometry (Montargès et al., 2016; Kervella et al., 2018). This kind of work was also done for another RSG star, CE Tau, for which the results are also in good agreement with interferometric images (Montargès et al., 2018).

We used the method presented in López Ariste et al. (2018) as a foundation of a new technique to infer 3-dimensional (3D) images of the photosphere of Betelgeuse. This technique is based upon the assumption that we are facing giant convective cells in Betelgeuse, and allows for detailed examination of the convection velocity in altitude. Studying the variation of convection velocity may shed light on the physical phenomena that are responsible for the significant mass-loss which RSG stars are known to exhibit. The method for 3D-imaging, and the results we obtain for the velocity of the convective motions in Betelgeuse are presented in a paper accepted for publication in the journal *Astronomy & Astrophysics (A&A)* (López Ariste et al., 2022).

Section 5.2 of the present chapter gives a detailed description of the method for surface imaging presented in López Ariste et al. (2018). In Section 5.3, the assumptions that allow the construction of 3D-images of the photosphere of Betelgeuse are presented in details and justified. The way that the 3D-images are constructed is described in Section 5.4, and the way that they should be analysed is explained in Section 5.5. The results obtained in López Ariste et al. (2022) are presented in Section 5.6, and the submitted version of the paper itself is presented in Section 5.7.

5.2 The method for 2D surface imaging

The imaging of the photosphere of Betelgeuse through spectropolarimetric observations by López Ariste et al. (2018) is only possible by relying upon many assumptions for the physical conditions in this RSG star. In order to understand and justify these assumptions, one must first be familiar with previous works that lay the foundations for them.

5.2.1 Discovery of linear polarization in the spectrum of Betelgeuse

Aurière et al. (2016) analyzed Narval observations of Betelgeuse in linear polarization obtained between 2013 and 2015. These authors interpret the net linear polarization signal seen in these data as a result from Rayleigh scattering in the continuum followed by depolarization in the spectral lines.

Betelgeuse is known to show linear polarization in its continuum beyond 0.5% in the blue (e.g. Hayes 1984; Clarke & Schwarz 1984; Nordsieck et al. 1994; Magalhaes & Nordsieck 2000 for recent studies), which is clearly a sign of anisotropy in its radiation field. It is generally considered that the linear polarization of the continuum is mainly caused by Rayleigh scattering (in the photosphere) and Mie scattering (by circumstellar dust), and that the anisotropy is due to one or several brightness spots (Schwarz & Clarke 1984; Clarke & Schwarz 1984; Doherty 1986; Magalhaes & Nordsieck 2000). Aurière et al. (2016) consider depolarization to be mainly occurring due to the incoherent process of absorption of photons, followed by their spontaneous re-emission at the origin of the spectral line, after which the initial polarization of the photon is lost. Since this process has the same probability for all spectral lines, it is expected that all lines should depolarize the continuum to the same degree. This is similar to the solar case, where most absorption lines have very small intrinsic polarization, and mainly depolarize the continuum, having almost identical linear polarization profiles (Stenflo et al., 1983). An important indication that this is also the dominating process in Betelgeuse comes from the polarization signatures of the NaD lines. According to Landi Degl’Innocenti & Landolfi (2004) the intrinsic polarization of the D1 line (at 589.6 nm) is much smaller than that of D2 (at 588.9 nm). However, in Betelgeuse the D1 line shows a degree of linear polarization comparable to that of D2, as can be seen in Figure 5.1 (from Aurière et al. 2016). This cannot be due to intrinsic polarization, but can instead only be explained by depolarization of the continuum in the spectral lines. Detecting depolarization in Narval observations this way can be expected, since there the continuum polarization level is set to zero and any depolarization instead appears as a net signal.

Scattering polarization is orthogonal to the plane of scattering, and so is observed to be at a tangent to the local limb: as the azimuth changes, the plane of polarization rotates (see the left panel of Figure 5.2). This means that in a spherically symmetric star with a uniform surface brightness distribution the observed net polarization signal would be zero, because the signals coming from every two points that have the same distance from the center of the disk and are 90-degree angle apart would cancel each other out. Since

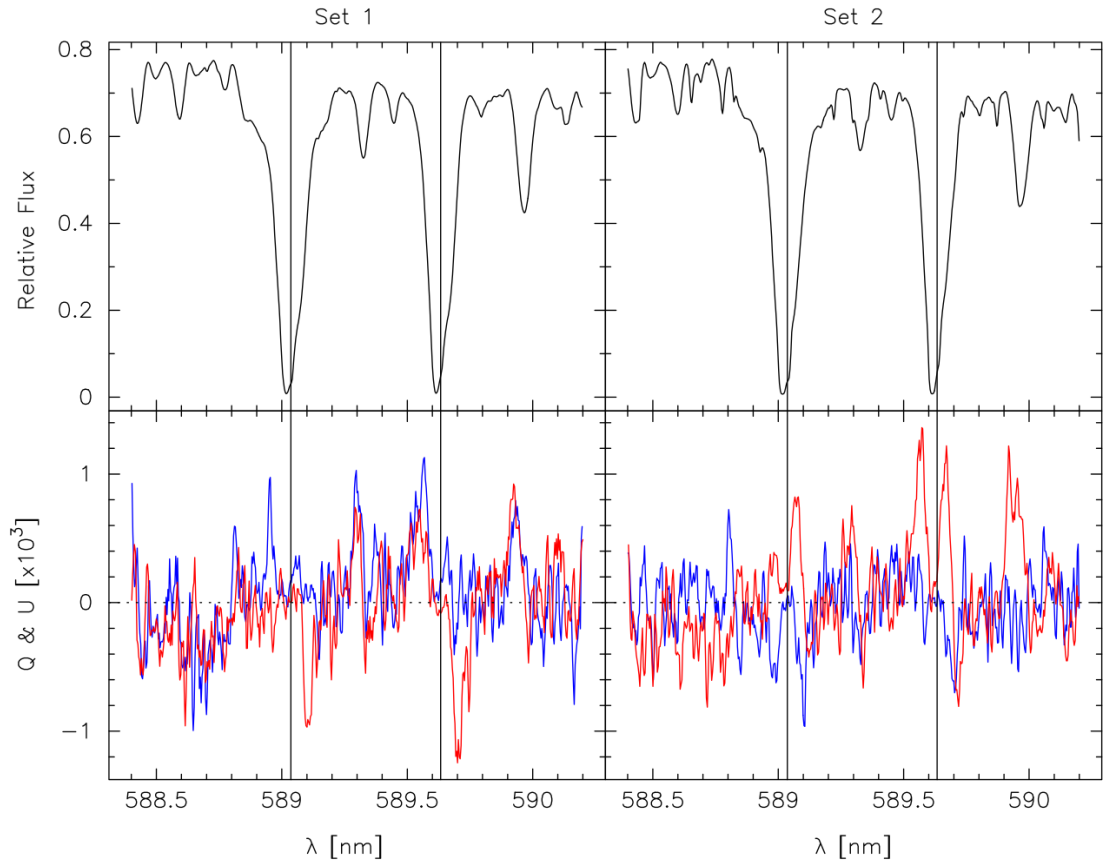


Figure 5.1: Linearly polarized spectra of Betelgeuse in the region of the NaI D lines for Sets 1 and 2 of Aurière et al. (2016) (corresponding respectively to observations taken on 2013/11/27, 2013/12/11, 2013/12/20 and 2014/01/09, left panel and observations from 2014/09/12-13, right panel). The intensity profiles are shown in the upper spectrum in black, while the lower spectra show the Stokes U and Q in red and blue, respectively. It can be seen that the apparent polarization signals of D1 and D2 have comparable intensity, indicating that they mostly depolarize the continuum. Figure from Aurière et al. (2016).

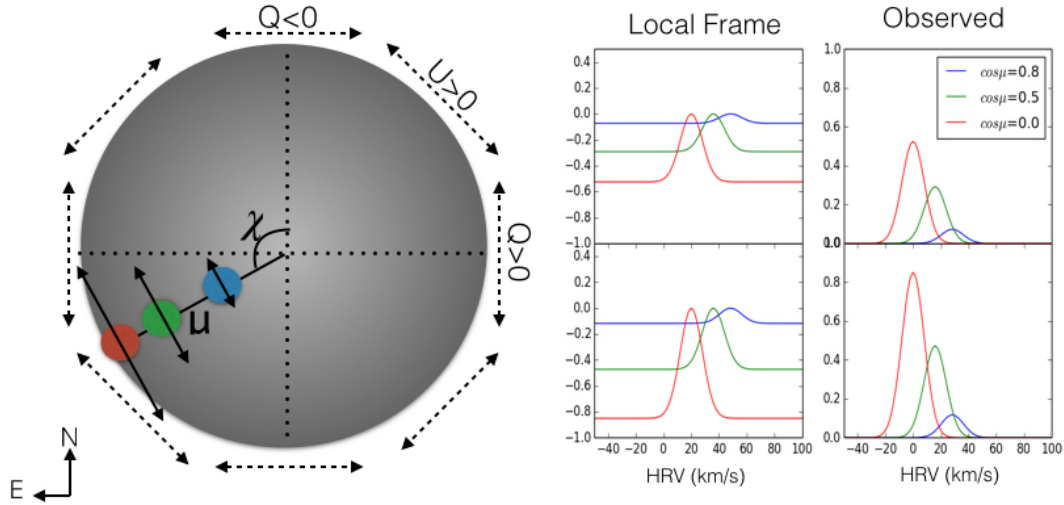


Figure 5.2: Coordinates on the disk of Betelgeuse and polarized spectra in the case of one bright spot in the model of Aurière et al. (2016). In the left of the figure a cartoon of the stellar disk shows the polar coordinates for three bright spots at the same positional angle χ between the radius and the North-South meridian of the disk, but at different projection angle μ between the spot and the disk center. Across each spot the arrow shows both the orientation and relative polarization expected. Around the disk the dashed arrows show the definition of the Stokes parameters Q , U . In the right part of the figure, the leftmost two plots show Stokes Q (top) and U (bottom) for the three spots as they would be seen in a resolved stellar disk. The two rightmost plots show what would be observed with Narval and the radial velocity scale is shifted to the HRV of Betelgeuse. Figure and caption from Aurière et al. (2016).

some signal still persists, and all observations and analysis indicate that Betelgeuse has in fact the shape of a sphere, the only possibility left is that its surface brightness is not uniform over the disk. This could be explained by the presence of bright spots that are in fact the rising hot plasma in convective cells, which is consistent with numerical simulations by Chiavassa et al. (2009, 2010, 2011b) and interferometric observations of Betelgeuse (e.g. Haubois et al. 2009).

5.2.2 First mapping of bright spots

Based on the assumption that bright spots are present at the surface of Betelgeuse, Aurière et al. (2016) construct a simple model to map the surface of this RSG star as a combination of bright spots over a homogeneously bright disk. From polarimetric observations, one can derive the coordinates of the source of the signal (i.e., the spot) on the disk of Betelgeuse (see Figure 5.2): the position angle χ between the radius and

the North-South meridian of the disk and the projection angle μ between the spot and the disk center. Each spot would create an excess of polarization with orientation θ , the polarization angle. What is directly obtained from the data is actually the polarization angle θ . Using the classical linear polarization relations, as described by Bagnulo et al. (2009), and considering that for Narval, positive Q is defined in the North-South direction and positive U is defined at 45° counterclockwise relative to positive Q , the polarization angle θ is given by:

$$\theta = 0.5 \arctan(U/Q) + c \quad (5.1)$$

The parameter $c = 0$ if $Q > 0$ and $U \geq 0$. $c = 180^\circ$ if $Q > 0$ and $U < 0$ and $c = 90^\circ$ if $Q < 0$. The position angle χ can be inferred from θ as $\chi = \theta \pm 90^\circ$. This ambiguity of 180° in the position angle is inherent to polarization measurements. The projection angle μ on the other hand is inferred by the authors from the radial velocity of the polarization signal: the velocity along the line of sight would be maximal for a bright spot at the disk center, and would decrease when approaching the limb. Aurière et al. (2016) represent the velocities as in the case of an expanding atmosphere and make the approximation that all photospheric motions and the motion of the scattering layer are radial, and that their velocities combine at the polarization level to an identical velocity V_{\max} , which they assign the ad hoc value of 50 km s^{-1} . The polarization signal coming from a spot at a projection angle μ from the disk center then has a radial velocity of $V = V_{\max} \cos \mu$. Aurière et al. (2016) use their model to map the location of bright spots on the surface of Betelgeuse between 2013 and 2016. In Figure 5.3, a comparison of the images obtained with this model and images obtained with quasi-simultaneous interferometric observations are shown.

5.2.3 Giant convective cells and imaging through spectropolarimetry

Mathias et al. (2018) present a study based on long-term (7.5 years) spectropolarimetric observations of Betelgeuse with Narval between September 2009 and April 2017, focusing on the circularly polarized signatures (Stokes V) and their common behaviour with Stokes Q & U . These authors find that the Stokes V signal is mostly redshifted with respect to the stellar restframe velocity and to the center of the intensity profile, which they suggest may indicate that its origin are areas that favour radially downward motions. They also perform a period analysis of the Stokes I , V , Q and U signatures and find that they all show variations on the same timescale, which indicates that linear and circular polarization may have a common origin in Betelgeuse. The authors detect a period of around 1850 d, which is close to the LSP of Betelgeuse (around 2000 d) and point out that giant convective cells have been suggested as the possible origin of LSP of RSG stars by Stothers (2010), who also compute the typical turnover timescale of 2500 d for Betelgeuse. Based on the conducted analysis, the authors confirm that giant convective cells are the origin of polarization in Betelgeuse, and propose that linear polarization originates from the bright and hot regions of upflowing plasma, and circular polarization originates from the dark intergranular lanes, where the cooling plasma sinks towards the stellar interior and the magnetic field lines are trapped by the convective flows.

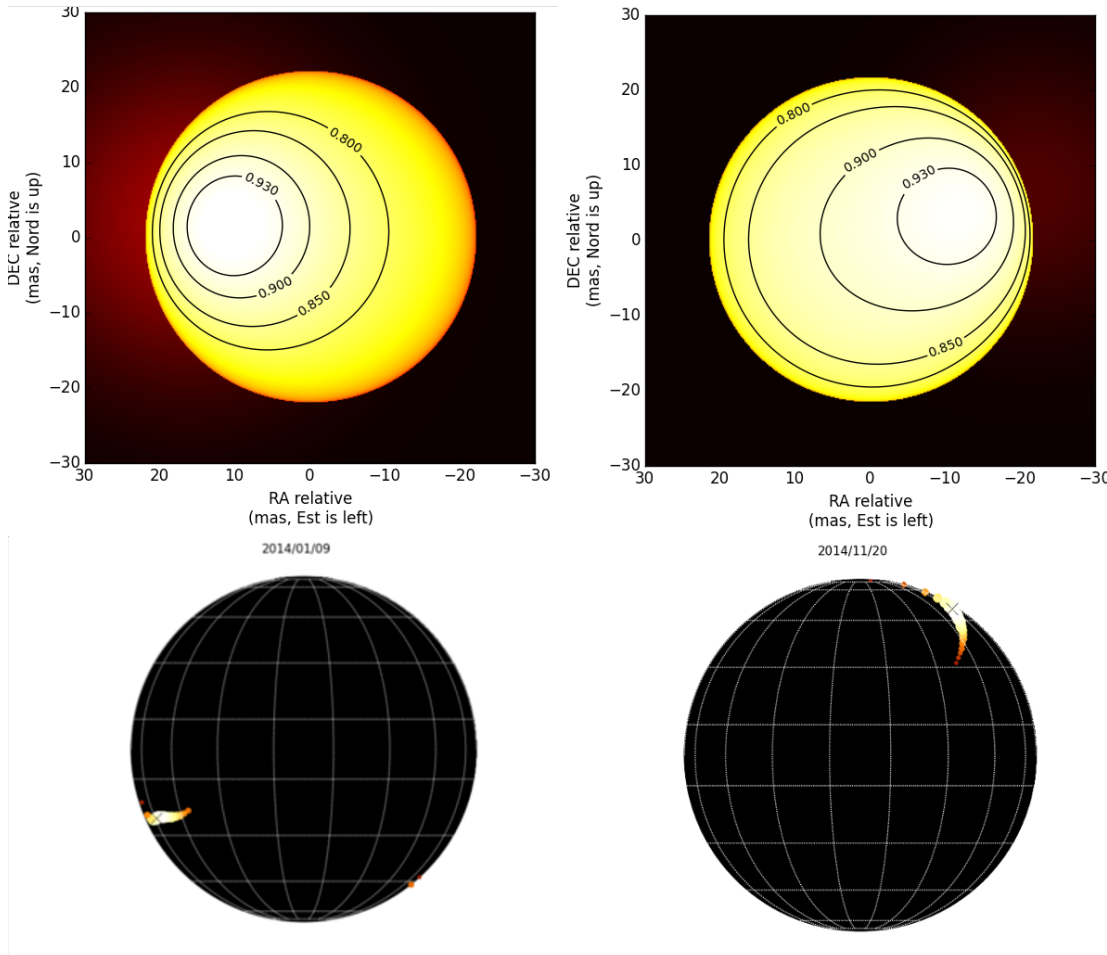


Figure 5.3: Comparison of intensity images of Betelgeuse obtained with VLTI/PIONIER (upper images, from Montargès et al. 2015) and with TBL/Narval (lower images) during the quasi-simultaneous observations of 2014: January (left) and November (right). North is up and east is left for all images. Figure and caption from Aurière et al. (2016).

Based on the works of Aurière et al. (2016) and Mathias et al. (2018) which strongly indicate that giant convective cells must be the origin of both linear and circular polarization in the spectrum of Betelgeuse, López Ariste et al. (2018) present a method for imaging the photosphere of RSG stars (in particular Betelgeuse) using high-resolution linear polarization measurements. The authors develop a new model that presents the surface brightness distribution of Betelgeuse using a linear combination of real spherical harmonics. In the model of López Ariste et al. (2018) the surface brightness B as a function of the distance μ from disk centre and the polar angle χ is defined by a set of parameters a_n and is given by

$$B(\mu, \chi) = \left\| \sum_{\substack{l=0, l_{max} \\ m=-l, +l}} a_l^m y_l^m(\mu, \chi) \right\|, \quad (5.2)$$

where l is the maximum allowed number of the spherical harmonics, and the function $y_l^m(\mu, \chi)$ is defined as

$$y_l^m(\mu, \chi) = \sqrt{2}(-1)^m \Re(Y_l^m(\mu, \chi)), \quad \text{if } m > 0, \quad (5.3)$$

$$y_l^m(\mu, \chi) = \sqrt{2}(-1)^m \Im(Y_l^m(\mu, \chi)), \quad \text{if } m < 0, \quad (5.4)$$

$$y_l^m(\mu, \chi) = \Re(Y_l^m(\mu, \chi)), \quad \text{if } m = 0, \quad (5.5)$$

where \Re and \Im are the real and imaginary parts of the spherical harmonics, respectively, and

$$Y_l^m(\mu, \chi) = \sqrt{\frac{2n+1}{4\pi} \frac{(n-m)!}{(n+m)!}} e^{im\chi} P_n^m(\mu), \quad (5.6)$$

where $P_n^m(\mu)$ is the associated Legendre polynomial.

López Ariste et al. (2018) argue that in the presence of convection, the radiative losses (and hence, the brightness) have to be balanced by the enthalpy flux (see Nordlund et al. 2009 for the case of solar granulation). Thus, brightness must depend on the radial component of the velocity as

$$B(\mu, \chi, V_z) \propto \sigma T_{\text{eff}}^4 \approx \rho V_z \left(\frac{5}{2} k_B T + x \Xi \right), \quad (5.7)$$

where on the left side we have the black body dependency between brightness and effective temperature, and on the right side we have the enthalpy flux, described by the density ρ , the vertical velocity V_z , the gas temperature T , the ionization fraction of hydrogen x and its ionization potential Ξ . However, since the brightness distribution $B(\mu, \chi, V_z)$ is adimensional and normalized, the authors calculate a velocity in standard units by defining a global velocity V_{max} that represents the maximum upflow velocity at the brightest point on the stellar disk. This V_{max} is set so that the maximum Doppler shift, which is observed at the disk centre, can cover the most blueshifted signals observed

in the stellar spectrum (see Figure 5.4). In the case of Betelgeuse, the authors point that this velocity must be at least 40 km s^{-1} . The Doppler velocity is then modelled at any point over the stellar disk as

$$V = V_{\max} \cos(\mu) B(\mu, \chi, V_z) \quad (5.8)$$

The authors note that points that are moving away from the observer (i.e. that have

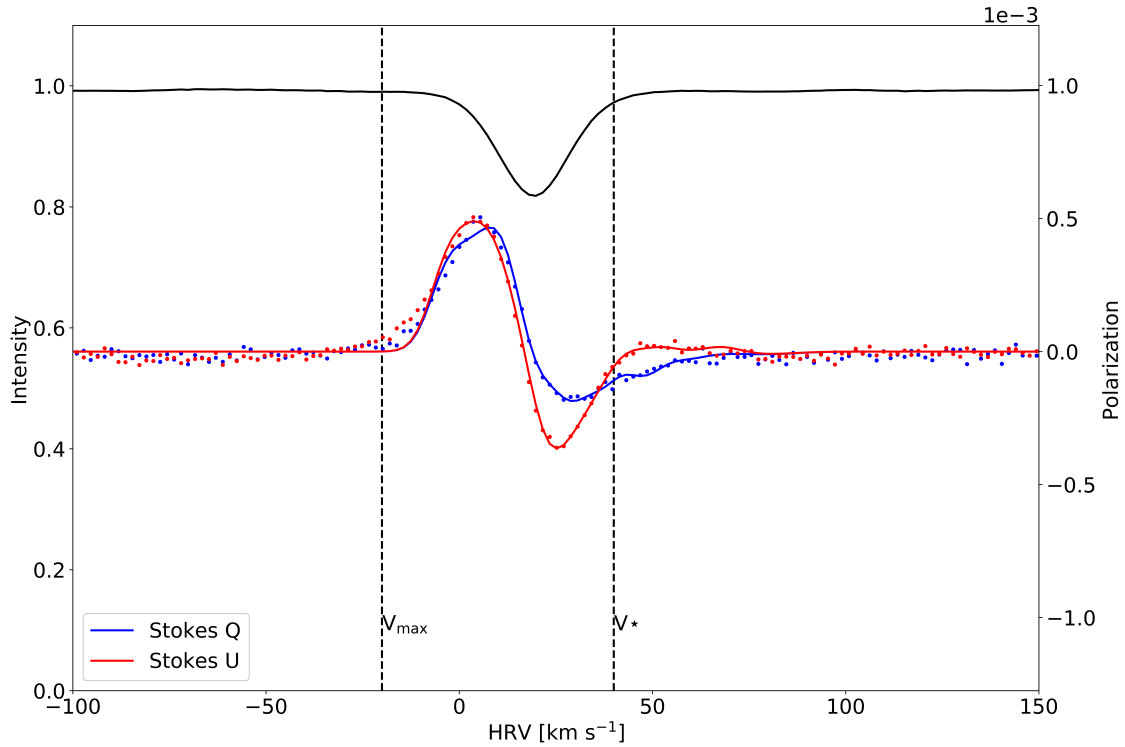


Figure 5.4: An example fit of the observed on 2013/12/20 Stokes Q and U signatures in the LSD profile of Betelgeuse using the method of López Ariste et al. (2018). The observed intensity spectrum is shown with a black solid line. The blue and red points correspond respectively to the observed Stokes Q and U measurements, and the solid blue and red lines - to their respective fits. The left and right vertical dashed lines indicate respectively the maximum global convective velocity V_{\max} (selected so that it covers the most blueshifted signals) and the restframe velocity of Betelgeuse V_* .

a redshifted signal) are assigned values close to zero instead of negative ones, which in practice only offsets the zero velocity definition. Furthermore, López Ariste et al. (2018) assume in their model that all the plasma moves only vertically, i.e. in a radial direction with respect to the center of star. This imposes a condition on the velocity fields. At the two extremes, the brightest plasma, wherever it is over the disk, is always assumed to move at the global maximum velocity V_{\max} , and the darkest plasma, wherever it is over the disk, is assumed to sink vertically at that same velocity V_{\max} . As the authors

point out, this assumption does not necessarily have to be true all the time, and most likely is not, since there is no reason why the convective motions should have the same velocity and keep it constant in time. However, in the absence of a way to precisely determine the individual maximum convective velocities for every single observation, the only possible solution is to select a single value which is large enough to encompass the span of polarized signatures in radial velocity space for all the observations. The plasma which has intermediate brightness also needs to be assigned a sign and velocity. López Ariste et al. (2018) impose in their model that the 75% brightest plasma is rising and the darkest 25% is sinking. The choice of this particular ratio is selected so that the brightness distribution resembles that of the solar granulation.

The reader may view these many assumptions as just guesses as to what the actual velocity distribution at the photosphere of Betelgeuse is. However, the final results of the method – the inferred images of the visible surface of Betelgeuse – appear in very good agreement with those obtained using interferometry, which would then justify the underlying assumptions.

Finally, in the model of López Ariste et al. (2018) the Stokes Q and U amplitudes integrated over the stellar disk are given by

$$Q(V) = \sum_{\mu, \chi, V_z} B(\mu, \chi) \sin^2 \mu \cos 2\chi e^{-(V-V_z)^2/6^2}, \quad (5.9)$$

$$U(V) = \sum_{\mu, \chi, V_z} B(\mu, \chi) \sin^2 \mu \sin 2\chi e^{-(V-V_z)^2/6^2}, \quad (5.10)$$

where $e^{-(V-V_z)^2/6^2}$ is a term that accounts for the instrumental profile of Narval. As the authors point out, the brightness distribution inferred from this model is only one of the possible distributions, mainly due to the 180° ambiguity described in Section 5.2.2. To pick the solution that best matches the actual surface brightness distribution of Betelgeuse, López Ariste et al. (2018) check the maps they obtain with images obtained (quasi-)simultaneously via interferometry. The correspondance between the brightness maps obtained using spectropolarimetry and interferometry is shown in Figure 5.5 for two observations of Betelgeuse and one of another RSG star, CE Tau.

The objective of the method of López Ariste et al. (2018) is for each pair of observational Stokes Q and U to find the set of parameters a_n in Eq. 5.2 that best fit the observed profiles (an example fit is shown in Figure 5.4). To do this, the authors use a Marquardt-Levenberg minimisation over the χ^2 difference between model and observation, limiting the maximum quantum number l_{max} of the spherical harmonics in Eq. 5.2 to $l_{max} = 5$ based on the resolution of their observations. The authors use the described method to obtain images of the surface brightness of Betelgeuse from observations between 2013 and 2018; their results are shown in Figure 5.6 (from López Ariste et al. 2018). The images inferred using the described method are in good agreement with direct imaging results for Betelgeuse obtained with interferometry (see Figure 5.5). From

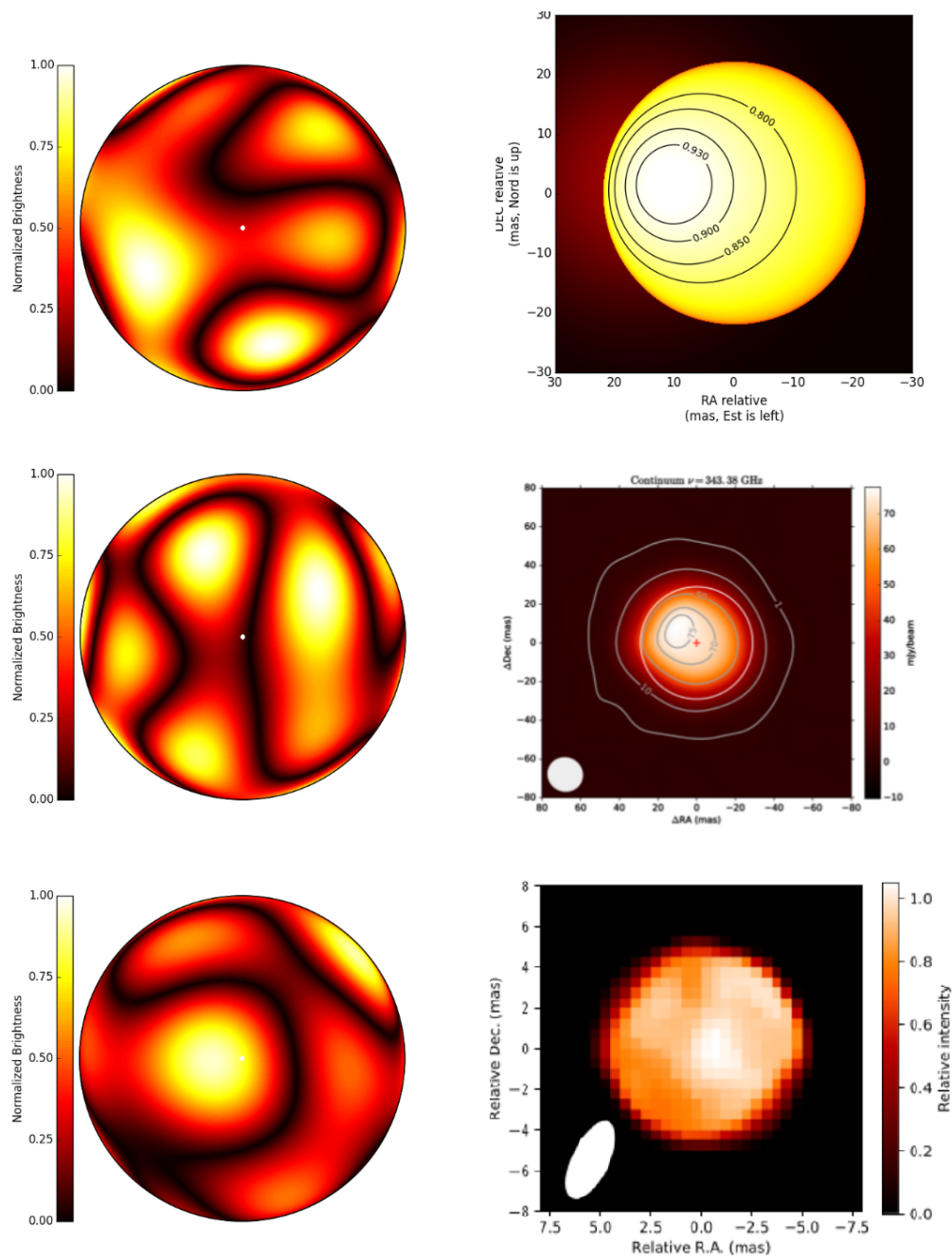


Figure 5.5: Top left: inferred image of Betelgeuse on January 9, 2014. Top right: reconstructed image from PIONEER interferometric observation on the same date (Montargès et al., 2015). Middle left: inferred image of Betelgeuse on December 9, 2015. Middle right: image from ALMA made from observations on November 9, 2015 (Kervella et al., 2018). Bottom left: inferred image of the RSG star CE Tau on December 17, 2016. Bottom right: image of CE Tau on December 22–23, 2016 reconstructed from CHARA interferometry (Montargès et al., 2018). Figure adapted from López Ariste et al. (2018).

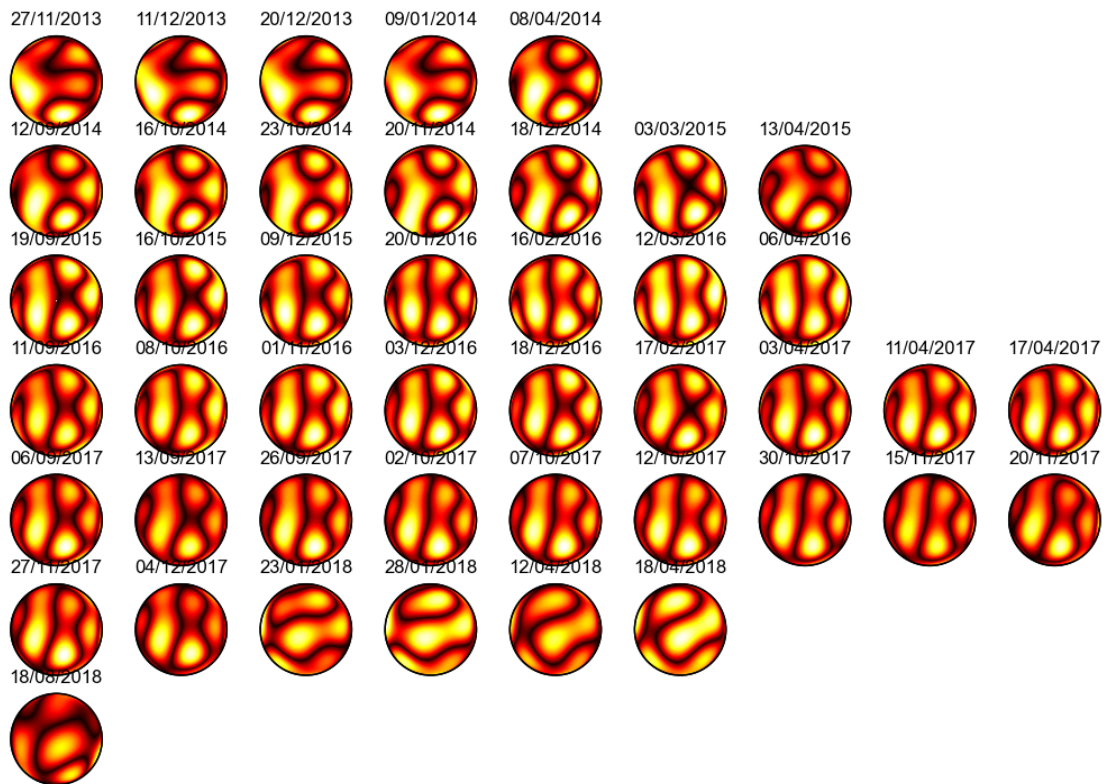


Figure 5.6: Inferred images from spectropolarimetric Narval observations of Betelgeuse from November 2013 to August 2018. Figure from López Ariste et al. (2018).

these reconstructed images the authors find that the typical size of convective cells at the surface of this RSG is 0.6 times the disk radius, their number is typically 3-5 over the visible hemisphere and their lifetime can be of the order of a few years. Using this method, the authors are also able to evaluate the characteristic velocities of the upflow and downflow of plasma at the surface of Betelgeuse to be of the order of 20 km s^{-1} .

5.3 The path to 3D-imaging of Betelgeuse

In this section, I will introduce our analysis of the profiles of Betelgeuse and discuss the points which led us to building the 3D-images of its photosphere in the paper accepted for publication in *A&A*. I will first explain the way we regard the intensity LSD profiles of Betelgeuse, since it differs from the way the intensity profiles of most other stars are viewed, including R Sct and the M giants studied previously in this Thesis. After this, I will turn to the linearly polarized signatures in Betelgeuse in order to re-evaluate the convective velocities established by López Ariste et al. (2018), and finally to introduce the assumptions that allow us to build 3D-images of the photosphere of this RSG star.

5.3.1 Analysing the intensity profiles

The rotational period of Betelgeuse is estimated to be in the range of 12 to 25 years (Uitenbroek et al., 1998; Kervella et al., 2018) which leads to a maximum rotational velocity of at most 10 km s^{-1} . Such a velocity is much smaller than the value we infer for the maximum convective velocity in Betelgeuse ($\sim 60 \text{ km s}^{-1}$, see Section 5.3.2). This is why, to simplify our model, we consider that Betelgeuse does not rotate, as it is also the case in López Ariste et al. (2018). In our model, the only process which contributes to the broadening of the LSD mean spectral line is convection, and its effect differs significantly from those of rotation and macroturbulence. While the latter two sources of broadening yield a symmetrical spectral profile for which the peak depth corresponds to the radial velocity of the star, in the case of convection the peak of the line is shifted to the blue of the true radial velocity. As explained in López Ariste et al. (2018), in this case the hot, rising plasma has the largest contribution in the formation of the spectral profile because it is brighter, and due to its upward motion yields a blueshifted signal; the cool, sinking plasma has a much smaller contribution to the spectral line profile, and the signal is redshifted due to its downward motion. Thus, the overall spectral line profile formed when convection dominates the velocity field is mostly blueshifted, since the majority of the signal comes from plasma moving upwards.

We retain the same assumption as in López Ariste et al. (2018) that the 75% brightest plasma is rising towards the surface of the star, while the darkest 25% are moving downwards, similar to the case of solar granulation. The 2D-images of Betelgeuse obtained by López Ariste et al. (2018) also rely on the same assumption. Since they match the images obtained using interferometry very well (see Figure 5.5), this suggests that this assumption is acceptable. This 75:25 ratio means that the larger and hotter part of the

plasma, which is also responsible for most of the signal in the intensity profile, is rising and so is blue-shifted with respect to the restframe of the star. The darker 25% portion has only a minor contribution to the intensity profile, diminished even further by its lower temperature, and is red-shifted from the stellar restframe since it moves towards the center of Betelgeuse and away from the observer. Because of this assumption of the distribution of brightness with respect to velocity, one must expect an intensity profile which is almost entirely blue-shifted from the center of mass of the star, as shown in Figure 5.4. It is important to note that this view of the intensity profile does not differ from the one adopted in López Ariste et al. (2018). In Section 5.3.2, we shall see precisely how to determine both the center of mass velocity V_* and the global maximum convective velocity V_{\max} .

5.3.2 Characteristic velocities

López Ariste et al. (2018) model the Doppler velocity at a given point over the disk of Betelgeuse using Equation 5.8. As it was explained in the previous section, the parameter V_{\max} represents the global maximum velocity of the convective motions over the disk. As López Ariste et al. (2018) point out, this velocity must be at least 40 km s^{-1} for Betelgeuse. Now, in the present work, we attempt to further precise this parameter and show that its value may be even higher.

Let us consider the way that the inversion algorithm of López Ariste et al. (2018) determines the position of a bright spot on the disk of Betelgeuse, and more specifically, the distance $\cos \mu$ from disk center. The algorithm considers that all the plasma moves at vertical velocity $V_z = \pm V_{\max}$, and it is only its projection V_l along the line-of-sight that changes for points over the disk with different $\cos \mu$. This means that any bright plasma at disk center is expected to move at velocity $V_l = V_{\max}$. If the velocity V_l of the plasma is lower than the maximum convective velocity V_{\max} , the inversion algorithm will place it away from disk center, to a position where $V_l = V_{\max} \cos \mu$. In other words, the algorithm will consider polarization signatures which appear close to the maximum velocity V_{\max} to be formed near the disk center, and signatures which have lower projected velocities to be formed further away from it. In the extreme case where the projected velocity V_l is equal to the center-of-mass velocity of the star V_* , the bright structure will be placed at the limb of Betelgeuse. The way that the distance of the spot from disk center is determined based on the position of the linearly polarized signal in radial velocity space is depicted in Figure 5.7.

In order to establish the global maximum velocity V_{\max} of the convective flows, I analysed the distribution of linear polarization signals in radial velocity space for the full set of Stokes Q and U observations of Betelgeuse available at the time from Narval and NeoNarval between November 2013 and February 2021. This dataset consists of 62 observational nights. I examined both the peaks and the limits of the signals; to select the latter, I located for each observation the bluemost and redmost radial velocities where the signal is still above 2.5 times the standard deviation of the continuum polarization.

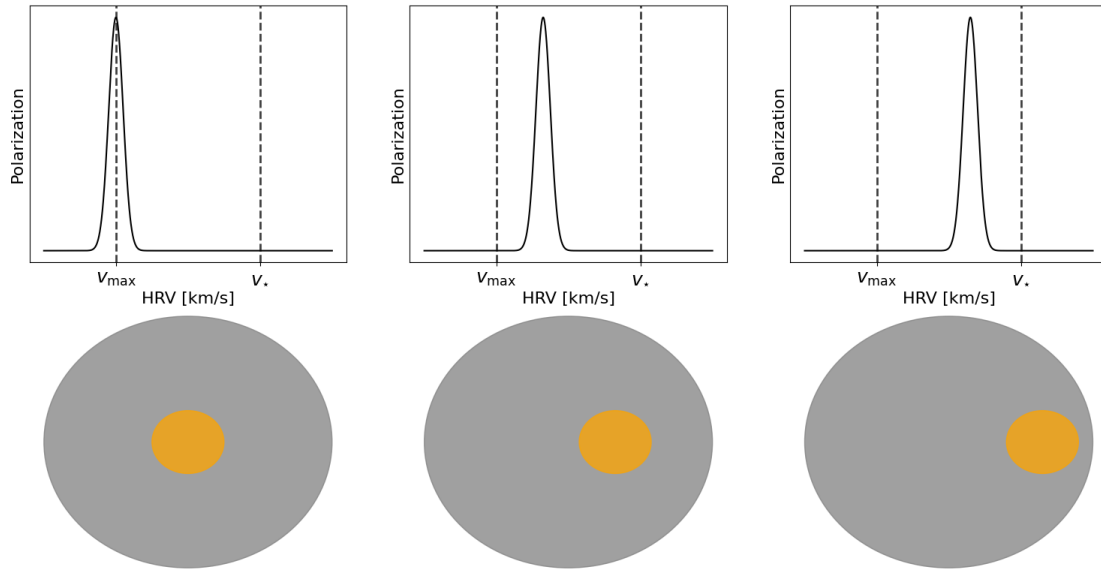


Figure 5.7: Top: representations of linearly polarized signals at three different radial velocities; bottom: representations of inferred bright spot positions for each of the corresponding velocities. The polar angle χ is not considered here. Notice that the further away the signal is from V_{\max} , the closer to the limb the position of the spot is inferred.

The two distributions are shown in Figure 5.8. There, the restframe velocity of Betelgeuse is shown by a red line and is chosen so that most of the polarization peaks would be blue-shifted with respect to it, as expected in the case where convection dominates the velocity fields (see the Section 5.3.1). With that being said, V_* is set at 40 km s^{-1} in the heliocentric restframe. From this stellar restframe velocity V_* , it can be seen that the polarized signatures can be found well up to 50 and even 60 km s^{-1} towards the blue. This is why in our analysis the parameter V_{\max} is set to 60 km s^{-1} with respect to V_* . This large velocity of the convective flows might be enough to result in mass-loss from Betelgeuse, provided it does not diminish much in altitude – which indeed appears to be the case.

5.3.3 Gray atmosphere

To simplify the model, in the present work all polarization of the continuum of Betelgeuse is assumed to be due to scattering. Let us define $Q(\nu)$ as the emergent polarization at a given frequency ν in the direction of the observer and $I_{\text{scattered}}(\nu)$ as the total intensity of scattered light at the same frequency. The anisotropy factor $w_\nu \approx \frac{Q(\nu)}{I_{\text{scattered}}(\nu)}$ is then computed in two extreme cases, in which: 1) the scattering occurs in a gray atmosphere, where we have a blackbody emission described by the Planck function; 2) the scattering occurs in the outer atmosphere, i.e. sufficiently far away from the photosphere that the radiation field is cylindrically symmetrical around the radial direction. It can be seen

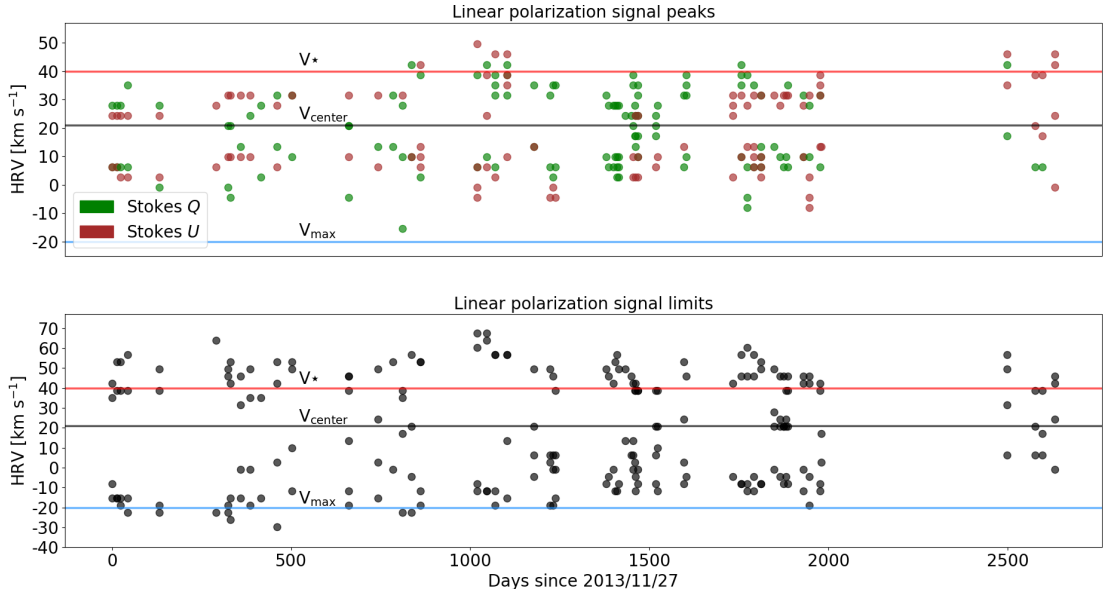


Figure 5.8: Upper panel: distribution of the observed peaks in the Stokes Q (green) and U (brown) signals in HRV-space in the spectra of Betelgeuse obtained with Narval and NeoNarval. Lower panel: distribution of the limits of the Stokes Q and U signals in HRV-space. NeoNarval data starts from day 2200 on. For both panels, the horizontal lines mark three velocities: $V_{\star} = 40 \text{ km s}^{-1}$ (red line), selected so that most of the observed signal peaks are found towards the blue with respect to it; the blue line corresponds to $V_{\text{max}} = 60 \text{ km s}^{-1}$ with respect to V_{\star} , selected so that all of the observed peaks in the signal are found towards the red with respect to it; $V_{\text{center}} = 22 \text{ km s}^{-1}$ (black line), the intensity line center.

in Figure 5.9 that the outer atmosphere scenario predicts very high local polarization levels ($\sim 10\%$) even at very low heights. The gray atmosphere on the other hand predicts much lower degrees of polarization when approaching the photosphere, which is consistent with both theoretical and observational estimations, as it will be shown next.

We consider that a gray atmosphere is the right approximation for the polarization in Betelgeuse for two reasons. First, Aurière et al. (2016) suggest that the observed net linear polarization in Betelgeuse is in fact due to depolarization of the continuum in atomic lines. The calculations of Josselin et al. (2015) and López Ariste et al. (2018) show that the degree of linear polarization in the continuum in this star is about 1% at the limb. This order of magnitude is in good accordance with the predictions of the gray atmosphere model. Second, we know from (Neo)Narval observations that the *disk-integrated* rate of linear polarization in Betelgeuse is between 0.05% and 0.1%. However, to compare the observations to the w_ν values computed from the gray atmosphere model, we must evaluate the *local* rate of polarization. In fact, if the disk of Betelgeuse were homogeneous in terms of surface brightness, local polarization would integrate to zero over it and we would not observe any net polarization signal. The fact that such a signal can be measured shows that brightness inhomogeneities exist at the photospheric level. It is these structures that López Ariste et al. (2018) consider to be convective cells and then model using spherical harmonics. In Figure 5.10 it is shown that if we model the surface of Betelgeuse using spherical harmonics with realistic brightness distributions, the most probable net polarization rate observed would be around 10% of the local polarization. Since we know that the disk-integrated polarization observed with (Neo)Narval is between 0.05% and 0.1%, the local polarization must be between 0.5% and 1%, in good agreement with the gray atmosphere approximation.

The gray atmosphere model agrees with both theoretical and observational estimations of the local polarization rate. For this reason, we use this approximation in order to build 3D-images of Betelgeuse. Following the right panel of Figure 5.9, a gray atmosphere would yield polarization rates of up to 1% in the optical depth interval $\log \tau$ between -1 and 0, and so the maps we produce are also constrained in this interval.

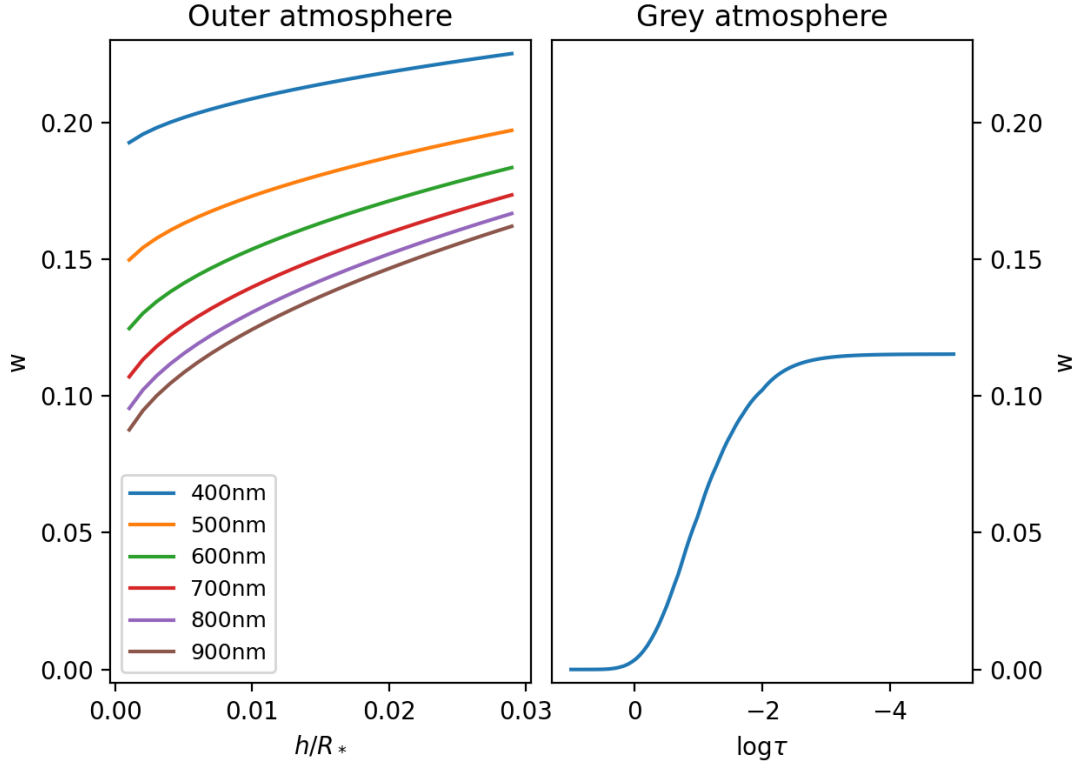


Figure 5.9: Calculations of the anisotropy factor w in the outer atmosphere (left) and in the gray atmosphere (right) approximations. The abscissae are different due to the nature of those approximations - distance to the photosphere (as a fraction of the stellar radius) for the outer atmosphere and optical depth for the gray atmosphere.

5.3.4 The linearly polarized profiles: an in-depth view

Aurière et al. (2016) present the variations of the linear polarization $P_L = \sqrt{Q^2 + U^2}$ with respect to the depth of spectral lines for four of their observations of Betelgeuse (obtained between November 2013 and January 2014): this is shown in Figure 5.11. The authors build ten excluding sub-masks based on line depth between 0 and 1 with a step of 0.1. After that, LSD is performed with each of the sub-masks and the respective values of P_L for each LSD output are computed. What is particularly interesting in Figure 5.11 is that the strength of the linearly polarized signals strictly follows the line depth: the deeper the lines, the stronger the polarization. In the present work, the same behaviour is found for most of the observations obtained between 2013 and 2021. Aurière et al. (2016) already note in their work this dependency of the linear polarization rate on the line depth, and point out that linear polarization in Betelgeuse must also strongly increase with altitude, since deeper lines are generally formed higher in the atmosphere.

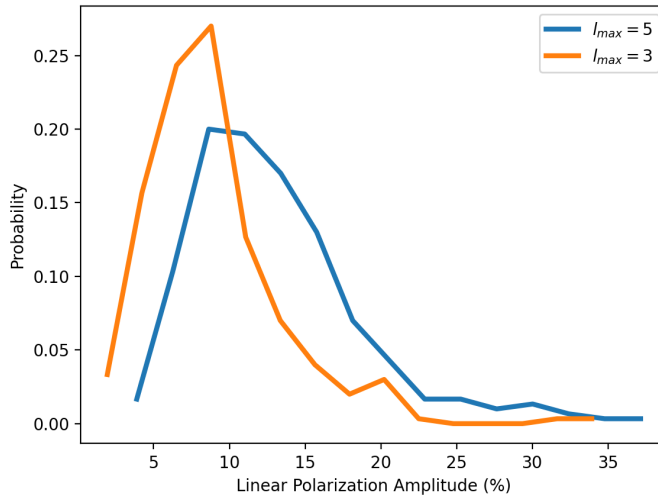


Figure 5.10: Expected net linear polarization rates from different realistic surface brightness distributions built from combinations of spherical harmonics of maximum order $l = 3$ and $l = 5$. The computations assume that local scattering results in 100% polarization. It can be seen that both distributions peak at around 10% – that is, the net polarization rate must be around 10% of the local polarization.

As we shall see next, this idea will turn out to be the key to building 3D-images of the photosphere of this supergiant star.

In the present work, we make the assumption that the continuum polarization is formed by a single scattering event in the formation of the continuum; this scattering event is then immediately followed by an in-place absorption of the polarized photon by an atom, which then re-emits the photon, now unpolarized (thus atomic lines depolarize the continuum). This assumption will be referred to as the *single scattering approximation*.

Using the single scattering approximation, the altitude of formation of spectral lines in each individual depth range (0.4-0.5, 0.5-0.6, etc.) can be inferred by approximating their peak polarization rate measured from their LSD profiles with the anisotropy factor w_ν in a gray atmosphere. This is shown in Figure 5.12, where it can be seen that the lines with highest linear polarization signal must form at optical depth $\log \tau = -0.4$, and those with the lowest - at $\log \tau = 0.4$.

To summarize, lines which show higher polarization rates must be formed higher in the atmosphere of Betelgeuse because the anisotropy of the radiation increases with altitude, and so does the degree of polarization (since $w_\nu \approx \frac{Q(\nu)}{I_{\text{scattered}}(\nu)}$). This relation is used to order the spectral lines by altitude of formation. It turns out that, in the general case, the deeper the spectral line is, the higher its polarization rate, and also the

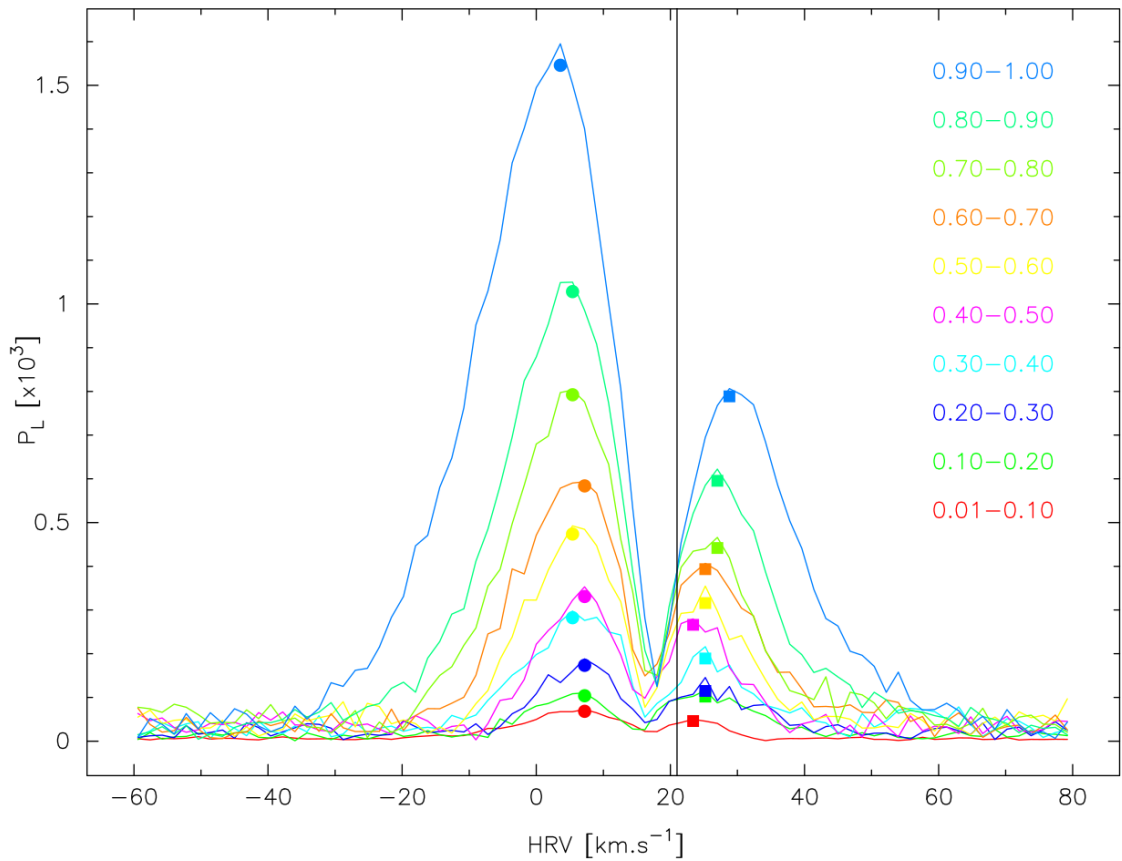


Figure 5.11: Variations of the linear polarization P_L of Betelgeuse from the LSD profiles with the depth of the lines. Ten sub-masks are used with line depth domains as indicated on the graph. The vertical line corresponds to Betelgeuse's heliocentric radial velocity as considered by Aurière et al. (2016). Figure from Aurière et al. (2016).

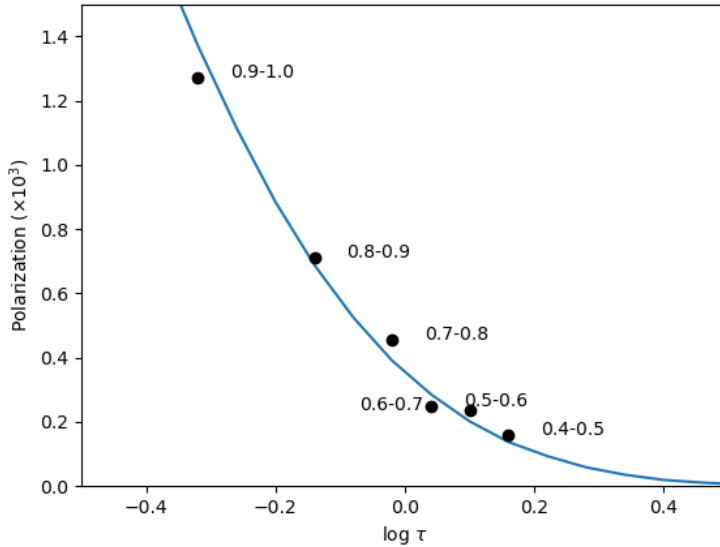


Figure 5.12: The blue line represents the dependence of the rate of polarization on the optical depth $\log \tau$ according to the gray atmosphere model assuming a 1% rate of local polarization. The black dots represent the observed linear polarization peak amplitudes for the 6 masks, and their abscissae are determined as the optical depth at which the grey atmosphere model fits the observed polarization amplitude.

higher it forms in the atmosphere. This goes well with the general notion that the deeper the line, the higher it forms. In the present work, 3D-images are built only for these observations in which this ordering is present, which make up most of the observational dataset. Following the gray atmosphere model, the deepest lines (which also show the strongest net linear polarization) must be formed at $\log \tau = -0.4$, while the shallowest ones must be formed at $\log \tau = 0.4$, which corresponds roughly to $1.1 - 1.3R_{\star}$.

5.4 Building the 3D-images

In order to create the 3D-images of Betelgeuse, a set of six different and excluding LSD line masks are used, computed using linelists from VALD for the known parameters of Betelgeuse: $T_{\text{eff}} = 3750$ K, $\log g = 0.0$ and microturbulence of 4 km s^{-1} (Josselin & Plez, 2007; Lambert et al., 1984). These are the same parameters Aurière et al. (2016) used in order to build their line masks. The different masks discriminate spectral lines based on their depth with respect to the continuum level, starting from 0.4 and going by steps of 0.1 up to 1.0, similar to the way it was done by Aurière et al. (2016). Following the gray atmosphere model presented in the previous section, the 0.4-0.5 mask is expected to probe optical depth of $\log \tau = 0.4$, the 0.9-1.0 one – $\log \tau = -0.4$, and the other

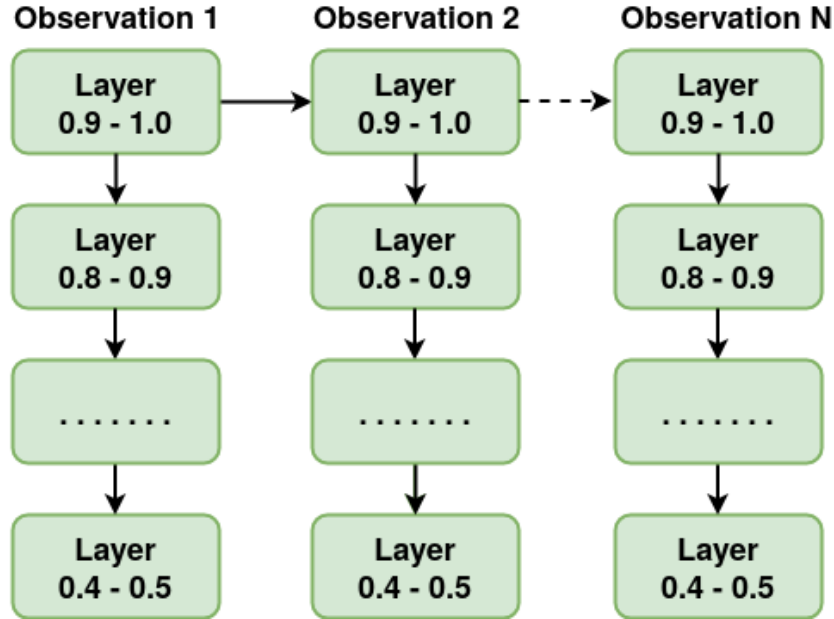


Figure 5.13: Order of fitting of the different LSD outputs corresponding to different layers of the atmosphere of Betelgeuse. The top layer (0.9-1.0) in the first observation starts with a random solution. For each individual observation, to ensure consistency between structures in the different layers, the fitting of each layer (except the top one) uses the fit of the previous (upper) layer as a starting solution. To ensure consistency in between structures in different observations, the top layer of each observation uses as a starting solution the fit of the top layer of the previous observation.

four masks to cover the layers inbetween in ascending order.

After computing for a given observation the six LSD profiles that correspond to the different line masks, the same inversion algorithm developed by López Ariste et al. (2018) is used to build a 2D-image of each of the six LSD outputs. To ensure that the individual 2D-images for any given date are consistent with each other, when treating any layer but the top one the inversion algorithm is forced to use as an initial solution for the spherical harmonics the solution of the layer above. On the other hand, to ensure that the 3D-images are consistent date-to-date, the solution of the top layer for the $(N - 1)^{\text{th}}$ observation in the data set is used as an initial solution for the top layer of the N^{th} observation. The top layer of the first observation in the data set starts with a random initial solution. This order of fitting of the different layers is shown schematically in Figure 5.13.

In the present work, I use the *python3* library *mayavi*¹ for 3D-visualization to draw

¹<https://docs.enthought.com/mayavi/mayavi/>

for each date of observation the six 2D-images on top of one another, placing them in the expected order. Simply drawing layers on top of each other, however, would not result in a true 3D-image; instead, by doing so only the top layer would be visible, while all the underlying ones would be hidden underneath. In order to be able to see structures in depth, the layers must be, to a certain degree, transparent. In the 3D-images we obtain, each pixel in the individual 2D-layers that constitute the full image can have a brightness value between 0 and 1. Since it is the bright structures (the ascending parts of convective cells) that are of most interest for the study, all pixels with brightness above 0.5 are set to have a 95% opacity, those with brightness between 0.15 and 0.5 – 15% opacity (i.e. to be mostly transparent), and those below 0.15 are fully transparent, meaning they are not drawn at all. In this way, the bright upflowing parts of convective cells can be easily traced, even if they are covered by dark areas of downflowing matter above them. An example 3D-image of Betelgeuse inferred from the observation on 2018/09/19 is shown in the left panel of Figure 5.14.

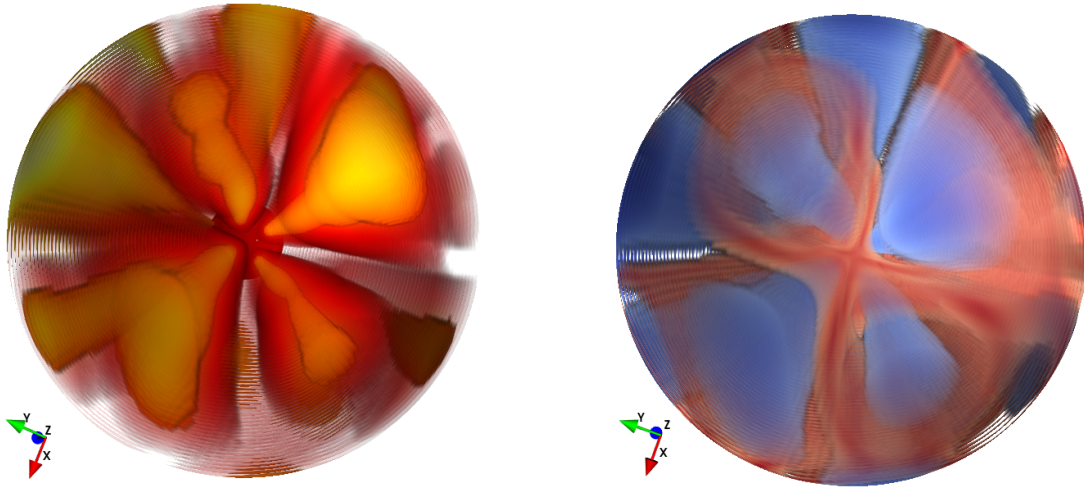


Figure 5.14: Example 3D-images of Betelgeuse on 2018/09/19 in brightness (left panel) and velocity (right panel). Left image: yellow shows the hotter regions, while red shows the cooler regions; the rising parts of convective cells are well defined, because they are non-transparent, while the dark intergranular cells are not shown (i.e., they are made fully transparent). Right image: the 3D-map of the same observation from the same point of view, but showing the convective velocity field instead – rising plasma is in blue, sinking plasma is in red. Both images are not up to scale, but instead the height of the probed atmospheric layers is exaggerated in order for variations in the convective structures in altitude to be more easily detectable.

Instead of drawing brightness, it is also possible to draw radial velocity in the exact same way. While in our model brightness is strictly related to velocity, and the information that is shown by drawing one or the other is the same, sometimes looking at

the same data in different ways can be beneficial. In the case where radial velocity is drawn, the transparency depends on its absolute value. This means that both upflows and downflows are opaque, while the pixels with radial velocity close to zero are fully transparent (and cannot be seen at all). An example of a 3D-image of the velocity fields in Betelgeuse is shown in the right panel of Figure 5.14.

Another assumption which must be taken into account is that all plasma moves at the global maximum velocity V_{\max} , and that it is only its line-of-sight component (the radial velocity) that changes over the visible disk of Betelgeuse. This is a strong assumption, which as we will see next will work to our advantage when tracing the velocity fields.

5.5 Reading the 3D-images

When looking at the 3D-images, one must be cautious of all the approximations made when building them. In particular, it must be kept in mind that the inversion algorithm is biased towards inferring vertical structures, since each layer uses the solution for the one above it as an initial solution (as described in Section 5.4), and so it is expected that the final 3D-image would show vertical structures that may resemble convective flows. These structures must always be viewed with caution. Let us imagine a rising flow of plasma that has a radial velocity of $V_{\text{rad,initial}} < V_{\max}$ at the very bottom layer and then decelerates in altitude due to gravity. At the lowest layer, considering Figure 5.7, a bright spot that has a radial velocity less than V_{\max} must be placed away from the disk center. Also, since the flow decelerates, in the upper layer its radial velocity will be less than $V_{\text{rad,initial}}$. The inversion algorithm is bound to now place this granule closer to the limb in the upper layer. As the plasma continues to decelerate in altitude, the inversion algorithm has no other choice but to place the bright spot further and further away from disk center in each subsequent layer. As a result, in the final 3D-image we would see a bright structure that progressively bends towards the limb, as it is the case for granule number 1 in Figure 5.15. In reality, the convective flow does not bend, but instead slows down in altitude. It is only depicted like this because apart from bending the structure towards the limb, the inversion algorithm has no other way of handling the decrease in velocity.

This also works in reverse: for flows that accelerate in altitude, the bright structure will be drawn as bending towards disk center for the same reason, as it is the case for granule number 2 in Figure 5.15. Finally, a vertical structure that rises without bending (such as, e.g., granule 3 in Figure 5.15) would mean that the convective flows maintain a constant velocity in altitude. While such vertical flows must always be viewed with caution since the inversion code is biased to inferring such structures (as explained above), convective flows that bend, either towards the limb or towards disk center, are not inherent to the algorithm and the implications they have on changes in velocity must be regarded as real.

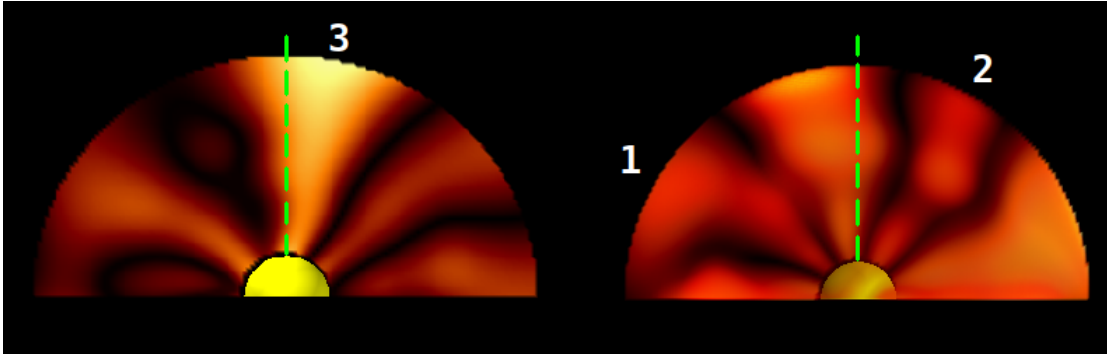


Figure 5.15: 2-dimensional cuts on the inferred atmosphere of Betelgeuse (not up to scale) on 2013/12/12 (left) and 2021/02/10 (right). In both panels, the line between the disk center and the observer is indicated by the dashed green line. In the right panel, granule 1 appears to be bending towards the limb as it rises. As explained in Section 5.5, this is due to the convective flow slowing down in altitude. Conversely, granule 2 (right panel) appears to be bending towards the disk center as it rises, indicating that the convective flow actually accelerates in altitude. Granule 3 (left panel) appears to have an almost vertical shape, showing no significant bending towards either the limb or the disk center.

5.6 Results and conclusion

In the present work, two example dates are shown at which observations of Betelgeuse are available: December 12th, 2013 and February 12th, 2021. At both these dates, we find the ordering of atomic lines by linear polarization rate and line depth, as it is shown in Figure 5.16. The 3D-images reveal several structures which bend towards the limb, indicating that plasma is slowing down due to gravity; however, structures that maintain a vertical profile can also be seen, showing that there must be at least one force present in the lower atmosphere ($1.1 - 1.3R_{\star}$) of Betelgeuse that counteracts gravity and keeps the vertical velocity of plasma constant. We also encounter structures that appear to change their acceleration with altitude: some begin their ascent at constant velocity and then decelerate (i.e. appear to bend towards the limb); one particular structure in the image from 2021 begins rising vertically in the bottom layers, and then bends towards disk center (granule 2 in Figure 5.15). This suggests that the plasma associated to it at a certain level actually begins to accelerate in altitude, another sign of the presence of a force that acts against gravity.

It is also shown in Figure 5.17 that, according to our model, the plasma does not reach escape velocity in the atmospheric layers probed by the 3D-images, but approaches it closely for some of the granules. If the force (or forces) counteracting gravity continues to act in the higher layers of the atmosphere and the plasma maintains the same velocity until $1.6R_{\star}$, it will escape the gravity of Betelgeuse and contribute to the stellar wind.

5.6. RESULTS AND CONCLUSION

We thus conclude that the mechanisms for wind-driven mass loss in Betelgeuse, and possibly other RSG stars, may already be present at the level of the photosphere.

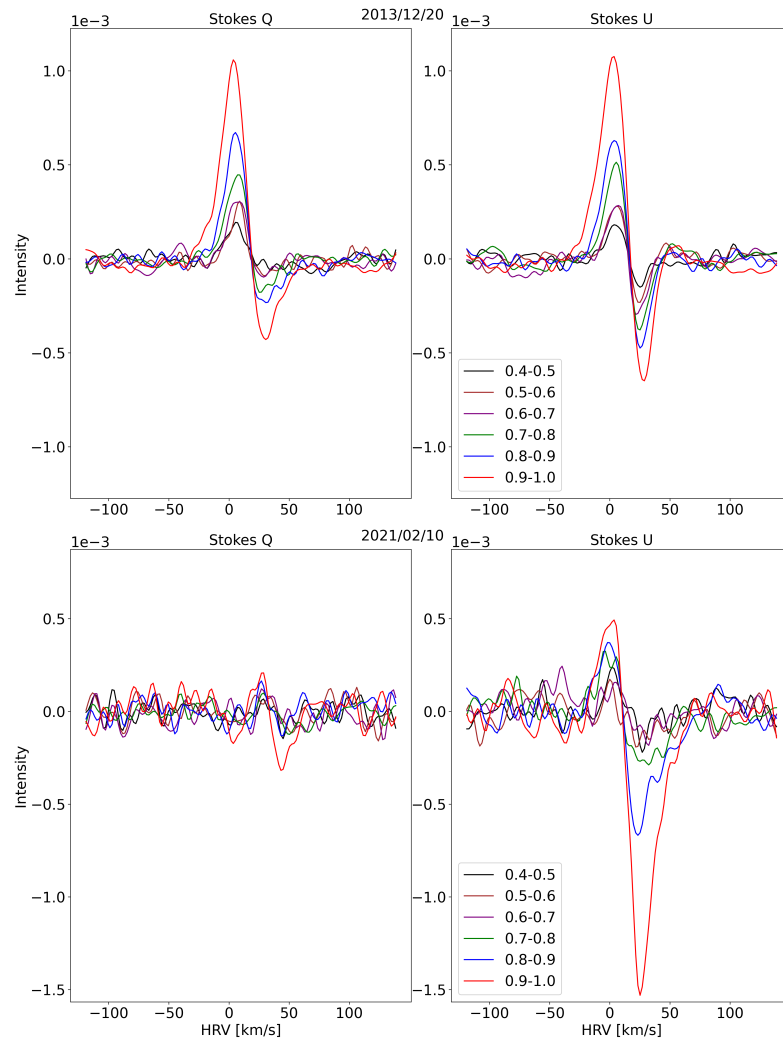


Figure 5.16: Upper panel: the Stokes Q and U LSD profiles of Betelgeuse on 2013/12/20 obtained with each one of the six masks which group the atomic lines in the spectrum of the star by their depth. Lower panel: the same for 2021/02/10. In both observations, deeper lines show stronger polarization, in agreement with the approximations made.

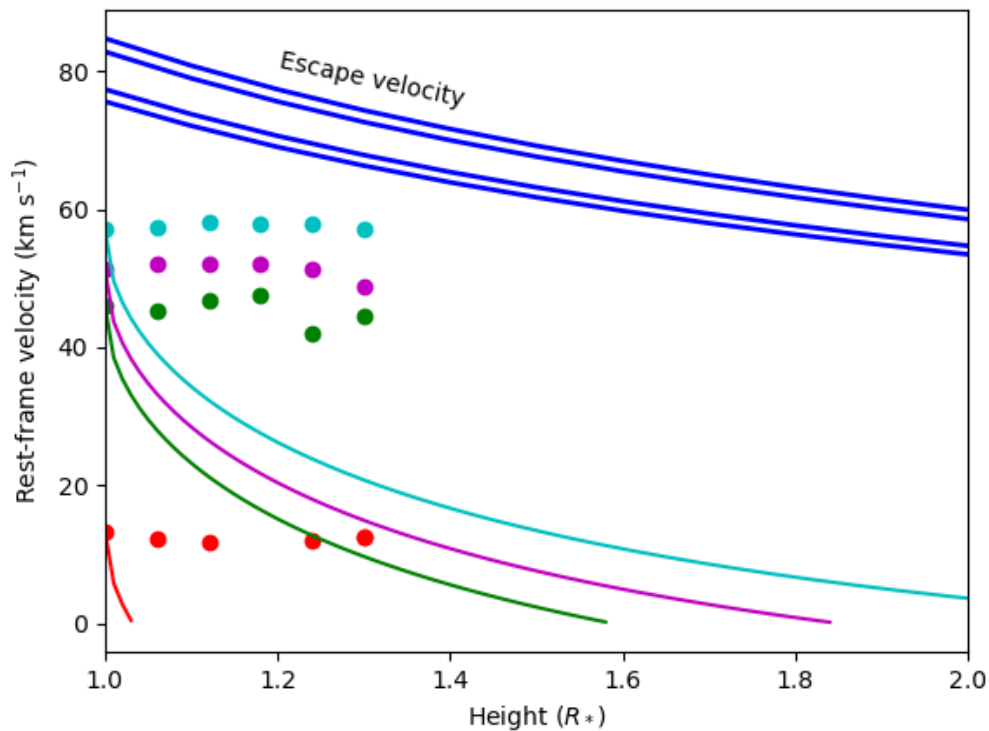


Figure 5.17: The four dark blue lines show the escape velocity of Betelgeuse as a function of height above the photosphere in the cases of stellar mass $15M_{\odot}$, $18M_{\odot}$ and stellar radius $955R_{\odot}$ and $1000R_{\odot}$. The light blue, pink, green and red dots indicate the velocities of four granules found in the 3D-image of 2013/12/12 at the six different altitudes probed by the inversion algorithm. It can be seen that for the granule represented by the blue dots, the convective velocity in the top layers is below the escape velocity, but only barely. The light blue, pink, green and red lines show the expected velocities of the granules if gravity was the only force acting upon the plasma.

5.7 Paper accepted for Astronomy & Astrophysics

3-dimensional imaging of convective cells in the photosphere of Betelgeuse

A. LÓPEZ ARISTE¹, S. GEORGIEV^{2,3}, PH. MATHIAS⁴, A. LÈBRE², M. WAVASSEUR¹, E. JOSSELIN², R. KONSTANTINOVA-ANTOVA³, TH. ROUDIER¹

¹ IRAP, Université de Toulouse, CNRS, CNES, UPS, 14, Av. E. Belin, 31400 Toulouse, France

² LUPM, Université de Montpellier, CNRS, Place Eugène Bataillon, 34095 Montpellier, France

³ Institute of Astronomy and NAO, Bulgarian Academy of Science, 1784 Sofia, Bulgaria

⁴ IRAP, Université de Toulouse, CNRS, UPS, CNES, 57 avenue d'Azereix, 65000, Tarbes, France

Received ...; accepted ...

ABSTRACT

Aims. Understanding convection in red supergiants and the mechanisms that trigger the mass-loss on these evolved stars are the general goals of most observations of Betelgeuse and its inner circumstellar environment.

Methods. Linear spectropolarimetry of the atomic lines of the spectrum of Betelgeuse contains information on the 3-dimensional distribution of brightness in its atmosphere. We model the distribution of plasma and its velocities and use inversion algorithms to fit the observed linear polarization.

Results. We obtain the first 3-dimensional images of the photosphere of Betelgeuse. Within the limits of the used approximations, we recover vertical convective flows and measure the velocity of the rising plasma at different heights in the photosphere. In several cases we observe this velocity to be constant with height, indicating the presence of other forces than gravity acting on the plasma and counteracting it. In some cases, these forces are sufficient to maintain plasma rising at 60 km s^{-1} at heights where this velocity is comparable to the escape velocity.

Conclusions. Mechanisms are present in the atmosphere of Betelgeuse that allow plasma to reach velocities close to the escape velocity. These mechanisms may suffice to trigger mass loss and sustain the observed large stellar winds of these evolved stars.

1. Introduction

Betelgeuse is a very interesting target for the observation and understanding of red supergiants (RSG). The study of the convective movements in these cold, low gravity stars sheds light on the understanding of turbulent fluid motions (Freytag et al. 2002; Chiavassa et al. 2011). This very same turbulence may give rise to magnetic fields that have been observed in Betelgeuse (Aurière et al. 2010; Mathias et al. 2018). And these convective motions in the photosphere may largely contribute to the increased mass-loss at these stages of the stellar evolution, forming a strong stellar wind which greatly contributes to the chemical enrichment of the circumstellar and interstellar medium.

Its large angular diameter (Montargès et al. 2021, 42.11 mas in the K band), due to its relative proximity (about 200 pc) but also to its actual size as an M1ab supergiant, has made of Betelgeuse a favourite target for interferometry, allowing for detailed images of its photosphere which have unveiled large convective structures (e.g., Haubois et al. 2009; Montargès et al. 2016). These have been confirmed recently through an unexpected technique based upon the discovery (Aurière et al. 2016) and interpretation (López Ariste et al. 2018) of linear polarization in the atomic lines of the spectrum of Betelgeuse. The analysis of these signals allowed López Ariste et al. (2018) to produce images of this star. These images were comparable to quasi-simultaneous interferometric images and unveiled large convective structures that we can call granulation, as in the Sun. Another result of this new technique was the observation of large convective velocities, of about 40 km s^{-1} , well above the predictions in the adiabatic approximation, but concurring with the results from numerical simulations of Freytag et al. (2002) and Chiavassa et al. (2011).

The amount of linear polarization observed in these atomic lines is often of few hundredths of a percent, and is therefore below the typical signal-to-noise ratios of single observations. It has been customary in stellar spectropolarimetry to add the signals of a large number of atomic lines in order to increase the signal-to-noise ratio of the resulting mean spectral line (Donati et al. 1997). Adding up different spectral lines from different atomic species may sound incongruous. But it is acceptable if the polarization signal is expected to be the same, up to a scale factor, for all the lines added. That this was the case for the linear polarization of Betelgeuse was justified by Aurière et al. (2016). The images inferred by López Ariste et al. (2018) depended upon the interpretation of the linear polarization of this mean line, result of the addition of over 10 000 atomic lines. But one can do better than adding up all those lines regardless of the properties of each individual line. Aurière et al. (2016) already produced a figure (their Fig. 4) where the line addition was made over lines with similar depth in the intensity profile. Six masks were thus produced which included lines with a line depth between 0.9 and 1, between 0.8 and 0.9, and so on. The authors did not go forward into the interpretation of the profiles shown in their figure. But it is apparent that those profiles, while similar, are not identical. And the differences cannot be attributed to noise. First, the amplitude changed in such a way that the deeper the line, the larger the amplitude of linear polarization. A more subtle result was that the maximum of emitted polarization did not appear at the same wavelength for different line depths. It is clear that these lines, grouped by the depth of their intensity profile, are not sounding the same photospheric structures. It is also obvious that, since line depth can be roughly seen as a proxy of height of formation, these lines contain information from dif-

ferent heights in the atmosphere. The present work stems from those observations and infers the first 3-dimensional images of the photosphere of Betelgeuse. Tomography based upon contribution functions is a well-known technique, even for the case of Betelgeuse and other red supergiants (Kravchenko et al. 2018). In this work, we are not doing it on the intensity but instead on the polarization spectra. As it will be discussed below, polarization shows particularities that make most of previous work on tomography basically non-relevant in the present case. These particularities will force us to re-derive the conditions and constraints that apply to our data.

In Section 2 we present our large set of observations collected from 2013 to 2020 with the spectropolarimeters, Narval and its upgraded version Neo-Narval, at the Telescope Bernard Lyot at Pic du Midi (France). In Section 3 we discuss the many approximations needed to produce those 3-dimensional images. If those approximations prevented a straightforward interpretation of the inferred images in the 2-dimensional case, they impose even stronger limits to the interpretation of 3-dimensional images. We nevertheless carry on and, in Section 4, we present two cases from data from 2013 and 2020 observed with Narval and its upgraded version Neo-Narval respectively. The inferred images unveil interesting aspects of the convective movements in the photosphere of Betelgeuse, in spite of all the approximations made. In Section 5, we focus on the dependence of the velocity of the rising plasma with height. We isolate particular cases in which the plasma rises at constant velocity. This reveals the presence of other forces counteracting gravity in the photosphere. These forces are present up to considerable heights. The large velocities measured, 40 and even 60 km s^{-1} in some cases, are kept constant up to heights where they are comparable to, but smaller than, the escape velocity. Even if we are yet unable to confidently estimate the actual heights, our results and conclusions (summarized in Section 6) are a tantalizing proof of the presence of forces in the photosphere that may allow this plasma to escape Betelgeuse into the circumstellar environment.

2. Spectropolarimetric data from Narval and Neo-Narval

We have been monitoring Betelgeuse in linear polarimetry since November 2013 with the Telescope Bernard Lyot at Pic du Midi (France, TBL). Until August 2019, the Narval spectropolarimeter was used, and this data set has been described by Aurière et al. (2016); Mathias et al. (2018) and López Ariste et al. (2018). In September 2019 Narval was deeply upgraded into Neo-Narval, and the first data of Betelgeuse were collected by February 2020.

Neo-Narval maintains the successful polarimeter of Narval, but has changed the detector for a new, more performant, iXon CCD by ANDOR. The faster readout times of the new detector (2 to 3 seconds) at readout noises comparable to the old detector of Narval (2 to 3 electrons in the usual configuration) and similar quantum efficiencies allow a more efficient use of telescope time. The spectrograph itself has been thermally stabilised with 3 concentric enclosures of which the middle one is actively controlled in temperature. The diffraction grating has been mounted inside an isobaric chamber. Altogether, the goal is a stabilisation of the spectrograph to allow it to measure velocities with a precision of 3 m s^{-1} . But it is not sufficient with thermal and pressure control of the spectrograph. The final sensibility to velocities is afforded by the introduction of a calibration beam fed with a stable Fabry-Perot. Each one of the 40 spectral orders seen by Neo-Narval is thus split in 3: two beams carry the orthogonal polarizations that allow the polarization modulation, while the third

one carries the Fabry-Perot spectrum. In order to introduce this 3rd calibration beam the camera optics and the cross-dispersing prisms were overhauled. As a result, the raw image of the spectral orders differs considerably from the previous one with Narval, and demanded an upgrade of the data reduction software. Rather than refurbishing the old Libre-Esprit code Donati et al. (1997), NeoNarval engaged in providing a completely new code written from scratch. For the present work, the modifications in Neo-Narval concerning velocity measurements are of no importance. The new DRS however had to be validated. Since January 2020, three major upgrades of the DRS have been implemented, and the data re-calibrated with the latest version of the code. Although the DRS shows still room for improvement, the tests with respect to Betelgeuse spectro-polarimetry show a continuity with Narval data. Some of the plots in this paper, presenting measurements made directly on the profiles, are particular examples of this continuous quality of the data.

For completeness, a list of observations of Betelgeuse made with Narval (August 2018 - August 2019) and Neo-Narval (February 2020 - February 2021) is presented in Table 1. Note that the upgrade of Narval into Neo-Narval resulted in an interruption of several months of our regular monitoring of Betelgeuse that was also very unfortunately coincident with its famous episode of great dimming in the period December 2019-February 2020 (Montargès et al. 2021).

3. Approximations and assumptions

The 2-dimensional images produced by López Ariste et al. (2018) are the result of fitting the observed linear polarization profiles with synthetic ones obtained from a model. The basic idea behind these reconstructed images is that the observed polarization is due to the non-uniform distribution of brightness over the stellar disk. The spatial distribution of the brightness can be inferred by realizing that, due to Rayleigh scattering, the polarization emitted by a bright spot over the disk will be tangent to the local limb, and therefore its ratio of Stokes Q to Stokes U linear polarization signals will provide the polar angle over the disk of such a spot. The distance of that spot to the center of the disk can be inferred from the wavelength at which a linear polarization signal is found. Assuming no rotation, the presence of convective motions will Doppler-shift the signals in such a way that a bright spot found near disk center will send its polarization to the blue wing of the atomic line, while a spot near the limb will send its signal onto the red wing, irrespective of its polar angle. Although analogous, notice that this projection of disk positions onto wavelength is completely different to the more familiar one of a rotationally broadened line. This basic idea can be extended to more complex scenarios with the help of an inversion algorithm and of a model for the continuous distribution of brightness and velocities over the disk, as described by López Ariste et al. (2018). This method to infer images rests, nevertheless, upon a generous amount of approximations and assumptions about the structure of the photosphere of Betelgeuse, radiative transfer, and the emission of polarization. All of them were vindicated by the observed similarities between the resulting images and those resulting from interferometric observations. Furthermore, it appeared that the main conclusions of that work were not fundamentally altered by them: the spatial scale of the observed structures was constrained by the spectral width of the observed polarization signals; the temporal scales were independently corroborated through time-frequency analysis of the spectra by Mathias et al. (2018); the maximum convective

Table 1. Log of Narval and Neo-Narval observations of Betelgeuse and polarimetric measurements since August 2018. Note that previous (Npolarizationarval) QU measurements are summarised by Aurière et al. (2016); Mathias et al. (2018) and López Ariste et al. (2018).

Date	Julian date	Stokes	Number of cycles averaged	Narval (N) or Neo-Narval (NN)
August 18, 2018	8349.648	Q	02	N
August 18, 2018	8349.654	U	02	N
September 19, 2018	8381.675	Q	02	N
September 19, 2018	8381.680	U	02	N
October 05, 2018	8397.694	Q	02	N
October 05, 2018	8397.700	U	02	N
October 23, 2018	8415.635	Q	02	N
October 23, 2018	8415.640	U	02	N
November 13, 2018	8436.590	Q	02	N
November 13, 2018	8436.596	U	02	N
January 04, 2019	8488.530	Q	02	N
January 04, 2019	8488.535	U	02	N
January 15, 2019	8499.432	Q	02	N
January 15, 2019	8499.436	U	02	N
January 21, 2019	8505.427	Q	02	N
January 21, 2019	8505.433	U	02	N
January 26, 2019	8510.458	Q	02	N
January 26, 2019	8510.463	U	02	N
March 11, 2019	8554.379	Q	02	N
March 11, 2019	8554.386	U	02	N
March 28, 2019	8571.365	Q	02	N
March 28, 2019	8571.370	U	02	N
April 27, 2019	8601.357	Q	02	N
April 27, 2019	8601.366	U	02	N
April 30, 2019	8604.332	Q	02	N
April 30, 2019	8604.341	U	02	N
August 20, 2019	8716.671	Q	02	N
August 22, 2019	8718.676	U	02	N
February 02, 2020	8882.332	Q	02	NN
February 02, 2020	8882.330	U	02	NN
February 14, 2020	8894.369	Q	02	NN
February 14, 2020	8894.366	U	02	NN
February 21, 2020	8901.378	Q	02	NN
February 21, 2020	8901.381	U	02	NN
February 24, 2020	8904.381	Q	02	NN
February 24, 2020	8904.384	U	02	NN
March 11, 2020	8920.289	Q	02	NN
March 11, 2020	8920.287	U	02	NN
August 22, 2020	9084.665	Q	02	NN
August 22, 2020	9084.662	U	02	NN
September 03, 2020	9096.654	Q	02	NN
September 03, 2020	9096.658	U	02	NN
September 29, 2020	9122.699	Q	02	NN
September 29, 2020	9122.701	U	02	NN
October 17, 2020	9140.667	Q	02	NN
October 17, 2020	9140.668	U	02	NN
October 30, 2020	9153.605	Q	02	NN
October 30, 2020	9153.607	U	02	NN
November 23, 2020	9177.468	Q	02	NN
November 23, 2020	9177.469	U	02	NN
December 17, 2020	9201.413	Q	02	NN
December 17, 2020	9201.415	U	02	NN
January 06, 2021	9221.400	Q	02	NN
January 06, 2021	9221.403	U	02	NN
February 10, 2021	9256.418	Q	02	NN
February 10, 2021	9256.421	U	02	NN

Notes. Columns give the date, the heliocentric Julian date (+2 450 000), the observed Stokes parameter, the number of Stokes QU collected and average, and the instrument used (N stands for Narval, NN for Neo-Narval).

tive velocities found were forced by the wavelength span of the observed polarization signal.

This state of affairs cannot be safely pursued when trying also to extract height information from the data. An examination of the validity and impact of those approximations is required before we trust the 3-dimensional images produced in the present work. The basic approximation taken is that polarization is emitted by the last scattering in a grey atmosphere. Under this assumption, we shall be able to order the atomic lines in terms of height of formation as we shall see, but we will be unable to compute its height. Next, we should assume certain values for both the heliocentric radial velocity of Betelgeuse V_* and the maximum upward speed of the convective fluxes V_{max} . Both parameters are constrained by observations, but not fixed. While there is a huge amount of information in the polarised profiles, it is not sufficient to unambiguously image the photosphere of Betelgeuse, and therefore there is a random choice of one solution. We shall next examine these approximations one by one.

3.1. Maximum and minimum velocities

Betelgeuse is modelled as a convective, non-rotating star. This implies that bright, hot plasma is rising, emitting blue-shifted profiles, while dark, cold plasma is sinking, emitting red-shifted profiles. In the absence of rotation, these are the only macroscopic velocity fields present. The net addition of spectral line profiles over the stellar disk (ignoring 3-D radiative transfer effects) will be dominated by the bright regions. From this argument, we should expect a net intensity profile which is blue-shifted with respect to the radial velocity of the center of mass of the star relative to us. The center of the intensity profile is not, for a convective non-rotating star, a measure of this radial velocity. If only convective velocities were present, this radial velocity, V_* , of the center of mass of the star in the heliocentric reference system would lie somewhere in the red wing of the observed line. Where it lies exactly depends on the contrast ratio between the bright rising plasma and the dark sinking plasma, and of the inhomogeneities of brightness at different parts over the visible disk. And this is a parameter that should be fixed for the inversions to be done.

If our model had included the presence of rotation, it would introduce a symmetrising effect on the atomic line. Were rotation velocities to dominate the profile shape, the true velocity V_* would be somewhere near the line center. A similar reasoning can be made for other line-broadening mechanisms: the eventual presence of macroturbulent velocity distributions would tend to symmetrize the profile around the true zero velocity of the center of mass. Determining this velocity V_* of the center of mass of the star requires therefore to disentangle the contribution to the line profile of these 3 very different velocities: convective velocities that tend to place V_* in the red wing of the observed intensity profile, and rotational and thermal velocities that tend to shift it towards the center of that profile. The presence of narrow lobes in the profiles of linear polarization, as illustrated in the profiles of Fig.4, is proof that thermal, micro- and macroturbulent broadenings are much smaller than the span of values attributed to convective velocities. The estimated rotational periods of Betelgeuse (Uitenbroek et al. 1998; Kervella et al. 2018, in the range of 12 to 30 years,) result in maximum rotation velocities of at most 5 or 10 km s⁻¹. Such rotational velocities are comparable to the thermal broadenings but, again, much smaller than the observed span of velocities (40 - 60 km s⁻¹) seen in the polarization signals. For these a priori reasons, our model neglects rotation and introduces an *ad-hoc* broadening, that also

takes into account the instrumental spectral resolution. And for these *a priori* reasons we expect V_* to lie somewhere in the red side of the observed intensity profile. But its true position is unknown and therefore constitutes a parameter of our model.

Examination of the observed line profiles in polarization provides important constraints on the velocity fields of our model. But its comparison with the intensity profiles makes the situation harder to interpret. Polarization profiles show large amplitudes in the far wings of the intensity profiles (an illustration of this can be found in the data for the dates retained for the present work which will be introduced and described later, Fig. 4). As a result, the polarization appears to emerge from an atomic line many times broader than the observed intensity profile. Our current framework for the interpretation of those polarization signals cannot justify this fact. Simple addition of the intensity over the 2D images produced by López Ariste et al. (2018) results in intensity profiles much broader than the observed ones. It could be argued that the present model used to fit the linear polarization profiles is simply wrong if it does not also fit the intensity profiles. But another possibility emerges when one takes into consideration the fact that most of the radiative transfer takes place in a moving atmosphere (Chandrasekhar 1945; Bertout & Magnan 1987). The recent example of Mira stars illustrates that radiative transfer through the moving shells, ejected by present and previous pulsations, is subject to a geometry weighing that favours the center of the stellar disk. The resulting disk-integrated profile is not the simple addition of the local intensity profiles over the whole disk, but just over a much smaller region around the disk center (Bertout & Magnan 1987; López Ariste et al. 2019). Were a similar phenomenon at work in Betelgeuse, the observed intensity profile would correspond to a reduced region of the disk justifying its narrow width and its lack of consistency with the polarization profiles. López Ariste et al. (2019) demonstrated that, in the case of the expanding atmosphere of the Mira star χ Cyg's, the linear polarization was also affected by a geometric factor composed of the product of the same geometric weight in the integral of the intensity over the stellar disk, which favoured the disk center, but also of a further $\sin^2 \theta$ weight, typical of scattering polarization. Polarization was, unlike intensity, sensitive to the whole disk.

At present, it is not clear if radiative transfer through a moving atmosphere may explain the differences seen between the intensity and polarization profiles in Betelgeuse. In what follows, we trust the information provided by polarization profiles alone, and assume that the intensity profile has somehow been restricted to represent a small portion of the disk, and does not provide information on the convective velocities present in the atmosphere of Betelgeuse. To determine V_* , we must rely only on the polarization signals. Figure 1 shows the velocities in the heliocentric reference frame of both the peaks and the wings of the polarization signals observed since 2013. The horizontal grey line in both plots shows the center of the intensity line. The ordinates are referred to the barycenter of our solar system. In this reference system, the estimated radial velocity V_* of the Betelgeuse center of mass is red-shifted. Its value of $V_* = 40$ km s⁻¹ is chosen so that most of the polarization peaks are blue-shifted, as expected from spectral profiles dominated by convective flows. The reason for not pushing V_* to a more extreme value is that we leave a margin of about 10 km s⁻¹, allowing for some red-shifted profiles. While very few peaks appear red-shifted with this choice, the second plot shows that there is a non-negligible amount of red-shifted signal. We attribute these red-shifted signatures mostly to the dark, sinking plasma. With this choice of V_* , the observed convective velocities span a range of at least

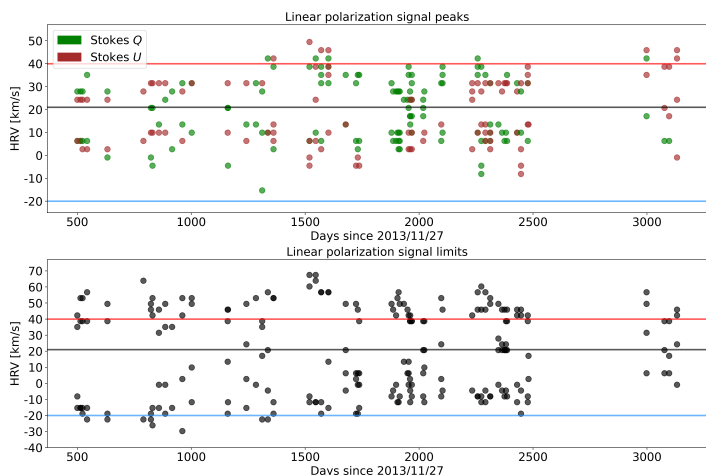


Fig. 1. Determination of the position of the observed peaks in polarization (top) and the maximum wavelength at which signal is still above noise (bottom) for all the data available since 2013. The grey horizontal line marks the intensity line center wavelength. The blue and red lines mark the chosen values of $V_{max} = 60 \text{ km s}^{-1}$ and $V_* = 40 \text{ km s}^{-1}$ respectively. Wavelengths are given in km s^{-1} and referred to the solar system barycenter reference. Neo-Narval data starts from day 2700 on.

40 to 50 km s^{-1} , with some examples at even 60 km s^{-1} . As we mentioned above this large range allows us to discard rotation as a primary source of line broadening. Similar arguments can be made to thermal, micro- and macroturbulent velocity fields.

It may be tempting, in spite of the *a priori* arguments given above and in view of these two plots in Fig. 1, to return to a symmetric distribution of velocities with V_* at the center of the intensity profile: the linear polarization signals appear symmetrically distributed respect to the observed center of the intensity line profile. To counter this possibility we produce a last argument: we must recall that López Ariste et al. (2018) inferred an image of CE Tau with a bright granule at disk center, concurrent with simultaneous interferometric images of Montargès et al. (2018). In the current framework, the presence of such bright granule at disk center was inferred from the observation of a strong linear polarization signal at the most blue-shifted wavelengths. The reality of such a structure forces us to conclude that, first, there is spatial information in the wavelength distribution of polarized signals and, second, that disk center emits signals at the bluest wavelengths and not at the center of the intensity profile. Any other modelling which would deny a relationship between wavelength and spatial position (as macroturbulent velocities do) or that would call for disk center to emit at the line center wavelength (as rotational velocities do) must be excluded.

Having fixed the value of V_* in the red wing of the line at 40 km s^{-1} within a margin of error of about 10 km s^{-1} , we turn our attention to the span of velocities present in the linear polarization signals. Our model assumes that the rising plasma can have a maximum velocity V_{max} . The determination of this second velocity parameter V_{max} is of paramount importance for our model and our conclusions. Due to the relationship between velocities and wavelength in the present model, with just convection and without rotation, a bright granule strictly at disk center emits its signal at the bluest wavelength, corresponding in velocity coordinates to $V_* - V_{max}$. Inspection of Fig. 1 shows that, over the last 7 years, peaks in polarization have been observed up to 60 km s^{-1} respect to the star’s zero radial velocity V_* . For signals in the wings, yet above noise, we should have considered even larger maximum convective velocities V_{max} : beyond

60 km s^{-1} in the stellar reference frame. Altogether, leaving a margin of 10 km s^{-1} , we can establish the maximum velocity of the rising plasma to $V_{max} = 60 \text{ km s}^{-1}$. Such high velocities of rising plasma seem to be partially justified by numerical simulations (Chiavassa et al. 2011).

Even if we can, from data, measure the maximum observed velocity V_{max} of the convective flux, we cannot expect this maximum velocity to be present at a given moment on Betelgeuse. But we cannot afford to have a different value of V_{max} for every observing date, and rather have to fix a constant V_{max} for our whole dataset. The relationship that our model establishes between wavelength and position over the disk implies that any bright plasma at disk center is assumed to move at velocity V_{max} . If at a particular date the plasma velocities present over the star are lower than this maximum V_{max} , the inversion algorithm will not place any bright structure at the center of the disk. The inferred bright structures will be placed off center just because their velocity is smaller than the maximum velocity. This is an important bias to keep in mind when analyzing the inferred images of Betelgeuse, and a bias that shall be exploited later on. In the absence of any independent method to fix the maximum velocity for every individual date, this is a limitation difficult to resolve.

3.2. Grey atmosphere

To simplify the computation of the emergent polarization $Q(\nu)$ in the direction of the observer, we assume that all polarized photons are due to scattering, and not to any process of dichroism. This allows us to write, following Landi Degl’Innocenti & Landolfi (2004), that

$$Q(\nu) = \frac{3}{2\sqrt{2}} (1 - \mu^2) \int_0^\infty \beta J_0^2(\nu) e^{-\frac{\nu}{\mu}} \frac{d\nu}{\mu} \quad (1)$$

with β the fraction of opacity due to scattering, $J_0^2(\nu)$ the irreducible spherical tensor of the illumination as a function of ν , the frequency of light, and μ the distance to disk center. It is useful to introduce the anisotropy factor

$$w_\nu = \sqrt{2} \frac{J_0^2(\nu)}{J_0^0(\nu)} \quad (2)$$

and rewrite the previous expression as

$$Q(\nu) = \frac{3}{4} (1 - \mu^2) w_\nu \int_0^\infty \beta J_0^0(\nu) e^{-\frac{\nu}{\mu}} \frac{d\nu}{\mu} = \frac{3}{4} (1 - \mu^2) w_\nu I_{scatt}(\nu) \quad (3)$$

At any given position over the disk of Betelgeuse, the emergent polarization will vary mostly following this anisotropy factor w_ν . In particular, at $\mu = 0$ we have

$$\frac{Q(\nu)}{I_{scatt}(\nu)} \approx w_\nu \quad (4)$$

Following closely Landi Degl’Innocenti & Landolfi (2004), where details of these calculations can be found, we can compute the anisotropy factor w in two extreme cases: scattering in the outer atmosphere and in a grey atmosphere.

In the first case, the scattering takes place sufficiently far away from the star that the illumination is cylindrically symmetric around the radial direction with only limb darkening to take into account. For distances which are small compared to the radius of the star, an approximation that appears as suitable for

photospheric lines in Betelgeuse, the anisotropy factor w_ν can be written as a correction to the factor at 0 height, $w_{\nu,0}$, in terms of the height h and the limb darkening functions $u_1(\nu)$ and $u_2(\nu)$:

$$w_\nu = w_{\nu,0} + \frac{9}{5} \frac{[1 - u_1(\nu) - u_2(\nu)][20 - 5u_1(\nu) - 8u_2(\nu)]}{[6 - 3u_1(\nu) - 4u_2(\nu)]^2} \sqrt{\frac{h}{2R_*}} \quad (5)$$

In the second case, the scattering takes place in the midst of a grey atmosphere, where all the emission is thermal and described by a Planck function. The radiative transfer equation for the integrated flux, an approximation to the mean line arising from Least-Squares Deconvolution (LSD), can be solved in terms of its moments, and one can derive an anisotropy factor w for any optical depth τ in the form

$$w(\tau) = \frac{q(\infty) - q(\tau)}{2[\tau + q(\tau)]} \quad (6)$$

in terms of the Hopf function $q(\tau)$.

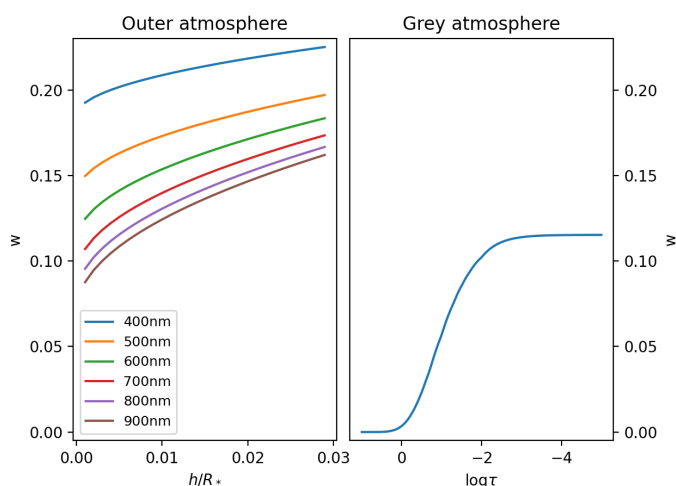


Fig. 2. Computation of the anisotropy factor for the case of the grey atmosphere (left) and the outer atmosphere (right) approximations. Due to the nature of those approximations, the abscissae are different: optical depth in the case of the grey atmosphere, distance to the photosphere in the outer atmosphere case. In this last approximation, computations are shown for 6 different wavelengths in the spectral domain of Narval.

In Fig. 2 we compute both cases, in terms of height above the star and a solar-like limb darkening for the extreme outer-atmosphere case, and in terms of optical depth for the case of the grey atmosphere. The importance of the figure lays on the extreme difference in the resulting values of the anisotropy factor. If one misreads Eq.(4) as an approximation of the observed linear polarization rate, the outer atmosphere scenario predicts a local polarization amplitude in the order of a few % even at very low heights. In the grey atmosphere, polarization amplitudes diminish monotonically down to much lower polarization amplitudes as one goes deeper into the atmosphere and radiation arrives isotropically from all directions.

Rather than a demonstration, the previous arguments are just an educated guess on what the best description for the emergent polarization of Betelgeuse may be. If this polarization is of the order of 10% we shall not be able to tell apart the two approximations without computing them in much more detail. But if the emitted polarization happens to be of the order of 1%, as it

will be shown to be the case, we will be able to conclude that the grey atmosphere is the right framework. Aurière et al. (2016) concluded that the observed polarization is just the polarization of the continuum depolarized by the atomic lines forming right above it. Continuum polarization in Betelgeuse has been rigorously computed by Josselin et al. (2015) or López Ariste et al. (2018) and seen to be of the order of 1% at the limb, overseeing wavelength variations, a figure that concurs with the few measurements available (Doherty 1986a,b; Schwarz & Clarke 1984). If the identification of Aurière et al. (2016) is correct, then a grey atmosphere is the right scenario. A further confirmation must come from observations. To compare with observed values we should recall that it is not the local polarization rate that one measures, either in the continuum or in the atomic lines of the observed spectrum, but the disk-integrated polarization. A perfectly homogeneous disk would perfectly cancel out the integrated polarization. The presence of inhomogeneities ensures that there is a non-zero integrated polarization, but with a reduced amplitude. We can estimate the reduction in polarization amplitude due to this disk integration by looking into the images inferred by López Ariste et al. (2018). In that work it was concluded that the observed polarization profiles could all be reproduced by assuming photospheric brightness distributions given in terms of spherical harmonics of maximum degree 5. We have launched random combinations of spherical harmonics of such degree to simulate the aspect of Betelgeuse and computed the net polarization expected compared to the initial local polarization.

Figure 3 shows histograms of this expected net polarization (the case of maximum degree 3 for the spherical harmonics is also shown). These histograms peak at roughly 10%. That is, integrating over the disk in the presence of brightness structures of the size of those observed in Betelgeuse roughly reduces the local polarization by a factor 10 to a mere 10% of the initial local polarization. We can now go to the observations and see what is the actual net polarization observed. Over 7 years of observations, the maximum amplitudes of polarization rates are seen to be of 0.05 to 0.1%. We must conclude that the local polarization in Betelgeuse must have been roughly of 0.5 to 1% in nice agreement with the radiative transfer computations of the polarization of the continuum.

A consistent picture appears. Assuming that the origin of polarization is Rayleigh scattering of the continuum, depolarized by atomic lines, we expect a maximum local polarization of about 1%. With that same hypothesis we can model the brightness distribution of the photosphere of Betelgeuse and fit the observed polarization profiles. The models that fit the observed profiles present bright structures of the size predicted by convective theory in red supergiants. Such brightness distributions would keep linear polarization from cancelling out in the disk-integrated spectra, but they would nevertheless diminish the observed net polarization by a factor 10. Starting from a maximum of 1%, we expect that observed polarization should be of 0.1%, which is the rough order of magnitude of the observed polarization. This match of predicted and observed amplitudes is a positive point for the inversion and imaging technique, given that at no point the inversion algorithms use the result of the expected local polarization amplitudes computed from radiative transfer.

Re-examination of Fig. 2 at this point leads us to the conclusion that only the grey atmosphere can be accepted as approximation. Indeed, equating the anisotropy factor with emergent polarization, a grey atmosphere would produce local polarization amplitudes of 1% for $\log \tau$ in the range $(-1, 0)$, while the outer atmosphere approximation would require heights of

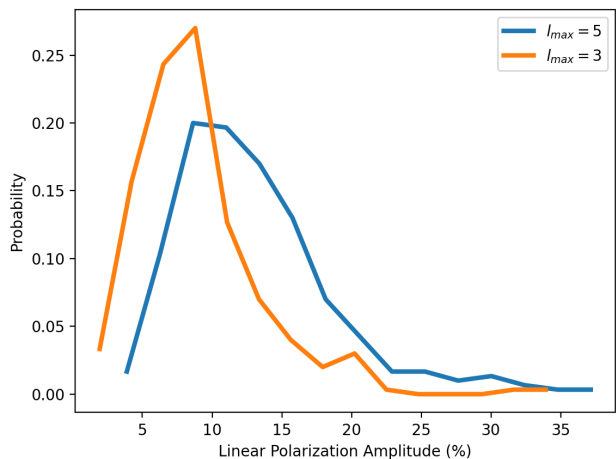


Fig. 3. Expected polarization rate from different brightness distributions assuming that local scattering results in 100% polarization. The histograms are built from realistic brightness distributions built with a combination of spherical harmonics of maximum order $l = 3$ and $l = 5$.

0.001 R_* to approach such low polarization amplitudes. Since at these heights, for Betelgeuse, it is not realistic to impose the approximation of light coming just from one direction that an outer atmosphere requires, it appears that we must keep the grey atmosphere as the appropriate approximation to compute our expected polarizations.

3.3. The single scattering approximation: Information along the optical path

Figure 4 shows the Stokes Q and U profiles for the dates of December 20th, 2013 (Narval instrument) and February 10th, 2021 (Neo-Narval instrument). LSD line-addition has been performed on the observed spectra using 6 different and excluding masks that classify the atomic lines of the spectrum of Betelgeuse in terms of the intensity line depth. The 6 masks correspond to line depths between 0.4 and 1 by steps of 0.1. As in Fig. 4 of Aurière et al. (2016), in our present Fig. 4 the observed amplitudes of linear polarization at these dates appear to be well ordered, and the deeper the line the larger the signal. This is not always the case, but it is a common feature of the observational data sets available.

To interpret this order in the signal's amplitudes, we make the hypothesis that the observed polarization comes from just one scattering event in the formation of the continuum at that wavelength, followed by an immediate and in-place absorption of the polarized photon by an atom which re-emits it unpolarized. This unique event must happen at a given depth in the atmosphere of Betelgeuse. At this place, we can write a unique simple form for the illumination moments in terms of the anisotropy factor w_ν and use it in Eq.3. Assuming all other terms in this Eq.3 identical, we insist as in Eq.4 in approximating the observed peak polarization amplitudes by the anisotropy factor w_ν and we plot this value at the optical depth at which it is predicted by a grey atmosphere. Fig. 5 shows the set of dots of the amplitudes of observed linear polarization peaks at the depths thus assigned. The grey atmosphere model, assuming this approximation of a single scattering event, allows us to easily interpret the observed ordering of the polarization signals in terms of height of formation: the deeper the line, the higher its core forms in the

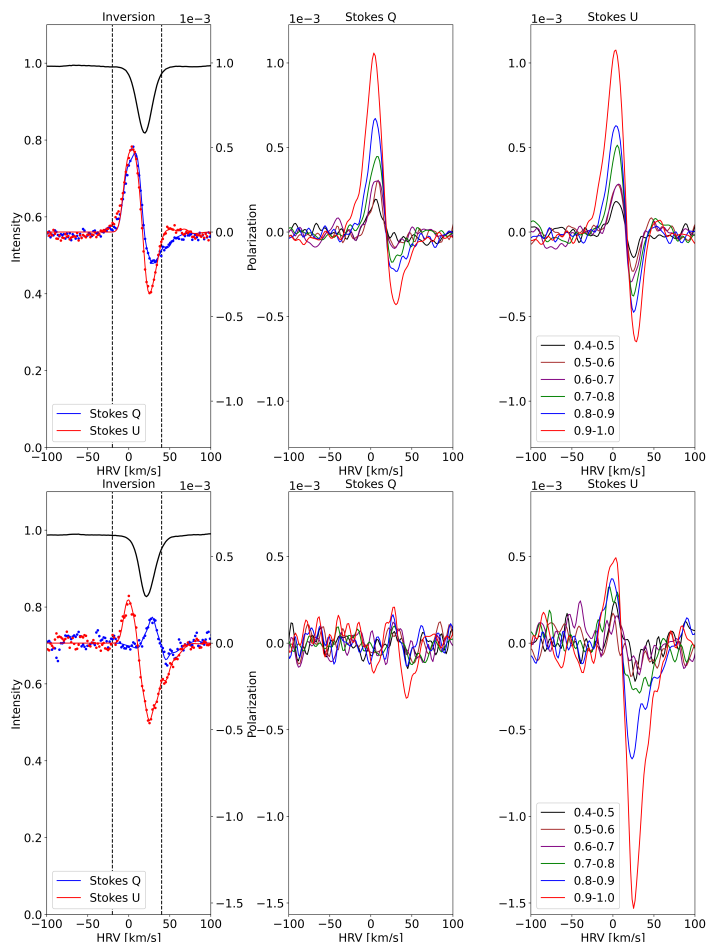


Fig. 4. Stokes Q and U profiles for the two studied dates (December 12th, 2013 above, and February 10th, 2021 below). Above and below, the left plot shows the observed Stokes Q and U profiles summed for the full spectral mask (blue and red dots respectively), as well as the fit produced by the inversion algorithm (full lines). The black line shows the intensity profile for reference. The dashed vertical lines indicate the adopted values of V_* (redshifted one) and V_{max} (blue shifted one). The center and right plots show the Stokes Q and U signals respectively, for each one of the masks grouping atomic lines of the spectra of Betelgeuse in terms of the depth of the line profile, from 0.4 to 1 in ranges of 0.1. For the two dates, a perfect ordering is seen: deeper lines show stronger polarization, comforting the validity of the approximations made. The Stokes U of December 12th, 2013 shows illustrations of the peaks drifting towards smaller (redder) velocities in one of the lobes, but being constant in wavelength for all heights in the other lobe.

atmosphere of Betelgeuse. It is tempting to look at the actual optical depths predicted by the grey atmosphere: the deepest lines, with the largest linear polarization, would form at $\log \tau = -0.4$ while the shallowest lines in our analysis (line depths of 0.4 thru 0.5) would form at $\log \tau = 0.4$. But at the same time, we must be cautious about this crude determination of heights of formation.

The ordering in height, and not the actual values, is the only information we shall use hereafter. We shall just claim that certain lines form above certain others and that we can therefore build a 3-dimensional image made of layers, each layer corresponding to a mask filtered by the depth of the intensity line, following the order given in Fig. 5. The two selected dates show the expected ordering of the signals and therefore allow us to order the masks in height and build a 3-dimensional image. It must be said that not all the observations available and presented in Table 1 present the right ordering of the signals explained by

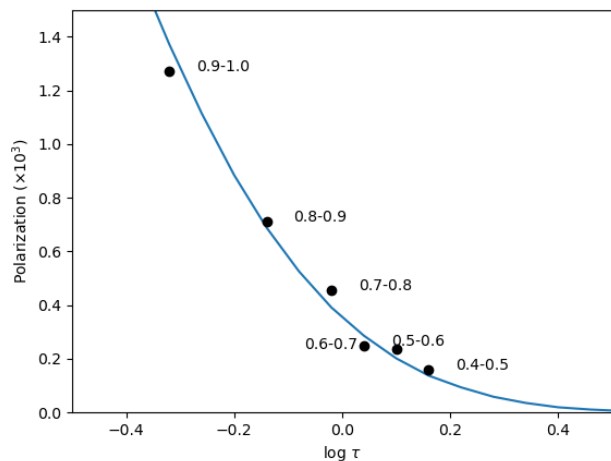


Fig. 5. Observed linear polarization peak amplitudes (dots) for the 6 masks on the polarization spectra, both Q and U, of December 12th, 2013. The abscissae of each dot is determined as the optical depth at which a grey atmosphere model fits the observed amplitude assuming a 1% rate of local polarization. The continuous line shows this model dependence.

our approximations. For those dates for which the ordering is not present, our model fails and we cannot assign a height to the masks, a 3-dimensional image is not feasible. But they are not the object of the present work.

It may be asked if one should not use the contribution functions of the intensity to improve our knowledge on the actual height of formation of different lines. The doubts about the interpretation of the intensity profile raised above are a strong argument against using those contribution functions of the intensity. The imposition of the hypothesis of a single scattering event in a grey atmosphere keeps us from also using contribution functions for the polarization. The validity of those approximations made so far is sufficient to order the heights of emergence of polarization, but not to go any further.

3.4. Ambiguous solutions

In spite of the large amount of information that is apparently available in the observed linear polarization spectra of Betelgeuse, it is not sufficient to produce a unique solution to the inverse problem of inferring an image which fits the observed spectrum. Part of this lack of unicity in the solution is due, as often, to the presence of noise. The broadening of the profiles, both instrumental and stellar (thermal, micro- and macroturbulence broadenings would need to be considered) smears out the details and makes the algorithm particularly insensitive to the position and brightness of the dimmer granules. Also, linear polarization carries over its infamous 180-degree ambiguity (López Ariste et al. 2018), and the whole inferred image can be rotated 180-degree with no change in the linear polarization profiles.

When comparing Betelgeuse and CE Tau images to those inferred by interferometry, Aurière et al. (2016) and López Ariste et al. (2018) could rely on that bright structures at disk center are not changed by these ambiguities and that the brightest structures impose a preferred axis of symmetry. This means that most

of the images produced could be compared to interferometric analogs after, at most, a 180 degree rotation, comforting the result that both techniques were detecting the same photospheric structures.

But in general, multiple ambiguous solutions are available to the inversion algorithm, and if it is left to handle one observation independently of other dates, there is no reason for which the solution found will preserve the same convention for the ambiguities of the other dates. We therefore select by hand one particular solution at an initial date, usually one for which we have simultaneous interferometric images, and use this solution as initial guess for the next date. We propagate one preferred solution among all the possible ones and are able to obtain a coherent picture from date to date.

The same strategy is applied for the inversion of each one of the masks filtered by line depth at any date. The solutions for the mask with the deepest lines, which in the studied data has always the largest signals and therefore the largest signal-to-noise ratio, is propagated as initial condition for the next date, but also as initial solution for the inversion of the next mask with shallower lines.

This strategy produces coherent solutions from date to date. But it has a vicious impact on the 3-dimensional images. Since the solutions are propagated from line mask to line mask, from one depth to the next one, the same structures tend to appear in one layer upon the other. The algorithm will tend to produce column-like 3-dimensional structures. While these can be a welcomed result in a convective scenario, we should remember that this is an implicit bias of the code. On the positive side, we may claim that any structure that varies with depth in the inferred images can be trusted as real: the inversion algorithm is biased to reproduce the structures from the layer above, so any change is necessarily forced by the presence of information in the profiles, in defiance of that bias.

3.5. The relation between velocity and brightness

Inferring a brightness distribution over the surface of Betelgeuse depends critically on retrieving spatial information on the polarized spectra. Simplistically, as described above, the ratio of Stokes Q to Stokes U gives information on the polar angle. The distance to disk center is recovered by considering that all light-emitting plasma is moving vertically at the same speed. The projection of this speed onto the line of sight results in a linear relationship between distance to disk center and wavelength. López Ariste et al. (2018) improved upon these rough rules by assuming a relationship between brightness and velocity, inspired by solar convection (see the appendix). All plasma moved vertically, but its velocity and sign depended on its brightness. The assumed relationship was that the brightest plasma, wherever it was over the disk, was rising at the maximum velocity V_{max} . This plasma would contribute to the signal at the wavelength given by the projection of that maximum velocity onto the line of sight. The darkest plasma, wherever it was, was sinking at this very same maximum velocity and would contribute to the signal at the appropriated projected velocity. All other plasma with intermediate brightness was given a velocity following a linear relationship such that the 25% darkest plasma was sinking and the 75% brightest was rising. The choice of this ratio of rising to sinking plasma was chosen by López Ariste et al. (2018) so that the resulting convective pattern showed a brightness contrast similar to the solar granulation.

It is clear that this is a strong and discutable constraint. To start with, if sinking plasma occupies only a quarter of the sur-

face, any mass conservation argument would lead to proposing sinking velocities larger than rising ones, subject to density changes. This is indeed what is observed in the Sun (see the appendix and the references therein). But taking this fact into account would imply a new parameter to be retrieved by the inversion algorithm, the sinking velocity, without much information left in the observations to constraint it. A better solution would be to infer this formal relationship between velocity and brightness from numerical simulations, with the result that observations would be dependent on simulations and therefore unable to confirm or infirm them. So we are left with this *ad hoc* relationship which, as all the others above, must be considered before validating any conclusion.

4. 3-dimensional imaging

Making 3-dimensional images requires simply to apply the inversion algorithm to each one of the LSD profiles resulting from masks filtered by the depth of the intensity profile. The grey atmosphere and the single scattering approximation can ensure us that if the observed LSD profiles show ordered amplitudes as described, with deeper lines showing larger polarization amplitudes, we can order in height the inferred images. Although we cannot give an exact, or even approximate, optical depth for these layers, it appears that we are moving in the range $\log \tau = (0.4, -0.4)$. This is very near where the continuum forms and we can safely claim that we are imaging the photosphere of Betelgeuse at all those heights.

For the present work, both selected dates from our observation data set show signal amplitudes which are well ordered with signal-to-noise ratios high enough. Our conditions to apply the listed approximations and build 3-dimensional images are thus fulfilled. Figures 6 and 7 present the inferred 3-dimensional images for the 2013 Narval data and the 2021 Neo-Narval data, respectively. In Fig. 6 we present two images of the brightness in 3 dimensions: one has a scale height related to what we believe best resembles the right geometrical heights, while in the other the photosphere is stretched so that we can better see the inferred structures. In Fig. 7 we present only the stretched case. We also produce, in both figures, a 3-dimensional image of the velocity along the radial direction which, we recall, is a monotonous function of the brightness. So there is no information here that is not also present in the brightness images, except that sometimes looking at the data in different manners can reveal different aspects. Brightness in those images is just a measure of polarization amplitude. For any given layer, at a constant height, the polarization amplitude is assumed constant and any change in the signal can only be attributed to changes in the emitted flux. Brightness in an image at constant height, represents therefore true contrast of the emitted flux at that height. But since the polarization amplitude increases with height, each layer in the image is attributed to a correspondingly higher brightness than the layer below, and no information is retrieved of the relationship between the emitted fluxes at different layers.

The upper limit of the imaged photosphere is estimated between $1.1 R_*$ and $1.3 R_*$, but this is just a rough estimate. This height range is suggested, on its upper boundary, by the presence of the molsphere (Perrin et al. 2004) at about $1.3 R_*$ which, we assume, marks the upper limit of formation of atomic lines in the mean atmosphere model of Betelgeuse. The lower boundary of $1.1 R_*$ is estimated from on-going studies on convective structures seen over the limb of Betelgeuse and μ Cep. The limb of the star acts as a geometrical horizon limiting the minimum height of the observed structures (López Ariste 2022). In optical

depth, the grey atmosphere indicates that the linear polarization profiles are consistent with a region going from $\log \tau = 0.4$ to -0.4 . A solid sphere in the center of the images indicates the surface $\log \tau = 1$.

5. Velocity profiles of the rising plasma

As described in 3.4, in order to keep the coherence between the solutions of one layer and the contiguous ones, we are using, for the top layer, the solution for the top layer from the previous date; for the first date a random initial guess is used for this top layer. For any other layer, at a given date, the solution for the layer above is used as initial condition. This ensures that the layers show coherent structures, but biases the algorithm to produce vertical structures that may be reminiscent of convective flows. Any such vertical structure in our images must be viewed with caution, due to this bias in the inversion algorithm.

Another approximation imposed in order to recover the 3D-images is that the maximum vertical velocity of the plasma is exactly identical for all the layers. We have described in some detail this approximation above. This maximum velocity is fixed once and for all after examination of the bluest wavelengths where signal can be observed (Fig. 1). This gives us a global maximum velocity for all the observations in our data set, but not the actual maximum velocity of the plasma at any particular date. And it is even more doubtful that at a layer the maximum velocity of the plasma is the same one as the layers above or below. Indeed, if the plasma is raising in a ballistic motion, subject to gravity alone, one would expect that this maximum velocity decreases with height. As in most other approximations described above, we are forced to impose this one because we cannot afford overwhelming the inversion algorithms with more free parameters.

But in the present case this imposed approximation carries an unexpected benefit. Once the maximum velocity of the plasma is fixed the inversion code will interpret any polarization signal at the wavelength corresponding to this maximum velocity as light emitted at disk center. The brightest plasma over the disk will also be assigned such maximum vertical velocity but projected onto the line of sight if it happens that it is somewhere else than disk center, so that its projected velocity corresponds to the wavelength where the strongest signal is observed. Now we can imagine a situation where, at the bottom layer, we have the brightest signal exactly at disk center. This plasma is moving vertically at the maximum speed. But its speed is decreasing with height. In the next layer above, this plasma still at disk center will be moving slower. Its polarization signal will be observed slightly to the red respect to the signal coming from the layer below. The inversion code, forced to conserve the same value of the maximum velocity for all layers, will infer that this signal is not coming from disk center anymore, but from a slightly offset position. Layer upon layer the situation is repeated: the plasma in Betelgeuse will still be at disk center and moving vertically but with smaller and smaller speeds; the inversion algorithm, however, will place it farther and farther off disk center forced by an imposed constant maximum velocity. Consequently, the inferred 3-dimensional structure will bend towards the limb. The same argument will apply to actually any other vertical flow anywhere over the disk as long as its velocity decreases with height.

This approximation of keeping the maximum velocity of the plasma independent of height will force any vertical flow subject to gravity to be inferred as a structure that bends towards the limb. From its curvature we could infer the effective gravity force if only we were able to figure out its geometrical height.

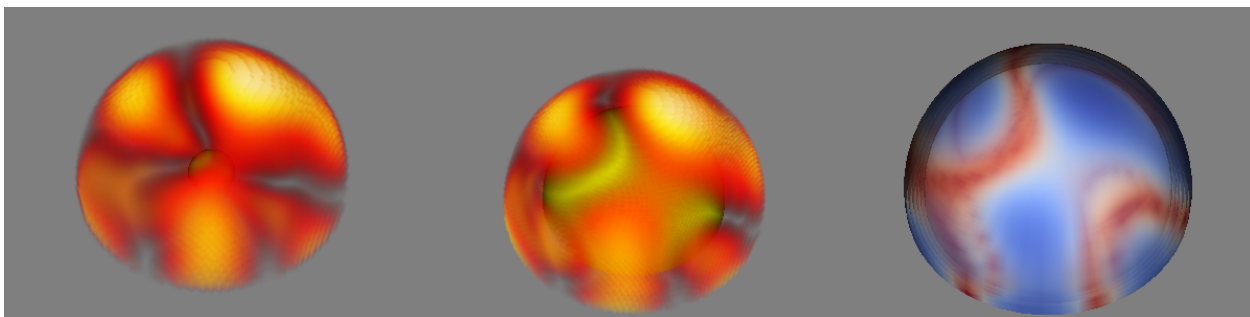


Fig. 6. 3-dimensional views of the photosphere of Betelgeuse on December, 20th 2013. At left, the explored region has been stretched to better see the inferred vertical structures. The darkest regions have been made transparent. At center, the star with the spatial scale that we consider closest to reality. At right, radial velocities, scaling from -60 to $+60$ km s^{-1} ; blue is rising plasma.

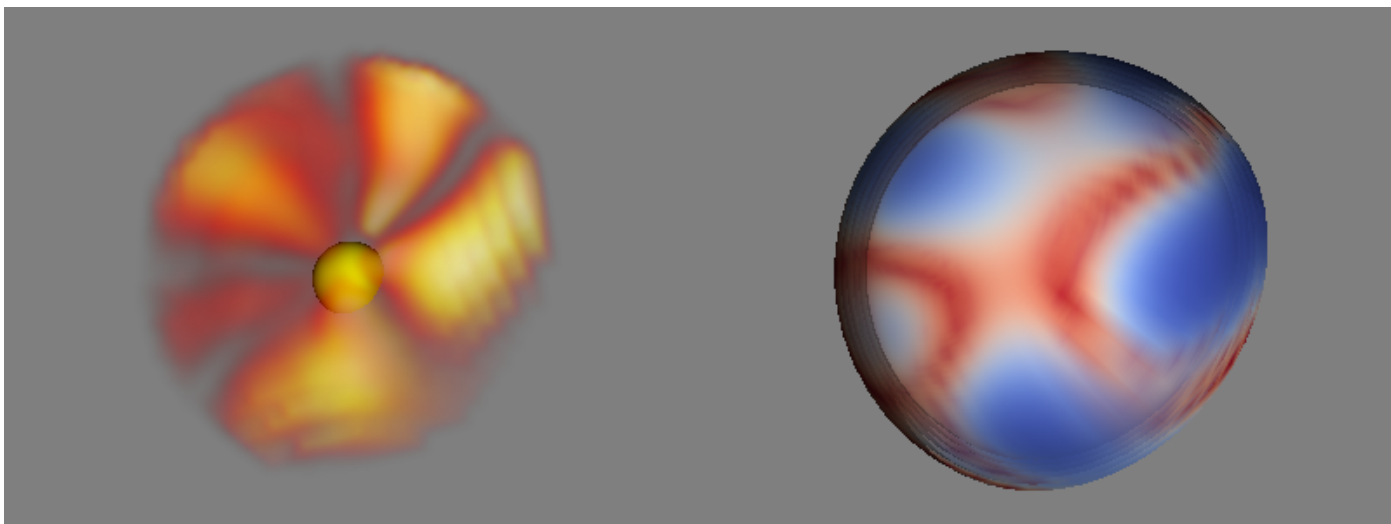


Fig. 7. 3-dimensional views of the photosphere of Betelgeuse on February, 10th 2021. See the caption of Fig. ?? for details.

Conversely, we could derive the geometrical height of the structures if assumed that gravity was the only force at work in this movement.

If the plasma, rather than slowing down, was accelerating, the contrary argument would apply. This cannot happen at disk center, since we have made sure when fixing the value of V_{max} that no observed signal exceeds this value. But it could happen for plasma off disk center whose projected velocity is below the threshold V_{max} . In such case, a true acceleration of the plasma in Betelgeuse would be seen as a polarization signal that, layer upon layer, shifts towards V_{max} . The inversion algorithm would infer in such case vertical structures bending towards disk center. Finally, with this approximation at work, the sole inferred vertical structures would be those with a velocity constant with height.

Figure 8 shows 2-dimensional cuts across the inferred images on the two selected dates. In both cases, we can easily identify structures bending towards the limb, and also structures rising radially. For the date of 2013, the image inferred from Narval data shows a disk center granule rising quite vertically if one looks at the brightest point at each layer (blue dot). The two structures on the sides of this center granule are, on the other hand, clearly bending towards their respective limbs. One could try to see in this blossoming of the structures as seen from Earth a coincidence: the granules are really bending and by chance they are doing so symmetrically as seen from Earth. It appears simpler to accept that the inversion algorithm, forced to accept a

maximum velocity constant with height is bending the structure in the inferred images in response to a decreasing velocity with height in Betelgeuse: these granules are just following a ballistic motion, slowing down as they rise. The central granule, however, shows a vertical structure. The symmetric expansion on both sides of the granule can be seen as a slowing down of some of its rising material. But if all the material were slowing down, the center of the granule would dim with height. It actually brightens. We must conclude that the inversion algorithm finds more and more polarization signal at the correct wavelength. There is always plasma moving at the maximum velocity at all heights, and so the velocity of the plasma is constant with height.

The data from Neo-Narval in 2021 provides another illustration of a common observation over the 7 years of data, independent of the instrument used. We see once more a limb-bending granule towards the left of the image, and a vertically rising granule near the center. This time the vertical granule is not exactly at disk center, yet both sides show a radial profile and the center of the granule is brighter with increasing height. We conclude, once more, that the plasma in this structure is moving at constant speed independently of height. The granule immediately to its right is also worth some attention. It shows a radial profile on its lower layers, then it bends towards disk center at the top. Interpretation in terms of velocities would lead us to conclude that the plasma in the bottom of this structure is rising at a constant velocity for half of its height, then accelerates in the top layers.

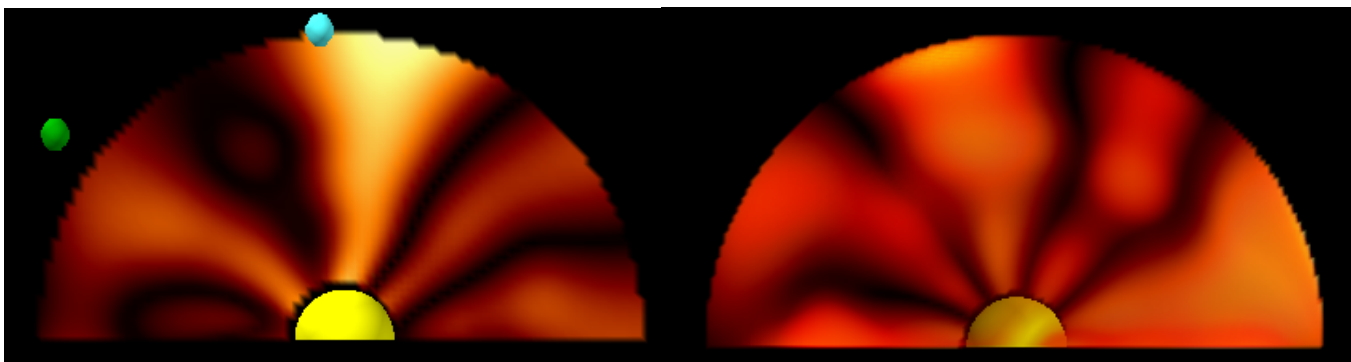


Fig. 8. 2-dimensional cuts on the inferred photosphere of Betelgeuse on December 12th, 2013 (left, Narval data) and February 10th, 2021 (right, NeoNarval data). Several limb-bending structures are seen in one and the other images, that we interpret as plasma slowing down as it rises, subject to gravity. Also visible are two structures showing a radial profile, that we interpret as presenting a velocity constant with height and, therefore, imply the presence of a vertical force countering gravity. The colored dots identify the two only granules followed in Fig. 9 which are visible in the image, though projected.

López Ariste et al. (2018) inferred quite high velocities of up to 40 km s^{-1} for the rising plasma. Figure 1 confirms such high speeds and even allows for higher values at some particular dates, the two under study in this work for example. Inspection of the 3-dimensional images suggests that this velocity is almost constant with height. Figure 9 shows the velocities as a function of height for 4 granules in the image of December 12th, 2013. To build this figure, we retained the position of the brightest point at every layer, inside several selected granules two of which are visible and marked in Fig. 8, and we impose that this is a radial flow, that is, that in truth all those points are physically one above the other. Accepting this hypothesis implies that any change in the distance of the brightest point in the granule to the center of the disk when changing height must be attributed to a change in velocity and not a change in position. The measured position of the brightest point in the granule gives us a measure of the actual velocity at each layer. We have computed these velocities as a function of the layer that would leave the bright centers of each granule at the same position and plotted them in Fig. 9. We have also plotted in that figure and with thick lines the escape velocities at each height, assuming masses of 15 and $18 M_{\odot}$ and radii of 955 and $1000 R_{\odot}$. Taking as initial velocity the one found in the deepest layer, we have also plotted the expected velocities as a function of height if gravity were the only force acting on the plasma. The figure confirms the impression obtained from the cuts in the 3-dimensional image: the plasma is moving at roughly constant speeds with height.

Two further conclusions are drawn from Fig. 9. One is that obviously there must be at least one other force at work compensating gravity almost perfectly to keep the velocity of the plasma constant with height. Of course, the flotability of the hot plasma makes it rise in any convective motion, so part of this constant velocity must be due to this Archimedes force. Yet numerical simulations indicate that this is not enough to keep velocities constant, and we must conclude that another force must be at work.

The second conclusion is that on the top layers this velocity may be very near the escape velocity for some of the observed plasma. For those fast granules, it is sufficient that the force or forces counteracting gravity continue doing it for just a little longer for the plasma to escape Betelgeuse's gravity and contribute to the stellar wind. By selecting the highest value of our estimate of height span to draw Fig. 9 we show the most tantalizing scenario in which this plasma is quite near escaping Betelgeuse's gravity and contributing to the stellar wind. Our

lower estimates of the maximum height at about $1.1 R_{*}$, would leave still room for this plasma to slow down and return to the star. But this is without taking into consideration that, through examination of the time evolution of these granular structures in López Ariste et al. (2018), we know that they are present for months at a time, and during that timescale the plasma does not seem to change much its velocity. If our measurements of the velocity of this plasma are valid through our long series of approximations, we captured it while escaping Betelgeuse and joining the stellar wind of this star.

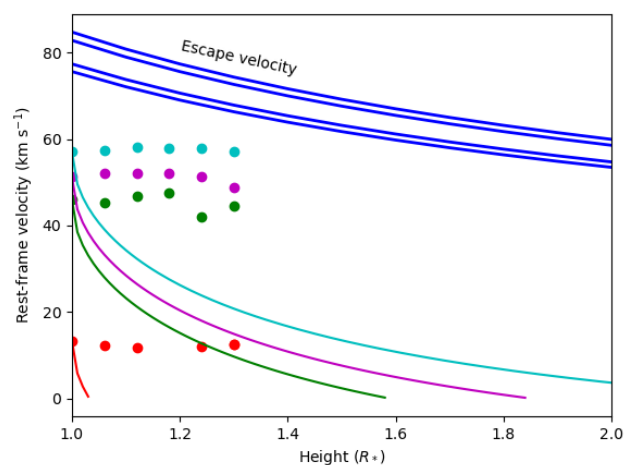


Fig. 9. The dots show the velocities as a function of height of the center of 4 granules from Dec 12th, 2013, two of which are identified in Fig. 8. These are assumed vertical structures and the velocity is computed by re-interpreting changes in the distance to disk center in terms of velocity. Two of those granules are identified in Fig. ??y their colour, are For comparison, the thin colored lines show the expected velocities in a ballistic scenario. The four thick blue lines show the escape velocity as a function of height for the 4 cases of mass 15 or $18 M_{\odot}$ and radius 955 or $1000 R_{\odot}$.

6. Conclusion

The examination of the linear polarization in the atomic lines of the spectrum of Betelgeuse led López Ariste et al. (2018) to infer images of the photosphere of this red supergiant. In order

to obtain enough signal-to-noise ratios, the polarization profiles of about 10 000 lines were added together. But we can also add polarization over smaller subsets of atomic lines and still recover signals. Here we classify them in groups for their line depth, and get, for each date of our observation data set spanning 7 years, several mean polarization profiles, function of line depth. Aurière et al. (2016) already illustrated that the signals change from one group of lines to the other, indicating that these groups of lines contain different information on the physical conditions that lead to the emission of polarization.

We have examined, and in some cases justified, the many approximations and hypothesis that lead to the inference of images from these polarization signals. Two of them, the assumption of a grey atmosphere and the single scattering approximation allow us to also interpret the changing profiles seen in lines with similar line depth. These two hypothesis together suggest that if the observed polarization amplitudes grow monotonically with line depth, one can assign an optical height to each group of lines. The actual value of the optical depth may not be reliable, but the ordering is. This matches the rough expectation that deeper lines, their cores, form higher in the atmosphere. Though we reach this result in disregard of the intensity profiles themselves. Not all datasets collected by Narval and Neo-Narval show the right ordering of polarization amplitudes that justify the two hypothesis of a grey atmosphere and single scattering. But for the majority of dates, this condition applies and we can use the polarization profiles to infer a 3-dimensional image of the photosphere of Betelgeuse. We present here 3-dimensional images of the photosphere of Betelgeuse for two particular dates in 2013 and 2021.

The many approximations and hypothesis required to infer such 3-dimensional images must caution against any direct, filterless, interpretation of them. The first date selected to create these 3-dimensional snapshots has also been studied by Aurière et al. (2016) and López Ariste et al. (2018). They showed that the inferred 2-dimensional image was comparable to interferometric images made close in time. This coincidence assigns a plausibility to the hypothesis used, and to that 2D image. The 3-dimensional images show how the observed granules form vertical coherent structures. This is somehow expected, since the inversion algorithm uses as initial condition for a given layer the solution from the layer above. Compelling as it is to interpret them as convection fluxes rising through the atmosphere, they must also be seen with caution.

The inferred images show, nonetheless, features that are not implicit in the inversion algorithm and that, in our opinion, must be regarded as real. In the present work we focus in the radial profile of those granules. The inversion algorithm uses as approximation an *a priori* maximum vertical velocity which is forced to be constant with height. Any plasma rising vertically through the photosphere and being slowed down by gravity will produce structures in the inferred image that bend towards the limb due to this approximation. We see several of them in the two investigated dates. But we also find examples of inferred vertical structures, that do not bend. The best interpretation of this unexpected feature is that the plasma in these structures is rising at constant speed.

This result can be traced back to the observed polarization profiles: the points of maximum polarization corresponding to those structures are seen to be at roughly the same wavelength independent of height. In our analysis, none of the involved hypothesis appears to be responsible of this observation. Both, the absence of an alternative explanation in terms of biases in the inference algorithm and the presence of an observational feature

supporting the result, are tantalizing arguments in favor of the rightness of our conclusion.

Plasma rising at constant velocity implies the presence of a force acting against gravity and compensating it. This force is already present in the low photospheric heights covered by our data. We have estimated that our top layer may be as high as $1.3 R_*$. At this maximum height, the observed velocities are still below the escape limit, but only barely. If the force countering gravity acts for a little longer and allows the plasma to reach $1.6 R_*$ with this same velocity, the plasma will escape gravity and enter the realm of Betelgeuse stellar wind. One or several forces must be counteracting gravity in the photosphere of Betelgeuse and maintaining plasma velocities up to large heights. Escape velocities are at reach if just these forces act a little longer. The mechanisms for wind triggering in Betelgeuse and other red supergiants appear to be at work already in the photosphere.

Appendix A: Brightness vs. velocity: the solar case

Both López Ariste et al. (2018) and the present work include a relationship between the velocity of the plasma and its brightness in the model used to fit the observed linear polarization profiles and infer the images (2- or 3-dimensional) of the photosphere of Betelgeuse. That such relationship must exist in a convective atmosphere is obvious: the hot and bright plasma rises in the atmosphere; as it cools down it slows down and is advected horizontally towards the edges of the convective cell; the cold and dark plasma sinks towards the inner layers of the atmosphere.

Koza et al. (2006) and Oba et al. (2017) have published such relationships for the solar granulation. The typical values of the solar convection appear in that data. The rising velocity of the hot plasma can be as high as 2 km s^{-1} . Similar values are seen for the sinking velocity, although supersonic velocities have often been measured in the intergranular lanes (Bellot Rubio 2009; Nesis et al. 1992; Solanki et al. 1996) and in general these sinking velocities are larger than the velocities of the rising plasma. Indeed, Koza et al. (2006) compare their measurements with numerical simulations by Stein & Nordlund (1998), which show higher sinking velocities apparently below the formation region of the spectral line used to measure the solar granulation.

In order to test the functional form given to this relationship for Betelgeuse, we have made our own measurements using a dataset of solar granulation observed with Hinode and treated and described by Malherbe et al. (2012). The time series of the patch of solar granulation contain measurements of both, the emergent intensity in the continuum near the Fe I line at 557.6nm and the velocity along the line-of-sight. Because of the position of the observed solar region near disk center, this velocity can be safely seen as the radial velocity of the plasma. Fig. A.1 shows a 2-dimensional histogram of the number of points for each pair of values of intensity and velocity.

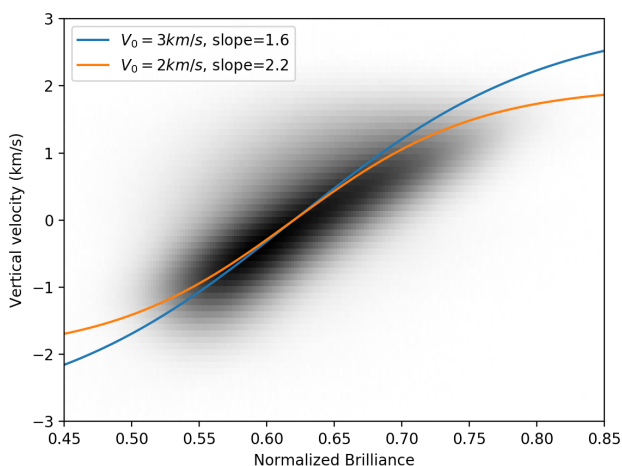


Fig. A.1. Histogram of pairs of values of radial velocity and relative intensity in the solar granulation using a dataset observed by Hinode (Malherbe et al. 2012). Two hyperbolic tangents are plotted over the histogram to illustrate how this function can capture the relationship between both observables.

Plotted over that histogram appear two curves following the function:

$$V = V_0 \tanh(\text{slope}(B - 0.62)/0.3) \quad (\text{A.1})$$

where the values of the parameters V_0 and slope are given in the figure. V and B are the radial velocity and the intensity of the

solar granulation respectively. The two other numerical parameters just make sure that the curve is well centered and suits to the relative scale used for brightness. The use of the hyperbolic tangent gets justified as a function which is linear in its core but which saturates at large values. This behaviour describes the quasi-linear relationship between brightness and velocity, while avoiding numerical issues if anomalous large values were to appear in the data.

The nice fit of this hyperbolic tangent functional relationship to the solar granulation is the sole justification to use the same function for Betelgeuse, adapting the numerical parameters to the velocities of up to 60 km s^{-1} observed in its photosphere

Acknowledgements. S.G. acknowledges support under the Erasmus+ EU program for doctoral mobility. S.G. and R.K.-A. acknowledge partial support by the Bulgarian NSF project DN 18/2.

References

- Aurière, M., Donati, J.-F., Konstantinova-Antova, R., et al. 2010, *Astronomy and Astrophysics*, 516, L2
- Aurière, M., López Ariste, A., Mathias, P., et al. 2016, *Astronomy and Astrophysics*, 591, A119
- Bellot Rubio, L. R. 2009, *The Astrophysical Journal*, 700, 284, aDS Bibcode: 2009ApJ...700..284B
- Bertout, C. & Magnan, C. 1987, *Astronomy and Astrophysics*, 183, 319
- Chandrasekhar, S. 1945, *Reviews of Modern Physics*, 17, 138
- Chiavassa, A., Freytag, B., Masseron, T., & Plez, B. 2011, *Astronomy and Astrophysics*, 535, A22
- Doherty, L. R. 1986a, *The Astrophysical Journal*, 307, 261, aDS Bibcode: 1986ApJ...307..261D
- Doherty, L. R. 1986b, *The Astrophysical Journal*, 307, 261
- Donati, J.-F., Semel, M., Carter, B. D., Rees, D. E., & Collier Cameron, A. 1997, *Monthly Notices of the Royal Astronomical Society*, 291, 658
- Freytag, B., Steffen, M., & Dorch, B. 2002, *Astronomische Nachrichten*, 323, 213
- Haubois, X., Perrin, G., Lacour, S., et al. 2009, *Astronomy and Astrophysics*, 508, 923
- Josselin, E., Lambert, J., Aurière, M., Petit, P., & Ryde, N. 2015, *Proceedings of the International Astronomical Union*, Volume 10, Symposium S305: Polarimetry: From the Sun to Stars and Stellar Environments, December 2014, 305, 299, conference Name: Polarimetry
- Kervella, P., Decin, L., Richards, A. M. S., et al. 2018, *Astronomy and Astrophysics*, 609, A67
- Koza, J., Kučera, A., Rybák, J., & Wöhl, H. 2006, *Astronomy and Astrophysics*, Volume 458, Issue 3, November II 2006, pp.941-951, 458, 941
- Kravchenko, K., Van Eck, S., Chiavassa, A., et al. 2018, *Astronomy and Astrophysics*, 610, A29
- Landi Degl'Innocenti, E. & Landolfi, M. 2004, *Polarization in Spectral Lines*, Vol. 307 (Kluwer Academic Publishers)
- López Ariste, A., Mathias, P., Tessore, B., et al. 2018, *Astronomy and Astrophysics*, 620, A199
- López Ariste, A., Tessore, B., Carlin, E. S., et al. 2019, *Astronomy and Astrophysics*, 632, A30
- López Ariste, A. e. a. 2022, *In Preparation*
- Malherbe, J.-M., Roudier, T., Rieutord, M., Berger, T., & Franck, Z. 2012, *Solar Physics*, 278, 241
- Mathias, P., Aurière, M., López Ariste, A., et al. 2018, *Astronomy and Astrophysics*, 615, A116
- Montargès, M., Cannon, E., Lagadec, E., et al. 2021, *Nature*, 594, 365, aDS Bibcode: 2021Natur.594..365M
- Montargès, M., Kervella, P., Perrin, G., et al. 2016, *Astronomy and Astrophysics*, 588, A130
- Montargès, M., Norris, R., Chiavassa, A., et al. 2018, *Astronomy and Astrophysics*, 614, A12
- Nesis, A., Bogdan, T. J., Cattaneo, F., et al. 1992, *The Astrophysical Journal*, 399, L99, aDS Bibcode: 1992ApJ...399L..99N
- Oba, T., Iida, Y., & Shimizu, T. 2017, *The Astrophysical Journal*, 836, 40
- Perrin, G., Ridgway, S. T., Coudé du Foresto, V., et al. 2004, *Astronomy and Astrophysics*, 418, 675
- Schwarz, H. E. & Clarke, D. 1984, *Astronomy and Astrophysics*, Vol. 132, p. 370-374 (1984), 132, 370
- Solanki, S. K., Ruedi, I., Bianda, M., & Steffen, M. 1996, *Astronomy and Astrophysics*, 308, 623
- Stein, R. F. & Nordlund, Å. 1998, *The Astrophysical Journal*, 499, 914, aDS Bibcode: 1998ApJ...499..914S
- Uitenbroek, H., Dupree, A. K., & Gilliland, R. L. 1998, *The Astronomical Journal*, 116, 2501

Chapter 6

Summary, main contributions and future prospects

In this final Chapter, I will give a brief summary of the study of cool evolved stars presented in my Thesis. I will also list my main contributions in the course of my PhD program. Finally, I will briefly discuss the prospects for future works on the subject of magnetism in cool evolved stars.

Summary

6.1	Summary and main contributions	188
6.1.1	M giant stars	188
6.1.2	R Scuti	189
6.1.3	Betelgeuse	189
6.2	Future prospects	191
6.2.1	M giant stars	192
6.2.2	R Scuti	195
6.2.3	Betelgeuse and other RSG stars	196

6.1 Summary and main contributions

In my Thesis, I study the subject of magnetism in cool evolved stars. This is a field difficult to investigate due to the great number of observational limitations – cool evolved stars have rotational periods so long that they are typically not known, their spectra contain many features (of both atomic and molecular origin) which often blend with each other, the velocity fields in their atmospheres are due to several effects that may be hard to disentangle. However, the late stages of stellar evolution are of importance not only to those who endeavor to study them, but to every single one of us as human beings, since they are the cosmic sources of chemical enrichment. Without the heavy elements produced and ejected by them, the Universe would not be as we know it, and we ourselves would not exist.

I focus on the study of surface magnetism in three M giant stars which show variable magnetic fields with different strength, different timescales of evolution, and, probably, different origins. I also study the possibility for a connection between the pulsations and the surface magnetic field in one post-AGB pulsating variable star, using a refined approach to focus primarily on the layers close to its photosphere and to filter out the contribution of the upper layers of its very extended atmosphere. Lastly, I study the convective motions which take place in the photospheric layers of the RSG Betelgeuse by building 3D-images of these layers from spectropolarimetric observations, and investigate their possible implications on the subject of mass loss in RSG stars.

6.1.1 M giant stars

Chapter 3 presents a study of three magnetically active M giant stars: RZ Ari, β Peg and EK Boo. From evolutionary point of view, β Peg and EK Boo are early-AGB stars. RZ Ari is also most likely at the early-AGB evolutionary stage, although there is a possibility that it is at the tip of the RGB. For each of the M giants, a variable surface magnetic field is measured and followed in a long term spectropolarimetric monitoring over several years.

RZ Ari shows a relatively strong longitudinal magnetic field (~ 10 G) while being outside the magnetic strips on the HRD (see Chapter 1). This means that for this star the Rossby number is $Ro \gg 1$, and so the magnetic dynamo is most certainly not of the $\alpha\Omega$ type. Two possibilities remain: an $\alpha^2\Omega$ type dynamo or a local type dynamo due to giant convective cells, if such cells exist in RZ Ari. The latter type of dynamo is known to be operating in the RSG star Betelgeuse (Aurière et al., 2010, 2016; Mathias et al., 2018). Giant convective cells were previously discovered using interferometric observations in the $1.5 M_{\odot}$ AGB star π^1 Gru (Paladini et al., 2018). The lithium content of RZ Ari is also abnormally high, considering its evolutionary status. This suggests that RZ Ari may have recently engulfed a nearby planet, which would explain its high lithium content and could also play a role in the magnetic activity of the star, due to an increase in angular momentum as a result of the engulfment.

β Peg shows a surface magnetic field which appears to have a simple poloidal topology, likely a dipole one, judging from the coherent variability of its longitudinal component B_l and that of the spectral lines CaH&K, H α and CaIRT, known to be indicators of magnetic activity. On the HRD, this star is inside the second magnetic strip, which means that the origin of its magnetic field could be an $\alpha\Omega$ dynamo. On the basis of the long term variability of its Stokes V signatures, I propose that the polarity of the magnetic field of β Peg changes once per year: see Section 2 of Chapter 3 and Section 6.2 of the present Chapter for more information.

EK Boo is also inside the second magnetic strip on the HRD, which means that an $\alpha\Omega$ dynamo is the likely origin of its surface magnetic field. Judging from the variability of its spectral activity indicators and B_l , the topology of the magnetic field of this star is probably a more complex one. EK Boo also shows a long term trend in its radial velocity, which is an indication that it is not a single star, but has a companion at a large distance. This companion is most likely an active M dwarf, since this could explain the large X-ray luminosity of EK Boo, which is not characteristic for its evolutionary status. EK Boo is also the only one of the three M giants studied in my Thesis for which I find net linear polarization signatures. These signatures are variable with time, and their origin is still unknown and out of the scope of the present work.

6.1.2 R Scuti

In Chapter 4, a study of the surface magnetism and atmospheric dynamics in the post-AGB pulsating variable R Sct is presented, using the longest monitoring of this star with high resolution spectropolarimetry. The periodic emergence of shockwaves from the photosphere of this star is confirmed and followed throughout the available dataset. The presence of Stokes V signatures is found in several observations, and their Zeeman origin is confirmed. A refined approach for the use of high resolution spectropolarimetric observations with LSD is proposed for the case of pulsating stars with extended atmospheres, hosting periodically propagating outward shockwaves, and is applied to the available observations of R Sct. In all the cases when the LSD Stokes I profile has a double peak, the Zeeman signature is only associated to its blueshifted lobe, which is formed in the part of the photosphere being affected and lifted by the propagation of a radiative shockwave. This indicates that the atmospheric dynamics and surface magnetism in R Sct are possibly connected, with the shockwaves locally amplifying – through a compression process – a weak surface magnetic field. Also, the presence of variable mean linearly polarized signatures associated to atomic lines in the spectrum of this star is reported.

6.1.3 Betelgeuse

The presence of giant convective cells at the surface of Betelgeuse has been proposed many times in the literature. Using spectropolarimetric observations in linear polariza-

tion, López Ariste et al. (2018) inferred images of the surface of Betelgeuse which are built assuming giant convective cells are present at the level of the photosphere. These authors obtain results which successfully match the direct images of the star obtained through interferometry, suggesting that indeed such giant cells are present in Betelgeuse.

The study presented in Chapter 5 of my Thesis is a continuation of the work of López Ariste et al. (2018). A careful inspection of the LSD profiles of Betelgeuse in linear polarization shows that the convective velocities in this RSG star may reach up to 60 km s^{-1} , close to the escape velocity of the star. By analyzing the way the Stokes Q and U amplitudes are ordered for atomic lines of different depths, the relative altitude of formation of these lines in the atmosphere of Betelgeuse is found. This allows the construction of 3-dimensional images of the low atmosphere ($1 - 1.3R_{\star}$) of the star, assuming a constant velocity of the convective flows with height. From the resulting images, this assumption appears to sometimes not be correct – some of the inferred convective cells appear to bend towards the limb as they ascend, suggesting that the convective flows decelerate with altitude. However, many others appear to be rising in a vertical manner, suggesting that the convective velocity is indeed constant for them. This requires the presence of at least one force which counteracts gravity by accelerating the particles upwards. The proposed velocity of 60 km s^{-1} is barely below the expected escape velocity in the layers probed by the 3-dimensional images, but if the force(s) counteracting gravity continue to act only a little higher, up to $1.6R_{\star}$, the convective flows could reach the escape velocity. Thus, it may be that the mechanisms which cause mass loss in RSG stars are already at work at the level of the photosphere.

Main technical contributions

My main technical contributions during the course of my PhD are:

1. I created a fully automated interface for LSD which not only performs autonomously all the computations necessary to produce the LSD profiles, but also runs the detection statistics, calculates the longitudinal magnetic field (for Stokes V observations), computes the spectral activity indicators and radial velocity using a gaussian fit on the Stokes I LSD profile.
2. In order to estimate the projected rotational velocity and the macroturbulent velocity of the M giant star RZ Ari, I developed an improvement of the classical method for determination of stellar parameters using spectrum synthesis and the LSD software.
3. During the time NeoNarval was still being set up, I helped the engineering team by analyzing the data obtained with the instrument and pointed out possible technical issues with the data reduction procedures.
4. I wrote a program which converts the data obtained with NeoNarval into the format of Narval. There was a large popular demand for such a tool, since it allows for

maximum consistency between measurements done with the two instruments. The program is available at the official TBL website.

5. During my 2-months stay (February and March 2021) under the ERASMUS EU program for doctoral mobility at the *Institut de Recherche en Astrophysique et Planétologie* (IRAP) in Toulouse, I wrote the software tool which creates the 3-dimensional images of Betelgeuse from Narval and NeoNarval observations.

Main scientific contributions

My main scientific contributions in the Thesis are:

1. I studied, using the LSD method, the surface magnetic field variation in the M giant stars β Peg and EK Boo, and showed that their topologies are probably different: a simple dipole-like one for β Peg and a more complex one for EK Boo.
2. I found a significant long-term variability in the radial velocity of EK Boo, confirming the existence of a companion star.
3. I report, for the first time in an M giant star, the presence of variable net linear polarization in the atomic lines of EK Boo.
4. I estimated the projected rotational velocity $v \sin i$ of RZ Ari to be 6 km s^{-1} , which allowed the computation of the upper limit of its rotational period.
5. I studied the surface magnetic field variation in RZ Ari. The origin of the magnetic activity of this star is still unknown, although some possible scenarios exist: an $\alpha^2\Omega$ type dynamo, or a local dynamo due to giant convective cells, if such cells exist in RZ Ari, and/or due to a planet engulfment event.
6. Using an improvement of the usual approach for the analysis of spectra of pulsating evolved stars via LSD, I studied the surface magnetic field in the post-AGB star R Sct. I showed that the surface magnetic field of this pulsating variable star could be linked to the atmospheric dynamics.
7. During my 2-months stay in Toulouse under the ERASMUS EU program, I worked under the direct supervision of Dr. Arturo López Ariste on a study of the convective motions at the level of the photosphere of Betelgeuse by building 3-dimensional images of its photosphere from spectropolarimetric observations. It was found that the convective velocity in this RSG star is very close to the escape velocity, which might explain the severe mass loss that RSGs are known to experience.

6.2 Future prospects

The long-term monitoring of M giant stars, R Sct and Betelgeuse using the TBL continues even after the shutting down of Narval – now using its successor, NeoNarval. In this

section, I will discuss the measurement of the spectral activity indicators using NeoNarval and how their values can be compared to those measured from Narval observations. I will then briefly list some of the prospects for future work concerning M giant stars, and will also list some of the questions regarding R Sct and Betelgeuse which remain to be answered by future studies.

6.2.1 M giant stars

An important proxy for the magnetic field in M giant stars are the spectral activity indicators (described in Section 5 of Chapter 2) which trace the magnetic heating in the stellar chromosphere. However, there are two key points that must be kept in mind when computing the spectral activity indicators from NeoNarval observations. The first point concerns comparing activity indicators computed from NeoNarval data to those computed using data from Narval, or from any other instrument in general. The activity indicators are calculated generally as a ratio between the flux inside certain spectral lines F_{lines} and the flux $F_{\text{continuum}}$ in some adjacent spectral window, considered to represent the level of the continuum. However, due to the instrumental differences between individual spectrographs, and the different ways the observations are processed by their respective data reduction softwares, the normalization to the continuum is not the same for data obtained with different instruments. Because of these differences, both F_{lines} and $F_{\text{continuum}}$ will usually depend on the instrument used, and so will the final value I of the activity indicator being computed. This is why the exact values of the activity indexes are *instrument dependent*. In the study of M giants presented in Chapter 3 of my Thesis, this is not a problem, since I use a homogeneous data set consisting solely of Narval observations. However, the $H\alpha$ and CaIRT activity indexes computed from NeoNarval data ($I_{\text{NeoNarval}}$) have systematically larger values than those obtained with Narval (I_{Narval}), and thus they cannot be directly compared to each other.

One way to solve this problem would be to find a function f such that $f(I_{\text{NeoNarval}}) = I_{\text{Narval}}$, i.e. to calibrate NeoNarval fluxes to the Narval ones. For example, this was done by Aurière et al. (2015) who calibrated the S-indexes of Narval and ESPaDOnS. In the future, such a calibration may be done for Narval and NeoNarval by measuring $I_{\text{NeoNarval}}$ for stars which have been observed with Narval that show no variability in their spectral activity indicators, i.e. chromospherically inactive stars.

Another solution would be to simply regard Narval and NeoNarval indicators separately. For long datasets, this is possible because it is only the variability of the indicators that is used to study the magnetic activity, and not their precise values. If looking at a dataset which consists of measurements of the activity indicators from both Narval and NeoNarval observations of a star with a variable magnetic field, one would be able to detect this variability in both the Narval and the NeoNarval subsets. What would not be possible is to detect any variability, or lack thereof, between the last Narval observation and the first NeoNarval one in the dataset.

The second key point that must be considered when computing spectral activity indicators with NeoNarval concerns the S-index, which measures the flux at the cores of the CaH&K lines. NeoNarval is less sensitive in the blue part of the spectrum than it is in the red. This has to be taken into account when picking exposure times in order for sufficient signal to be acquired in the CaH&K lines. Unfortunately, for the observations of M giant stars obtained so far (up to September 2021), this different sensitivity was not considered. Because of this, the CaH&K lines show practically no signal in any of them. This is why no values of the S-index could be computed for these observations.

RZ Arietis

Interferometric observations of RZ Ari are scheduled with the interferometer CHARA at Mount Wilson, California. The purpose of these observations is to obtain images of the surface of RZ Ari, in order to establish if giant convective cells are present in this M giant (as it has already been found to be the case for the AGB star π^1 Gru by Paladini et al. 2018). If such cells exist in RZ Ari, then the magnetic field of this star could be caused by a local dynamo operating between them, as it has been established to be the case in the RSG star Betelgeuse. The interferometric observations will be quasi-simultaneous with observations in high resolution spectropolarimetry using NeoNarval, and in this way information on the surface magnetic field will also be available.

β Pegasi

β Peg continues to be observed in circular polarization using NeoNarval. So far, 10 such observations have been obtained in the period September 2019 - September 2021. For 3 observations, a definite detection of Stokes V signatures is obtained: 2020/07/06, 2020/08/23 and 2021/06/06. The polarity of the calculated magnetic field is negative in 2020 and positive in 2021. This is in good agreement with the hypothesis I make in Section 2.2 of Chapter 3 that the magnetic field of β Peg changes polarity once every year, with the exception of an unexpected change that occurred at some point in time between December 2016 and June 2018. Future observations may be necessary in order to prove or disprove this suggested periodicity.

EK Boötis: is it possible to map M giant stars?

Certainly, a future prospect for the study of EK Boo is the exploration of its linear polarization signatures. Having a spectral type of M5III, EK Boo is the coolest and most evolved of the three M giants presented in my Thesis. It could be that this is the reason why linear polarization is present in its spectrum, while it is not present in the spectra of RZ Ari and β Peg.

The origin of these linearly polarized signatures in EK Boo remains so far unexplained. One may wonder if it is possible to apply the method developed by López Ariste et al.

(2018), either directly or after some modification, to map the surface brightness of an M giant star such as EK Boo. While at the time of writing of this Thesis no such maps have been produced, in the present section I will give some thoughts in this direction, in hope to provide inspiration and a good starting point for future works.

Firstly, direct application of the inversion code to observations of M giants, EK Boo in particular, will likely not yield any meaningful results, since certain observational characteristics (mentioned below) of these stars appear to be rather different than those of RSGs such as Betelgeuse. The model of López Ariste et al. (2018) is based on the key fact that the linear polarization signal observed in the spectrum of Betelgeuse is caused by the polarized (due to Rayleigh scattering) continuum being depolarized in atomic lines which form above it. A key discovery that leads to this conclusion is the fact that the D1 and D2 lines of the sodium doublet show similar degrees of linear polarization; following Aurière et al. (2016), this is a clear sign that these signatures are not formed by intrinsic polarization, but are instead likely due to depolarization of the continuum. Aurière et al. (2016) generalize this result, suggesting that this is the case for most atomic lines, and so that the net linear polarization of Betelgeuse is caused by depolarization of the continuum in the lines and is detectable due to surface brightness inhomogeneities. This leads to the conclusion that for each point across the disk of the star, there is a direct link between the surface brightness and the observed degree of polarization.

With the data present at this time, the same claim cannot be made however for EK Boo: while average signatures can be seen in the LSD profiles of this M giant, no signal has been found so far inside individual spectral lines, including the NaD. This likely means that in EK Boo there is a linearly polarized signal associated to atomic lines (as it is detected in its averaged profiles using LSD), but this signal is simply too faint to be detected in individual lines, as it might be below the noise level. Still, we could suppose that the linear polarization profiles of the NaD spectral lines of EK Boo have the same relative amplitudes as those found in Betelgeuse, but that we are unable to confirm it due to the low SNR. We could then further assume that perhaps the linearly polarized signatures in EK Boo are also due to depolarization of the continuum in the atomic lines, and in turn attempt to link the polarization rate and the surface brightness based on this assumption. While the currently available observations do not point towards this scenario, they do not exclude it either.

However, even if we assume that the net linear polarization observed in EK Boo has the same physical origin as in Betelgeuse and other RSGs, there still remain differences in these two types of stars that need to be considered. One such difference can be found in the position of the polarization signal in radial velocity space. Following Mathias et al. (2018), in Betelgeuse the Stokes V signal appears redshifted with respect to the centre of gravity of the Stokes I profile, which these authors interpret as the magnetic field being locally constrained to areas where downflow movements of the plasma dominate (i.e.

the dark intergranular lanes between convective cells). The Stokes Q & U signatures, on the other hand, are strongly blue-shifted in Betelgeuse, which López Ariste et al. (2018) consider to be caused by the upflowing bright parts of convection cells. These two phenomena play a key role in the model of Betelgeuse proposed by López Ariste et al. (2018). There, the local brightness at a given point of the photosphere depends on the local radial velocity: red-shifted motion corresponds to lower brightness, and blue-shifted motion – to higher brightness.

This does not seem to be the case for the EK Boo. In its LSD spectrum, neither linear nor circular polarization profiles show any significant radial velocity displacement with respect to the Stokes I . Thus, the relation between velocity and brightness, which is fundamental when building images of the photospheres of RSGs, does not appear to be present in the M giant EK Boo.

The differences in rotation are also a point which must be considered. Because the velocity fields in Betelgeuse are completely dominated by convection (the convective flows having velocities as high as 60 km s^{-1}), in the models of López Ariste et al. (2018) and López Ariste et al. (2022) the star is considered to not be rotating. This is not a good approximation for M giants, and especially β Peg, where we observe strong indications of rotational modulation of both the B_l and the spectral activity indicators.

To summarize, in RSGs linear polarization reflects both the radial velocity and surface brightness distributions, while it may not be the case for EK Boo. This fact, along with stellar rotation, must be taken into account when constructing an inversion model for this M giant star. Future observations with higher SNR are crucial to give a definitive answer to the question for the origin of linear polarization signals in the spectrum of EK Boo, and to give insight whether surface mapping using these signatures is possible or not. Interferometric observations of EK Boo and other M giant stars are also necessary in order to establish if surface brightness inhomogeneities, such as giant convective cells are present at their surfaces. The presence of such structures has already been confirmed for the AGB star π^1 Gru by Paladini et al. (2018).

6.2.2 R Scuti

The study of R Sct presented in Chapter 4 of my Thesis aims to study the surface magnetic field in this pulsating post-AGB star, to trace the dynamics in its atmosphere and to find if there is an interplay between them. While the results of this study show that such a connection between dynamics and magnetism is indeed possible, the observations available from Narval are insufficient to give a definitive answer if it exists or not. Future observations of R Sct in circular polarization with NeoNarval could be the key to prove or disqualify the existence of such a connection.

In Chapter 4, I also report the presence of mean linear polarization in the atomic lines in the spectrum of R Sct. Another point which remains yet to be studied is the physical origin of these polarized signatures. One possible such origin are asymmetrical velocity

fields caused by the radiative shockwaves, as it has been proposed by López Ariste et al. (2019) for the Mira star χ Cyg.

In the study presented in Chapter 4, I use a refined LSD mask, consisting only of atomic lines with high excitation potential ($\chi \geq 2$ eV) to probe the magnetic field and dynamics only at the level of the photosphere. One direction future studies could take is to embark on a full tomographic analysis of R Sct (see, e.g., Kravchenko et al. 2018), in order to build a very detailed picture of the atmospheric dynamics in its extended atmosphere.

6.2.3 Betelgeuse and other RSG stars

In Chapter 5, I have presented the methods for 2D and 3D imaging of Betelgeuse using spectropolarimetric observations. In these methods, the radial velocity of the linearly polarized signatures is used to infer the distance from disk center of the source of polarization signal: signals associated to the maximum convective velocity V_{\max} are considered to be connected to structures at disk center, while signals associated to the restframe velocity of the star V_{\star} are considered to originate from the limb of Betelgeuse. However, in some of the observations obtained with Narval and NeoNarval, signatures are also seen beyond V_{\star} . One way to interpret these signatures, which seem to originate from structures beyond the limb of the star, is to consider that they are formed in convective cells which are located on the far side of Betelgeuse, just beyond the visible edge of the disk, but are so high in altitude that they can be seen emerging over the limb. Such beyond-the-limb structures, if they are indeed the correct explanation for the observed polarization signals, may give precious information on the maximum height a convective cell may reach above the photosphere of Betelgeuse. This would in turn lead to a better understanding of the origin of mass loss in Betelgeuse, as well as in other stars where beyond-the-limb structures are suspected, e.g. the RSG μ Cep.

Acknowledgements

I would like to thank the LUPM, the UM and the ED I2S doctoral school for their hospitality and for the good working conditions while I was in Montpellier.

For the work presented in Chapters 3 and 5, I acknowledge partial support by the Bulgarian NSF project DN 18/2, including also a part of the observations used.

I acknowledge partial support from the Projet MAGEVOL (AAP2017) from I-Site MUSE (PI: Agnès Lèbre).

For the work presented in Chapter 6, I acknowledge partial support from the ERASMUS EU program for doctoral mobility. I would also like to thank IRAP-Toulouse for their hospitality and good working conditions while I was in Toulouse.

This work was supported by the "Programme National de Physique Stellaire" (PNPS) of CNRS/INSU, co-funded by CEA and CNES.

I would like to thank all the colleagues at IA-Sofia, LUPM-Montpellier and IRAP-Toulouse with whom I've worked during the three years of my PhD. It is a true pleasure to know such bright and kind people.

To my supervisors, Agnès and Renada. I thank you deeply for all your support, for all the knowledge and skills that you gave me, and for your hard work that taught me how to be a scientist. Thank you.

To Arturo López Ariste. Thank you for your mentorship, for your patience and understanding, and for the pleasure of working with you on such an exciting topic.

To Eric Josselin. Thank you for sharing your rich expertise with me on so many occasions.

To Loann Brahim. Thank you for your friendship, your trust, and your great support in times when I needed it the most.

To Radoslav Sotirov. Thank you for being my friend and for the inspiration you've given me. Surely, were it not for you, I would not be gazing at the stars today.

To my family. Thank you for being the giants upon whose shoulders I stand.

Bibliography

- Airapetian, V. S., Ofman, L., Robinson, R. D., Carpenter, K., and Davila, J.: 2000, *Astrophysical journal* **528**, 965
- Alvarez, R., Jorissen, A., Plez, B., et al.: 2001, *A&A* **379**, 305
- Alvarez, R., Jorissen, A., Plez, B., Gillet, D., and Fokin, A.: 2000, *A&A* **362**, 655
- Asplund, M., Grevesse, N., Sauval, A. J., and Scott, P.: 2009, *ARA&A* **47**, 481
- Aurière, M.: 2003, *EAS Publications Series* **9**, 105–105
- Aurière, M., Donati, J.-F., Konstantinova-Antova, R., et al.: 2010, *A&A* **516**, L2
- Aurière, M., Konstantinova-Antova, R., Charbonnel, C., et al.: 2015, *A&A* 574
- Aurière, M., Konstantinova-Antova, R., Petit, P., et al.: 2011, *A&A* **534**, A139
- Aurière, M., López Ariste, A., Mathias, P., et al.: 2016, *A&A* 591
- Bagnulo, S., Landolfi, M., Landstreet, J. D., et al.: 2009, *Publications of the Astronomical Society of the Pacific* **121(883)**, 993–1015
- Borisova, A., Aurière, M., Petit, P., et al.: 2016, *A&A* **591**, A57
- Cameron, A. G. W.: 1955, *ApJ* **212**, 144
- Cameron, A. G. W. and Fowler, W. A.: 1971, *ApJ* **164**, 111
- Charbonneau, P.: 2010, *Living Rev. Solar Phys.* **7**, 3
- Charbonnel, C., Decressin, T., and Lagarde, N. e. a.: 2017, *Astronomy and Astrophysics* **605**, A102
- Charbonnel, C. and Do Nascimento, J. D.: 1998, *A&A* **336**, 915
- Charbonnel, C. and Zahn, J. P.: 2007, *A&A* **476**, L29

BIBLIOGRAPHY

- Chiavassa, A., Freytag, B., Masseron, T., and Plez, B.: 2011a, *A&A* **535**, A22
- Chiavassa, A., Haubois, X., and Young, J. S., e. a.: 2010, *A&A* **515**, A12
- Chiavassa, A., Pasquato, E., and Jorissen, A., e. a.: 2011b, *A&A* **528**, A120
- Chiavassa, A., Plez, B., Josselin, E., and Freytag, B.: 2009, *A&A* **506**, 1351
- Clarke, D. and Schwarz, H. E.: 1984, *A&A* **132**, 375
- Cotton, D. V., Bailey, J., Horta, A. D., Norris, B. R. M., and Lomax, J. R.: 2020, *Research Notes of the American Astronomical Society* **4**, 39
- de Boer, K. S. and Seggewiss, W.: 2008, *Stars and Stellar Evolution*, EDP Sciences
- Dearborn, D., Eggleton, P., and Schramm, D.: 1976, *ApJ* **203**, 455
- Dearborn, D. S. P.: 1992, *Phys. Rep.* **210**, 367
- Doherty, L. R.: 1986, *ApJ* **307**, 261
- Donati, J.-F. and Brown, S. F.: 1997, *A&A* **326**, 1135
- Donati, J.-F., Catala, C., Landstreet, J., and Petit, P.: 2006a, *Solar Polarization Workshop n4, ed. R. Casini, B. Lites* **358, ASPC Ser.**, 362
- Donati, J.-F., Howarth, I., Jardine, M., et al.: 2006b, *MNRAS* **370**, 629
- Donati, J.-F., Semel, M., Carter, B. D., Rees, D. E., and Cameron, A. C.: 1997, *Monthly Notices of the Royal Astronomical Society* **291(4)**, 658–682
- Dorch, S. B. F.: 2004, *A&A* **423**, 1101
- Dorch, S. B. F. and Freytag, B.: 2003, *IAU Symp.* **210**, 12
- Dumont, T., Charbonnel, C., Palacios, A., and Borisov, S.: 2021a, *arXiv e-prints, arXiv:2107.12060*
- Dumont, T., Palacios, A., Charbonnel, C., et al.: 2021b, *A&A* **646**, A48
- Duncan, D., Vaughan, A., Wilson, O., et al.: 1991, *The Astrophysical Journal Supplement Series* **76**, 383
- Dupree, A. K., Strassmeier, K. G., Matthews, L. D., et al.: 2020, *ApJ* **899**, 68
- Famaey, B.: 2005, *Radial velocities for 6691 K and M giants, Catalogue*
- Freytag, B., Steffen, M., and Dorch, B.: 2002, *Astron. Nachr.* **323**, 213
- Georgiev, S., Konstantinova-Antova, R., Lèbre, A., et al.: 2020a, *Bulgarian Astronomical Journal* **33**, 87

BIBLIOGRAPHY

- Georgiev, S., Lèbre, A., Josselin, E., Konstantinova-Antova, R., and Morin, J.: 2020b, *Astronomische Nachrichten* **341(5)**, 486–492
- Gillet, D., Duquennoy, A., Bouchet, P., and Gouiffes, C.: 1989, *A&A* **215**, 316
- Gillet, D., Maurice, E., and Baade, D.: 1983, *A&A* **128**, 384
- Gilliland, R. L.: 1985, *ApJ* **299**, 286
- Gilliland, R. L. and Dupree, A. K.: 1996, *ApJ* **463**, L29
- Goldberg, J. A., Jiang, Y.-F., and Bildsten, L.: 2021, *arXiv e-prints* p. arXiv:2110.03261
- Gray, D.: 1992, *The observation and analysis of stellar photospheres*, Cambridge University Press
- Gray, D.: 2013, *AJ* **146**, 29
- Guinan, E., Wasatonic, R., Calderwood, T., and Carona, D.: 2020, *The Astronomer's Telegram* **13512**, 1
- Gustafsson, B., Edvardsson, B., Eriksson, K., et al.: 2008, *Astronomy & Astrophysics* **486(3)**, 951–970
- Halabi, G. M. and El Eid, M.: 2016, *in Journal of Physics Conference Series* **703**, 012019
- Hartmann, L. and Avrett, E. H.: 1984, *Astrophysical journal* **284**, 238
- Haubois, X., Perrin, G., Lacour, S., et al.: 2009, *A&A* **508**, 923
- Hayes, D. P.: 1984, *The Astrophysical Journal Supplement Series* **55**, 179
- Höfner, S.: 2008, *A&A* **491**, L1
- Hünsch, M., Konstantinova-Antova, R., Schmitt, J. H. M., et al.: 2004, *Proc. IAU Symp.* **219**, 223
- Hünsch, M., Schmitt, J. H. M. M., Schröder, K. P., et al.: 1998, *A&A* **330**, 225
- Iben, I.: 1985, *Stellar Evolution Physics, Volume 1: Physical Processes in Stellar Interiors*, Cambridge University Press
- Josselin, E., Lambert, J., Aurière, M., Petit, P., and Ryde, N.: 2015, *Proc. IAU Symp.* **305**, 299
- Josselin, E. and Plez, B.: 2007, *A&A* **469**, 671
- Joyce, M., Leung, S., Molnár, L., et al.: 2020, *ApJ* **902**, 63
- Jura, M.: 1986, *ApJ* **309**, 732

BIBLIOGRAPHY

- Karakas, A. I. and Lattanzio, J. C.: 2014, *PASA* **31**, e030
- Kervella, P., Decin, L., Richards, A. M. S., et al.: 2018, *A&A* **609**, A67
- Kipper, T. and Klochkova, V. G.: 2013, *Baltic Astronomy* **22**, 77
- Kiss, L. L., Szabó Gy, M., and Bedding, T. R.: 2006, *MNRAS* **372**, 1721
- Konstantinova-Antova, R., Aurière, M., Charbonnel, C., et al.: 2010, *Astronomy and Astrophysics* **524**, A57
- Konstantinova-Antova, R., Aurière, M., Charbonnel, C., et al.: 2013, *Bulgarian Astronomical Journal* **19**, 14
- Konstantinova-Antova, R., Aurière, M., Charbonnel, C., et al.: 2014, in P. Petit, M. Jardine, and H. C. Spruit (eds.), *Magnetic Fields throughout Stellar Evolution*, Vol. 302, pp 373–376
- Konstantinova-Antova, R., Aurière, M., Schröder, K.-P., and Petit, P.: 2009, *Cosmic Magnetic Fields: From Planets, to Stars and Galaxies* p. 433
- Konstantinova-Antova, R., Lèbre, A., Aurière, M., et al.: 2018, *Proceedings of the XI Bulgarian-Serbian Astronomical Conference (XI BSAC), Publ. Astron. Soc. "Rudjer Bošković"* **18**, 93
- Korhonen, H.: 2014, *Magnetic Fields throughout Stellar Evolution* **302**, 350
- Kravchenko, K., Van Eck, S., Chiavassa, A., et al.: 2018, *A&A* **610**, 29K
- Krishna Swamy, K. S.: 1966, *ApJ* **145**, 174
- Kunder, A., Kordopatis, G., Steinmetz, M., et al.: 2017, *AJ* **153**, 75
- Kupka, F., Piskunov, N., Ryabchikova, T. A., Stempels, H. C., and Weiss, W. W.: 1999, *Astronomy and Astrophysics Supplement Series* **138(1)**, 119–133
- Lagarde, N., Decressin, T., Charbonnel, C., et al.: 2012a, *A&A* **543**, 108
- Lagarde, N., Decressin, T., Charbonnel, C., et al.: 2012b, *A&A* **543**, A108
- Lambert, D. L., Brown, J. A., Hinkle, K. H., and Johnson, H. R.: 1984, *ApJ* **284**, 223
- Landi Degl’Innocenti, E. and Landolfi, M.: 2004, *Polarization in Spectral Lines*, ASSL
- Landstreet, J. D.: 2004, *Proc. Magnetic stars* p. 11
- Lebzelter, T., Hinkle, K. H., Straniero, O., et al.: 2019, *ApJ* **886**, 117
- Levesque, E. M. and Massey, P.: 2020, *ApJ* **891**, L37
- Lomb, N.: 1976, *Ap&SS* **39**, 447

BIBLIOGRAPHY

- Lèbre, A., Aurière, M., Fabas, N., et al.: 2014, *A&A* **561**, A85
- Lèbre, A., Aurière, M., Fabas, N., et al.: 2015, *Proceedings of the International Astronomical Union* **10**, 47–52
- Lèbre, A. and Gillet, D.: 1991a, *A&A* **246**, 490
- Lèbre, A. and Gillet, D.: 1991b, *A&A* **251**, 549
- López Ariste, A., Georgiev, S., Mathias, P., et al.: 2022, *A&A*
- López Ariste, A., Mathias, P., Tessore, B., et al.: 2018, *A&A* 620
- López Ariste, A., Tessore, B., Carlín, E., et al.: 2019, *A&A* **632**, A30
- Magain, P.: 1984, *A&A* **134**, 189
- Magalhaes, A. M. and Nordsieck, K. H.: 2000, *Proc. IAU Symp.* **177**, 433
- Massarotti, A., Latham, D., Stefanik, R., and Fogel, J.: 2008a, *AJ* **135**, 209
- Massarotti, A., Latham, D. W., Stefanik, R. P., and Fogel, J.: 2008b, *AJ* **135**, 209M
- Mathias, P., Aurière, M., López Ariste, A., et al.: 2018, *A&A* 615
- Moffatt, H.: 1978, *Magnetic field generation in electrically conducting fluids*, Cambridge Univ. Press
- Montargès, M., Cannon, E., Lagadec, E., et al.: 2021, *Nature* **594**, 365
- Montargès, M., Kervella, P., Perrin, G., et al.: 2015, *A&A* **588**, A130
- Montargès, M., Kervella, P., Perrin, G., et al.: 2016, *A&A* **588**, A130
- Montargès, M., Norris, R., Chiavassa, A., et al.: 2018, *A&A* **614**, A12
- Mosser, B., Goupil, M., Belkacem, K., et al.: 2012, *A&A* **548**, 10
- Mucciarelli, A.: 2011, *A&A* **528**, A44
- Nordhaus, J., Busso, M., Wasserburg, G. J., et al.: 2008, *ApJ* **684**, L29
- Nordlund, A., Stein, R. F., and Asplund, M.: 2009, *Living Reviews in Solar Physics* **6**, 117
- Nordsieck, K., Rao, L., Meade, M., et al.: 1994, *BAAS* **26**, 864
- Ohnaka, K., Weigelt, G., Millour, F., et al.: 2011, *A&A* **529**, A163
- O’Gorman, E., Harper, G. M., Ohnaka, K., et al.: 2020, *A&A* **638**, A65
- Paladini, C., Baron, F., Jorissen, A., et al.: 2018, *Nature* **553**, 310

BIBLIOGRAPHY

- Percy, J. R. and Deibert, E.: 2016, *The Journal of the AAVSO* **44(2)**, 94
- Percy, J. R., Mashintsova, M., Nasui, C. O., et al.: 2008, *PASP* **120(867)**, 523
- Plez, B.: 2012, *Astrophysics Source Code Library, record ascl:1205.004*
- Plez, B. and Lambert, D. L.: 2002, *A&A* **386**, 1009
- Prugniel, P., Vauglin, I., and Koleva, M.: 2011, *Astronomy and Astrophysics* **531**, A165
- Rees, D. E. and Semel, M. D.: 1979, *A&A* **74**, 1
- Richichi, A., Fors, O., Merino, M., et al.: 2006, *Astronomy and Astrophysics* **445(3)**, 1081
- Rosby, C. G.: 1939, *J. Marine Res.* **2**, 38
- Sabin, L., Wade, G. A., and Lèbre, A.: 2015, *MNRAS* **446**, 1988
- Salaris, M., Cassisi, S., and Weiss, A.: 2002, *PASP* **114**, 375
- Samus, N., Kazarovets, E., O.V., D., et al.: 2017, *GCVS 5.1, Astronomy Reports* **61**, No. 1, 80
- Scargle, J. D.: 1982, *ApJ* **1:263**, 835
- Schwarz, H. E. and Clarke, D.: 1984, *A&A* **132**, 370
- Schwarzschild, M.: 1975, *ApJ* **195**, 137
- Semel, M.: 1989, *A&A* **225**, 456
- Siess, L. and Livio, M.: 1999, *Monthly Notices of the RAS* **304**, 925
- Simon, T. and Drake, S.: 1989, *ApJ* **346**, 303
- Smith, N., Humphreys, R. M., Davidson, K., et al.: 2001, *AJ* **121**, 1111
- Soker, N. and Zoabi, E.: 2002, *Monthly Notices of the RAS* **329**, 204
- Soubiran, C., Bienayme, O., Mishenina, T. V., and Kovtyukh, V.: 2008, *A&A* **480**, 91S
- Stenflo, J. O., Twerenbold, D., and Harvey, J. W.: 1983, *A&ASS* **52**, 161
- Stothers, R.: 2010, *ApJ* **725**, 1170
- Tabur, V., Bedding, T. R., Kiss, L. L., et al.: 2009, *Monthly Notices of the RAS* **400(4)**, 1945
- Tessore, B., Lèbre, A., Morin, J., et al.: 2017, *A&A* **603**, A129
- Tsuji, T.: 2008, *A&A* **489**, 1271

BIBLIOGRAPHY

- Tsvetkova, S., Petit, P., Aurière, M., et al.: 2013, *A&A* **556**, A43
- Uitenbroek, H., Dupree, A. K., and Gilliland, R. L.: 1998, *AJ* **116**, 2501
- van Dyck, H., van Belle, G., and Thomson, R. e. a.: 1998, *AJ* **116**, 981
- van Loon, J. T.: 2006, Vol. 353, p. 211
- Villaume, A., Conroy, C., Johnson, B., et al.: 2017, *Astrophysical Journal, Supplements* **230(2)**, 23
- Wallerstein, G. and Cox, A. N.: 1984, *PASP* **96**, 677
- Willson, L. A.: 2000, *Annual Review of Astron and Astrophys* **38**, 573
- Xu, Y., Takahashi, K., Goriely, S., et al.: 2013, *Nucl. Phys. A* **918**, 61
- Zamanov, R., Bode, M., Melo, C., et al.: 2007, *MNRAS* **380**, 1053
- Zamanov, R., Bode, M., Melo, C., et al.: 2008, *MNRAS* **390**, 377